



The
University
Of
Sheffield.

Exploring the effects of d^{10} and d^0 cations on the magnetic interactions in perovskite structures

Charlotte Pughe

Thesis submitted for the degree of Doctor of Philosophy (PhD)

Department of Materials Science and Engineering

Supervisor: Prof Eddie Cussen

July 2022

Abstract

This thesis focuses on the effects of non-magnetic d^{10} and d^0 B'' cations in $A_2B'B''O_6$ perovskites with magnetic B' cations. Non-magnetic $B'' = d^{10}$ or d^0 cations can induce different types of magnetic ordering, as well as introduce frustration that suppresses magnetic ordering.

The d^{10}/d^0 effect was first investigated in Ba_2MnTeO_6 and Ba_2MnWO_6 . These are ideal structures for $Te^{6+} d^{10}$ vs $W^{6+} d^0$ comparisons as they are isostructural, cubic and have classical spin-only $Mn^{2+} S = 5/2$ interactions described using a simple J_1 - J_2 Heisenberg model. The research in chapter 3 confirmed Ba_2MnTeO_6 and Ba_2MnWO_6 are isostructural and display different types of antiferromagnetic order. This resulted from the contrasting d^{10} vs d^0 contributions to superexchange. The filled $Te^{6+} 4d^{10}$ orbital did not contribute to next-nearest neighbour (J_2) superexchange, whereas the empty $W^{6+} 5d^0$ orbital did. This established the d^{10}/d^0 effect where $Te^{6+} d^{10}$ promotes a strong nearest neighbour (J_1) interaction and $W^{6+} d^0$ promotes a strong J_2 interaction leading to different types of magnetic order.

The d^{10}/d^0 effect was highlighted in a number of double perovskite structures. Chapter 4 investigated whether the d^{10}/d^0 effect can be extended to hexagonal perovskites using a mixture of d^{10} and d^0 cations at the B'' site. Site-selective $W^{6+} d^0$ substitution at the corner-sharing site was identified in the hexagonal perovskite $Ba_2CuTe_{1-x}W_xO_6$. Magnetic characterization in chapter 5 showed this led to d^{10}/d^0 tuning of the magnetic interactions from a spin ladder towards a spin chain. The disorder introduced by the competing strong J_1 (Te^{6+}) vs strong J_2 (W^{6+}) prevented Néel ordering. Therefore, demonstrating the d^{10}/d^0 effect can be applied to both simple and complex perovskite structures to tune magnetic interactions.

Continuing with the Ba_2CuTeO_6 structure, chapter 6 investigated the effect of non-magnetic Zn^{2+} (d^{10}) substitution at the Cu^{2+} site in Ba_2CuTeO_6 . Removal of Cu^{2+} cations changed the magnetic behaviour, with evidence of suppressed magnetic ordering beyond $x > 0.1$ in $Ba_2Cu_{1-x}Zn_xTeO_6$. This demonstrates non-magnetic cations can be employed to modify the spin ladder behaviour at both the B' and B'' site. Further work is needed to determine how closely the magnetic structure of the $x = 0.1, 0.2$ and 0.3 $Ba_2Cu_{1-x}Zn_xTeO_6$ samples resembles a two-leg spin ladder.

Contents

Abstract	2
Chapter 1: Introduction	4
Chapter 2: Experimental	24
Chapter 3: An introduction to the d^{10}/d^0 effect in a cubic perovskite: $\text{Ba}_2\text{MnTeO}_6$	50
Chapter 4: Site-selective W^{6+} (d^0) substitution in $\text{Ba}_2\text{CuTe}_{1-x}\text{W}_x\text{O}_6$	85
Chapter 5: Effects of site-selective W^{6+} substitution on the magnetic properties of $\text{Ba}_2\text{CuTe}_{1-x}\text{W}_x\text{O}_6$	116
Chapter 6: Non-magnetic Zn^{2+} cations in $\text{Ba}_2\text{Cu}_{1-x}\text{Zn}_x\text{TeO}_6$	144
Conclusions and further work	171

Chapter 1: Introduction

Contents

1. Abstract
2. Introduction to the perovskite structure
 - a. *B*-cation displacement
 - b. Octahedral tilting
 - c. Octahedral distortion
3. Magnetism in metal oxides
4. Magnetic frustration
 - a. Spin ices
 - b. Spin liquids
 - c. Spin glasses
5. Magnetism in double perovskites
6. Conclusion
7. References

1. Abstract

This chapter provides a background to the perovskite structure and magnetism in perovskites. The perovskite structure is discussed in general, before magnetism in metal oxides is introduced and discussed in relation to perovskites. Magnetic frustration is also considered as this is a property featured in various perovskite structures, including the structures presented in this thesis. This provides the background to support the subsequent research chapters where the main focus is studying d^{10} vs d^0 effects in $A_2B'B''O_6$ double perovskites.

2. Introduction to the perovskite structure

Magnetism arises due to the interaction between atoms with unpaired electrons. Many materials display magnetic properties. Magnetic materials are applied in every-day life and have an ever-expanding list of applications, including data storage, energy, magneto-optics, magnetic control, materials design, to name but a few examples.¹ Many magnetic materials are metal oxides. Metal oxides exhibit a diverse range of magnetic interactions as they commonly contain transition metal or rare earth ions with unpaired electron configurations. They are widely researched as in addition to their rich magnetic properties, they also display a range of dielectric and superconducting behaviours.² Metal oxides can adopt many structures, including the perovskite structure.

The perovskite family consists of a large range of compounds with the general formula: ABX_3 . The name is derived from the mineral perovskite ($CaTeO_3$), from which the perovskite structure was first identified. There are two different types of cations: the *A*-cation and the *B*-cation. The *A*-cation is large and typically a group 2 cation. The *B*-cation is small and is often a transition metal or rare earth cation. In metal oxides, the *X*-anion is oxygen, but it is also possible to have perovskites with nitrogen or halide *X*-anions. Perovskite structures are found naturally throughout the Earth's crust, but are also widely synthesised due to their wide ranging properties.³ Famous examples include barium titanate, $BaTiO_3$, whose ferroelectric and dielectric properties are used in various electronic applications such as in capacitors and transducers.⁴ Many other perovskites and perovskite-related structures have been discovered in addition to $BaTiO_3$. This is largely a result of the versatility of the perovskite structure, which can accommodate a range of atomic substitutions. Atomic substitution

of the A- and B-cations alters the chemical and physical behaviour meaning new perovskite properties (and hence applications) are still being discovered today.

The single perovskite structure (ABO_3) is shown in Fig 1.1a. The structure is described using the cubic $Pm\bar{3}m$ space group and consists of a network of corner-sharing BO_6 octahedra. The A-cations sit in the cubo-octahedral interstitial sites of the BO_6 network. Substitution at either the A- or B-cation site produces the double perovskite structure $A'A''B_2O_6$ or $A_2B'B''O_6$. Substitution of the B-site cations is popular as they influence many of the perovskites magnetic and electronic properties. Substitution of B-cations produces either: (1) Rock salt ordering or (2) layered ordering. In Rock salt ordering, the B-sites are occupied by alternating B' and B'' cations and follow the same pattern as the Na^+ cation and Cl^- anion ordering in NaCl, hence the name *Rock salt* ordered. In layered ordering, each layer contains only B' or B'' , but the cation type alternates between layers.

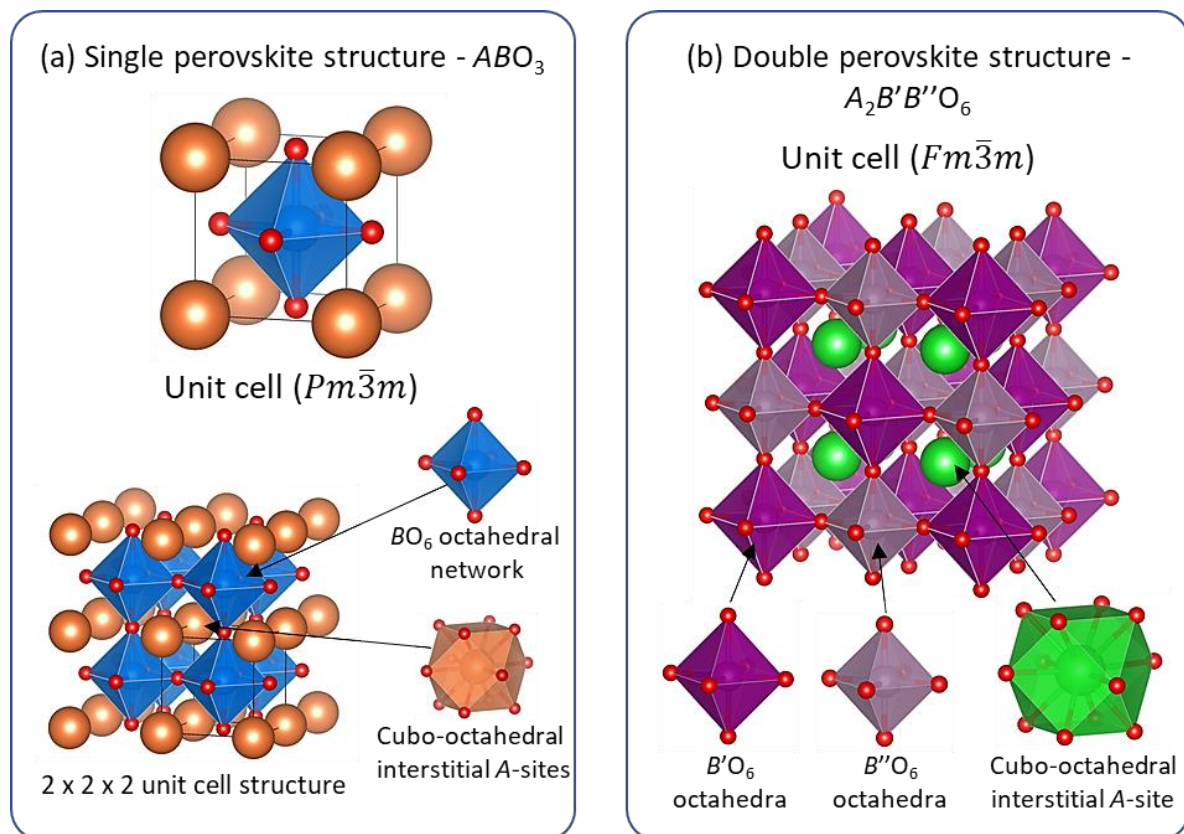


Fig. 1.1 (a) The single ABO_3 perovskite structure with $Pm\bar{3}m$ symmetry. (b) The double $A_2B'B''O_6$ perovskite structure with $Fm\bar{3}m$ symmetry.

Rock salt ordering is more electrostatically favourable as the distance between the highly charged B-site cations is maximized. Rock salt ordering increases the volume of the unit cell by a factor of 8. The unit cell is now face centred instead of primitive. This changes the space group of the *ideal* perovskite structure from $Pm\bar{3}m$ to $Fm\bar{3}m$. The *ideal* Rock salt double perovskite structure is shown in Fig. 1.1b. Both the single perovskite and double perovskite structures compared in Fig. 1.1 are sensitive to changes in the A- and B-cation. A- or B-site substitution can lead to distortion of the *ideal* perovskite structure. Distortions arise because of three common effects: B-cation displacement, octahedral tilting and octahedral distortion.

Hexagonal perovskite structures are also affected by the same type of distortions. Hexagonal perovskites differ to double perovskites in that they have both corner- and face-sharing octahedra.

As Fig. 1.1b shows, all of the BO_6 octahedra in double perovskites are corner-sharing. Alternatively, the mixture of corner- and face-sharing in hexagonal perovskites results in different stacking sequences to produce a variety of structures. The closer cation-cation distance associated with face-sharing can generate different magnetic properties to double perovskites. The types of distortion affecting double and hexagonal perovskites are outlined in the next section.

a. B -cation displacement

B -cation displacement occurs when the B -cations move along one of the symmetry axes. B -cation displacement occurs due to the second order Jahn-Teller effect, whereby filled and empty orbitals of similar symmetry interact to increase the electronic stability by symmetry breaking.⁵ This can occur for degenerate or nondegenerate orbitals and leads to structural distortion. To accommodate the small B -cation, the surrounding O^{2-} cations in the BO_6 octahedra retain their positions while the B -cation is displaced along the tetra-, triad, or diad-axis. This lowers the perovskite symmetry from the *ideal* cubic to tetragonal (tetra (C_4) -axis), orthorhombic (triad (C_3) -axis) or trigonal (diad (C_2) -axis). The three types of B -cation displacements are illustrated in Fig. 1.2.

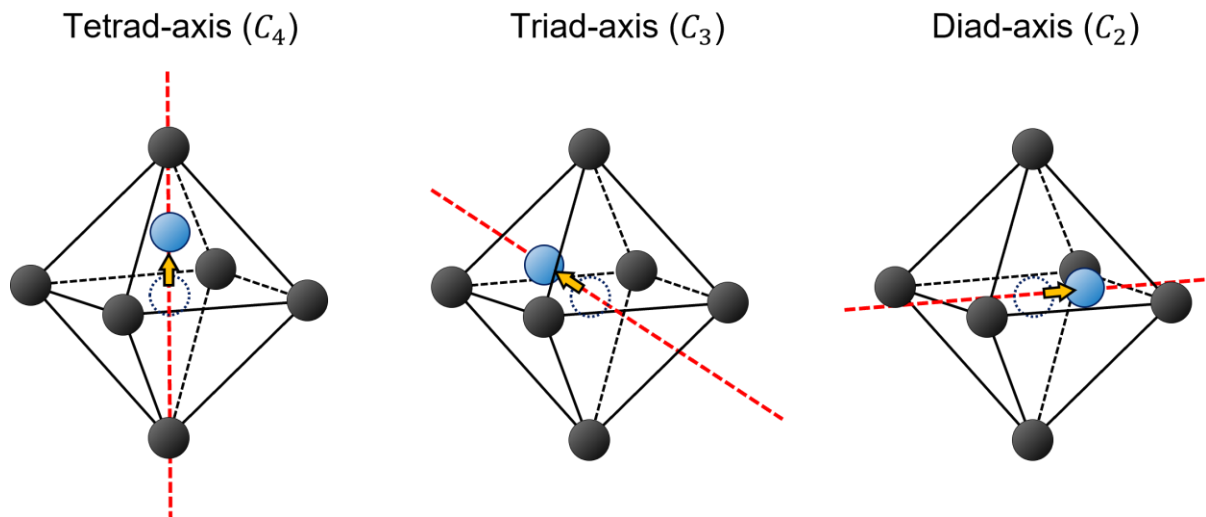


Fig. 1.2 Illustration of B -cation displacement along the tetrad-, triad- and diad- axis of the BO_6 octahedra in perovskites.

b. Octahedral tilting

In most instances, octahedral tilting is caused by small A -cations that struggle to fill the cubo-octahedral interstitial sites in the perovskite structure.⁶ In response, the BO_6 octahedra tilt to avoid long A -O cation distances. The shape of the BO_6 octahedra is retained upon rotation (or 'tilted') about the tetra-, triad, or diad-axis. The corner-sharing connectivity means tilting of one BO_6 unit affects all the other octahedral units, creating a 'ripple effect' throughout the BO_6 network. The nomenclature used to describe octahedral tilting is known as Glazer notation.⁷ Glazer notation uses the letters a , b and c to represent the degree of rotation away from the corresponding parallel x , y and z axes. For example, for the Glazer tilt $a^0b^+c^-$, a^0 represents no tilting along a (parallel to x), b^+ represents an in-phase tilt along b (parallel to y), and c^- represents an anti-phase tilt along c (parallel to z). If tilting is the same in more than one of the x , y and z axes, the symbol is repeated. For example, $a^0a^0c^+$ denotes there is no tilting in either the a or b direction, but there is an in-phase tilt along the c direction as depicted in Fig. 1.3. There are 10 possible Glazer tilt combinations. Using these 10 tilt combinations, 23 different tilt systems can be derived from the *ideal* cubic perovskite structure. Of the 23 tilt systems, 12 are known to be exhibited by the double perovskite

structure and are known as subgroups of the $Fm\bar{3}m$ space group.⁸ The 11 subgroups of the $Fm\bar{3}m$ space group and their Glazer tilts are shown in Fig. 1.4.

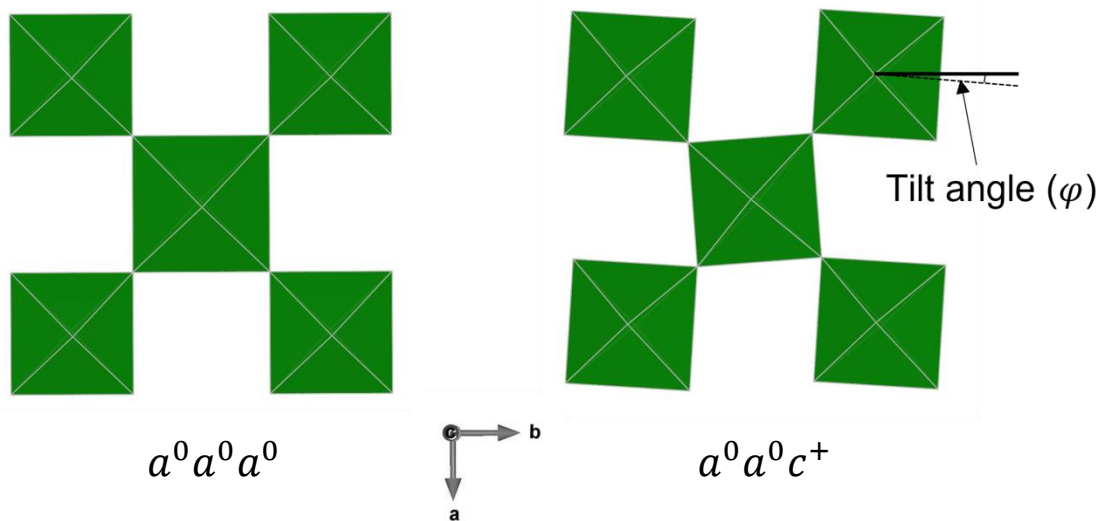


Fig. 1.3 Illustration of the $a^0a^0c^+$ Glazer tilt. Left shows the ideal cubic perovskite structure before the Glazer tilt is applied. The structure on the right shows the distorted perovskite structure after application of the $a^0a^0c^+$ tilt. $a^0a^0c^+$ tilts the BO_6 octahedra in the c direction, which points out the plane of the page. The octahedra along c are tilted in-phase by a tilt angle of φ . There is no octahedral tilting in the plane of the page, along the a or b directions.

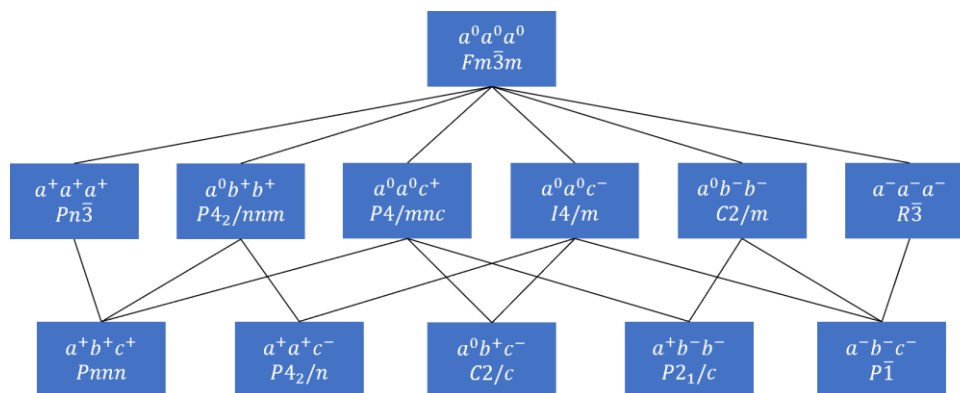


Fig. 1.4 The relationship between the $Fm\bar{3}m$ space group of the ideal double perovskite structure and the 11 subgroups derived from octahedral tilting. The Glazer tilt associated with each subgroup is shown.

c. Octahedral distortion

Octahedral distortion arises from the first order Jahn-Teller effect.⁹ The first order Jahn-Teller (J-T) effect is exhibited by cations with symmetric atomic configurations, but asymmetric degenerate electronic ground states. Half-filled degenerate d -orbitals are an example of an asymmetric degenerate electronic ground state. When transition metals form chemical bonds with anions, they move from a spherical field to either an octahedral, tetrahedral, or square planar field etc. depending on the coordination number. This results in crystal field splitting where the d -orbitals split into the higher energy degenerate $e_g(d_{z^2}$ and $d_{x^2-y^2})$ orbitals and lower energy degenerate $t_{2g}(d_{zy}, d_{xy}$ and $d_{zx})$ orbitals. The energy difference (known as the crystal field splitting parameter,

Δ_0) between the e_g and t_{2g} levels depends on the BO_6 complex under discussion. If the e_g or t_{2g} orbitals are half-filled, further crystal field splitting occurs. $Cu^{2+} d^9$ is a classic example. The e_g level consists of two degenerate d -orbitals, one of which is filled and the other half-filled. To remove the unstable asymmetric electronic degeneracy, the e_g and t_{2g} orbitals split further. The result is elongation or compression of two $B-O$ bonds along the C_4 -axis (i.e. z -axis). Elongation/compression of the $B-O$ bonds along z due to crystal field splitting is known as the Jahn-Teller effect. The energy level diagrams for elongation and compression along z are shown in Fig. 1.5, along with an illustration of the distorted BO_6 octahedra.

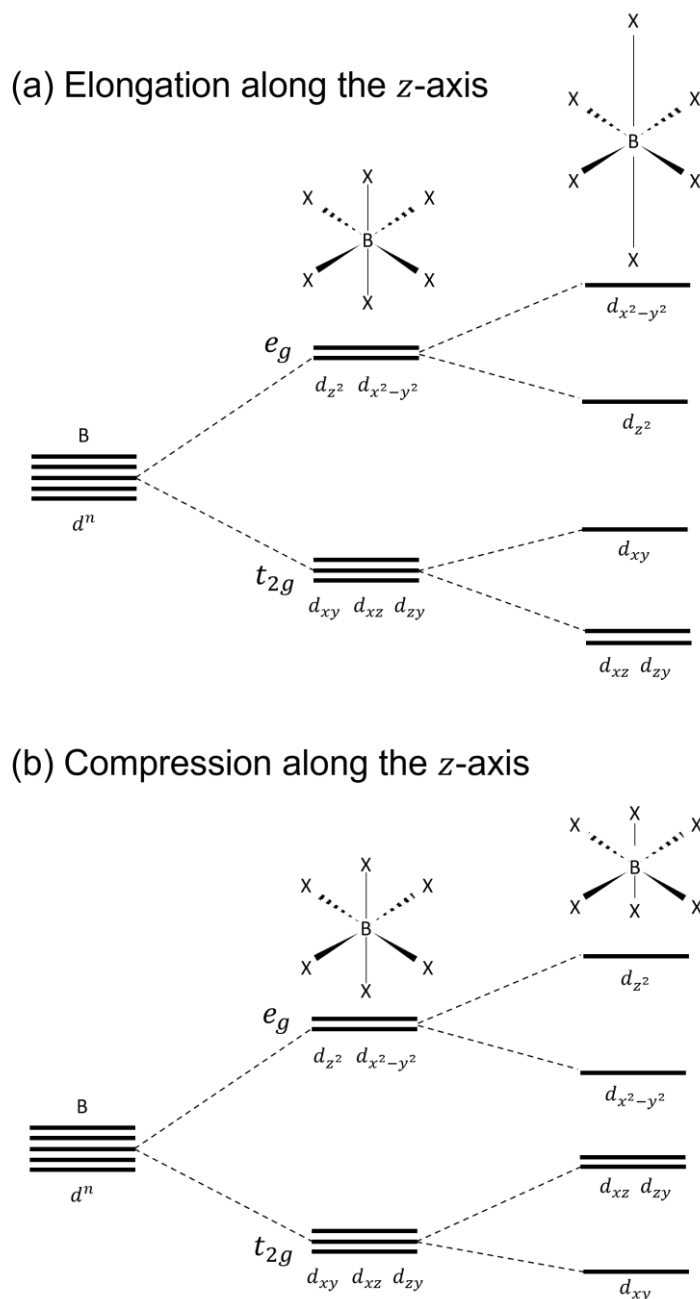


Fig. 1.5 Energy level diagrams for the two forms of Jahn-Teller distortion: (a) elongation along the z -axis and (b) compression along the z -axis. Also, shown are diagrams illustrating the effect of Jahn-Teller distortion on the $B-O$ bonds along the z -axis in the BO_6 octahedra.

3. Magnetism in metal oxides

In metal oxides, magnetic ions with unpaired electrons possess an atomic magnetic moment. The atomic magnetic moment of an individual ion is composed of a spin and orbital component. The spin moment (μ_S) arises from the intrinsic spin of the electron. The orbital moment (μ_L) comes from the motion of electrons in orbitals around the nucleus. Equations for both μ_S and μ_L are given in equations 1.1 and 1.2.

$$\mu_S = -\frac{e}{m_e} \mathbf{S} \quad (1.1)$$

$$\mu_L = -\frac{e}{2m_e} \mathbf{L}, \quad (1.2)$$

$$\text{or } \mu_L = -\gamma_L \mathbf{L} \text{ where, } \gamma_L = \frac{e}{2m_e}$$

Here, e is the charge, m_e is the mass of the electron, γ_L is the gyromagnetic ratio, \mathbf{L} is the orbital angular momentum and \mathbf{S} is the spin angular momentum. \mathbf{L} and \mathbf{S} are calculated from their respective total angular momentum quantum numbers, L and S , defined in equations 1.3 and 1.4. The values of L and S are calculated for the ground state electron configuration using Hund's rules. Hund's rules state the ground state configuration will have maximum multiplicity (i.e. the highest S) and as a result also have maximal L . The values for L and S can be calculated for the ground state configuration which satisfies both these conditions by summing the spin momentum quantum numbers (m_S) and orbital angular momentum quantum numbers (m_L) of the electrons:

$$|\mathbf{S}| = \sqrt{S(S+1)}\hbar, \text{ where } S = m_S(1) + m_S(2) + m_S(3) \dots m_S(n) \quad (1.3)$$

$$|\mathbf{L}| = \sqrt{L(L+1)}\hbar, \text{ where } L = m_L(1) + m_L(2) + m_L(3) \dots m_L(n) \quad (1.4)$$

The total angular momentum quantum number, J , is given by:

$$\mathbf{J} = |\mathbf{L} \mp \mathbf{S}| \quad (1.5)$$

If the valence shell is less than half-filled, L and S are subtracted. If the valence shell is more than half-filled, L and S are added. The total angular momentum is given by $\mathbf{J} = \sqrt{J(J+1)}\hbar$ and is equivalent to the vector sum of \mathbf{L} and \mathbf{S} . Because of the gyromagnetic term, the total magnetic moment is not parallel to the total angular momentum: $\mu_{total} = \mu_L + \mu_S$. Instead, μ_{total} precesses around \mathbf{J} producing the effective magnetic moment (μ_{eff}) given in equation 1.6. This is illustrated in the vector diagram in Fig. 1.6.

$$\mu_{eff} = -g \frac{e}{2m_e} \mathbf{J} \quad (1.6)$$

In equation 1.6, g is the Landé g -factor given by,

$$g = \frac{3}{2} + \frac{S(S+1) - L(L+1)}{2J(J+1)} \quad (1.7)$$

For a collection of magnetic ions, J points in any direction in no applied field leading to no overall net magnetic moment when summed over all ions. Application of a magnetic field causes splitting of the total angular momentum into $2J + 1$ energy levels. Magnetisation is quantized into $+J_Z$ to $-J_Z$ energy levels. If the field is applied along the z -axis, the maximum magnetic moment along z is obtained when all ions are in the $-J_Z$ energy level. The maximum moment along z is given by:

$$|\mu_z| = g J \mu_B \quad (1.8)$$

Where, $\mu_B = e\hbar/2m_e$ is the Bohr magneton. Under this condition the system is said to be saturated and can be macroscopically viewed as having rotated all the magnetic moments in the direction of the magnetic field, H . The magnetisation (M) measures the net magnetic moment parallel to the applied field. For N ions, the magnetisation at saturation is given by equation 1.9, in which N is the number of magnetic atoms.

$$M = N\mu_Z \quad (1.9)$$

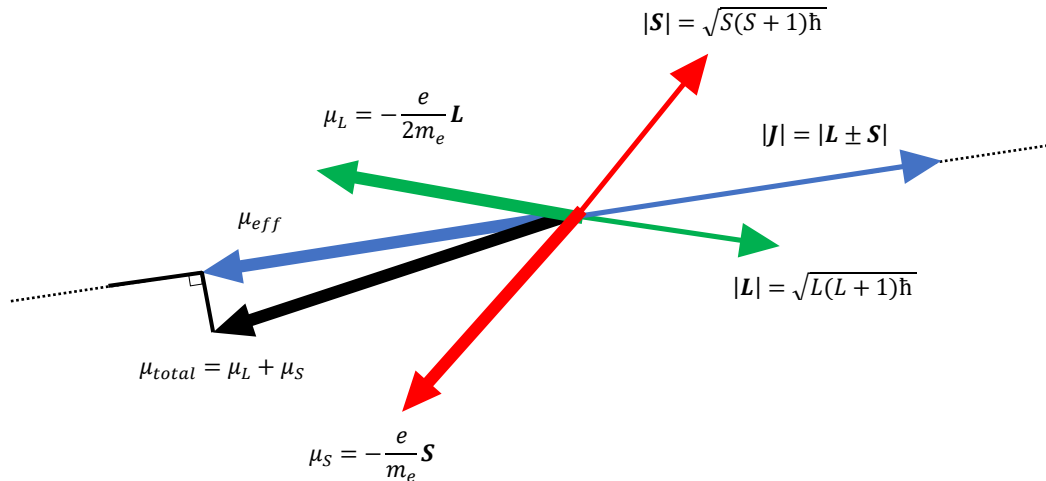


Fig. 1.6 Vector diagram illustrating the combination of the spin (\mathbf{S}) and orbital (\mathbf{L}) angular momentum vectors to give a total angular momentum vector (\mathbf{J}). This generates the total magnetic moment (μ_{total}) that precesses around \mathbf{J} to produce the effective magnetic moment (μ_{eff}) of the magnetic ion.

Curie's Law can be used to determine the magnetisation at low fields. According to Curie's Law, the magnetisation (M) is expressed as:

$$M = \frac{N J(J+1)g^2 \mu_B^2 H}{3k_B T} \quad (1.10)$$

Here, k_B is the Boltzmann constant, N is the number of magnetic atoms, T is the temperature, g the Landé g -factor, μ_B is the Bohr magneton and H the externally applied magnetic field. From equation 1.10, an expression for the magnetic susceptibility (χ) can be derived. The magnetic susceptibility measures the degree of magnetisation in an applied field (H). The expression for χ is:

$$\chi = \frac{M}{H} = \frac{N_A J(J+1)g^2 \mu_B^2 H}{3k_B T H} \quad (1.11)$$

The constants in this equation are collected into the Curie constant below allowing the expression for χ to be simplified as follows:

$$\text{Curie constant } (C) = \frac{N_A J(J+1)g^2 \mu_B^2}{3k_B} \quad (1.12)$$

$$\chi = \frac{C}{T} \quad (1.13)$$

Curie's Law assumes there is no interaction between ions. In reality, magnetic ions interact, and this interaction affects the magnetic susceptibility. To account for this, Weiss developed the mean field theory. The mean field approach assumes a given magnetic cation experiences an average

interaction known as a 'molecular field' from the surrounding magnetic ions. Curie's Law was modified to include mean field effects by introducing the Weiss constant (θ_w). The Weiss constant (θ_w) indicates the strength of the magnetic interactions between ions. The resulting Curie-Weiss Law is shown in equation 1.14.

$$\chi = \frac{C}{T - \theta_w} \quad (1.14)$$

If the inverse magnetic susceptibility ($1/\chi$) is plotted as a function of temperature, the magnitude and sign of θ_w can be determined from the intercept. A value of zero for θ_w suggests the material is paramagnetic and obeys Curie's law. Magnetic moments are randomly aligned in different directions. A positive value of θ_w suggests the material is ferromagnetic and the magnetic moments are aligned parallel. A negative value of θ_w indicates antiferromagnetism, where spins are aligned anti-parallel. Other types of magnetism exist, such as diamagnetism where the material does not contain magnetic ions, but through Lenz's Law generates a small field that opposes the applied magnetic field resulting in a negative χ . Materials can also be ferrimagnetic. Ferrimagnetic materials have antiferromagnetically ordered moments that do not completely cancel, producing a net magnetic moment. These different types of magnetic ordering are summarized in Fig. 1.7. Fig. 1.7 shows types of ordering where spins are co-parallel. However, it is also possible for spins to order in a canted fashion. In a spin canted antiferromagnet, the spins are tilted by a given angle instead of being at 180° with respect to one another.

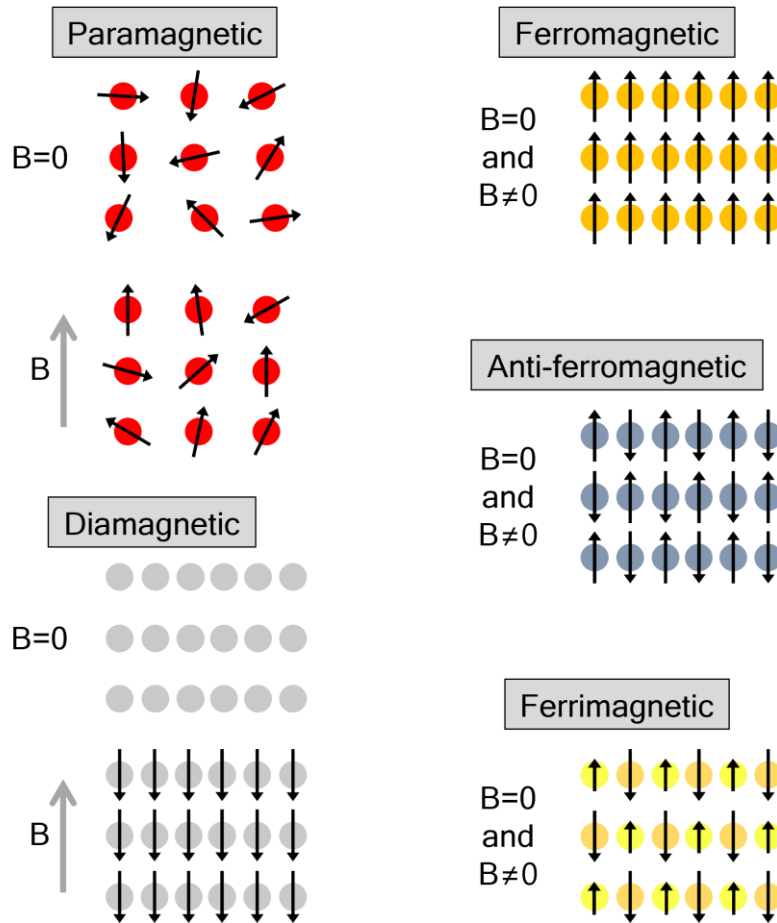


Fig. 1.7 The different types of magnetic ordering including paramagnetic, diamagnetic, ferromagnetic, antiferromagnetic and ferrimagnetic ordering. The paramagnetic and diamagnetic response in both no external field and an externally applied field (B) is shown. In a paramagnet, the magnetic moments point in all directions when no external field is applied; but quickly align when a field is applied. A diamagnetic material possesses no magnetic spins, but when an external field is applied, a small field is generated to oppose the external field.

Above a certain temperature all magnetic materials are paramagnetic. However, as the temperature is reduced, the thermal energy becomes comparable to the energy of the interaction between magnetic ions. A magnetic transition occurs from the disordered paramagnetic state to an ordered magnetic state, resulting in magnetic symmetry breaking. The mean field approach provides an adequate description of the magnetic interactions, but it is purely phenomenological. Instead of an 'average interaction', it is more accurate to describe magnetic interactions using a quantum mechanical description known as the exchange interaction. It is the exchange interaction and not a 'molecular field' that drives long-range ordering in metal oxides. The exchange interaction is represented using the Heisenberg Hamiltonian:

$$H = -2 \sum_{ij} J_{ij} S_i S_j \quad (1.15)$$

S_i and S_j are the spins on atoms i and j . J_{ij} is known as the exchange integral. The sign of J_{ij} indicates whether the material is antiferromagnetic (negative J_{ij}) or ferromagnetic (positive J_{ij}). The magnitude of J_{ij} indicates the strength of the magnetic interaction. The strength of the magnetic interaction is mediated by the degree of orbital overlap between the i and j atoms. Thus, J_{ij}

depends on the atomic separation between the i and j atoms, r_a , and the diameter of the overlapping orbitals, r_b . The Bethe-Slater curve shown in Fig. 1.8 plots the exchange interaction J_{ij} as a function of the ratio of r_a and r_b .^{10,11} The exchange interactions for several 3d transition metals are indicated and follow the Bethe-Slater curve exactly. 3d transition metals with large ionic distances are ferromagnetic so reside in the portion of the curve above the horizontal axis (positive J_{ij}). Parallel alignment is favourable as spins are further apart. For 3d transition metals with small ionic distances, antiparallel alignment is more favourable as the spins cancel. Therefore, 3d transition metals with small ionic distances are placed in the bottom portion of the curve below the horizontal axis (negative J_{ij}).

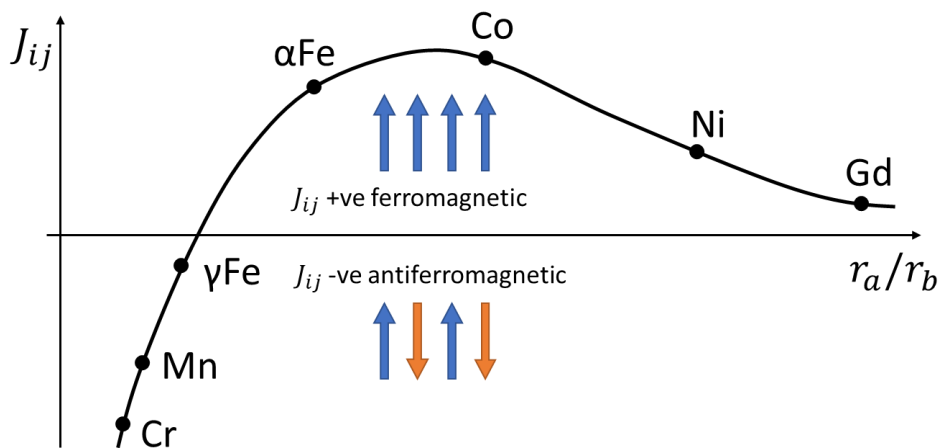
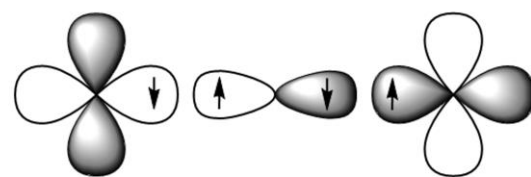


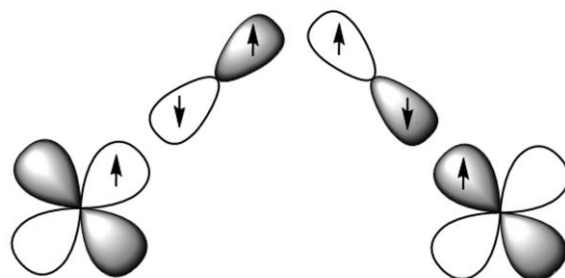
Fig. 1.8 The Bethe-Slater curve in which materials below the horizontal axis have a negative J_{ij} exchange interaction (antiferromagnetic) and above the horizontal axis have a positive J_{ij} exchange interaction (ferromagnetic). Whether J_{ij} is negative or positive, depends on the atomic separation (r_a) and the diameter of the overlapping orbitals (r_b).

In the 3d transition metals marked on the Bethe-Slater curve in Fig. 1.8, the exchange interactions occur directly. This means the magnetic i and j ions communicate via a direct orbital overlap between the 3d orbitals to form metal-metal ($M-M$) interactions. In metal oxides, exchange is more complex. Instead, the J_{ij} exchange occurs indirectly through the oxygen anions. The d -orbitals of the M ions overlap with the $2p$ orbitals of neighbouring oxygen anions. Overlap of multiple M ions with the same oxygen anion results in the formation of metal-oxygen-metal ($M-O-M$) linkages through which magnetic exchange is communicated. This indirect $M-O-M$ exchange is known as superexchange.

As with direct exchange, the strength of the superexchange interaction depends on the distance between magnetic cations in the $M-O-M$ linkage. Superexchange is also highly dependent on the geometry of the $M-O-M$ pathway. In metal oxides, there are two main geometries: (1) 180° superexchange and (2) 90° superexchange. The two geometries for superexchange are shown in Fig. 1.9. In 180° superexchange the $M-O-M$ bonding angle is 180° and the M d -orbitals and O $2p$ orbitals overlap along a linear trajectory (Fig. 1.9a). Alternatively, $M-O-M$ overlap can occur at a 90° bonding angle resulting in 90° superexchange (Fig. 1.9b).



(a) 180° superexchange



(b) 90° superexchange

Fig. 1.9 The two metal-oxygen-metal ($M-O-M$) superexchange pathways at (a) 180° and (b) 90° in metal oxides.

Alignment of the spins on the magnetic M ions is predicted using the Goodenough-Kanamori rules.¹²⁻¹⁴ The Goodenough-Kanamori rules define whether $M-O-M$ superexchange is antiferromagnetic or ferromagnetic based on the Pauli exclusion principle. The rules state that $M-O-M$ superexchange involving half-filled d and $2p$ orbitals is antiferromagnetic (J_{ij} negative). Whereas superexchange involving mixtures of filled and half-filled, or empty and half-filled orbitals results in ferromagnetic exchange (J_{ij} positive). In distorted perovskite structures, it is possible for the superexchange angles to deviate from 90° and 180°, sometimes at the expense of weaker superexchange. The geometric requirements for antiferromagnetic exchange are less strict compared to ferromagnetic exchange.¹⁵ Hence, antiferromagnetic exchange results in most metal oxides.

It is also possible for indirect exchange to involve another bridging ion in addition to oxygen. This so-called extended superexchange $M-O-M'-O-M$ interaction involves another metal ion (M'), but this ion is non-magnetic, for example a d^0 or d^{10} cation.¹⁶ Like $M-O-M$ superexchange, the exchange angle can be 180° or 90° and alignment of the magnetic moments is still predicted using the Goodenough-Kanamori rules. Extended superexchange occurs in $A_2B'B''O_6$ double and hexagonal perovskites in which B' is a magnetic cation and B'' is a non-magnetic cation. In such cases, the magnetic B' cations communicate via $B'-O-B''-O-B'$ superexchange via the non-magnetic B'' cation.

4. Magnetic frustration

In insulating materials such as metal oxides, where the interactions between magnetic ions are mediated by superexchange, a phenomenon known as magnetic frustration can occur. Magnetic frustration arises when there are multiple competing interactions between magnetic centres in a material.¹⁷ Evidence of magnetic frustration is manifested as suppressed magnetic ordering, partial magnetic ordering, or in extreme cases prevention of magnetic ordering. Suppressed magnetic ordering behaviours were first identified in ferrite materials in the 1950s by Anderson.¹⁸ In the 1970s, the term 'magnetic frustration' was coined to account for the lack of magnetic ordering in

spin glass materials.¹⁹ In a spin glass material, magnetic frustration causes the magnetic moments to freeze in random directions, without any long-range magnetic ordering. In addition to spin glass behaviour, various other exotic magnetic behaviours arise in frustrated materials, for example spin liquid and spin ice behaviour.²⁰ Interest in magnetically frustrated materials has grown and been discovered in a wide range of crystal systems, including perovskites.²¹

The interest in magnetic frustration has been driven by the desire to understand the influence of frustrated interactions on the behaviours of technologically relevant materials, such as high temperature superconductors.²² Frustrated magnetic systems have also provided scientists with a wealth of exotic magnetic states to discover and investigate. Magnetic frustration is caused by either the geometry of the lattice or competing interactions. Magnetic frustration caused by the geometry of the lattice is known as geometric frustration.

Geometric frustration arises in lattices with triangular and tetrahedral magnetic motifs. These magnetic motifs are shown in Fig. 1.10. The triangular motif in Fig. 1.10a is an equilateral triangle with a magnetic ion placed on each of the three vertices. Frustration arises when the spins attempt to order antiferromagnetically. This requires the spin on one of the vertices to be both up and down simultaneously to be antiparallel with the other two spins. Both interactions cannot be satisfied simultaneously so the system is said to be ‘frustrated’. A similar situation occurs in the three-dimensional tetrahedral motif. The tetrahedral motif in Fig. 1.10b requires two of the spins to be spin-up and spin-down simultaneously. The more competing interactions, the more frustrated the lattice, hence lattices composed of tetrahedral motifs are more frustrated compared to triangular lattices.²⁰ The square lattice motif in Fig. 1.10c can also exhibit geometric frustration, but only when the interactions along the face of the square (the nearest neighbour interaction) and the diagonal of the square (the next-nearest neighbour interaction) are comparable.

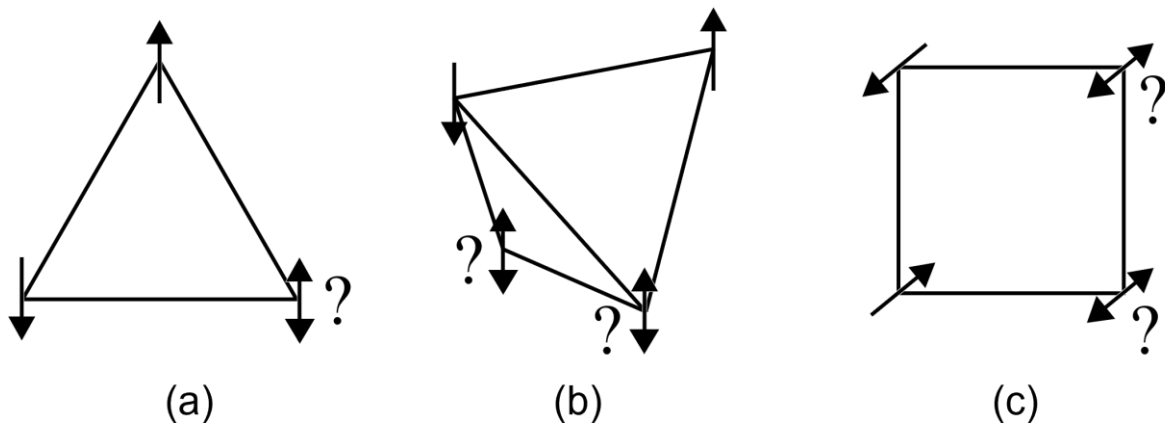


Fig. 1.10 Geometric frustration in the (a) triangular, (b) tetrahedral and (c) square lattice motifs.

The geometrically frustrated motifs connect to form geometrically frustrated lattices. There are four main geometrically frustrated crystal lattices: the triangular, kagomé, pyrochlore and face centred cubic (*fcc*) lattices. In all four of these crystal systems, the lattices consist of an array of triangular or tetrahedral motifs. Frustration is measured using the frustration index. The frustration index in equation 1.16 is a quantitative measure of the degree of frustration.²⁰

$$f = \frac{|\theta_w|}{T_C} \quad (1.16)$$

The frustration index (f) is given by the ratio of the Weiss constant (θ_w) and the critical temperature (T_C) at which long-range order occurs. If $f \sim 1$, the system is not frustrated and magnetically orders

at a temperature exactly determined by the strength of the magnetic interactions. For values of $f = 2-4$, the system is only weakly frustrated. However, when $f > 10$, the system is frustrated and may not exhibit long-range magnetic order at extremely low temperatures close to zero Kelvin. Instead, frustration could lead to the formation of a range of exotic magnetically disordered states such as spin ices, spin liquids and spin glasses.

a. Spin ices

Despite being a seemingly simple system, water ice has a deceptively complex ground state.²³ The ground state of water ice is periodic due to the tetrahedral arrangement of the oxygen atoms. However, because of the large difference between the O-O and O-H bond lengths, two covalent bond distances arise resulting in two protons sitting close to the oxygen atom while the other two are kept further away. There are multiple ways this proton arrangement can be achieved within the structure leading to a highly degenerate ground state.²⁴

The pyrochlore lattice has been found to be an analogy for water ice.^{25,26} The pyrochlore lattice consists of a tetrahedral motif of magnetic ions with an oxygen ion in the centre of the tetrahedra. The vertices of the tetrahedra are connected along the $\langle 111 \rangle$ crystallographic axis. This creates a highly anisotropic geometry and forces all the spins on the vertices of the tetrahedra to be Ising in nature. Ising spins only point in two directions: 'in' or 'out' of the tetrahedra. In a spin ice, the ground state consists of a 'two-in, two-out' configuration where two Ising spins point into the centre of the tetrahedra and two Ising spins point out of the tetrahedra. For a single tetrahedron, there are six different ways this configuration can be achieved.²⁷ When the 'two-in, two-out' Ising arrangement is extrapolated throughout the pyrochlore lattice, there are many energetically equivalent spin arrangements. This leads to a highly degenerate ground state that does not show long-range magnetic ordering and remains disordered even at zero Kelvin. Because of the analogy to water ice, pyrochlore systems displaying this behaviour are called 'spin ices'. $\text{Ho}_2\text{Ti}_2\text{O}_7$, $\text{Dy}_2\text{Ti}_2\text{O}_7$ and $\text{Ho}_2\text{Sn}_2\text{O}_7$ are examples of the pyrochlores which have been most conclusively identified as true ferromagnetic Ising spin ice systems.^{26,28-30}

b. Spin liquids

Spin ices and spin liquids both have highly degenerate ground states and show no long-range magnetic order. The main distinction is the spins are not Ising in a spin liquid. Instead of being frozen along a particular axis, the spins remain dynamic at absolute zero and are said to be Heisenberg spins as they can point in any x , y and z direction in space.²⁰ Spin liquids can be classical or quantum mechanical depending on the magnitude of the spin, S .²⁷ In a classical spin liquid, $S > 1/2$ and the dynamic behaviour is caused by thermal fluctuations. If $S < 1/2$, quantum effects come into play. In a quantum spin liquid, the $S = 1/2$ spins remain dynamic as magnetic frustration prevents the spins from ordering. This leads to strong quantum fluctuations. The fluctuating spins can be arranged in a multitude of ways creating many energetically equivalent configurations. The many degenerate configurations superimpose to form a strongly correlated ground state.

Understanding the behaviour of strongly correlated materials is a key focus in condensed matter physics.³¹ Strongly correlated materials have applications in microelectronics, where entanglement of spins is required for realising quantum computation.³² Synthesis of spin liquid systems could provide models to understand strong correlations in quantum materials.³³ Numerous models and predictions have been developed to describe spin liquid behaviour.^{34,35} However, finding quantum spin liquid candidates that can be synthesised experimentally is challenging. On top of this, proving candidate materials are 'true' representatives of quantum spin liquid behaviour is difficult and requires a combination of techniques, as well as theoretical support.^{36,37} Consequently, only a few

candidate spin liquids have been identified. The candidate materials have geometrically frustrated 2D (triangular and kagomé) or 3D (hyperkagomé and distorted kagomé) lattices.²⁷

c. Spin glasses

Magnetism in the 1970s was dominated by the study of dilute metal alloys such as CuMn, AgMn and AuFe.³⁸ At specific concentrations, dilute metal alloys display a sharp cusp in their magnetic susceptibility vs temperature curve (χ vs T), which is not seen for normal ferromagnets or antiferromagnets.³⁹ This observation was shown to be characteristic of spin glass behaviour where the cusp represents the freezing temperature, T_f . At T_f , the magnetic moments freeze in random directions forming a metastable 'glassy' state where there is no long-range order. The spin glass state can be distinguished from antiferromagnets and ferromagnets using AC susceptibility (χ_{Ac}) measurements. About the freezing temperature the formation of the spin glass state is dynamic, shifting through a complex potential energy surface as the spins gradually freeze.⁴⁰ As a result, the position and magnitude of T_f depends on the timescale of the measurement. When measuring χ_{Ac} vs T in an alternating magnetic field with increasing frequencies, there will be an observable shift in T_f .⁴¹ In ferromagnets and antiferromagnets ordering is instantaneous so there is no frequency dependent transition temperature.

In addition to metal alloys, spin glass behaviour has been identified in insulators, including double perovskites. Formation of a spin glass requires randomness and competing interactions, otherwise the material will assume antiferromagnetic/ferromagnetic order.¹⁶ A number of disordered perovskites with frustrated magnetic interactions have been identified. They all have B -site cation disorder, which evokes spin glassiness as the spins feel a distribution of exchange interactions. An example is the disordered $\text{Sr}_2\text{Fe}B''\text{O}_6$ family where a spin glass forms if $B'' = \text{Nb, Ta or Ru}$.⁴²⁻⁴⁴ Spin glass behaviour is believed to arise from the competition between the two magnetic B -cations, Fe^{+3} and M^{+5} (Na/Ta/Ru), distributed randomly across the B' and B'' sites with vacancies throughout. Different M^{+5} cations such as Sb^{5+} have been investigated in $\text{Sr}_2\text{Fe}B''\text{O}_6$, but they do not exhibit spin glass behaviour.⁴³ This is supposedly due to the difference in cation size, reflecting the influence of the B -site cations on the magnetic and electric properties of the perovskite structure. Other double perovskite spin glasses include: $\text{La}_2B'B''\text{O}_6$ ($B'/B'' = \text{Co, Ni or Mn}$)^{45,46}, $\text{Sr}_2\text{CaReO}_6$ ⁴⁷ and $\text{Sr}_2\text{MgReO}_6$ ⁴⁸.

5. Magnetism in double perovskites

Incorporating magnetic B -site cations into double perovskites produces interesting magnetic behaviours. The correct combination of B -site cations can lead to the formation of interesting low temperature magnetic behaviour, such as spin glassiness. However, as noted above in the $\text{Sr}_2\text{Fe}B''\text{O}_6$ example such behaviour requires disorder of the B' and B'' site cations to introduce the competing interactions that lead to magnetic frustration. While disordered perovskites may form exotic magnetic ground states, the vast majority of B'/B'' site ordered perovskites adopt antiferromagnetic or ferromagnetic ordering. Ferromagnetic order is less common because antiferromagnetic superexchange is favoured in metal oxides.^{15,49} Ferromagnetism exist mainly in Rock salt ordered $A_2B'B''\text{O}_6$ perovskites where both B' and B'' are magnetic.¹⁶ Special synthesis conditions such as high-pressures or thin-layer depositions are required to produce a high degree of cation order and avoid disordered antiferromagnetic interactions.^{50,51} Notable examples of ferromagnetic double perovskites are $\text{La}_2\text{NiMnO}_6$ and $\text{La}_2\text{CoMnO}_6$.⁵² Both display attractive properties for electronic devices, including multiple magnetic, magnetoelectric, and semiconducting properties close to room temperature (Curie temperatures, $T_C = 310$ K ($\text{La}_2\text{NiMnO}_6$) and 270 K ($\text{La}_2\text{CoMnO}_6$)).⁵³⁻⁵⁵

Ferrimagnetism also exists in perovskites. Ferrimagnetic double perovskites have two magnetic cations ordered antiferromagnetically but with different magnetic moments which partially cancel to produce a net magnetic moment. Based on this definition, it could be deduced that all antiferromagnetically ordered systems with two magnetic cations are in fact ferrimagnetic. However, the interactions are not only based upon superexchange; they rely heavily on coupling between itinerant (unbound) electrons within the structure.¹⁶ Consequently, most examples of ferrimagnetic double perovskites are half-metallic structures, such as $\text{Sr}_2\text{FeMoO}_6$ and $\text{Sr}_2\text{FeReO}_6$.^{56,57}

Most perovskites order antiferromagnetically as super-exchange between B -cations with the same d -orbital configurations is most often antiferromagnetic. For a Rock salt ordered double perovskite with one magnetic B -cation, the M^{n+} cations form a face-centred cubic (fcc) sub-lattice. The fcc sub-lattice shown in Fig. 1.11 has two superexchange interactions: the nearest neighbour (NN, J_1) and next-nearest neighbour (NNN, J_2) exchange interactions. In a perfectly cubic perovskite, these interactions occur within three dimensionally equivalent square motifs. Distortion to lower symmetry introduces more superexchange interactions as the interactions are no longer equivalent in three-dimensions.⁵⁸ The strength of these magnetic interactions depends on the degree of orbital overlap. Hence, if these interactions form by elongation of the cubic unit cell, they are weaker than the original interactions before distortion. This can lead to quasi two- or one-dimensional magnetic interactions.

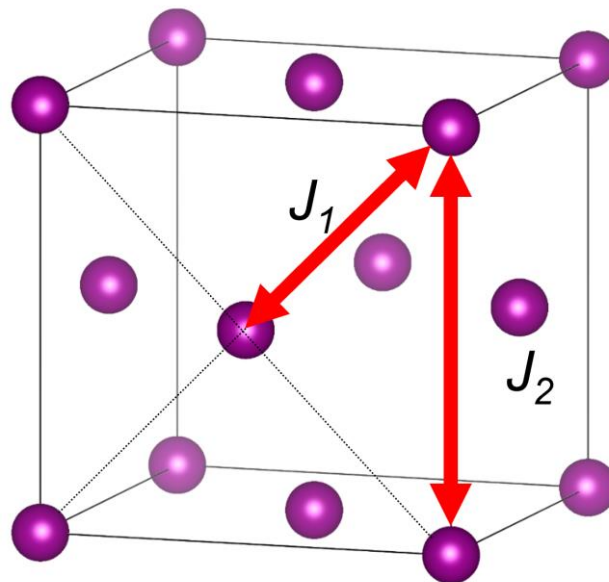


Fig. 1.11 The nearest neighbour (J_1) and next-nearest neighbour (J_2) superexchange interactions in the fcc sub-lattice.

Depending on the magnitude and sign of the J_1 and J_2 interactions there are three stable types of antiferromagnetic ordering in the fcc lattice.⁵⁹ These are labelled type I, type II and type III and are shown in Fig. 1.12. The ratio of J_2 and J_1 defines the phase boundary between the three phases. The boundary between the type I and type II phases lies at $J_2/J_1 = 0$ and the boundary between the type III and type II phases at $J_2/J_1 = 0.5$.^{60,61} In the type I phase, J_2 is positive (i.e. ferromagnetic) and J_1 is negative (i.e. antiferromagnetic) leading to ferromagnetically ordered layers along the (001) axis which are coupled antiferromagnetically. In both the type II and type III phase, J_2 and J_1 are antiferromagnetic leading to more complex ordering. The type II phase can be viewed as a derivative of the type I phase, however instead ferromagnetic interactions are in the (111) planes of the fcc sub-lattice with antiferromagnetic interactions between the (111) planes. The type III phase is most complex as the fcc sub-lattice is further sub-divided into one corner and three face-sharing

antiferromagnetically interacting lattices. In all three phases, the J_1 and J_2 interactions are described using the Heisenberg J_1 - J_2 model where the Hamiltonian for the interactions is given by:⁶¹

$$H = -J_1 \sum_{\langle ij \rangle} \mathbf{S}_i \cdot \mathbf{S}_j - J_2 \sum_{\langle\langle ij \rangle\rangle} \mathbf{S}_i \cdot \mathbf{S}_j \quad (1.17)$$

Here, J_1 is the NN interaction, J_2 is the NNN interaction, S_i is the spin on atom i and S_j is the spin on atom j . Both S_i and S_j are summed over all the NN and NNN interactions. Note, the J_1 and J_2 interactions in equation 1.17 are defined so ferromagnetic interactions have a positive exchange interaction and antiferromagnetic exchange interactions have a negative exchange interaction.

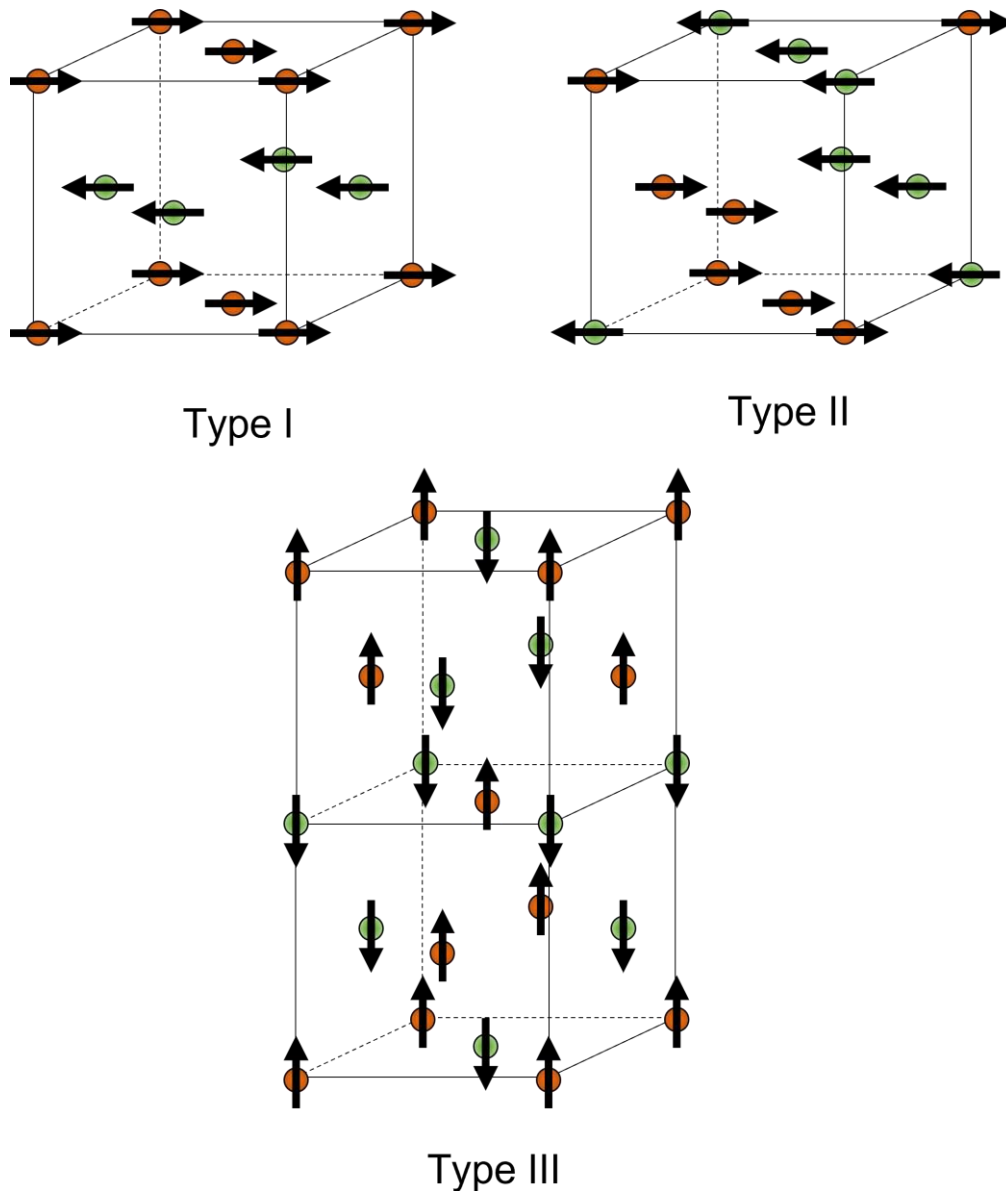


Fig. 1.12 Types of antiferromagnetic order in the fcc sub-lattice.

Disorder creates frustration in double perovskites due to the multiple competing superexchange interactions. In addition, double perovskites exhibit geometric frustration. When considering only the J_1 interactions, the fcc sub-lattice seen in Fig. 1.13 is composed of interconnected tetrahedral motifs producing frustration between nearest neighbour spins. Geometric frustration is maximized when the J_2 interaction is suppressed; and can lead to the formation of the degenerate magnetic

spin glass, spin liquid and spin ice states discussed above.⁶² Alternatively, geometric frustration can suppress magnetic ordering so T_N occurs at temperatures lower than expected.⁶³ The identity of the A-site and B'' site cation can have a dramatic effect on the degree of frustration in double perovskites. It has been demonstrated that the size of the A-site cation has a large effect on the 90° nearest neighbour interaction, irrespective of the identity of the B-site cations.⁶³ Disorder introduced by the substitution of non-magnetic B-site cations can also reduce the magnetic ordering temperature, and even prevent ordering from occurring.^{64,65} For example, substitution of Te^{6+} d^{10} for W^{6+} d^0 suppresses antiferromagnetic ordering in $\text{Sr}_2\text{CuTe}_{1-x}\text{W}_x\text{O}_6$ due to the disorder induced frustration introduced by the competing d^{10} and d^0 interactions.⁶⁶

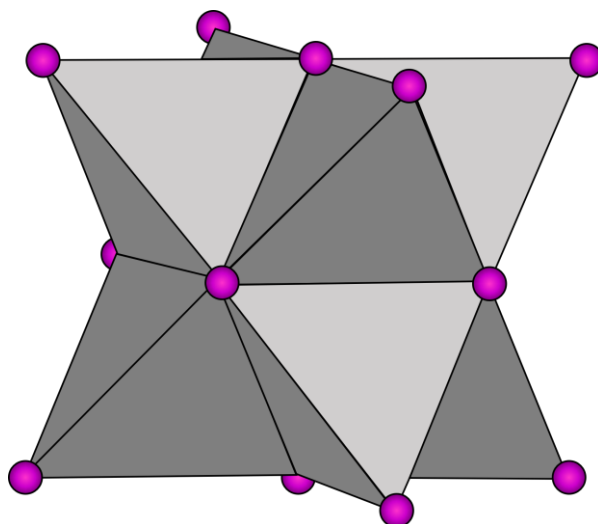


Fig. 1.13 Geometrically frustrated tetrahedral motifs in the fcc lattice.

6. Conclusions

This introductory chapter provides the background theory for investigating d^{10}/d^0 interactions in $A_2B'B''O_6$ perovskites. The discussion on magnetic frustration aids research chapters where mixtures of d^{10} and d^0 cations in $A_2B'B''O_6$ perovskites are studied. d^{10} and d^0 mixtures introduce competing magnetic interactions leading to frustration that could prevent magnetic ordering and generate exotic disordered magnetic states.

7. References

1. Sander, D. *et al.* The 2017 Magnetism Roadmap. *J. Phys. D: Appl. Phys.* **50**, 363001 (2017).
2. Tokura, Y. & Hwang, H. Y. Complex oxides on fire. *Nat. Mater.* **7**, 694 (2008).
3. Tilley, R. J. D. *Perovskites: Structure-Property Relationships*, John Wiley & Sons. (2016).
4. Buscaglia, V., Buscaglia, M. T. & Canu, G. BaTiO₃-Based Ceramics: Fundamentals, Properties and Applications, *Encyclopedia of Materials: Technical Ceramics and Glasses*. 311–344 (2021).
5. Pearson, R. G. The Second-order Jahn-Teller Effect. *J. Mol. Struct.* **103**, 25–34 (1983).
6. Woodward, P. M. Octahedral Tilting in Perovskites. II. Structure Stabilizing Forces. *Acta Crystallogr. Sect. B Struct. Sci.* **53**, 44–66 (1997).
7. Glazer, A. M. The classification of tilted octahedra in perovskites. *Acta Cryst.* **28**, 3384–3392 (1972).
8. Howard, C. J., Kennedy, B. J. & Woodward, P. M. Ordered double perovskites - a group-

- theoretical analysis research papers. *Acta Cryst.* **59**, 463–471 (2003).
9. Lufaso, M. W. & Woodward, P. M. Jahn-Teller distortions, cation ordering and octahedral tilting in perovskites. *Acta Cryst.* **60**, 10–20 (2004).
 10. Cardias, R. *et al.* The Bethe-Slater curve revisited; new insights from electronic structure theory. *Sci. Rep.* **7**, 4058 (2017).
 11. Slater, J. C. Cohesion in monovalent metals. *Phys. Rev.* **35**, 509 (1930).
 12. Goodenough, J. B. An interpretation of the magnetic properties of the perovskite-type mixed crystals $\text{La}_{1-x}\text{Sr}_x\text{CoO}_{3-\lambda}$. *J. Phys. Chem. Solids* **6**, 287–297 (1958).
 13. Goodenough, J. B. Magnetism and the Chemical Bond. in *Interscience Monographs on Chemistry*, John Wiley, New York 1–385 (1963).
 14. Kanamori, J. Superexchange interaction and symmetry properties of electron orbitals. *J. Phys. Chem. Solids* **10**, 87–98 (1959).
 15. Orchard, A. F. *Magnetochemistry*, Oxford Chemistry Press. (2003).
 16. Vasala, S. & Karppinen, M. $A_2B'B''O_6$ perovskites: A review. *Prog. Solid State Chem.* **43**, 1–36 (2015).
 17. Harrison, A. First catch your hare: The design and synthesis of frustrated magnets. *J. Phys. Condens. Matter* **16**, 553–572 (2004).
 18. Anderson, P. W. Ordering and antiferromagnetism in ferrites. *Phys. Rev.* **102**, 1008–1014 (1956).
 19. Toulouse, G. Theory of the frustration effect in spin glasses: I. *Commun. Phys.* **2**, 115–119 (1977).
 20. Greedan, J. E. Geometrically frustrated magnetic materials. *J. Mater. Chem.* **11**, 37–53 (2001).
 21. Hossain, A., Bandyopadhyay, P. & Roy, S. An overview of double perovskites $A_2B'B''O_6$ with small ions at A site: Synthesis, structure and magnetic properties. *J. Alloys Compd.* **740**, 414–427 (2018).
 22. Dionne, G. F. & Dionne, G. F. Magnetic frustration in high- T_c superconductors. *J. Appl. Phys.* **69**, 5194 (1991).
 23. Castelnovo, C., Moessner, R. & Sondhi, S. L. Spin ice, fractionalization, and topological order. *Annu. Rev. Condens. Matter Phys.* **3**, 35–55 (2012).
 24. Pauling, L. The Structure and Entropy of Ice and of Other Crystals with Some Randomness of Atomic Arrangement. *J. Am. Chem. Soc.* **57**, 2680–2684 (1935).
 25. Bramwell, S. T. & Gingras, M. J. P. Spin ice state in frustrated magnetic pyrochlore materials. *Science*. **294**, 1495–1501 (2001).
 26. Harris, M. J., Bramwell, S. T., McMorrow, D. F., Zeiske, T. & Godfrey, K. W. Geometrical frustration in the ferromagnetic pyrochlore $\text{Ho}_2\text{Ti}_2\text{O}_7$. *Phys. Rev. Lett.* **79**, 2554–2557 (1997).
 27. Balents, L. Spin liquids in frustrated magnets. *Nature* **464**, 199–208 (2010).
 28. Matsuhira, K., Hiroi, Z., Tayama, T., Takagi, S. & Sakakibara, T. A New Macroscopically Degenerate Ground State in the Spin Ice Induced by a Magnetic Field. *J. Phys. Condens. Matter* **14**, 559–565 (2002).

29. Kadowaki, H., Ishii, Y., Matsuhira, K. & Hinatsu, Y. Neutron scattering study of dipolar spin ice $\text{Ho}_2\text{Sn}_2\text{O}_7$: Frustrated pyrochlore magnet. *Phys. Rev. B* **65**, 144421 (2002).
30. Ehlers, G. *et al.* Low energy spin dynamics in the spin ice $\text{Ho}_2\text{Sn}_2\text{O}_7$. *J. Phys. Condens. Matter* **24**, 076005 (2012).
31. Quintanilla, J. & Hooley, C. The strong-correlations puzzle. *Phys. World* **22**, 32–37 (2009).
32. Jiang, H. C., Wang, Z. & Balents, L. Identifying topological order by entanglement entropy. *Nat. Phys.* **8**, 902–905 (2012).
33. Ramirez, A. P. A flood or a trickle? *Nat. Phys.* **4**, 442–443 (2008).
34. Savary, L. & Balents, L. Quantum spin liquids: A review. *Reports Prog. Phys.* **80**, 016502 (2017).
35. Anderson, P. W. RESONATING VALENCE BONDS: A NEW KIND OF INSULATOR? *Mater. Res. Bull.* **8**, 153–160 (1973).
36. Lee, P. A. An end to the drought of quantum spin liquids. *Science*. **321**, 1306–1307 (2008).
37. Wen, J., Yu, S. L., Li, S., Yu, W. & Li, J. X. Experimental identification of quantum spin liquids. *npj Quantum Mater.* **4**, 1–9 (2019).
38. Huang, C. Y. Some experimental aspects of spin glasses: A review. *J. Magn. Magn. Mater.* **51**, 1–74 (1985).
39. Binder, K. & Young, A. P. Spin glasses: Experimental facts, theoretical concepts, and open questions. *Rev. Mod. Phys.* **58**, 801–976 (1986).
40. Mydosh, J. A. Disordered magnetism and spin glasses. *J. Magn. Magn. Mater.* **157–158**, 606–610 (1996).
41. Lecomte, G. V., Löhneysen, H. v. & Wassermann, E. F. Frequency dependent magnetic susceptibility and spin glass freezing in PtMn alloys. *Zeitschrift für Phys. B Condens. Matter* **50**, 239–245 (1983).
42. Rodriguez, R. *et al.* Spin glass behaviour in an antiferromagnetic non-frustrated lattice: $\text{Sr}_2\text{FeNbO}_6$ perovskite. *J. Phys. C Solid State Phys.* **18**, 401–405 (1985).
43. Kashima, N., Inoue, K., Wada, T. & Yamaguchi, Y. Low temperature neutron diffraction studies of Sr_2FeMO_6 ($M=\text{Nb, Sb}$). *Appl. Phys. A* **74**, 805–807 (2002).
44. Battle, P. D., Gibb, T. C., Jones, C. W. & Studer, F. Spin-glass behavior in $\text{Sr}_2\text{FeRuO}_6$ and BaLaNiRuO_6 : A comparison with antiferromagnetic BaLaZnRuO_6 . *J. Solid State Chem.* **78**, 281–293 (1989).
45. Wang, X. L., James, M., Horvat, J. & Dou, S. X. Spin glass behaviour in ferromagnetic $\text{La}_2\text{CoMnO}_6$ perovskite manganite. *Supercond. Sci. Technol.* **15**, 427–430 (2002).
46. Choudhury, D. *et al.* Near-room-temperature colossal magnetodielectricity and multiglass properties in partially disordered $\text{La}_2\text{NiMnO}_6$. *Phys. Rev. Lett.* **108**, 127201 (2012).
47. Greedan, J. E., Derakhshan, S., Ramezanipour, F., Siewenie, J. & Proffen, T. H. A search for disorder in the spin glass double perovskites $\text{Sr}_2\text{CaReO}_6$ and $\text{Sr}_2\text{MgReO}_6$ using neutron diffraction and neutron pair distribution function analysis. *J. Phys. Condens. Matter* **23**, 164213 (2011).
48. Wiebe, C. R. *et al.* Frustration-driven spin freezing in the $S=1/2$ fcc perovskite $\text{Sr}_2\text{MgReO}_6$.

- Phys. Rev. B* **68**, 134410 (2003).
49. Cheong, S. W. The exciting world of orbitals. *Nat. Mater.* **6**, 927 (2007).
 50. Mishra, R., Soliz, J. R., Woodward, P. M. & Windl, W. Ca₂MnRuO₆: Magnetic order arising from chemical chaos. *Chem. Mater.* **24**, 2757–2763 (2012).
 51. Dass, R. I. & Goodenough, J. B. Multiple magnetic phases of La₂CoMnO_{6-δ} (0 ≤ δ ≤ 0.05). *Phys. Rev. B* **67**, 014401 (2003).
 52. Bull, C. L., Gleeson, D. & Knight, K. S. Determination of B-site ordering and structural transformations in the mixed transition metal perovskites La₂CoMnO₆ and La₂NiMnO₆. *J. Phys. Condens. Matter* **15**, 4927–4936 (2003).
 53. Lin, Y. Q. & Chen, X. M. Dielectric, ferromagnetic characteristics, and room-temperature magnetodielectric effects in double perovskite La₂CoMnO₆ ceramics. *J. Am. Ceram. Soc.* **94**, 782–787 (2011).
 54. Zhu, M. *et al.* Electronic and magnetic properties of La₂NiMnO₆ and La₂CoMnO₆ with cationic ordering. *Appl. Phys. Lett.* **100**, 062406 (2012).
 55. Pal, S. *et al.* Effect of anti-site disorder on magnetism in La₂NiMnO₆. *Phys. Rev. B* **97**, 165137 (2018).
 56. Fang, Z., Terakura, K. & Kanamori, J. Strong ferromagnetism and weak antiferromagnetism in double perovskites: Sr₂FeMO₆ (M = Mo, W, and Re). *Phys. Rev. B* **63**, 180407 (2001).
 57. Solovyev, I. V. Electronic structure and stability of the ferrimagnetic ordering in double perovskites. *Phys. Rev. B* **65**, 144446 (2002).
 58. Walker, H. C. *et al.* Spin wave excitations in the tetragonal double perovskite Sr₂CuWO₆. *Phys. Rev. B* **94**, 064411 (2016).
 59. Battle, P. D. & Jones, C. W. The Crystal and Magnetic Structures of Ba₂LuRuO₆, Ba₂YRuO₆, and Ba₂LuRuO₆. *J. Solid State Chem.* **78**, 108–116 (1989).
 60. Tahir-Kheli, R. A., Callen, H. B. & Jarrett, H. Magnetic ordering in cubic crystals with first and second neighbor exchange. *J. Phys. Chem. Solids* **27**, 23–32 (1966).
 61. Sun, N. N. & Wang, H. Y. The J₁-J₂ model on the face-centered-cubic lattices. *J. Magn. Magn. Mater.* **454**, 176–184 (2018).
 62. Kuz'min, E. V., Ovchinnikov, S. G. & Singh, D. J. Frustrated antiferromagnetism in the Sr₂YRuO₆ double perovskite. *J. Exp. Theor. Phys.* **96**, 1124–1130 (2003).
 63. Bos, J. W. G. & Attfield, J. P. Magnetic frustration in (LaA)CoNbO₆ (A = Ca, Sr, and Ba) double perovskites. *Phys. Rev. B* **70**, 174434 (2004).
 64. Marjerrison, C. A. *et al.* Magnetic ground states in the three Os⁶⁺ (5d²) double perovskites Ba₂MOsO₆ (M=Mg,Zn,and Cd) from Néel order to its suppression. *Phys. Rev. B* **94**, 134429 (2016).
 65. Mustonen, O. *et al.* Tuning the S=1/2 square-lattice antiferromagnet Sr₂Cu(Te_{1-x}W_x)O₆ from Néel order to quantum disorder to columnar order. *Phys. Rev. B* **98**, 064411 (2018).
 66. Mustonen, O. *et al.* Spin-liquid-like state in a spin-1/2 square-lattice antiferromagnet perovskite induced by d¹⁰-d⁰ cation mixing. *Nat. Commun.* **9**, No. 1085 (2018).

Chapter 2: Experimental techniques

Contents

1. Crystal structure determination using X-rays and Neutrons
 - a. Diffraction instruments
 - b. Analysis of powder diffraction patterns – Rietveld refinement
2. Inelastic neutron scattering spectroscopy
3. Extended X-ray Absorption Fine Structure (EXAFS)
4. Superconducting Quantum Interference Device (SQUID) magnetometry
5. Heat Capacity
6. Muon Spin Relaxation (μ SR)
7. Polarized neutron scattering

1. Crystal structure determination using X-rays and neutrons

Crystal structure determination is underpinned by the interaction of X-rays and neutrons with the particles in crystalline materials. The diffraction limit tells us that for an object to be resolvable, the wavelength of the radiation employed must be of the same scale. In the electromagnetic spectrum, X-ray radiation has a wavelength of $\sim 1 \text{ \AA}$. This is comparable to the distances between atoms; therefore, crystalline structures can be observed using X-rays. While neutrons are more frequently regarded as particles, wave-particle duality means they can also be described as waves. Using the de Broglie relationship and kinetic energy equations given below it is possible to relate the neutron energy to its corresponding wavelength.

$$\lambda = \frac{h}{p}, \text{ where } p = m_n v \text{ (de Broglie)} \quad (2.1)$$

$$E = \frac{1}{2} m_n v^2 \text{ (Kinetic energy)} \quad (2.2)$$

Substituting equation 2.1 into 2.2 gives:

$$E = \frac{h^2}{2m_n \lambda^2} \quad (2.3)$$

From this relationship, it can be deduced that neutrons of energy 81.8 meV have a wavelength that is comparable to inter-atomic distances of $\sim 1 \text{ \AA}$. This is lower than the X-ray energy required to meet the diffraction limit, where a wavelength of $\lambda = 1 \text{ \AA}$ corresponds to an X-ray energy of 12.4 keV.

Not only are the energies different, X-rays and neutrons also interact differently with the atomic nuclei in crystals. While X-rays are scattered by the interaction with the electron density surrounding the atom, neutrons interact with the atomic nuclei. This has several consequences discussed below.

Firstly, scattering from the atomic nuclei allows neutrons to penetrate deeper into the sample. The short-range nuclear forces between neutrons and atomic nuclei are weak compared to the long-range electromagnetic forces between X-rays and electrons. Consequently, the nuclei can be regarded as point scatterers. This affects the angular dependence of the scattering intensity versus X-rays. With X-rays, the long-range electronic forces spread out the electron density so it is comparable to the X-ray wavelength. Hence, the spread of the electronic density cloud and X-ray wavelength are of a similar magnitude. As a result, the X-ray scattering intensity is highly angle dependent and decreases quickly as the incident scattering angle increases. With neutrons, point

scattering leads to a significant difference between the nuclear density and neutron wavelength, so there is almost no angular dependence on the scattering intensity. The different angular dependence for the X-ray and neutron scattering intensity is illustrated in Fig. 2.1. While the neutron scattering intensity is clearly weaker than the X-ray in Fig. 2.1, the angle independence allows data to be collected over a wider angle providing more structural information compared to X-rays.

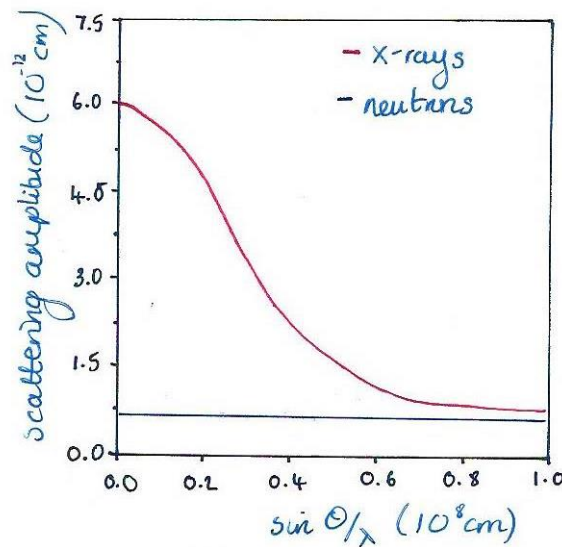


Fig. 2.1 Comparison of the angular dependence on the scattering intensity for X-rays (red line) and neutrons (blue line).

Secondly, neutrons are more sensitive towards secondary scattering mechanisms, such as the interaction between the neutron magnetic moment and magnetic moments in the sample. In a magnetically ordered material, this interaction results in magnetic scattering. Hence, neutron scattering can provide information on both the nuclear and magnetic structure. Given X-rays are electromagnetic waves, magnetic X-ray scattering also occurs from the interaction between X-rays and unpaired electrons in the sample. However, the small scattering cross-section leads to very weak magnetic X-ray scattering. Hence, magnetic neutron scattering is widely preferred.

Thirdly, there are differences in element contrast between X-rays and neutrons. X-rays are more sensitive to heavier atoms as the X-ray scattering intensity depends on atomic number (Z). This complicates structural determination if the material contains numerous light elements (e.g. Li, H, O etc.). Conversely, neutron scattering is not a straightforward function of Z and is isotope specific. Light elements can be seen more clearly with neutrons and isotopes distinguished (e.g. hydrogen and deuterium). X-ray and neutron scattering are often used as complementary techniques, the former providing information on heavy elements in the sample, while the latter determining the position of light elements, and possibly information on the magnetic structure.

Irrespective of their differences, X-ray and neutron scattering are described using the same theory. In an analogous manner to an optical grating, the regularly repeating structure within a crystal produces a diffraction pattern from constructive and destructive interference of scattered X-ray or neutron waves. This diffraction process can be described rigorously using the Laue method which considers diffraction from a 3D arrangement of atoms. Although more representative of a 3D crystal, this analysis is complex so the Bragg method is preferred. In the Bragg method, crystals are considered as sets of lattice planes separated by an inter-planar d -spacing, d . The lattice planes are assigned using Miller indices (hkl). h , k and l are determined from the inverse of the points where the

lattice plane intercepts the lattice vectors a , b and c . Bragg's Law is derived in Fig. 2.2 by considering diffraction of two X-ray/neutron waves from two planes, 1 and 2, belonging to a set of adjacent lattice planes separated by d .

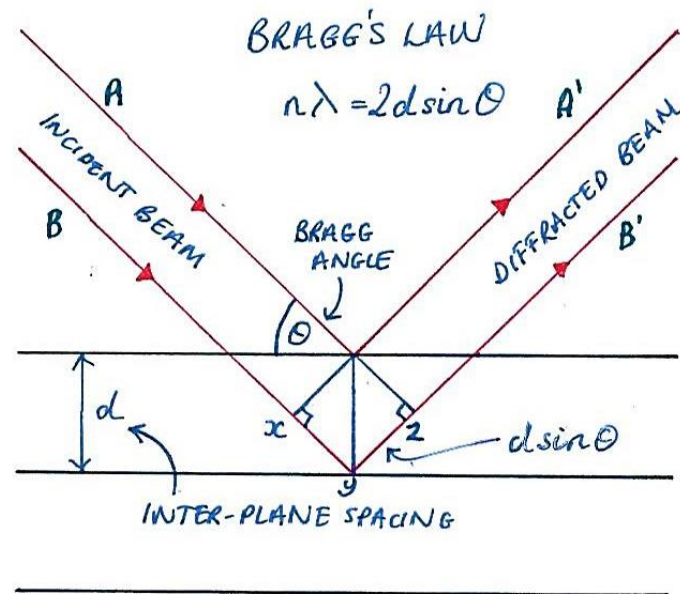


Fig. 2.2 Derivation of Bragg's law

In Fig. 2.2, the wave labelled BB' has to travel an extra distance of xyz compared to the AA' wave. Using simple trigonometry, the xyz distance is given by:

$$xyz = 2d\sin(\theta) \quad (2.4)$$

Where θ , is the angle of incidence (also known as the Bragg angle). For interference to be constructive, xyz must be equal to an integer number of wavelengths (i.e. $xyz = n\lambda$), thus defining Bragg's Law:

$$n\lambda = 2d\sin(\theta) \quad (2.5)$$

For a given d -spacing, the Bragg condition is only met at particular angles of incidence. A variation in θ by more than $\sim 0.001^\circ$ is enough to break the Bragg condition and result in complete destructive interference of the scattered waves. By measuring the intensity of the scattered waves as a function of incident angle, a diffraction pattern containing peaks at particular angles of incidence is produced. By rearranging Bragg's Law, the peak position is used to calculate the d -spacing between lattice planes; hence providing the unit cell dimensions. The peak positions are solely dependent on the crystal structure. A diffraction pattern is often referred to as a 'fingerprint' that is unique for a given crystal. Further information about the contents of the unit cell is obtained by considering the intensity, number and shape of the diffraction peaks.

Peak intensity

One of the most important factors affecting the peak intensity is the contents of the lattice plane. In the case of X-rays, planes containing heavier elements (i.e. more electron density) have higher intensities compared to planes with light elements. Thus, peak intensity (I_{hkl}) is linked to atomic position within the unit cell and is proportional to the X-ray structure factor, F_{hkl} (equation 2.6). F_{hkl} describes the amplitude and phase difference (α_{hkl}) for a given hkl reflection:

$$I_{hkl} \propto |F_{hkl}|^2 \quad (2.6)$$

$$F_{hkl} = \sum_j f_j \exp(i \alpha_{hkl}) \quad (2.7)$$

F_{hkl} is summed over all j atoms in the unit cell. f_j is the X-ray atomic form factor of a single j atom and is given by the Fourier transform of the charge density:

$$f(Q) = \int \rho(x) \exp^{-iQ \cdot x} dx \quad (2.8)$$

Where, $\rho(x)$ is the charge density of the scatterer as a function of position, x , in real space and Q is the momentum transfer. Q represents the change in momentum during scattering and is given by the difference in the incident (k_i) and scattered (k_f) wavevectors of the wave i.e. $Q = k_i - k_f$. The k_i and k_f wavevectors are related to the wavelength by $k = 2\pi/\lambda$. Bragg's Law is concerned with elastic scattering (also known as Thompson scattering) where there is no change in momentum. In this case $k_i = k_f$, so the momentum is conserved and scattering is elastic, but the direction changes by Q as shown in Fig. 2.3. Again, using simple trigonometry, it is possible to relate the momentum transfer in Q -space, to the scattering angle and wavelength using the relationship $k = 2\pi/\lambda$:

$$Q = \frac{4\pi \sin(\theta)}{\lambda} \quad (2.9)$$

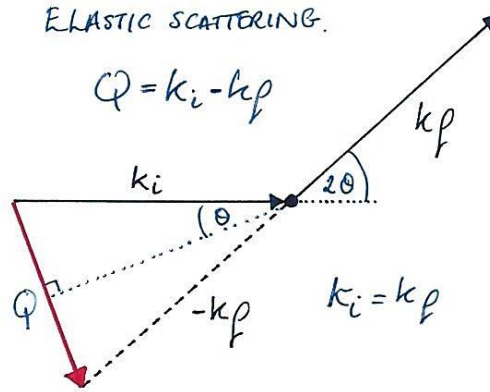


Fig. 2.3 Elastic scattering in momentum space.

Referring back to the form factor equation, it can be seen the larger the charge density $\rho(x)$, the larger the scattering amplitude; hence, reasoning the strong dependence on the atomic number of the scattering atom. It is also true that the greater the spread in $\rho(x)$, the faster the decay in $f(q)$ with Q . Equation 2.9 also shows the atomic form factor depends on both the scattering angle and wavelength since both θ and λ affect the magnitude of Q .

The structure factor in equation 2.7 can also be expressed in terms of the hkl values for the lattice plane and fractional x, y, z coordinates of the atoms using the following relationship: $\alpha_{hkl} = 2\pi(hx + ky + lz)$. α_{hkl} represents the difference in phase between the atoms at the unit cell origin and atoms at a fractional position (x, y, z) for a given hkl lattice plane in any 3D unit cell. The X-ray structure factor is now expressed as:

$$F_{hkl} = \sum_j f_j \exp(2\pi i (hx_j + ky_j + lz_j)) \quad (2.10)$$

The neutron structure factor is different to the X-ray structure factor in a subtle, but very important way. The neutron structure factor displayed in equation 2.11 resembles that of equation 2.10 for X-rays, but the X-ray atomic form factor, f_j , has been replaced by b_j . b_j is known as the neutron scattering length. As discussed, neutrons are point scatterers, therefore b_j does not depend on the incident angle. Neither does b_j depend on Q ; so accordingly, b_j is also θ and λ independent. Instead, b_j varies irrationally for each isotope and must be determined experimentally for each elemental isotope. It is also possible for elements to have a negative neutron scattering length, for example vanadium for which the coherent (elastic) neutron scattering length is $b_{coh} = -0.38 \text{ fm}$. Consequently, vanadium canisters are used as sample holders in elastic neutron diffraction experiments as they contribute no Bragg peaks to the diffraction pattern.

$$F_{hkl} = \sum_j b_j \exp(2\pi i (hx_j + ky_j + lz_j)) \quad (2.11)$$

Using the structure factor, it is possible to calculate the intensity of any hkl reflection if the x, y, z coordinates in the unit cell are known. For example, the body centred cubic structure has a basis consisting of two atoms at x, y, z positions $(0,0,0)$ and $(\frac{1}{2}, \frac{1}{2}, \frac{1}{2})$. For this basis, the X-ray structure factor is given by:

$$F_{hkl} = f_j \exp(2\pi i (h0 + k0 + l0)) + f_j \exp(2\pi i (h\frac{1}{2} + k\frac{1}{2} + l\frac{1}{2})) \quad (2.12)$$

$$F_{hkl} = f_j [1 + (\exp(\pi i))^{h+k+l}]$$

Using Euler's identity ($\exp(\pi i) = -1$) this simplifies to:

$$F_{hkl} = f_j [1 + (-1)^{h+k+l}] \quad (2.13)$$

For F_{hkl} to be non-zero, the sum of $h + k + l$ must be even to give $F_{hkl} = 2f_j$. If $h + k + l = \text{odd}$, $(-1)^{h+k+l}$ will be raised to an odd power and $F_{hkl} = 0$ so no reflections are observed. This imposes a reflection condition on the body centred cubic structure where only $h + k + l = \text{even}$ reflections are observed (e.g. the (110), (200), (222) reflections). The $h + k + l = \text{odd}$ reflections (e.g. (100), (111), (201) etc.) are said to be forbidden or systematically absent. Systematic absences occur in all non-primitive lattices and impose different reflection conditions depending on the lattice type. Using Fig. 2.4 it is possible to see why $F_{hkl} = 0$ for the (100) plane in the body centred cubic lattice, I . The presence of the second atom at $(\frac{1}{2}, \frac{1}{2}, \frac{1}{2})$ between lattice planes results in destructive interference at the Bragg angle as the waves diffracted from the $(0,0,0)$ and $(\frac{1}{2}, \frac{1}{2}, \frac{1}{2})$ planes are $\lambda/2$ out of phase with each other. Consequently, they completely cancel and the (100) reflection is absent. If the lattice were primitive, the (100) reflection would be observed as there is no body centring atom in-between the planes to prevent complete constructive interference. The reflection conditions for the different lattice centring are summarized in Table 2.1.

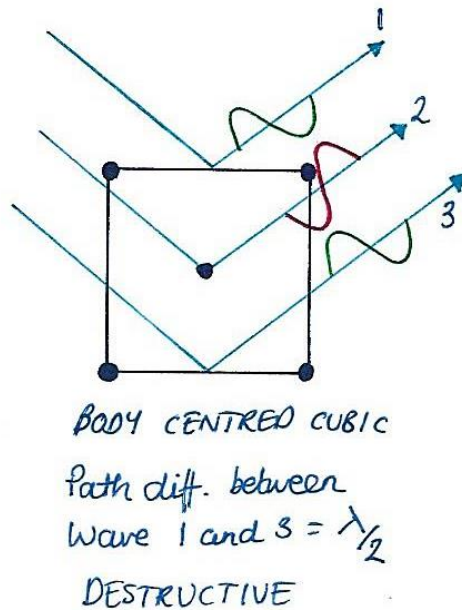


Fig. 2.4 Systematic absences in the body centred cubic lattice.

Table 2.1 Reflection conditions for the 7 different lattice centring.

Lattice type	Lattice points	Reflection conditions
Primitive (P)	(0,0,0)	None
Body centred (I)	(0,0,0); ($\frac{1}{2}, \frac{1}{2}, \frac{1}{2}$)	$h + k + l = 2n$
Face centred (F)	(0,0,0); ($\frac{1}{2}, \frac{1}{2}, 0$); ($\frac{1}{2}, 0, \frac{1}{2}$); ($0, \frac{1}{2}, \frac{1}{2}$)	h, k, l either all odd or all even
Base centred (A)	(0, 0, 0); ($0, \frac{1}{2}, \frac{1}{2}$)	$k + l = 2n$
Base centred (B)	(0, 0, 0); ($\frac{1}{2}, 0, \frac{1}{2}$)	$h + l = 2n$
Base centred (C)	(0, 0, 0); ($\frac{1}{2}, \frac{1}{2}, 0$)	$h + k = 2n$
Hexagonal centred (R)	$\pm(\frac{2}{3}, \frac{1}{3}, \frac{1}{3})$ or $\pm(\frac{1}{3}, \frac{2}{3}, \frac{1}{3})$	$-h + k + l = 3n$ or $h - k + l = 3n$

There are other factors which can affect the peak intensity. Structural multiplicity and temperature factors also need to be considered to formulate a complete expression for the hkl peak intensities, I_{hkl} . Sample absorption can be an issue depending on the elements present. Absorption issues are indicated when the modelled peak intensities are higher than the observed intensity. In a powdered sample, preferred orientation might affect the peak intensity. Powder samples composed of non-spherical crystallites (e.g. needle-like crystals) may order in stacked arrangements when preparing the sample on a plate holder. Crystal stacking means not all hkl planes are viewed with equal probability, thus skewing the intensity in the diffraction pattern towards hkl planes that are more 'visible' to the X-ray/neutron beam. Preferred orientation effects can be reduced by using capillary

sample holders. Generally, powder samples are disordered so preferred orientation should not be an issue.

Peak number

The number of peaks in a diffraction pattern provides an indication of the crystal symmetry. Higher symmetry crystal structures have fewer peaks due to peak overlap caused by multiple equivalent hkl reflections. The multiplicity (M) defines the number of equivalent hkl reflections contributing to a given peak. For example, in the cubic crystal the unit cell lengths are the same (i.e. $a = b = c$), and consequently the $(h00)$, $(\bar{h}00)$, $(0h0)$, $(0\bar{h}0)$, $(00h)$ and $(00\bar{h})$ reflections are equivalent and can be represented as $\{h00\}$, where the curly brackets indicate the $M = 6$ equivalent reflections. The bar denotes the inverse (i.e. $\bar{h} = -h$). Therefore, 6 reflections contribute to the $\{h00\}$ peak in the diffraction pattern. If the symmetry is lowered, for example by having $a = b \neq c$ as in the tetragonal unit cell, the multiplicity of the $\{h00\}$ reflections is reduced. The diffraction planes along c are no longer equivalent to those along a and b . This leads to two peaks in the diffraction pattern: the $\{h00\}$ reflection of $M = 4$ ($(h00)$, $(\bar{h}00)$, $(0h0)$ and $(0\bar{h}0)$) and the $\{00l\}$ reflection of $M = 2$ ($(00l)$ and $(00\bar{l})$). If the symmetry was further lowered to orthorhombic (i.e. $a \neq b \neq c$), there would be three peaks for $\{h00\}$, $\{0k0\}$ and $\{00l\}$ each with a multiplicity of $M = 2$.

Peak shape

In an 'ideal' world, diffraction peaks would be observed as sharp lines. In reality, there are instrumental and sample-related factors that cause peak broadening. Instrumental influences typically cause Gaussian broadening of the peaks and originate from sample height and transparency. Instrumental Gaussian broadening depends entirely on the diffractometer in question. A standard sample (e.g. silicon or LaB_6) is measured to optimize the diffractometer parameters and minimize instrumental broadening. Sample-related broadening results in Lorentzian broadening of the peaks and may occur due to factors such as particle size and microstrain.

In most cases, diffraction peaks display a combination of instrumental and sample-related broadening that can be modelled using the Pseudo-Voigt function. The Pseudo-Voigt function uses both Gaussian and Lorentzian contributions to model the peak shape. Peak shapes are also not always symmetric. Neutron diffraction patterns collected at pulsed neutron sources have asymmetric peak shapes due to the highly asymmetric neutron pulse from the moderator. The peak shape in time-of-flight neutron diffraction patterns is modelled using the Ikeda-Carpenter function, in which a Gaussian function is convoluted with a non-Gaussian function to describe the asymmetry.

Temperature factors

Temperature factors also affect the peak intensity. At all temperatures, the atoms in a crystal are vibrating. Atomic vibration causes the electron density to spread out. This increases destructive interference as the X-rays/neutrons scatter from different parts of the same vibrating atom. Temperature factors are stronger at higher temperatures as atomic vibration increases. Temperature factors are accounted for by including an additional term in the structure factor, so equations 2.10 and 2.11 become:

$$F_{hkl} = \sum_j f_j \exp(2\pi i (hx + ky + lz)) \cdot \exp(-M) \quad (\text{X-rays}) \quad (2.15)$$

$$F_{hkl} = \sum_j b_j \exp(2\pi i (hx + ky + lz)) \cdot \exp(-M) \quad (\text{neutrons})$$

Assuming atomic vibration is isotropic (equal in all directions) the expression for M is given by:

$$M = B \frac{\sin^2 \theta}{\lambda^2} \quad (2.16)$$

Note, the angle dependence in equation (2.16). As well as sample temperature, the Bragg angle also affects the value of M in such a way that temperature factors become worse as θ increases. In equation 2.16, B is the isotropic temperature factor. B is related to the thermal atomic vibration using the expression in equation 2.17.

$$B = 8 \pi^2 u^2 \quad (2.17)$$

Here, $u^2 = U$, where u^2 is the mean squared atomic displacement. Temperature effects are parametrized either in terms of B or U . A more complex expression for M is employed for anisotropic atomic vibration.

Magnetic diffraction

It has been noted that neutrons are sensitive towards magnetic moments in crystalline samples. Neutrons are uncharged, but possess an effective magnetic dipole moment of $\mu_n \sim 0.001 \mu_B$ owing to their $S = \frac{1}{2}$ spin. The neutron magnetic dipole interacts with magnetic fields produced by unpaired electrons in the sample leading to magnetic scattering. Magnetic scattering is weaker compared to nuclear scattering and depends on the ions present in the sample (i.e. the number of unpaired electrons). Unlike X-rays, neutron magnetic scattering does not increase with atomic number, but it does depend on a form factor known as the magnetic form factor. The magnetic form factor has a greater angle dependence compared to the X-ray form factor; and decreases faster as a function of Q as illustrated in Fig. 2.5. This is because scattering typically arises from unpaired electrons in the outer d and f orbitals whose electron density is more spread out; so like temperature factors, magnetic scattering becomes weaker at increasing angles.

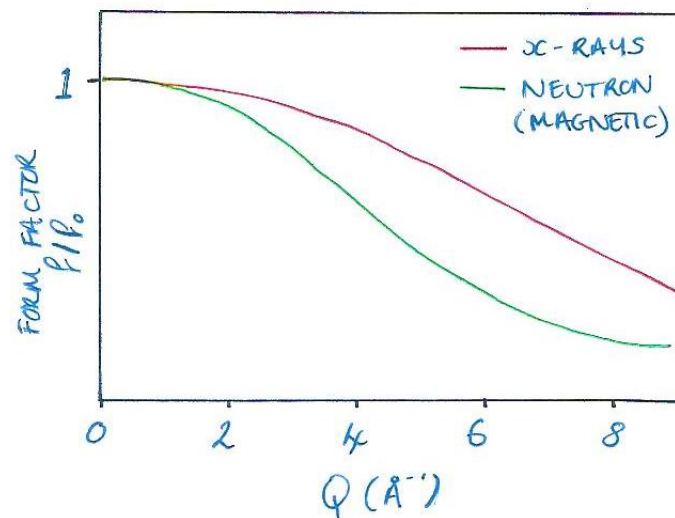


Fig. 2.5 The X-ray form factor (red line) and magnetic form factor for neutrons (green line) as a function of momentum transfer, $Q = 4\pi \sin(\theta)/\lambda$.

In a paramagnet, neutrons are scattered incoherently as the magnetic moments are disordered. Incoherent paramagnetic scattering contributes to the background intensity. If the material is magnetically ordered, coherent magnetic scattering results in a similar manner to nuclear scattering. The major difference is that magnetic scattering is not isotropic. Magnetic neutron scattering is only observed from magnetic moments (μ) that are perpendicular to the momentum transfer vector, Q . The M represents the overall direction of magnetisation and is comprised of the vectors M_{\parallel} and M_{\perp} . If Q is parallel to M_{\parallel} , only scattering from the M_{\perp} component of the magnetisation will be observed. The opposite is true when Q is parallel to M_{\perp} (i.e. only scattering from M_{\parallel} observed). The

magnetic structure factor (F_{mag}) is a vector whose magnitude depends on the direction of the magnetic moments with respect to Q .

$$F_{mag}(hkl) = \sum_j \mu_j f_j(Q) \exp(2\pi i (hx + ky + lz)) \quad (2.18)$$

Here, μ_j is the magnetic moment within the sample and $f_j(Q)$ the magnetic form factor. The structure factor for scattering of unpolarized neutrons is given by the combination of the nuclear and magnetic scattering processes.

$$F_{total}(hkl) = F_{nuc}(hkl) + F_{mag}(hkl) \quad (2.19)$$

Ferromagnetically ordered materials possess the same symmetry as the nuclear unit cell due to parallel alignment of the spins. Below the Curie temperature (T_C), neutron and magnetic scattering superimpose, causing the peak intensity to increase as illustrated in Fig. 2.6a. In an antiferromagnetic material, symmetry breaking occurs due to antiparallel alignment below the Néel temperature (T_N). The nuclear and magnetic unit cells are no longer equivalent. Extra magnetic Bragg peaks are observed at different positions to the nuclear Bragg peaks, as illustrated in Fig. 2.6b. The magnetic unit cell is related to the nuclear unit cell using the propagation vector, k . k is the factor by which the nuclear periodicity must be multiplied to match the magnetic periodicity (i.e. magnetic periodicity = n x nuclear periodicity). If n is a rational number (e.g. 1 or $\frac{1}{2}$), then the nuclear and magnetic unit cells are said to be commensurate. If the nuclear periodicity is multiplied by an irrational value of n , the nuclear and magnetic unit cells are incommensurate.

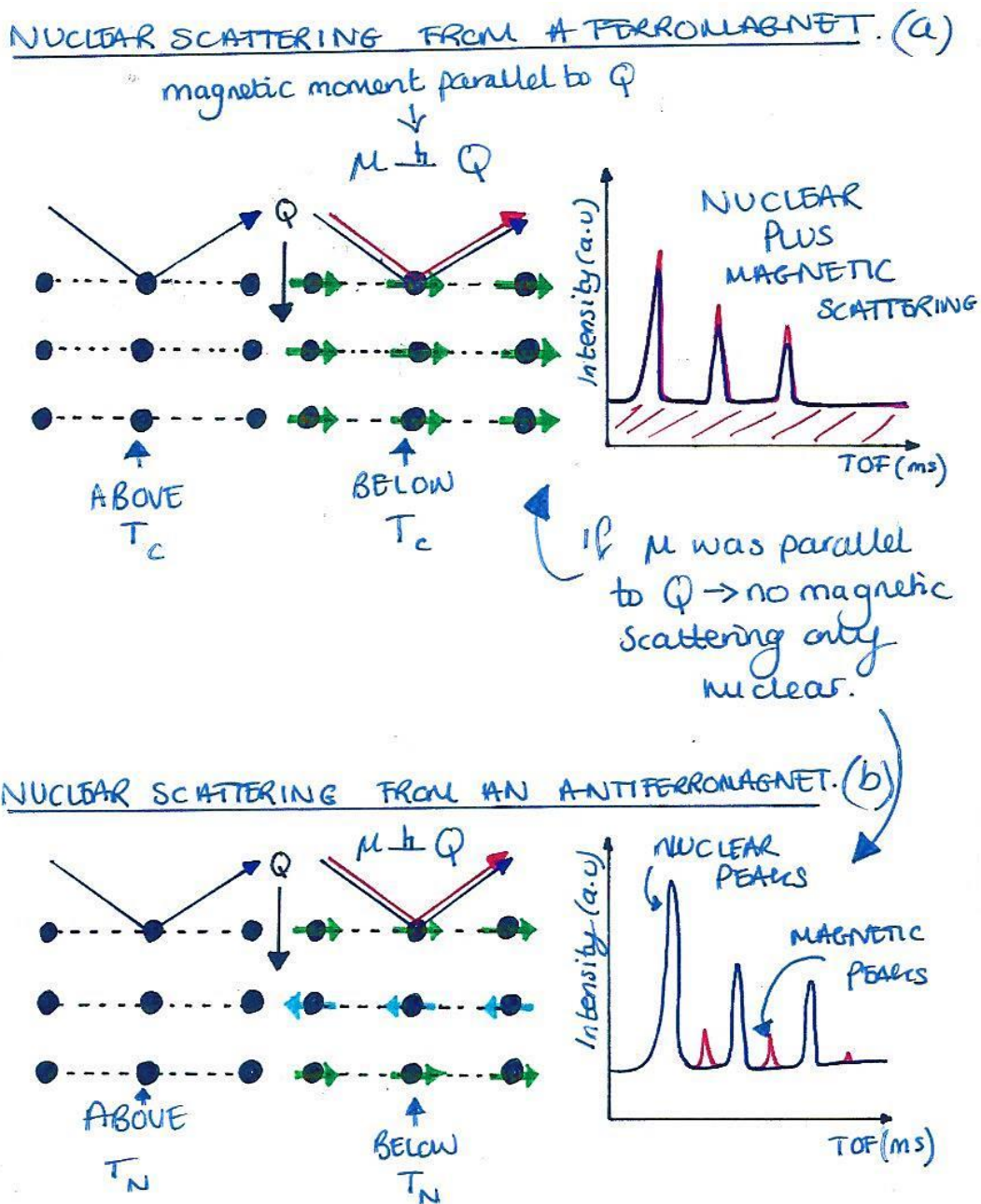


Fig. 2.6 (a) Neutron scattering from a ferromagnet. Above the ferromagnetic ordering temperature (T_C) only nuclear scattering is observed. Below T_C , magnetic scattering occurs in addition to nuclear scattering when the magnetic moment (μ) is perpendicular to Q . The result is an increase in the peak intensity. (b) Magnetic scattering from an antiferromagnet. Now, the nuclear unit cell and magnetic unit cell are inequivalent resulting in additional peaks in the diffraction pattern below the antiferromagnetic ordering temperature (T_N). Again, magnetic scattering is observed only when the magnetic moment (μ) is perpendicular to the momentum transfer vector (Q).

a. Diffraction Instruments

Laboratory Powder X-ray diffractometers

Laboratory powder X-ray diffractometers are the most accessible instrumentation for diffraction analysis. There are three main components to a laboratory X-ray diffractometer: the X-ray source, the sample and detector. X-rays are produced at the source by heating a tungsten filament causing

the filament to emit electrons that are accelerated towards a target material (commonly made from copper or molybdenum metal). Electron collision with the target produces two types of X-ray radiation: characteristic and continuous. Characteristic X-rays are produced by removal of a core electron from an atom in the target material. This results in quantum transitions where electrons from higher energy levels 'drop down' to fill the electron hole and emit X-rays of characteristic wavelength. Continuous X-rays (known as Bremsstrahlung radiation) are produced by electron deceleration upon collision with the target. The X-ray emission spectrum consists of characteristic lines corresponding to quantum transitions from the K , L , M ... shells of the target atom, on top of a background of continuous X-ray radiation.

Powder X-ray diffraction patterns were performed on a Rigaku Miniflex diffractometer using a copper source. A filter is used to separate weaker K_{β} X-ray radiation ($3p(M \text{ shell})-1s(K \text{ shell})$) from the more intense K_{α} ($2p(L \text{ shell})-1s(K \text{ shell})$) radiation. This produces two characteristic $\text{Cu-}K_{\alpha}$ wavelengths of $\lambda = 1.5405$ and 1.5443 \AA for diffraction. The X-rays are focused onto the sample using a series of slits. Bragg-Brentano geometry is used in the Rigaku Miniflex diffractometer. In Bragg-Brentano geometry (Fig. 2.7) the powder sample is placed onto a flat specimen holder in the centre of the diffraction circle. The source and detector sit on the circumference of the diffraction circle allowing the incident and diffracted beams to be focused on a fixed radius from the sample. The source is fixed while the sample and detector are rotated by θ and 2θ , respectively.

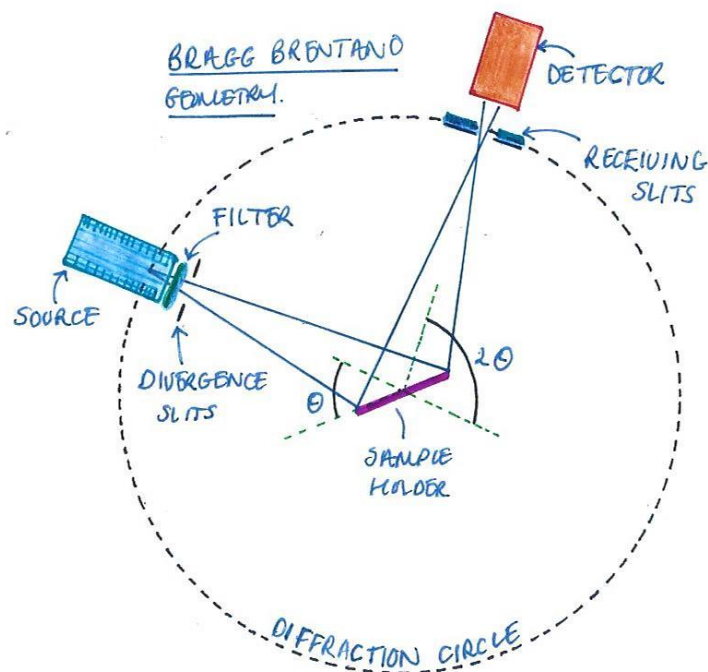


Fig. 2.7 Powder diffraction in Bragg-Brentano geometry.

Synchrotron X-ray diffraction

Synchrotron X-ray diffraction is performed at a synchrotron X-ray source. Synchrotron X-rays are produced by accelerating electrons to relativistic speeds in a storage ring. Changing the electrons direction using magnetic fields results in the emission of high intensity X-rays that are either continuous (bending magnet or wiggler magnet) or pulsed (undulator magnet). The X-rays from the storage ring are focused into experimental hutches placed around the circumference of the storage ring. Each hutch contains specialised synchrotron X-ray diffraction and/or spectroscopic instruments.

Synchrotron X-ray sources are expensive, both in terms of infrastructure and operation; therefore, they are located at large scale national facilities.

Synchrotron X-ray diffraction is highly sought for several reasons. The most celebrated advantage is the superior brilliance. Synchrotron sources like the ESRF and Diamond are more than 1 billion times brighter than laboratory sources. In addition, the X-rays emitted from electron deceleration are near parallel and have less beam divergence compared to in a laboratory diffractometer. The high intensity combined with parallel X-rays offers greater intensity and angle precision. Consequently, the resolution in a synchrotron X-ray diffraction pattern is far superior to that of a laboratory X-ray diffraction pattern. The X-ray wavelength can also be tuned to match atomic excitations in the material providing spectroscopic information.

Neutron powder diffraction

Like synchrotron X-rays sources, neutron sources are located at national facilities due to their expense. Neutron sources are either pulsed or continuous.

Continuous sources

The ILL in Grenoble, France, is a continuous neutron source. Neutrons are produced by nuclear fission in a nuclear reactor using a highly enriched uranium source. The neutrons produced are too 'hot' (too high energy) for diffraction experiments, so they are slowed down using a moderator. By collision with different moderators (liquid D₂, liquid D₂O or graphite), neutron wavelengths between 1-20 Å are obtained. The thermal neutrons of $\lambda = 1-3$ Å obtained with a liquid D₂O moderator are suited to diffraction experiments. The thermal neutrons are collimated using Soller slits and monochromated using single crystals. The identity of the single crystal monochromator determines the wavelength and the width of the Soller slits determines the spread of the wavelength. A common single crystal monochromator is germanium 333 which via Bragg's law filters neutrons of $\lambda = 1.089$ Å into a single wavelength beam. The monochromatic neutron beam is then focused onto the sample. Like in powder X-ray diffraction, the intensity of the diffracted neutrons is measured as a function of 2θ .

Pulsed sources

At a continuous source, the neutron beam consists of a constant stream of neutrons. At a pulsed source the neutrons arrive in 'bunches' known as pulses. Each pulse last for a duration known as the pulse width. The pulse frequency is the number of pulses per second. Pulsed neutron sources, such as The ISIS Neutron and Muon source, use spallation to produce a pulsed neutron beam. An ion source produces H⁻ ions that are accelerated and separated into bunches using a quadrupole accelerator. A linear accelerator (LINAC) further accelerates the H⁻ bunches and injects them into a synchrotron ring. In the synchrotron ring, H⁻ is converted to H⁺ using a thin aluminium foil. When there are sufficient protons in the ring the, the protons are collected into two large bunches and are extracted by a kicker magnet that accelerates the protons at 84% of the speed of light towards a tungsten target. Collision with the target results in spallation, a reaction in which the high energy protons disintegrate the nuclei in the target releasing neutrons. The neutrons emerging from the target are moderated and collimated into a pulsed neutron beam.

Spallation sources are approximately 10 times brighter per unit heat compared to continuous sources, however the neutron pulse contains a large spread of wavelengths. While it is possible to use monochromators and choppers to select specific neutron wavelengths, this greatly reduces the intensity of the incident beam. Instead, the neutron time-of-flight (TOF, t) over a fixed path length (L) is measured in a pulsed neutron diffraction experiment. Bragg's law is still in place, but instead of varying the diffraction angle, the wavelength is varied while θ is fixed. The neutron wavelength is

related to the neutron velocity ($v = L/t$) using equation 2.1. In equation 2.20, the neutron time-of-flight is related to the neutron wavelength.

$$\frac{h}{\lambda} = \frac{m_n L}{t} \quad (2.20)$$

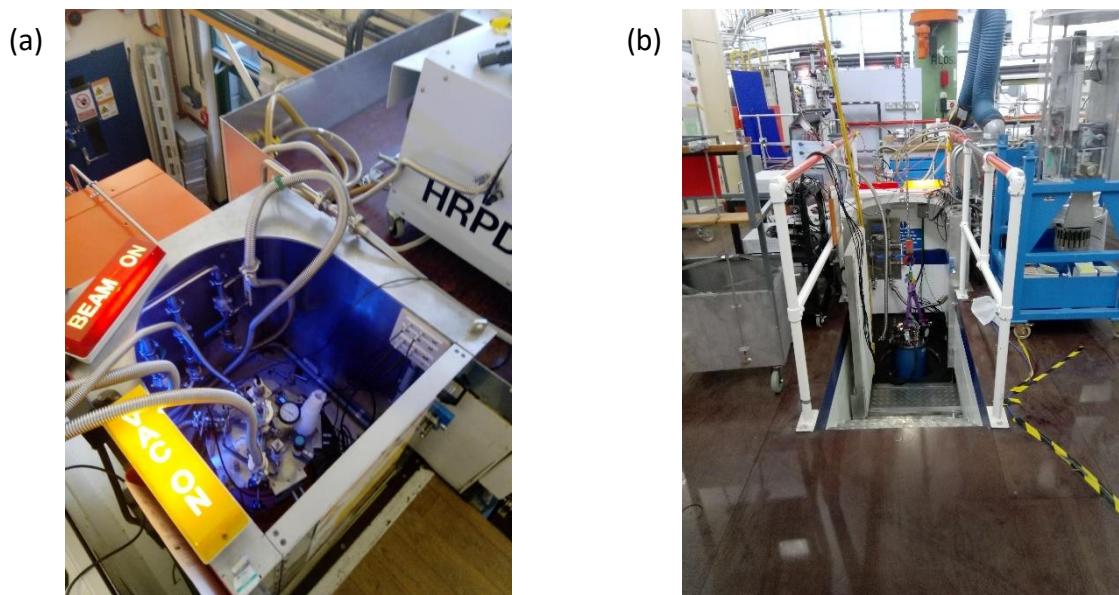
h is Planck's constant and m_n the neutron mass. Combining equation 2.20 with Bragg's law ($\lambda = 2d\sin(\theta)$) yields an expression relating the TOF to the inter-planar d -spacing:

$$\lambda = \frac{ht}{m_n L} = 2d\sin(\theta) \quad (2.21)$$

Rearranging to make t (in milliseconds) the subject gives:

$$t(\text{msec}) = 505.56 L(\text{m})d(\text{\AA})\sin\theta \quad (2.22)$$

Hence, structural information is extracted from a time-of-flight neutron powder diffraction pattern in much the same way as that produced by a continuous source using the Rietveld method described below. Time-of-flight diffraction experiments were performed on the HRPD (picture 2.1a) and GEM (picture 2.1b) beamlines at the ISIS Neutron and Muon Source.



Picture 2.1 (a) The High Resolution Powder Diffractometer (HRPD) and (b) the General Purpose Diffractometer (GEM) at the ISIS Neutron and Muon source.

b. Analysis of powder diffraction patterns – Rietveld refinement

In the powder diffraction pattern, only the intensity and not the phase of the diffracted wave is measured. The loss of phase information means it is not possible to determine the 3D structure from the intensities alone. To overcome the phase problem, Hugo Rietveld developed the Rietveld method to extract structural information from the height, width and position of the reflections in a 1D histogram pattern. The Rietveld method is a least squares minimization method and has been used since the 1960s to analyse powder diffraction patterns.

The recipe for the Rietveld method requires two key ingredients: (1) an experimental diffraction pattern and (2) a starting model of the 3D crystal structure. The first stage in the Rietveld method is to choose an appropriate model of the 3D crystal structure. The crystal structure for the compound

may already be known, in which case the space group and atomic positions for the known structure are used to create the 3D model. If the structure is unknown, either the model is developed using the structure from a related material, or a prediction is made based on the number of reflections, peak intensities, and peak positions. After developing a model, the powder pattern for the model can be calculated and compared to the experimental data. Initially, there will be a large difference between the experimentally observed (Y_{Obs}) and calculated (Y_{Calc}) pattern, as the example in Fig. 2.8 shows, where the blue difference curve ($Y_{Obs} - Y_{Calc}$) shows points of noticeable deviation from zero. To improve the description of the experimental pattern the model parameters are ‘refined’.

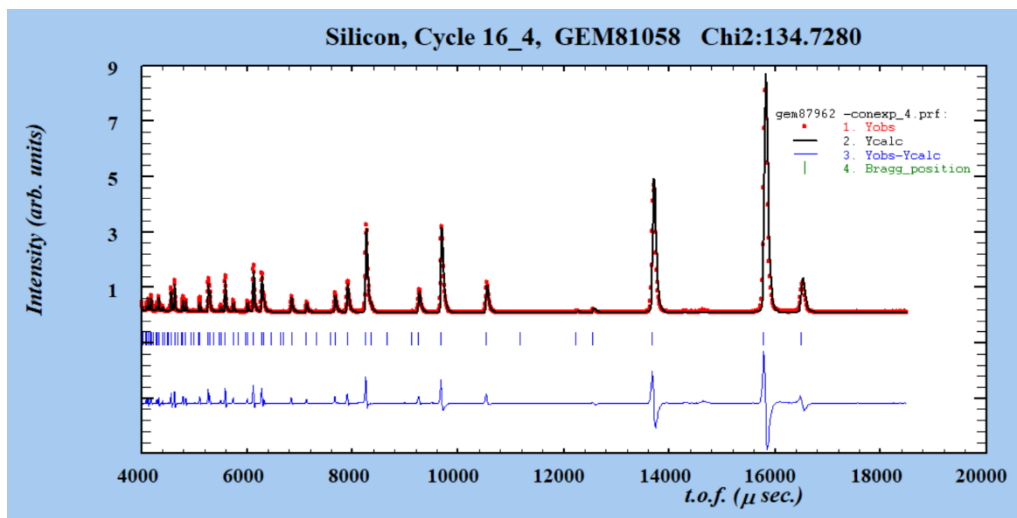


Fig. 2.8 Initial refinement results for Ba_2MnTeO_6 showing a poor fit between the observed and calculated powder pattern.

The model parameters are refined using the Rietveld least squared minimisation algorithm. In the Rietveld algorithm, the model parameters (unit cell size, atomic positions, thermal displacement and sample absorption) and instrumental parameters (e.g. sample height and sample absorption) are varied in order to minimise the weighted sum of the squared difference between the observed ($Y_{Obs,i}$) and calculated ($Y_{Calc,i}$) intensities at each point, i . The sum of the square differences is expressed as:

$$SUM = \sum_i w_i (Y_{Obs,i} - Y_{Calc,i})^2 \quad (2.23)$$

The weighting factor (w_i) is equal to $\frac{1}{\sigma^2[Y_{Obs,i}]}$, where $\sigma[Y_{Obs,i}]$ is the standard uncertainty. The standard uncertainty is the amount by which the experimental intensity ($Y_{Obs,i}$) deviates from the ‘true’ value of the intensity (Y_T). Y_T is determined by measuring the intensity an infinite number of times. This is impractical; therefore $\sigma[Y_{Obs,i}]$ is determined indirectly by counting the number of individual phonons or neutrons reaching the detector, in which case $Y_{Obs,i} = \sigma^2[Y_{Obs,i}]$.

This minimization procedure is repeated iteratively until the sum of the square differences is minimized. All the parameters are not refined at the same time due to parameter correlation. Strong correlation means minimization of one parameter will result in a large shift in another parameter. Consequently, the system diverges away from the minimum. Instead, parameters are introduced to the refinement in a sequence with the parameters that have the largest effect on the square differences refined first. A typical refinement sequence starts with refinement of the scale. Then unit cell parameters and the sample height are included. Subsequent parameters which have less effect on the fit are then introduced. For example, the peak shape, atomic positions and sample

absorption are introduced until the Rietveld algorithm converges to give a ‘good’ fit between the observed and calculated pattern.

Whether a ‘good’ fit is obtained is determined using fitting parameters, known as R -factors. The profile R -factor, R_p , is given by equation 2.24:

$$R_p = \left[\frac{\sum_i (Y_{obs,i} - Y_{calc,i})^2}{\sum_i (Y_{obs,i})^2} \right]^{1/2} \quad (2.24)$$

Alternatively, the R_p can be expressed as the weighted profile R -factor, R_{wp} , where the expression for R_p is scaled by the weighted intensity.

$$R_{wp} = \left[\frac{\sum_i w_i (Y_{obs,i} - Y_{calc,i})^2}{\sum_i w_i (Y_{obs,i})^2} \right]^{1/2} \quad (2.25)$$

The values of R_p and R_{wp} arguably provide the best indication of how well the Rietveld minimization has progressed as they contain the term which is being minimized: $(Y_{obs,i} - Y_{calc,i})^2$. The ‘best possible R_{wp} ’ is called the experimental R -factor, R_{exp} . R_{exp} is determined by assuming the model accurately predicts $Y_{O,i}$, hence $(Y_{obs,i} - Y_{calc,i})^2$ is equal to $\sigma^2[Y_{obs,i}]$. As a result, $w_i (Y_{obs,i} - Y_{calc,i})^2 = 1$. This is because w_i is equal to $\frac{1}{\sigma^2[Y_{obs,i}]}$, and so $\frac{1}{\sigma^2[Y_{obs,i}]} \times \sigma^2[Y_{obs,i}] = 1$. R_{exp} can then be expressed as:

$$R_{exp} = \left[\frac{N}{\sum_i w_i (Y_{obs,i})^2} \right]^{1/2} \quad (2.26)$$

Where, N is the number of data points. Another statistical measure of the fit is ‘Chi squared’, χ^2 . χ^2 is defined as:

$$\chi^2 = \frac{1}{N} \frac{\sum_i w_i (Y_{obs,i} - Y_{calc,i})^2}{\sigma^2[Y_{obs,i}]} \quad (2.27)$$

This is equivalent to the square of the ratio of R_{wp} and R_{exp} :

$$\chi^2 = \left[\frac{R_{wp}}{R_{exp}} \right]^2 \quad (2.28)$$

In the refinement, χ^2 starts out large as the model is poor. As more parameters are included, the model improves causing χ^2 to decrease as R_{wp} becomes smaller. However, χ^2 should never drop below 1. If $\chi^2 < 1$, this means R_{wp} is less than R_{exp} and the result is false as the model can never fit better than the actual data. Reasons why this situation may occur include over-estimation of the standard uncertainty, or refining too many parameters so the model also describes noise in the experimental data. Overall, the goal of Rietveld refinement is to obtain reasonably low R -factors (R_p , R_{wp} and R_{exp} all less than 10) and a $\chi^2 > 1$.

2. Inelastic Neutron Scattering (INS) spectroscopy

Neutron diffraction is an elastic scattering process (i.e. $k_i = k_f$). Neutrons can also be scattered inelastically. In an inelastic scattering process, there is a change in the neutron momentum so $k_i \neq k_f$. The neutron either gains energy from the sample or transfers some of its energy to the sample resulting in an overall change in momentum. The wavevector diagrams for both neutron energy loss and energy gain are shown in Fig. 2.9.

Neutron energy loss occurs when collision of the neutron with the sample leads to excitations. These excitations could correspond to lattice vibrational modes (known as phonons), atomic motions (diffusion), rotations, crystal field transitions or magnetic excitations. Measuring the change in neutron energy and momentum provides information about dynamics in the material. For example, phonon excitation provides information about the thermal and electrical properties of the sample. Magnetic excitations such as spin waves occur if the sample is magnetically ordered. Spin waves are collective oscillations of spins about an ordered ground state. The collective oscillations have a well-defined energy dispersion in wavevector space and for each magnetic ion in the sample there is a corresponding spin wave branch.

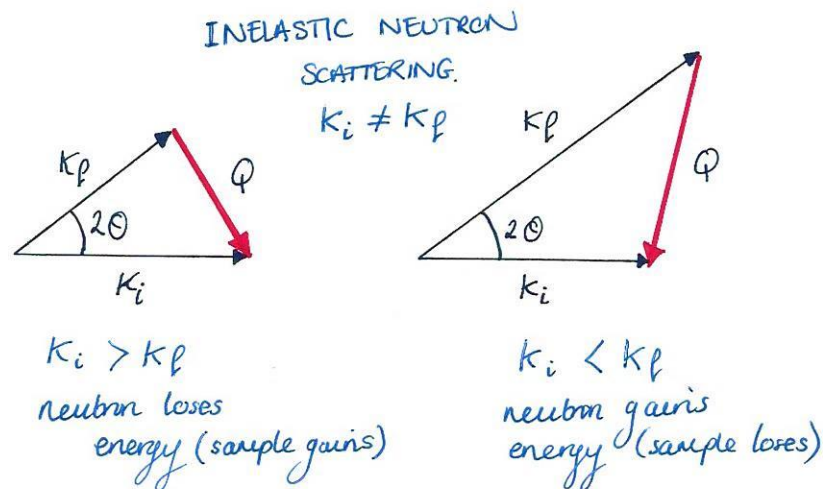


Fig. 2.9 Inelastic neutron scattering in momentum space showing energy loss and energy gain with respect to the neutron.

Inelastic neutron scattering is described using the dynamic structure factor: $S(Q, \omega)$. Q is the momentum transfer vector and $\omega\hbar$ (where $\omega = 2\pi/\lambda$) is the energy change experienced by the sample (i.e. amount of energy transferred to the sample). By measuring the energy change as a function of momentum transfer, an inelastic neutron spectrum is produced. Inelastic neutron scattering spectroscopy can be performed using triple axis spectrometers (continuous neutron sources) or time-of-flight spectrometers (pulsed neutron sources). With a triple axis spectrometer, the neutron energy before and after collision with the sample is measured. The three-step process involves: (1) monochromation of the incident neutron wavelength; (2) sample interaction and (3) analysis of the scattered neutron energy using a crystal analyser. The crystal analyser is rotated to detect the multiple scattered neutron energies using Bragg's Law. The scattering intensity in Energy-Momentum ($E - Q$) space is obtained by scanning the neutron energy (E) with constant k_i or k_f while Q is constant, and the momentum transfer (Q) in any direction while E is constant. In a triple axis experiment the wavelength (i.e. energy) of the neutrons is determined by the scattering angle. Alternatively, when performing inelastic neutron scattering using a time-of-flight spectrometer the initial and final neutron energies are instead selected based on the time it takes for the neutron to travel through the spectrometer to the detector. From the flight time over a known distance, the neutron energy is determined. The main advantage of time-of-flight spectrometers is that E and Q are measured simultaneously so a large region of $E - Q$ space, possibly containing multiple excitations, can be observed quickly. Overlap of magnetic and phonon excitations is generally avoided as phonon excitations are observed at large Q and diminish with reduced temperature.

Conversely, magnetic excitations diminish quickly with increasing Q and become stronger at low temperatures.

3. Extended X-ray Absorption Fine Structure (EXAFS)

The tuneable X-ray wavelength at synchrotron X-ray sources allows spectroscopy as well as diffraction to be performed. X-ray absorption occurs when the energy of a monochromatic beam of synchrotron X-rays matches the energy difference between the atomic energy levels of the sample atoms. Absorption results in the excitation or ejection of a core-electron. Through secondary processes, this results in fluorescence or electron emission as the core hole is filled by an electron from a higher energy level. By measuring changes in the beam intensity, sample fluorescence or number of ejected electrons, an X-ray absorption spectrum is produced. Fig. 2.10 shows an illustration of a typical X-ray absorption spectrum.¹

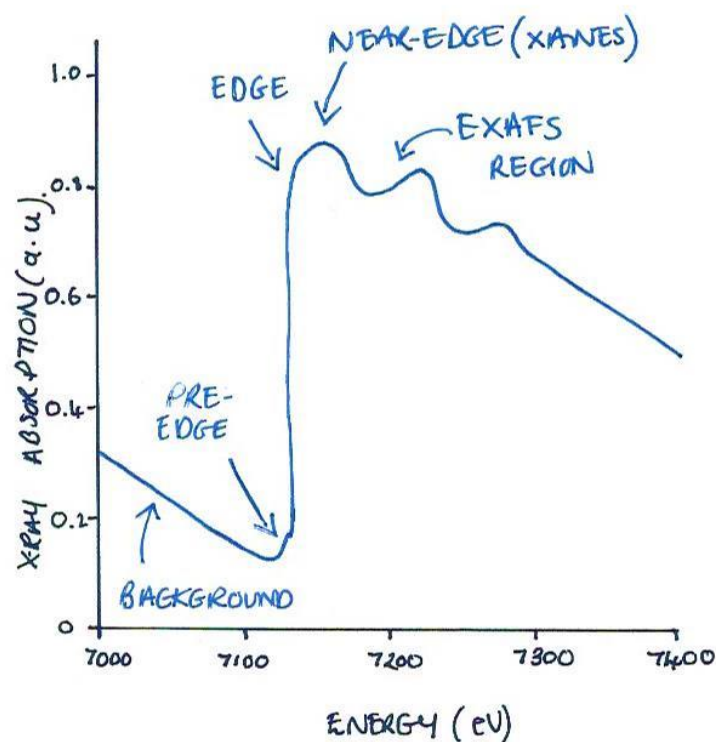


Fig. 2.10 Illustration of a typical X-ray absorption spectrum.

The sharp rise in X-ray absorption is known as the absorption edge. Below the absorption edge the X-ray photon energy is insufficient to excite a core-electron in the atom. At the edge, the X-ray energy is sufficient and X-ray absorption rises sharply. Above the edge, the X-ray absorption is low and gradually decreases as the probability of absorption decreases with increasing photon energy. Near the edge there may be shoulders or features. This is known as the X-ray Absorption Near-Edge Structure (XANES) and provides information about the local bonding between atoms. Above the edge, there are oscillations which represent the Extended X-ray Absorption Fine Structure (EXAFS). An electron ejected from an atom because of X-ray absorption processes can be viewed as a wave radiating from the atom in all directions. The electron wave interacts with the neighbouring atoms resulting in interference that is observed in the Extended X-ray Absorption Fine Structure. Hence, the EXAFS region provides information about the local structure surrounding the absorbing atom. The X-ray energy can be tuned to a specific core energy level to obtain element specific information on the local structure of a chosen atom through EXAFS.

4. Superconducting Quantum Interference Device (SQUID) magnetometry

A Superconducting Quantum Interference Device (SQUID) is a very sensitive magnetic detector that can detect very weak magnetic fields (e.g. magnetic fields in living organisms). Weak magnetic fields are detected using Josephson Junctions. A Josephson Junction consists of a thin, non-superconducting barrier separating two superconducting electrodes. The thickness of the barrier is such that electrons can 'tunnel' through the barrier at a critical current with no resistance. Below the critical current the voltage across the junction is zero, but above the critical current the voltage is non-zero and oscillates with time.

A DC SQUID uses two Josephson junctions arranged in parallel to form a loop.² The loop is connected to a detection coil forming a superconducting loop. A magnetically active sample is placed within the detection coils and calibrated to move up and down the coil between fixed distances. As the sample moves, the magnetic fields in the sample induce an electric current in the detection coils. The change in current changes the voltage across the Josephson junctions. The change in voltage is proportional to the change in current, which in turn depends on the strength of the magnetic fields in the sample. Josephson Junctions are sensitive to very small changes in current and using the linear current-to-voltage conversion can detect fields smaller than $\leq 10^{-8}$ emu.³ This is the sensitivity limit of the Quantum Design MPMS 3 SQUID magnetometer used to perform measurements in this thesis.

Other components of the MPMS 3 magnetometer include a superconducting magnet and sample temperature controls. A superconducting magnet can generate large magnetic fields between -7 to 7 Tesla (T).⁴ This allows the samples magnetic response in an external field to be measured over a wide field range by producing a M vs H curve. A M vs H curve shows how the sample magnetization (M) changes as a function of external magnetic field (H) at a fixed temperature. The sample magnetization can also be measured as a function of temperature (T) using the MPMS 3 sample temperature control system. In this thesis, the closed-cycle helium cryostat was used to control the sample temperature and produce M vs T curves in the temperature range of 2-300 K or 2-400 K. Both M vs H and M vs T measurements were performed in DC SQUID mode.

The MPMS 3 can also be operated in alternating current (AC) mode. AC magnetometry employs an AC magnetic field in addition to a DC field.⁵ The AC field varies with time, therefore the sample moment is also time-dependent. The time-dependent magnetic moment is detected without moving the sample through the detector coil. The detection circuit is configured to detect a narrow frequency band corresponding to the frequency of the AC field. At low frequencies, AC measurements are useful for detecting small shifts in the magnetic behaviour. At low AC frequencies, the AC M vs H curve follows the same shape as a DC M vs H curve. The AC moment in the M vs H curve is given by:

$$M_{AC} = \left(\frac{dM}{dH} \right) \cdot H_{AC} \sin(\omega t) \quad (2.29)$$

Here, H_{AC} is the amplitude of the AC drive field and ω is the AC drive frequency. The slope of the M vs H curve is the AC susceptibility: $\chi_{AC} = dM/dH$. As the AC field increases, during the M vs H measurement, small changes in the magnetic response are detected from the change in the χ_{AC} slope. The AC frequency increases and the AC moment becomes dynamic and may lag behind the driving field. The detector circuit monitors both the magnitude of the AC susceptibility and the shift in the phase of the AC frequency relative to the drive frequency. These are designated as the real in-phase (χ') and imaginary out-of-phase (χ'') components of the AC susceptibility. χ' is the value of the slope χ_{AC} in the M vs H curve. χ'' is commonly zero, but in cases where the imaginary

component is non-zero, this indicates there are dissipative processes in the sample. A non-zero value of χ'' is observed for spin-glasses due to relaxation and irreversibility. The spin glass freezing temperature is observed by a cusp in the χ' vs T AC susceptibility data. Irreversible spin freezing causes the position of the cusp to shift as the AC frequency changes. Consequently, AC susceptibility is a key technique for observing spin glass behaviour.

5. Heat Capacity

Heat capacity is defined as the amount of heat (Q) required to raise the temperature (T) of a substance by a given temperature increment (dT). Under constant pressure the equation for the heat capacity (C_p) is:

$$C_p = \left(\frac{dQ}{dT} \right)_p \quad (2.30)$$

The laws of thermodynamics govern processes involving heat transfer. The second law of thermodynamics relates the change in heat to the entropy of the system and states that the entropy (degree of disorder) always increases for a spontaneous process. A spontaneous process occurs without any external influence under a specific set of conditions. The equation for the second law of thermodynamics is given by:

$$dQ = TdS \quad (2.31)$$

By combining and rearranging equations 2.30 and 2.31, the heat capacity between T_{min} and T_{max} is related to the entropy in equation 2.32.⁶

$$S = \int_{T_{min}}^{T_{max}} \left(\frac{C_p}{T} \right) dT \quad (2.32)$$

Measuring the heat capacity provides a means to determine how the entropy of the system changes with temperature. The entropy, and hence the heat capacity, depends on the number of degrees of freedom (i.e. more degrees of freedom = higher entropy/heat capacity). Several factors contribute towards the total heat capacity (C_{tot}) in equation 2.33.

$$C_{tot} = C_{lat} + C_{mag} + C_{el} + C_{nuc} \quad (2.33)$$

C_{lat} is the lattice contribution due to excitation of vibrational modes known as phonons in the lattice. C_{mag} is the magnetic contribution originating from excitation of magnetic modes known as spin waves. Spin waves are collective oscillations of the magnetic spins in the material. C_{el} is the electronic Schottky contribution arising from thermal emission of electrons. C_{nuc} is the hyperfine contribution arising from the interaction between the magnetic moments and the quadrupolar moment of the nuclei. In a magnetic lattice, the main contributions to consider are C_{lat} and C_{mag} .⁷ If there are no phase transitions, C_{tot} as a function of temperature should be a smooth slope with a positive gradient as the C_{lat} contribution to C_{tot} increases at higher temperatures. Structural and magnetic phase transitions involve a large change in entropy and can be identified by a sharp 'kink' in the C_p/T vs T data. These kinks are called lambda transitions as their shape resembles the Greek letter λ . Therefore, C_{tot} vs T measurements offer another means to identify magnetic ordering in materials. Heat capacity measurements were performed using a Quantum Design PPMS.

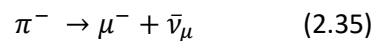
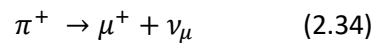
6. Muon Spin Relaxation (μ SR)

Muon spin relaxation employs the muon's intrinsic spin to study structural and dynamic processes in bulk materials on an atomic scale.⁸ Muons are unstable elementary particles with a lifetime of 2.2

μ s. They can be +1 or -1 charged and have a mass that depends on their charge. While seemingly short-lived, muons actually have the second longest lifetime of all fundamental unstable particles and exist long enough to be used as probes in bulk materials. For example, muons are commonly implanted as probes in bulk magnetic materials wherein they can sense very weak magnetic fields. Furthermore, muons are sensitive towards both local static and dynamic magnetism; and can detect dynamic magnetic fields fluctuating at rates between $\sim 10^4 - 10^{11} \text{ s}^{-1}$. Muons have a strong advantage over bulk techniques such as SQUID magnetometry and heat capacity measurements. Bulk techniques provide information on the average magnetism of the whole sample, so cannot distinguish between local uniform and non-uniform magnetic behaviour. Muons are often called 'local magnetic probes' and can detect magnetic behaviours which bulk techniques cannot.

a. Muon production

Muons are produced from the decay of unstable subatomic particles called pions (π). Pions are produced from the collision of high energy particles (e.g. protons) with a target. The mean pion lifetime for π^+ and π^- is much shorter than the muon ($\sim 26 \text{ ns}$) so they quickly decay into μ^+ or μ^- :



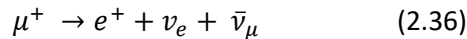
Atmospheric muons are produced when high energy particles in cosmic rays collide with atomic nuclei in the Earth's upper atmosphere. Atmospheric muons are useful for archaeological applications such as muography, where natural and man-made structures are imaged from the absorption or scattering of muons. The muon flux at ground level is too low for most other scientific applications. Instead, dedicated pulsed and continuous muon sources have been developed.

The ISIS Neutron and Muon source is a pulsed source. As well as generating pulsed neutrons, ISIS also creates pulsed muons using a second graphite target placed upstream from the tungsten neutron target. Pulses of protons from the synchrotron ring collide with the target generating pions. The pions decay in flight or at the target surface forming a pulsed muon beam. Surface muons are most useful as they possess the highest degree of spin polarization. This ensures the muons are implanted in the sample with the same initial spin direction. Continuous sources, such as the Paul Scherrer Institut (PSI), use a cyclotron ring to generate a continuous muon beam. Protons are injected into the centre of the cyclotron ring and are accelerated using magnetic fields on a spiral path. The protons then collide with the graphite target to produce pions. The muons arrive randomly at the sample as a continuous beam. Continuous sources offer much better time resolution as it is possible to individually determine the arrival time of each muon using a muon counter. However, counting each muon event lengthens the measurement time compared to pulsed sources where many muon events are captured simultaneously within each muon pulse timescale.

b. Muons spin relaxation and magnetism

Muons are implanted into the sample with 100% spin polarization, with the muon spin pointing anti-parallel to the direction of travel. In polycrystalline samples, muons reside in interstitial sites within the crystalline structure. There may be more than one interstitial muon stopping site in the material. Once implanted, the muon decays to produce a positron (e^+). Positron emission violates parity with a positron being emitted asymmetrically in the direction of the muon spin. Detectors are placed around the sample (as illustrated in Fig. 2.11), enabling the direction of positron emission to be determined. The positron detectors around the sample can also be seen in picture 2.2. Picture 2.2 is an image of the MUSR muon spectrometer (ISIS) that was used to perform muon experiments in this

thesis. As shown in equation 2.36, muon production also results in the production of an electron neutrino (ν_e) and a muon antineutrino ($\bar{\nu}_\mu$).



By detecting the positron emission, it is possible to measure the asymmetry of the muon decay. The asymmetry ($A(t)$) is determined by taking the difference in positron counts between the forward (N_F) and backwards (N_B) detectors.

$$A(t) = (N_F - \alpha N_B) / (N_F + \alpha N_B) \quad (2.37)$$

The α term is a constant to correct for any differences in detector efficiency between the forwards and backwards positron detectors. The asymmetry of the muon signal is directly related to the muon polarization $P(t)$ as shown below:

$$A(t) = A_0 P(t) \quad (2.38)$$

The initial asymmetry (A_0) is the total asymmetry at time zero. By measuring $A(t)$ as a function of time, it is possible to determine how the local magnetic environment affects the muon spin polarization. In a magnetically ordered polycrystalline material, the muon spin precesses around the static magnetic field. The muon spin polarization oscillates generating an oscillation in the $A(t)$ signal when no external field is applied (known as a zero-field (ZF) measurement). Therefore, oscillations in the $A(t)$ signal indicate long-range magnetic ordering. The magnetic ordering temperature can be determined using transverse-field (TF) measurements. In a TF muon measurement, an external B_{TF} field is applied perpendicular to the initial muon spin polarization in the direction of the incoming muon beam. This is illustrated by the red arrow in Fig. 2.11. Upon implantation, the muons feel the effect of the applied field and the muon spin precesses around the B_{TF} field. On approaching the ordering temperature, the oscillation of the transverse-field asymmetry (A_{TF}) is dampened as the muons begin to couple to the internal magnetic field instead of B_{TF} . The transition temperature is located by plotting A_{TF} as a function of temperature (T).

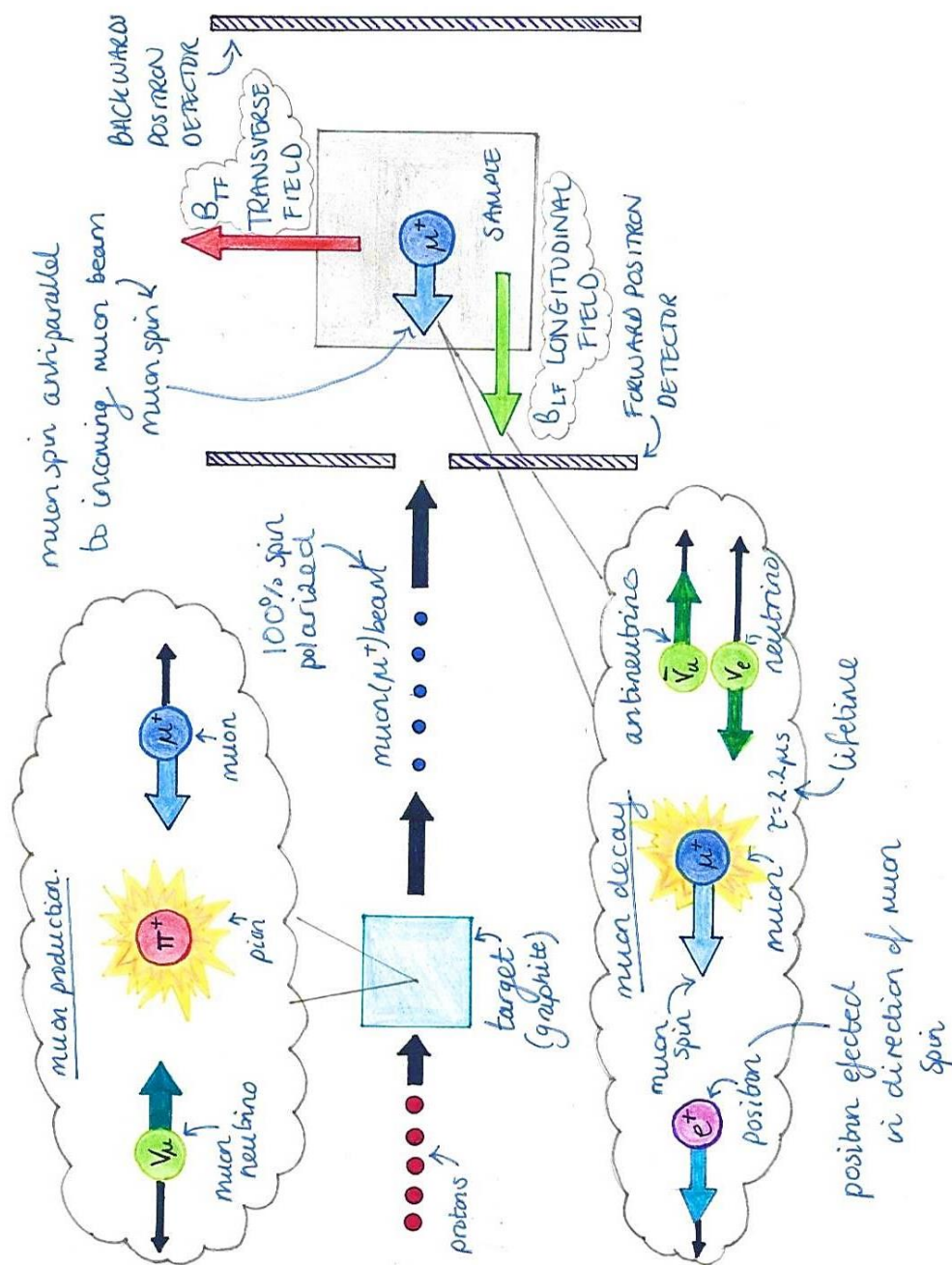
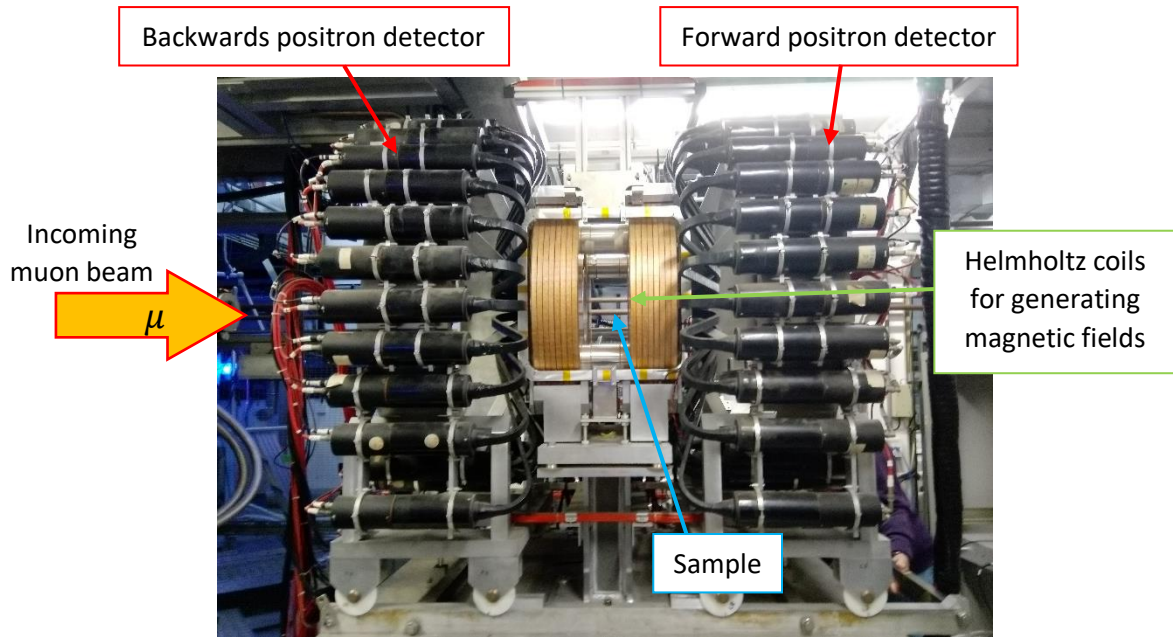


Fig. 2.11 Illustration of the set-up for a muon spin relaxation experiment. The illustration shows muon generation by collision of protons with the target to produce pions that decay into muons. The muons are then collimated into a muon beam where they are counted, before implantation into the sample. Forwards and backwards positron detectors surround the sample. The muons are implanted into the sample with 100% spin polarization. Local fields within the sample affect the muons spin polarization. Positrons are emitted in the direction of the muon spin. By comparing the positron count of the forward and backwards detectors, information about the muon spin relaxation is obtained. The muon spin relaxation may be measured in zero-field, or a field may be applied to observe the effect of external fields on the muon polarization. External fields are applied either parallel or perpendicular to the direction of the initial muon polarization. These are known as longitudinal-field (LF) measurements (green arrow) and transverse-field (TF) measurements (red arrow).



Picture 2.2 The MUSR muon spectrometer at the ISIS Neutron and Muon source.

Muons can also detect other types of magnetic behaviour. For example, instead of long-range magnetic order, the magnetic moments in a material may still be static, but in a disordered arrangement. In this case the muon spin feels a distribution of local internal fields in the x , y and z directions. This field distribution may be Gaussian or Lorentzian, with the latter a more likely description in dilute magnetic systems. In the case of a static Gaussian field distribution, the muon polarization functions for the different B_{int} fields superimpose so on average the muon asymmetry follows a static Kubo-Toyabe function (equation 2.39) as illustrated in Fig. 2.12a. Initially, there is a sharp drop in the initial asymmetry at low times followed by a 1/3 recovery of the initial asymmetry. The 1/3 tail represents the 1/3 of the magnetic fields that are parallel or antiparallel to the muon spin in the z direction. The result is the static Gaussian Kubo-Toyabe function defined in equation 2.39, in which σ_s/γ_μ is the width of the field distribution and t is time (σ_s is the Gaussian decay rate and γ_μ the gyromagnetic ratio of the muon). There is an analogous static Kubo-Toyabe function for Lorentzian fields describing dilute static disorder. The expression for the static Lorentzian Kubo-Toyabe function is shown in equation 2.40, where the width of the distribution is given by λ_s/γ_μ (λ_s is the Lorentzian decay rate). The static Lorentzian Kubo-Toyabe function plotted in Fig. 2.12b has a similar shape to the static Gaussian Kubo-Toyabe function in Fig. 2.12a, but the 1/3 tail is recovered more slowly.⁹

$$\text{Static Gaussian Kubo - Toyabe} \rightarrow P(t) = \frac{1}{3} + \frac{2}{3}e^{-\frac{1}{2}\sigma_s^2 t^2} (1 - \sigma_s^2 t^2) \quad (2.39)$$

$$\text{Static Lorentzian Kubo - Toyabe} \rightarrow P(t) = \frac{1}{3} + \frac{2}{3}e^{-\lambda_s t} (1 - \lambda_s t) \quad (2.40)$$

Muons are also sensitive to dynamic behaviour. In a dynamic muon environment, the magnetic field felt by the muon fluctuates rather than being constant. Dynamic fields can arise due to muon hopping. Once implanted the muon does not necessarily remain stationary and may migrate or 'hop' between muon sites. As the muon hops, it experiences different magnetic fields. Alternatively, instead of the muon being dynamic, the surrounding magnetic fields may fluctuate, while the muon remains stationary. Fluctuation in the surrounding magnetic fields could originate from a variety of

different behaviours e.g. spin liquid. The fluctuating magnetic fields depolarise the muons so the $A(t)$ signal follows an exponential relaxation.

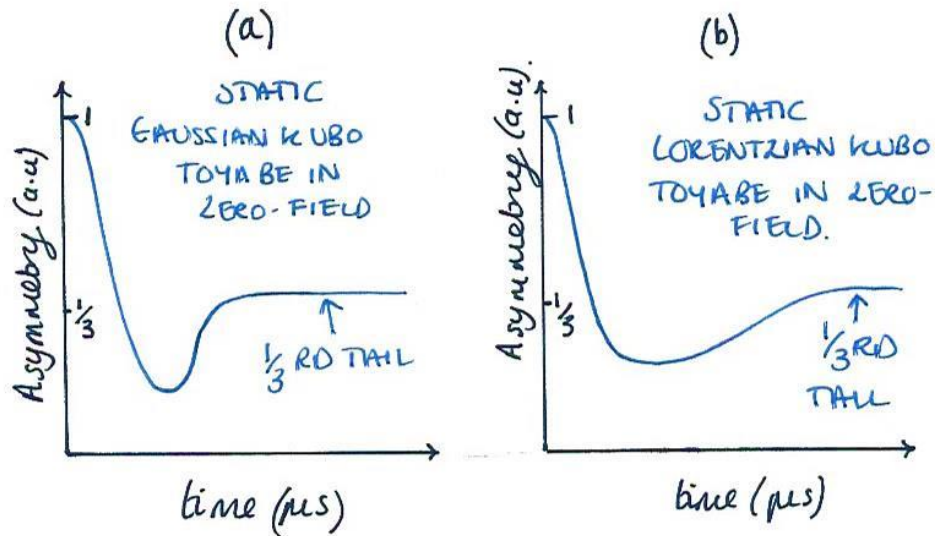


Fig. 2.12 Illustration of (a) the static Gaussian Kubo-Toyabe muon spin relaxation function and (b) the static Lorentzian Kubo-Toyabe muon spin relaxation function.

Transitions from static disorder to dynamic behaviour can be followed by measuring the $A(t)$ signal at various temperatures above and below the transition. At temperatures close to zero Kelvin, the muon spin relaxation follows a static Gaussian Kubo-Toyabe function. As the temperature increases, the $1/3$ tail is reduced as the surrounding magnetic fields start to become dynamic. As the dynamics speed up, the muon relaxation transitions into an exponential relaxation function and at high fluctuation rates is described by the function in equation 2.41.

$$P(t) = e^{-\lambda t} \quad (2.41)$$

Here, $\lambda = \frac{2\Delta^2}{\nu}$ is the relaxation rate of the muon polarization, where Δ is the field distribution and ν the field fluctuation rate. The muon relaxation rate is inversely proportional to the field fluctuation rate because of motional narrowing. As the field fluctuation rate becomes faster, the muon spin begins to see more of an 'average' field and experiences less fluctuation in magnetic field. Therefore, the relaxation rate drops off more slowly as the surrounding field becomes more dynamic. It is useful to measure dynamic muon spin relaxation in the presence of an increasing external field that is applied in the direction (longitudinal) of the initial muon spin polarization as illustrated in Fig. 2.11. Measuring the longitudinal-field (LF) muon spin relaxation with increasing LF fields shows the strength of the field required to repolarize the muon spins. This gives an indication of the strength and nature (i.e. electronic or nuclear) of the dynamic magnetic fields.

7. Polarized neutron scattering

Polarized neutron scattering is another form of neutron scattering. The neutron diffraction pattern of a magnetically ordered crystalline material has both coherent and/or diffuse magnetic scattering contributions. Coherent magnetic scattering originates from the magnetically ordered moments. Diffuse magnetic scattering is caused by paramagnetic moments which arise from disorder or deviations from long-range magnetic order. Diffuse scattering provides information about magnetic correlations in the material and how they evolve with temperature. Studying diffuse scattering using

neutron diffraction is difficult as the scattering is dominated by coherent magnetic and nuclear scattering. Using polarized neutron scattering, it is possible to separate the magnetic and nuclear scattering to isolate the diffuse magnetic scattering.¹⁰

To achieve this, polarized neutron scattering analyses the xyz -polarization of the neutron scattering using a dedicated xyz -polarization analysis spectrometer, such as D7 at the Institut Laue-Langevin (ILL). This instrument uses a polarized neutron beam in which the neutrons $S = \frac{1}{2}$ spins are aligned in one direction prior to scattering. The effect of the sample magnetisation on the initial neutron polarization is measured. If there is no change in the neutron polarization (non-spin-flip (NSF) scattering), the component of the sample magnetization is parallel to the neutron spin. If the neutron spin is flipped (spin-flip (SF)) scattering, the perpendicular components of the sample magnetisation are sensed. In xyz -polarization analysis, the neutron polarization can be changed so the neutrons are polarized along x , y or z . By measuring the NSF and SF scattering with the initial neutron polarization along x , y and z ; it is possible to separate out the magnetic scattering contribution using the equations below.¹⁰ These equations show the scattering contributions towards the NSF and SF neutron scattering cross sections along x , y and z .

$$\left(\frac{d\sigma}{d\Omega}\right)_x^{\text{NSF}} = \frac{1}{2} \sin^2 \alpha \left(\frac{d\sigma}{d\Omega}\right)_{\text{mag}} + \frac{1}{3} \left(\frac{d\sigma}{d\Omega}\right)_{\text{si}} + \left(\frac{d\sigma}{d\Omega}\right)_{\text{nuc}} \quad (2.42)$$

$$\left(\frac{d\sigma}{d\Omega}\right)_x^{\text{SF}} = \frac{1}{2} (\cos^2 \alpha + 1) \left(\frac{d\sigma}{d\Omega}\right)_{\text{mag}} + \frac{2}{3} \left(\frac{d\sigma}{d\Omega}\right)_{\text{si}} \quad (2.43)$$

$$\left(\frac{d\sigma}{d\Omega}\right)_y^{\text{NSF}} = \frac{1}{2} \cos^2 \alpha \left(\frac{d\sigma}{d\Omega}\right)_{\text{mag}} + \frac{1}{3} \left(\frac{d\sigma}{d\Omega}\right)_{\text{si}} + \left(\frac{d\sigma}{d\Omega}\right)_{\text{nuc}} \quad (2.44)$$

$$\left(\frac{d\sigma}{d\Omega}\right)_y^{\text{SF}} = \frac{1}{2} (\sin^2 \alpha + 1) \left(\frac{d\sigma}{d\Omega}\right)_{\text{mag}} + \frac{2}{3} \left(\frac{d\sigma}{d\Omega}\right)_{\text{si}} \quad (2.45)$$

$$\left(\frac{d\sigma}{d\Omega}\right)_z^{\text{NSF}} = \frac{1}{2} \left(\frac{d\sigma}{d\Omega}\right)_{\text{mag}} + \frac{1}{3} \left(\frac{d\sigma}{d\Omega}\right)_{\text{si}} + \left(\frac{d\sigma}{d\Omega}\right)_{\text{nuc}} \quad (2.46)$$

$$\left(\frac{d\sigma}{d\Omega}\right)_z^{\text{SF}} = \frac{1}{2} \left(\frac{d\sigma}{d\Omega}\right)_{\text{mag}} + \frac{2}{3} \left(\frac{d\sigma}{d\Omega}\right)_{\text{si}} \quad (2.47)$$

α is the angle between the scattering vector and an arbitrarily chosen x axis. The total mag – magnetic, si – spin incoherent and nuc – nuclear scattering contributions are determined from linear combinations of the neutron scattering cross section equations above (see equations 2.48 to 2.50).

$$\left(\frac{d\sigma}{d\Omega}\right)_{\text{mag}} = 2 \left(\frac{d\sigma}{d\Omega}\right)_x^{\text{SF}} + 2 \left(\frac{d\sigma}{d\Omega}\right)_y^{\text{SF}} - 4 \left(\frac{d\sigma}{d\Omega}\right)_z^{\text{SF}} \quad (2.48)$$

$$\left(\frac{d\sigma}{d\Omega}\right)_{\text{nuc}} = \frac{1}{6} \left[2 \left(\frac{d\sigma}{d\Omega}\right)_{\text{total NSF}} - \left(\frac{d\sigma}{d\Omega}\right)_{\text{total SF}} \right] \quad (2.49)$$

$$\left(\frac{d\sigma}{d\Omega}\right)_{\text{si}} = \frac{1}{2} \left(\frac{d\sigma}{d\Omega}\right)_{\text{total SF}} - \left(\frac{d\sigma}{d\Omega}\right)_{\text{mag}} \quad (2.50)$$

Having separated the magnetic contribution, the diffuse magnetic scattering can be plotted as a function of wavevector ($|Q|$) space. Diffuse magnetic scattering data is analysed using SPINVERT. SPINVERT uses a reverse Monte Carlo approach to simulate the experimental diffuse magnetic scattering data.¹¹ In simple terms, SPINVERT is provided a box of defined size containing the spin configuration of the magnetic unit cell. The spin orientation is changed and the changes either accepted or rejected depending on the improvement in the fit to the experimental data. The process is repeated until a spin configuration is obtained that best replicates the experimental diffuse

scattering data. From this spin configuration, the spin-spin correlations between the magnetic centres in the sample are determined. Performing polarized neutron scattering experiments at various temperatures shows how the spin-spin correlations evolve with temperature.

References

1. Calvin, S. *XAFS for Everyone*. CRC Press, Boca Raton (2013). doi:10.1201/b14843
2. Fagaly, R. L. Superconducting quantum interference device instruments and applications. *Rev. Sci. Instrum.* **77**, 101101 (2006).
3. <https://www.qdusa.com/products/mpms3.html>. Accessed: 12/01/2022 Available at: <https://www.qdusa.com/products/mpms3.html>.
4. <https://www.qdusa.com/siteDocs/productBrochures/1500-102.pdf>. Accessed: 12/01/2022
5. Martien, D. Introduction to: AC Susceptibility. *Quantum Design Manual*: <https://www.qdusa.com/siteDocs/appNotes/1078-201.pdf> doi:10.4324/9780203478004_chapter_11
6. Gopal, E. S. R. *Specific heats at low temperatures*. Plenum Press, New York (1966). doi:10.1007/978-1-4684-9081-7
7. Morrison, J. A. & Newsham, D. M. T. Analyses of low-temperature heat capacities containing two or more contributions: Application to the rare earth metals. *J. Phys. C (Proc. Phys. Soc.)* **1**, 370–377 (1968).
8. Nagamine, K. *Introductory Muon Science*. Cambridge University Press, New York (2003).
9. Tan, C. *et al.* Slow magnetic fluctuations and critical slowing down in $\text{Sr}_2\text{Ir}_{1-x}\text{Rh}_x\text{O}_4$. *Phys. Rev. B* **101**, 195108–1 (2020).
10. Stewart, J. R. *et al.* Disordered materials studied using neutron polarization analysis on the multi-detector spectrometer, D7. *J. Appl. Crystallogr.* **42**, 69–84 (2009).
11. Paddison, J. A. M., Ross Stewart, J. & Goodwin, A. L. Spinvert: A program for refinement of paramagnetic diffuse scattering data. *J. Phys. Condens. Matter* **25**, 454220 (2013).

Chapter 3: An introduction to the d^{10}/d^0 effect in a cubic perovskite: $\text{Ba}_2\text{MnTeO}_6$

Contents

1. Abstract
2. Introduction
3. Experimental
4. Results
 - a. SQUID magnetometry
 - b. Heat capacity
 - c. Crystal structure
 - i. Laboratory X-ray diffraction
 - ii. Neutron diffraction
 - d. Magnetic structure
 - e. Inelastic neutron scattering
 - f. Polarized neutron scattering
 - g. Density functional theory calculations
5. Discussion
6. Conclusions
7. References

1. Abstract

Non-magnetic d^{10} and d^0 B'' cations can affect the behaviour of magnetic B' cations in $A_2B'B''O_6$ double perovskites. d^{10}/d^0 effects have mainly been studied in distorted double perovskites, some of which have complex magnetic behaviours e.g. spin-orbit coupling or quantum effects. A comparison of d^{10} vs d^0 cations in an *ideal* cubic perovskite system is required to establish the d^{10}/d^0 effect as a general feature of $A_2B'B''O_6$ perovskites. $\text{Ba}_2\text{MnTeO}_6$ and Ba_2MnWO_6 are predicted to be cubic and have a classical Mn^{2+} $S = 5/2$ spin with no spin-orbit coupling. The structural and magnetic properties of Ba_2MnWO_6 are well known, but information on $\text{Ba}_2\text{MnTeO}_6$ was lacking. Characterization of $\text{Ba}_2\text{MnTeO}_6$ confirmed $\text{Ba}_2\text{MnTeO}_6$ and Ba_2MnWO_6 are isostructural, but exhibit different types of magnetic order due to the d^{10}/d^0 effect, where d^{10} cations promote a strong nearest neighbour (J_1) interaction and d^0 cations promote a strong next-nearest neighbour (J_2) interaction. The d^{10}/d^0 effect extends beyond $\text{Ba}_2\text{Mn}(\text{Te}/\text{W})\text{O}_6$ to a range of ordered double perovskites.

2. Introduction

Incorporation of Mn^{n+} cations into perovskite structures often procures valuable magnetic and electrical behaviours, for example magnetoresistance. Magnetoresistive materials change their electrical resistance in response to an externally applied field and have widespread applications in spintronic devices (e.g. magnetic read heads in hard disks, biosensors and random access memory storage).¹⁻⁴ A classic example is the single perovskite $\text{La}_{1-x}\text{A}_x\text{MnO}_3$, where A is a 2+ cation (e.g. Ca, Sr, Ba or Pb) leading to a mixture of $\text{Mn}^{3+}/\text{Mn}^{4+}$ cations. The mixture of $\text{Mn}^{3+}/\text{Mn}^{4+}$ cations facilitates 'colossal magnetoresistance' via double exchange.⁵ Polycrystalline Mn^{n+} double perovskites also display magnetoresistance, but instead of double exchange, magnetoresistance originates from the formation of spin-polarized ferro-/ferrimagnetic domains across which electrons tunnel.⁶⁻⁹ The

discovery of near-room temperature magnetoresistance in $\text{La}_2\text{NiMnO}_6$ and $\text{La}_2\text{CoMnO}_6$ prompted the exploration of a range of $A_2\text{MnB}''\text{O}_6$ perovskites with different A and B'' cations.^{10,11}

By selectively changing the A - and B'' -site cations, the structural and magnetic properties of $A_2\text{MnB}''\text{O}_6$ perovskites can be altered. Changing the A -site cation affects the perovskite structure through octahedral tilting.¹²⁻¹⁴ The B'' cation can also affect the structure, but also plays an important role in the magnetic superexchange interactions. Magnetic cations (M^{n+}) couple indirectly through mediating oxygen $2p$ orbitals in a 90° or $180^\circ M^{n+}\text{-O-}M^{n+}$ superexchange interaction.¹⁵⁻¹⁷ If B'' is a magnetic cation, then two magnetic sub-lattices are formed in $A_2\text{MnB}''\text{O}_6$: one for each of the magnetic Mn^{n+} and B'' cations. This occurs in $\text{La}_2\text{NiMnO}_6$ and $\text{La}_2\text{CoMnO}_6$ as both $\text{Co}^{2+/3+}$ and $\text{Ni}^{2+/3+}$ have unpaired electrons. If B'' is non-magnetic (i.e. d^{10} or d^0) the magnetic Mn^{2+} cations are further apart and extended superexchange interactions form through the O^{2-} anions and the non-magnetic B'' cation i.e. $\text{Mn-O-B}''\text{-O-Mn}$.

Different combinations of $A = \text{Ca}^{2+}$, Sr^{2+} and Ba^{2+} with non-magnetic $B'' = \text{W}^{6+}$, Te^{6+} and Mo^{6+} cations have been studied in $A_2\text{MnB}''\text{O}_6$ double perovskites. Table 3.1 provides a summary of the key structural and magnetic results for the 9 different structural combinations to date.

Table 3.1: Structural and magnetic properties of the $A_2\text{MnB}''\text{O}_6$ ($A = \text{Ca}^{2+}$, Sr^{2+} , Ba^{2+} and $B'' = \text{W}^{6+}$, Te^{6+} , Mo^{6+}) double perovskites

$A_2\text{MnB}''\text{O}_6$ composition	Crystal structure	Type of magnetic order	Néel temperature (T_N , K)	Ref.
Ba_2MnWO_6	Cubic ($Fm\bar{3}m$)	AFM Type II $k = (\frac{1}{2} \frac{1}{2} \frac{1}{2})$	8-9	18-20
Sr_2MnWO_6	Monoclinic ($P2_1/n$)*	AFM Type II $k = (\frac{1}{2} 0 \frac{1}{2})$	13	21,22
Ca_2MnWO_6	Monoclinic ($P2_1/n$)	AFM Type II $k = (0 \frac{1}{2} \frac{1}{2})$	16-17	22,23
$\text{Ba}_2\text{MnMoO}_6$	Cubic ($Fm\bar{3}m$)	AFM Type II $k = (\frac{1}{2} \frac{1}{2} \frac{1}{2})$	11	24,25
$\text{Sr}_2\text{MnMoO}_6$	Tetragonal ($P4_2/n$)	AFM Type II $k = (\frac{1}{2} 0 \frac{1}{2})$	12-15	22,24,26
$\text{Ca}_2\text{MnMoO}_6$	Monoclinic ($P2_1/n$)	AFM	-	27,28
$\text{Ba}_2\text{MnTeO}_6$	-	-	-	29
$\text{Sr}_2\text{MnTeO}_6$	Monoclinic ($P2_1/n$)	AFM Type I $k = (0 0 0)$	20	30,31
$\text{Ca}_2\text{MnTeO}_6$	Monoclinic ($P2_1/n$)	AFM	10	32

* Space group originally reported as tetragonal $P4_2/n$ by refs.^{33,34}, but later determined to be better described as monoclinic $P2_1/n$ by refs.^{21,22}

There are clear trends associated with the identity of the A - and B'' -site cation in Table 3.1. Table 3.1 shows when $A = \text{Ba}^{2+}$, the $A_2\text{MnB}''\text{O}_6$ structure is cubic. Whereas when $A = \text{Sr}^{2+}$ or Ca^{2+} , the structure distorts from the *ideal* perovskite structure to a lower symmetry structure. The cation size decreases up Group 2: Ba^{2+} (1.61 Å) < Sr^{2+} (1.44 Å) < Ca^{2+} (1.34 Å).³⁵ The ionic radii of Ba^{2+} is 'optimum' for the cubic structure, but as the cation size decreases, Sr^{2+} and Ca^{2+} struggle to fill the A -site. The MnO_6

and $B''O_6$ octahedra tilt to optimize the A-O bond distances leading to a reduction in symmetry.¹³ This demonstrates the effect of the A-site cation on the crystal structure.

The identity of the B-site cation affects the magnetic properties of the compositions in Table 3.1. Structures with $B'' = Mo^{6+}$ and W^{6+} (d^0 cations) exhibit type II antiferromagnetic order. Alternatively, when $B'' = Te^{6+}$ (d^{10} cation) type I results. Fig. 3.1 depicts (a) type I and (b) type II ordering in the *fcc* sub-lattice. In both types of order, there are two main magnetic interactions.^{36,37} These are the nearest neighbour (NN)- J_1 and next-nearest neighbour (NNN)- J_2 interactions. The magnitude and sign of J_1 and J_2 determines whether type I or type II order is observed. The J_1 and J_2 interactions are described using the simple cubic Heisenberg J_1 - J_2 model depicted in Fig. 3.1c. This J_1 - J_2 model is described using the following Hamiltonian:³⁸

$$\hat{H} = -J_1 \sum_{\langle ij \rangle} \mathbf{S}_i \cdot \mathbf{S}_j - J_2 \sum_{\langle\langle ij \rangle\rangle} \mathbf{S}_i \cdot \mathbf{S}_j \quad (3.1)$$

Here, J_1 is the NN interaction, J_2 is the NNN interaction, S_i is the spin on atom i and S_j is the spin on atom j . Both S_i and S_j are summed over all the NN and NNN interactions. In type I order, J_1 is positive (ferromagnetic) and J_2 is negative (antiferromagnetic) leading to ferromagnetically ordered layers of magnetic cations along the (001) axis that are coupled antiferromagnetically (Fig. 3.1a). Alternatively, both J_1 and J_2 are negative (antiferromagnetic) in type II order. This leads to ferromagnetic layers along the (111) planes of the *fcc* sub-lattice with antiferromagnetic interactions between the (111) planes (Fig. 3.1b).

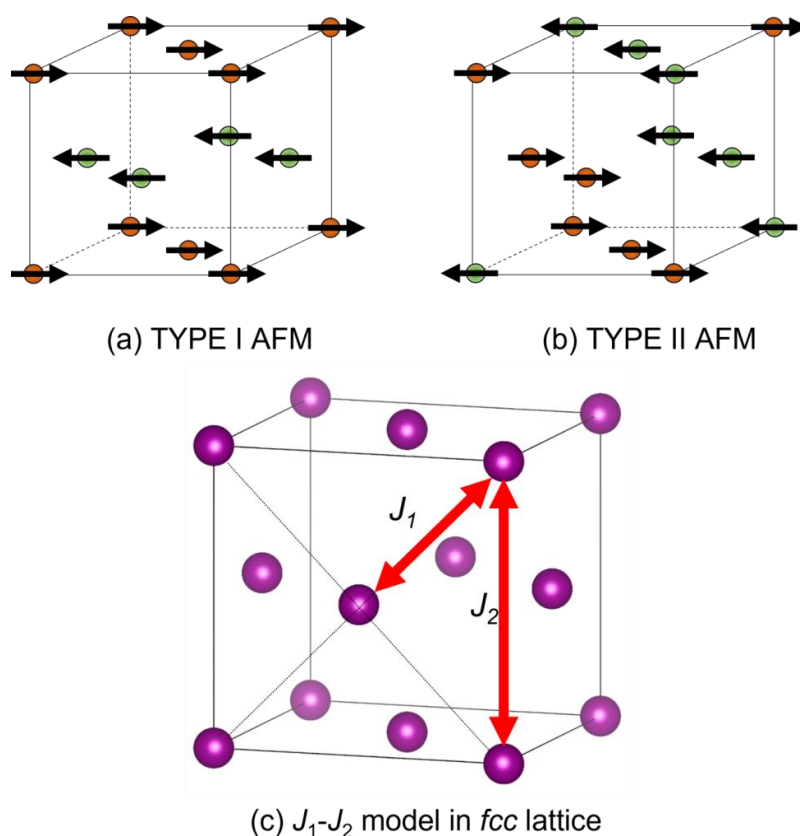


Fig. 3.1 The different types of antiferromagnetic ordering observed for cubic $Ba_2MnB''O_6$ perovskites with different $B'' = d^0$ or d^{10} cations; where (a) shows type I ordering of the Mn^{2+} cations observed when $B'' = Te^{6+}$ (d^{10}) and (b) shows type II ordering observed when $B'' = W^{6+}$ or Mo^{6+} (d^0). The magnetic interactions in the Mn^{2+} *fcc* sub-lattice are described using the simple cubic Heisenberg J_1 - J_2 model shown in (c). The magnitude and sign of the J_1 and J_2 interactions in (c) determines whether (a) type I or (b) type II ordering is observed.

The J_1 and J_2 interactions are facilitated by superexchange via O^{2-} and B'' . The different types of magnetic ordering observed for the $B'' = W^{6+}/Mo^{6+}$ and $B'' = Te^{6+}$ compositions in Table 3.1 suggest the valence of the outer d -orbital plays an important role in Mn-O- B'' -O-Mn superexchange. B'' cations with completely filled or empty d -orbitals affect the magnetic interactions in other perovskite systems. For example, the antiferromagnetic ordering temperature (T_N) of the osmium double perovskite, $Sr_2B'O_6$, depends on whether $B' = Sc^{3+} (3d^0)$, $Y^{3+} (4d^0)$ or $In^{3+} (4d^{10})$.³⁹⁻⁴¹ Sr_2ScOsO_6 , Sr_2YO_6 and Sr_2InOsO_6 all exhibit monoclinic ($P2_1/n$) symmetry but have different unit cell volumes (V_{cell}).³⁹ V_{cell} decreases so $V_{cell}(Y) > V_{cell}(In) > V_{cell}(Sc)$. It might be expected that T_N increases as V_{cell} decreases as contraction of the unit cell reduces the B' -O and Os-O bond lengths, generating stronger superexchange. However, T_N does not depend on V_{cell} , and follows a different trend: $T_N(Sc^{3+} (92 K)) > T_N(Y^{3+} (53 K)) > T_N(In^{3+} (26 K))$.⁴⁰ Instead, the strength of superexchange depends on the B' cations contribution to Os-O- B' -O-Os superexchange. The $Sc^{3+} 3d^0$ and $Y^{3+} 4d^0$ d -orbitals are closer in energy to the $O^{2-} 2p$ orbitals leading to stronger hybridization in Os-O-(Sc/Y)-O-Os superexchange.⁴¹ Alternatively, the $In^{3+} 4d^{10}$ orbital energy lies far below the $O^{2-} 2p$ orbitals leading to weak hybridisation. Hence, the Os-O-In-O-Os superexchange interactions are weak leading to a lower T_N for Sr_2InOsO_6 compared to Sr_2ScOsO_6 and Sr_2YO_6 . Similar trends in T_N have been observed for the barium analogue, $Ba_2B'O_6$ ($B' = Sc^{3+}, Y^{3+}, In^{3+}$) and have also been attributed to differences in superexchange involving d^{10}/d^0 cations.⁴²

d^{10} vs d^0 cations have also been investigated in copper perovskites, for example, Sr_2CuTeO_6 and Sr_2CuWO_6 . These isostructural tetragonal perovskites exhibit different types of magnetic order depending on whether the B'' site is $Te^{6+} 4d^{10}$ or $W^{6+} 5d^0$.⁴³⁻⁴⁶ These structures have attracted significant interest as mixtures of W^{6+}/Te^{6+} cations can be introduced to form a $Sr_2CuTe_{1-x}W_xO_6$ solid solution. The disorder induced by the d^{10} vs d^0 competition destabilises magnetic ordering over a wide portion of the $Sr_2CuTe_{1-x}W_xO_6$ solid solution, leading to unusual quantum magnetic behaviour.^{47,48} Perovskites containing d^{10} vs d^0 mixtures will be the subject in subsequent chapters. Differences in magnetic ordering have also been observed in the cubic perovskite $CaCu_3B''_4O_{12}$, which is ferromagnetically ordered when $B'' = Ge^{4+} (3d^{10})$ or $Sn^{4+} (4d^{10})$.⁴⁹ But when $B'' = Ti^{4+} (3d^0)$, antiferromagnetic order results as the greater $Ti^{4+} 3d^0$ contribution strengthens antiferromagnetic superexchange interactions that overcome the ferromagnetic interactions.

While the d^{10}/d^0 effect can be observed in a number of perovskite structures, there is no study comparing the d^{10} and d^0 B'' cations in a simple cubic $A_2B'B''O_6$ system. There are several reasons why the d^{10}/d^0 effect observed in the manganese, osmium and copper systems are not ideal examples to establish the d^{10}/d^0 effect in double perovskites. To begin with, the majority of these Mn^{2+} , Os^{5+} and Cu^{2+} double perovskites are distorted. Octahedral tilting changes the B' -O and B'' -O bond lengths and angles, therefore the $B'-O-B''-O-B'$ superexchange pathways are not uniform in all directions. For example, the interactions in $Sr_2Cu(Te/W)O_6$ are highly two-dimensional as a result of Jahn-Teller distortion of the Cu^{2+} cations.⁵⁰ Other factors can also affect the magnetic behaviour. For example, spin-orbital coupling may be present in osmium and manganese perovskites with oxidation states different to Os^{5+} and Mn^{2+} .^{51,52} Quantum effects also need to be considered in copper containing double perovskites, where quantum fluctuations are likely due to the small $Cu^{2+} S = 1/2$ spin.⁵³

The $Ba_2MnTe(d^{10})O_6$ and $Ba_2MnW(d^0)O_6$ perovskites in Table 3.1 are an ideal structure to compare d^{10} and d^0 interactions without the complications above. Ba_2MnWO_6 has an ideal cubic perovskite structure. The ionic radii of W^{6+} and Te^{6+} are nearly identical ($Te^{6+} - 0.56 \text{ \AA}$ and $W^{6+} - 0.6 \text{ \AA}$).³⁵ Hence, the Goldschmidt tolerance factors (t) for Ba_2MnTeO_6 and Ba_2MnWO_6 are nearly identical and predict cubic symmetry: $t(Ba_2MnTeO_6) = 0.9965$ and $t(Ba_2MnWO_6) = 0.9873$.⁵⁴ Therefore, Ba_2MnTeO_6 is also

predicted to be cubic. As a result, superexchange can be regarded as equivalent in three dimensions and there are only two magnetic interactions to consider: the NN- J_1 and NNN- J_2 interactions. Mn^{2+} has a large spin ($S = 5/2$) so magnetism can be viewed classically. And there is no spin-orbital coupling as Mn^{2+} has zero orbital momentum.

While Ba_2MnWO_6 has been well characterized, Table 3.1 shows information on Ba_2MnTeO_6 is lacking. To perform d^{10} vs d^0 comparisons, the structural and magnetic properties of Ba_2MnTeO_6 were characterized.

3. Experimental

Synthesis

Polycrystalline samples of Ba_2MnTeO_6 were prepared using the solid-state 'shake 'n' bake' method. High purity $BaCO_3$ (99.997%), MnO_2 (99.9%) and TeO_2 (99.995%) were mixed in an agate mortar. The Te^{4+} is oxidised to Te^{6+} during the reaction, resulting in a corresponding reduction of Mn^{4+} to Mn^{2+} . The reactant mixture was pressed into a pellet using a load of 1 tonne, before calcination at 900 °C in air. The calcined pellets were broken, re-ground and pressed again, before firing at reaction temperature of 1100 °C for 24 hours. Slow heating rates (1°C per minute) were used to prevent evaporation of TeO_2 . The reactant mixture was re-ground, pressed and heated again at 1100 °C for 24 hours. This process was repeated while monitoring the sample purity using laboratory X-ray diffraction (Rigaku Miniflex diffractometer (Cu $K\alpha_1/K\alpha_2$ ($\lambda = 1.5405$ and 1.5443 Å))). The reaction was stopped when there was no change between successive firings.

Neutron diffraction

Time-of-flight neutron diffraction patterns were collected using the General Materials Diffractometer (GEM) at the ISIS Neutron and Muon source. The sample (~6 g) was loaded into a cylindrical vanadium can (8 mm diameter). The can was mounted into a low temperature cryostat aligned with the neutron beam. After cooling to 2 K, NPD patterns were recorded on warming at various temperatures between 2-100 K. Measurements were performed using smaller temperature intervals about the antiferromagnetic transition. The data were corrected for sample absorption and analysed using the FullProf refinement software package.⁵⁵

SQUID magnetometry

Magnetic susceptibility measurements were performed using a Quantum Design MPMS 3 SQUID magnetometer. The sample was prepared by loading ~100 mg of Ba_2MnTeO_6 into a gelatine capsule. The capsule was sealed using PTFE tape and secured inside a plastic straw. The plastic straw was mounted into the MPMS 3 and cooled to 2 K in the absence of a magnetic field. The DC magnetic susceptibility was measured on warming from 2-300 K in an external field of 0.1 T producing a zero-field cooled (ZFC) measurement. A field cooled (FC) measurement was made by measuring the DC magnetization in the presence of a weak magnetic field (0.1 T) on cooling from 300-2 K.

Heat capacity

Heat capacity measurements were performed using a Quantum Design PPMS-9. The heat capacity contribution from the sample platform (called the sample puck) and mounting grease was measured between 2-60 K. This is known as an addenda measurement. Afterwards, a shard of sintered pellet weighing 6.84 mg was placed into the sample puck using the grease as an adhesive to improve thermal contact. The heat capacity of the sample and puck was measured between 2-60 K. The heat capacity of the sample was obtained by subtracting the addenda measurement.

Inelastic neutron scattering

Inelastic neutron scattering measurements were performed on the MERLIN time-of-flight direct geometry spectrometer at the ISIS Neutron and Muon Source. The sample was loaded into an aluminium can and cooled using a helium cryostat. Inelastic neutron scattering spectra were collected on warming at 6 K, 44 K and 109 K using an incident neutron energy of 10 meV and a Q-space range of 0 - 4 Å⁻¹.

Polarized neutron scattering

Polarized neutron scattering experiments were performed on the D7 *xyz*-polarization analysis spectrometer at the Institut Laue-Langevin (ILL). Ba₂MnTeO₆ and Ba₂MnWO₆ were measured using an incident polarized neutron wavelength of 4.8 Å, equating to an incident neutron energy of 3.55 meV. Non-spin-flip (NSF) and spin-flip (SF) scattering was measured with the incident neutron beam polarized along *x*, *y* and *z*. From this it was possible to separate the magnetic scattering from the nuclear scattering contributions. Diffuse magnetic scattering spectra were obtained at various temperatures above T_N for Ba₂MnTeO₆ and Ba₂MnWO₆ and were analysed using SPINVERT.⁵⁶

4. Results

a. SQUID magnetometry

Fig. 3.2 shows the DC susceptibility curve (χ vs T) of Ba₂MnTeO₆ between 2-300 K. Ba₂MnTeO₆ undergoes a paramagnetic to antiferromagnetic transition on cooling. In the paramagnetic phase, the susceptibility increases with reduced temperature, until reaching a broad cusp at ~ 20 K. Below 20 K, the susceptibility decreases indicating antiferromagnetic ordering. The exact location of the Néel transition was determined from the first derivative $d\chi/dT$ vs T . This placed T_N at 20.3(2) K, which is higher than the T_N of Ba₂MnWO₆ ($T_N \sim 8$ K).¹⁹ The transition is not featureless; there is a broad shoulder peak at ~ 40 K. This represents trace amounts of ferrimagnetic Mn₃O₄ in the sample.^{31,54} Mn₃O₄ is often observed in the χ vs T curve of A₂MnB'O₆ perovskites synthesised in air, including those in Table 3.1.^{20,23,31,33} The amount of Mn₃O₄ is sufficiently small that it cannot be detected in the laboratory X-ray or neutron diffraction data. With SQUID magnetometry, the strong sensitivity to weak magnetic fields means even traces of magnetic impurity are detectable. The ZFC and FC divergence in the χ vs T curve below 20 K also indicates the presence of ferrimagnetic Mn₃O₄. Divergence between the ZFC and FC curves is often observed for ferromagnetic/ferrimagnetic moments.⁵⁷ It was not possible to remove the Mn₃O₄ impurity by heating under reducing conditions as this risked also reducing Te⁶⁺. However, Mn₃O₄ is present in such trace amounts that it was only detectable in the SQUID data and does not affect the other magnetic characterization results.

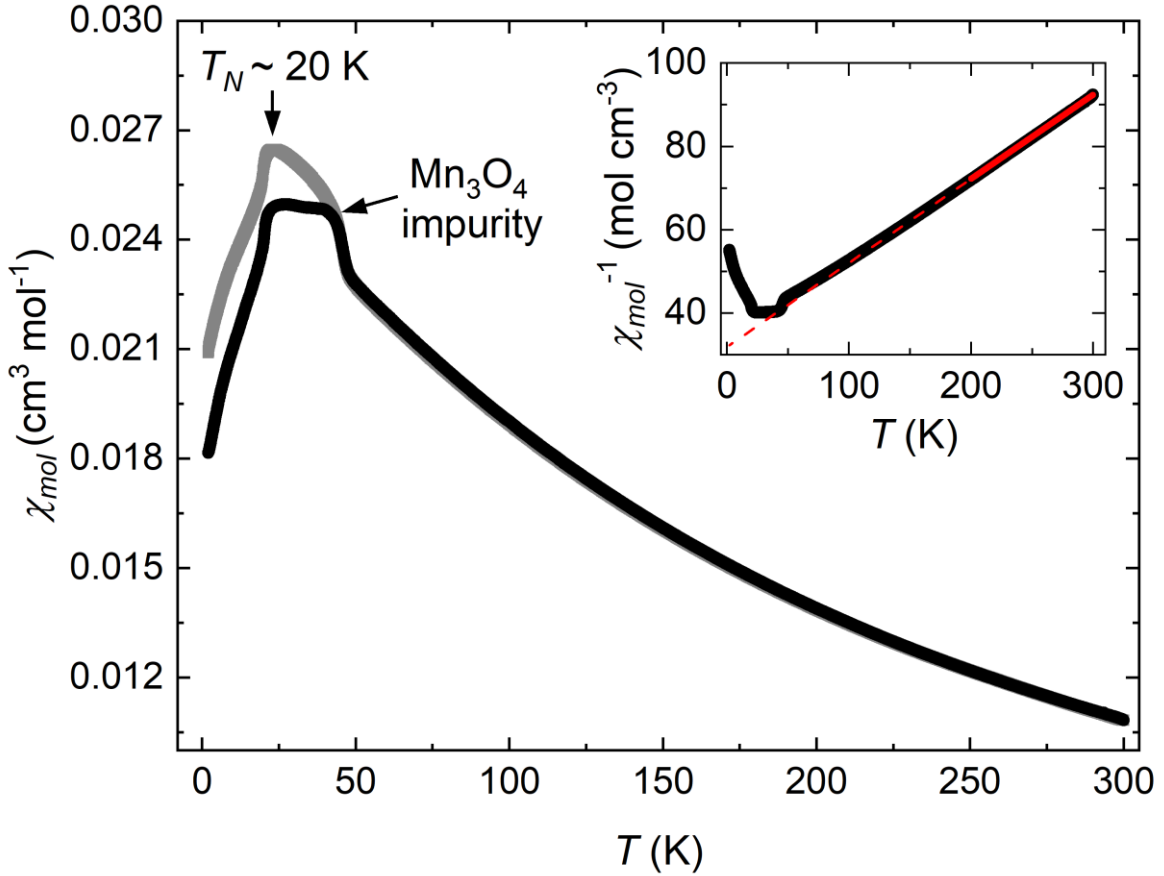


Fig. 3.2 DC susceptibility data (χ vs T) of $\text{Ba}_2\text{MnTeO}_6$ between 2-300 K. The inset shows the Curie-Weiss fit (solid red line) to the 150-300 K inverse susceptibility ($1/\chi$ vs T) curve. The dotted red line is an extrapolation of the Curie-Weiss fit.

Above 150 K, the χ vs T data is linear and can be described using the inverse Curie-Weiss law in equation 3.2.

$$\frac{1}{\chi} = \frac{T - \theta}{C} \quad (3.2)$$

The inset in Fig. 3.2 shows the Curie-Weiss fit to the inverse $1/\chi$ vs T data. The Curie constant (C) and Weiss constant (θ_w) were determined from the gradient and intercept, respectively. $\theta_w = -157(1)$ K is strongly negative indicating strong antiferromagnetic interactions in $\text{Ba}_2\text{MnTeO}_6$. $C = 4.96(1) \text{ cm}^3 \text{ K mol}^{-1}$ was used to calculate the effective magnetic moment (μ_{eff}) using the equation below:

$$\mu_{eff} = 2.84 \sqrt{\chi T} \quad (3.3)$$

Where in equation 3.3, $C = \chi T$. The calculated $\mu_{eff} = 6.31(7) \mu_B$ per Mn^{2+} was found to be close to the theoretical spin-only moment of a Mn^{2+} ion ($\mu_{eff}(\text{spin-only}) = 5.92 \mu_B$ per Mn^{2+}). This confirmed successful reduction of Mn^{4+} to Mn^{2+} . The frustration index (f) was determined by dividing the Weiss constant by the transition temperature ($f = \theta_w/T_N$).⁵⁸ For $\text{Ba}_2\text{MnTeO}_6$, $f \sim 8$, showing the system is moderately frustrated, but not enough to prevent antiferromagnetic ordering.

b. Heat capacity

The heat capacity (C_p) of $\text{Ba}_2\text{MnTeO}_6$ is plotted in Fig. 3.3. There is a single large lambda (λ)-peak at 20.1 K in the plot of C_p/T vs T . The position of the λ -peak agrees very well with the T_N determined in the DC susceptibility measurements; hence, represents the antiferromagnetic ordering transition. There are no other peaks or features present in the C_p/T vs T curve. This confirms the broad peak at 40 K in the DC susceptibility curve is from Mn_3O_4 and not a feature of the magnetic behaviour of $\text{Ba}_2\text{MnTeO}_6$.

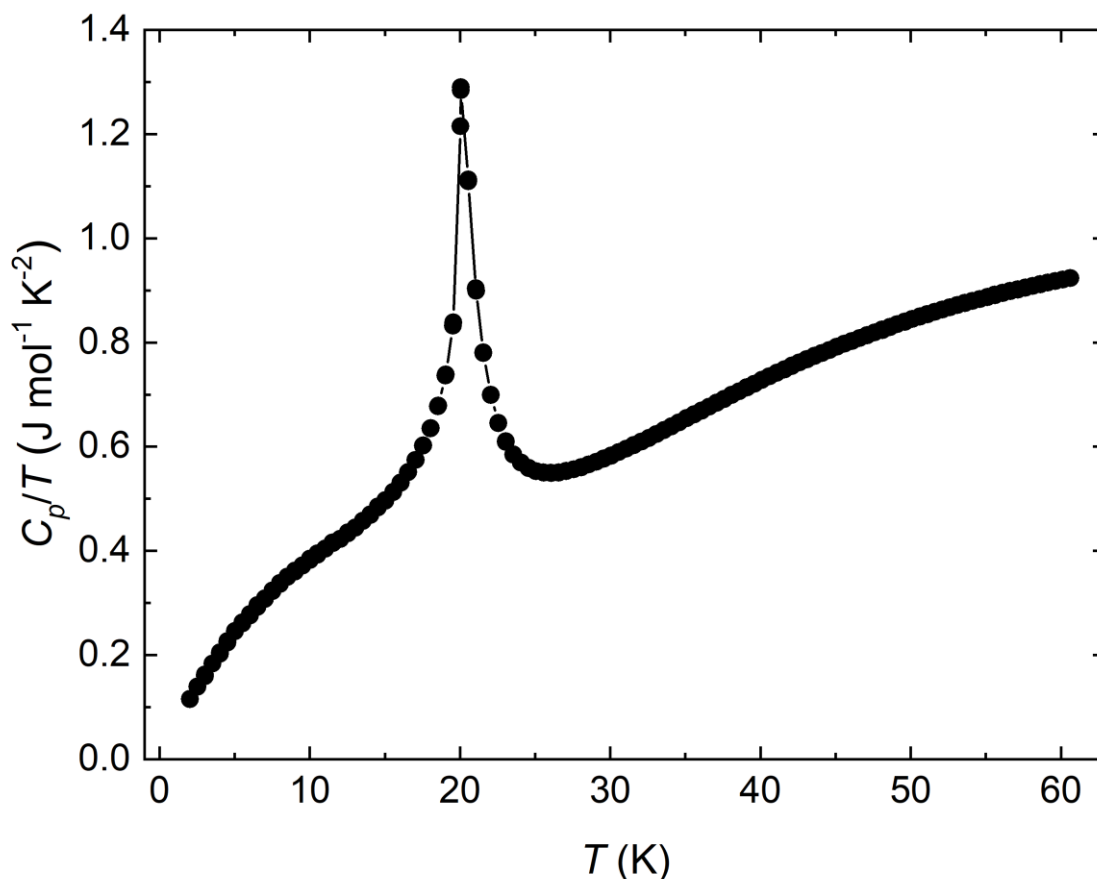


Fig. 3.3 Heat capacity data of $\text{Ba}_2\text{MnTeO}_6$ between 2-60 K.

c. Crystal structure

The crystal structure of perovskites can be predicted using the Goldschmidt tolerance factor: $t = (r_A + r_O)/\sqrt{2}(r_B + r_O)$, where r_A and r_B are the ionic radii of the A and B cations, respectively. r_O is the radius of O^{2-} . The Goldschmidt tolerance factor for $\text{Ba}_2\text{MnTeO}_6$ is close to unity ($t = 0.9965 \sim 1$) and closely matches the values of t calculated for the cubic W^{6+} and Mn^{6+} analogues of $\text{Ba}_2\text{MnB}''\text{O}_6$: Ba_2MnWO_6 ($t = 0.9873$) and $\text{Ba}_2\text{MnMoO}_6$ ($t = 0.9896$). This value of t suggests $\text{Ba}_2\text{MnTeO}_6$ is cubic, $Fm\bar{3}m$. However, a single crystal diffraction study has suggested $\text{Ba}_2\text{MnTeO}_6$ is rhombohedral, $R\bar{3}m$.²⁹ Subsequent studies in the literature have chosen to model $\text{Ba}_2\text{MnTeO}_6$ using $R\bar{3}m$ symmetry^{59,60}, while others have argued $Fm\bar{3}m$ symmetry.^{61,62} The $Fm\bar{3}m$ and $R\bar{3}m$ structural models are illustrated in Fig. 3.4a and Fig. 3.4b, respectively. The Goldschmidt tolerance factor only provides an indication of the possible perovskite structure; diffraction is essential for accurate structural determination. X-ray and neutron diffraction were performed and the data analysed using the $Fm\bar{3}m$ and $R\bar{3}m$ structural models. The results show the correct description of the $\text{Ba}_2\text{MnTeO}_6$ crystal structure is cubic, $Fm\bar{3}m$.⁶²

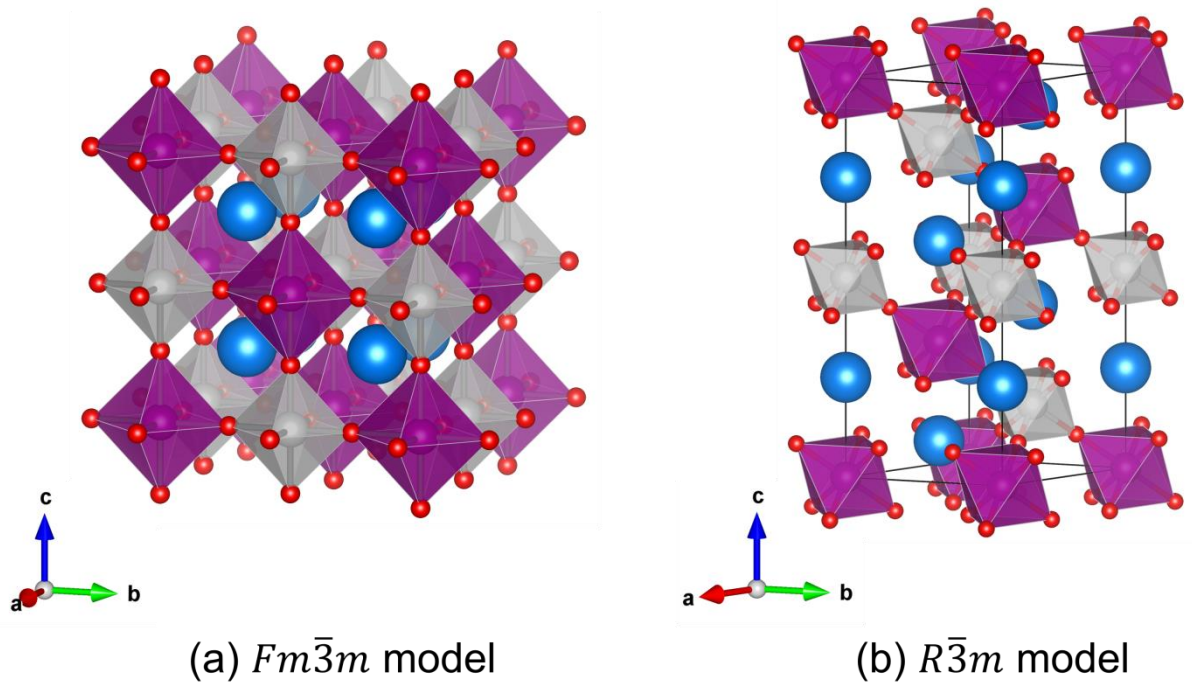


Fig. 3.4 The two proposed structures for Ba_2MnTeO_6 : (a) cubic, $Fm\bar{3}m$ and (b) rhombohedral, $R\bar{3}m$. The cations and anions have the same colours in both structures: Ba^{2+} (blue), Mn^{2+} (purple), Te^{6+} (grey) and O^{2-} (red).

i. Laboratory X-ray diffraction

The laboratory X-ray diffraction pattern of Ba_2MnTeO_6 is shown in Fig. 3.5a. The additional Bragg peaks belong to a minor $BaMnO_3$ impurity ($P6_3cm$, 1.0(1) weight %). No other impurities (e.g. Mn_3O_4) were detected. The X-ray diffraction pattern was used to refine the $Fm\bar{3}m$ and $R\bar{3}m$ structural models. Fig. 3.5b and Fig. 3.5c compare the Rietveld fits for each model. Visually, both models provide a good description of the experimental data. The R -values in Table 3.2 support this and are almost identical for $Fm\bar{3}m$ vs $R\bar{3}m$. Generally, the $R\bar{3}m$ model has slightly lower R -values. In the $R\bar{3}m$ model, there are additional degrees of freedom associated with the lattice parameters and Ba^{2+} and O^{2-} atomic positions. Hence, the slightly lower R -values result from the additional refineable parameters in the $R\bar{3}m$ model. The additional degrees of freedom upon $Fm\bar{3}m$ to $R\bar{3}m$ distortion result from octahedral tilting, whereby the Glazer tilt changes from $a^0a^0a^0$ to $a^-a^-a^-$. Displacement of light atoms is difficult to detect using X-rays as scattering is dominated by heavy elements i.e. Ba^{2+} , Mn^{2+} and Te^{6+} . The X-ray data showed Mn^{2+} and Te^{6+} are fully ordered with no anti-site disorder between the B' and B'' sites. However, to accurately determine the O^{2-} anions positions neutron diffraction was required. This demonstrates why both X-ray and neutron diffraction are essential for accurate perovskite structural determination.⁶³

Table 3.2: Comparison of the R -factors for the $Fm\bar{3}m$ and $R\bar{3}m$ models refined using the X-ray data in Fig. 3.5.

R -values	$Fm\bar{3}m$ model	$R\bar{3}m$ model
R_{wp} (%)	11.3	11.2
R_p (%)	9.36	9.41
R_{exp} (%)	4.37	4.36
χ^2	6.66	6.56

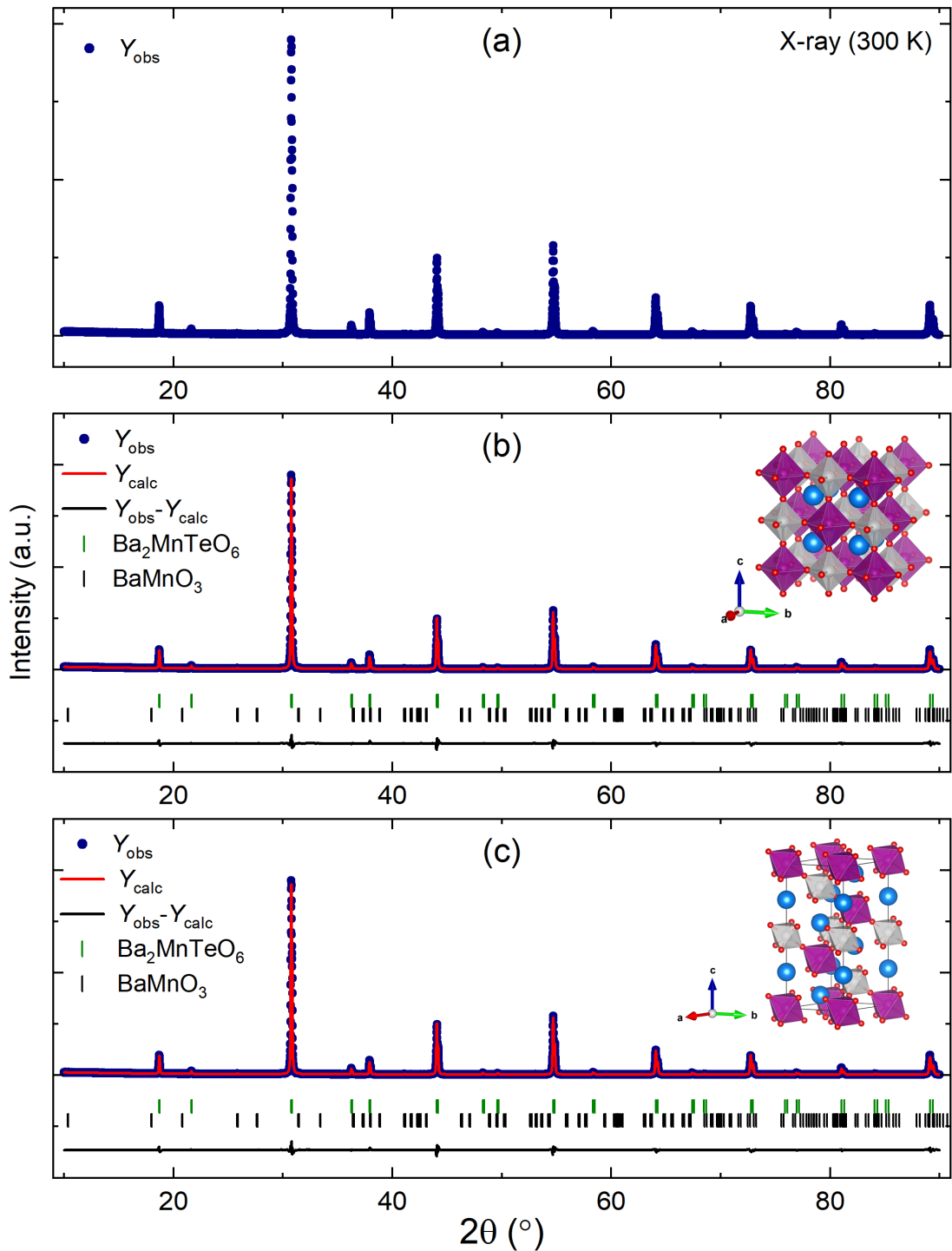


Fig. 3.5 (a) The laboratory X-ray diffraction pattern of $\text{Ba}_2\text{MnTeO}_6$ at 300 K. Panels (b) and (c) are Rietveld fits to the 300 K X-ray data using the $Fm\bar{3}m$ model (b) and $R\bar{3}m$ model (c). Both models appear to provide a good description of the experimentally observed diffraction pattern. The additional Bragg reflections are due to a minor BaMnO_3 impurity (1 wt%).

ii. Neutron diffraction

Neutron diffraction patterns of $\text{Ba}_2\text{MnTeO}_6$ were collected between 2-100 K. No additional nuclear Bragg peaks were observed on cooling to 2 K. This shows the crystal symmetry is the same at 2 K, 100 K and 300 K. Hence, except for the change in lattice parameter(s), the 100 K neutron diffraction pattern closely represents the room temperature crystal structure. Fig. 3.6a shows the 100 K

neutron diffraction pattern of $\text{Ba}_2\text{MnTeO}_6$. The peak intensities are affected by small displacements in the O^{2-} anion positions. The simulated neutron diffraction patterns for the $Fm\bar{3}m$ and $R\bar{3}m$ models are shown in Fig. 3.6b and Fig. 3.6c, respectively. The simulated pattern for the $Fm\bar{3}m$ model closely resembles the observed pattern in Fig. 3.6a. In contrast, there are clear discrepancies between the simulated $R\bar{3}m$ pattern and observed pattern. The arrows in Fig. 3.6c indicate several peaks whose intensity is greater than in the observed pattern.

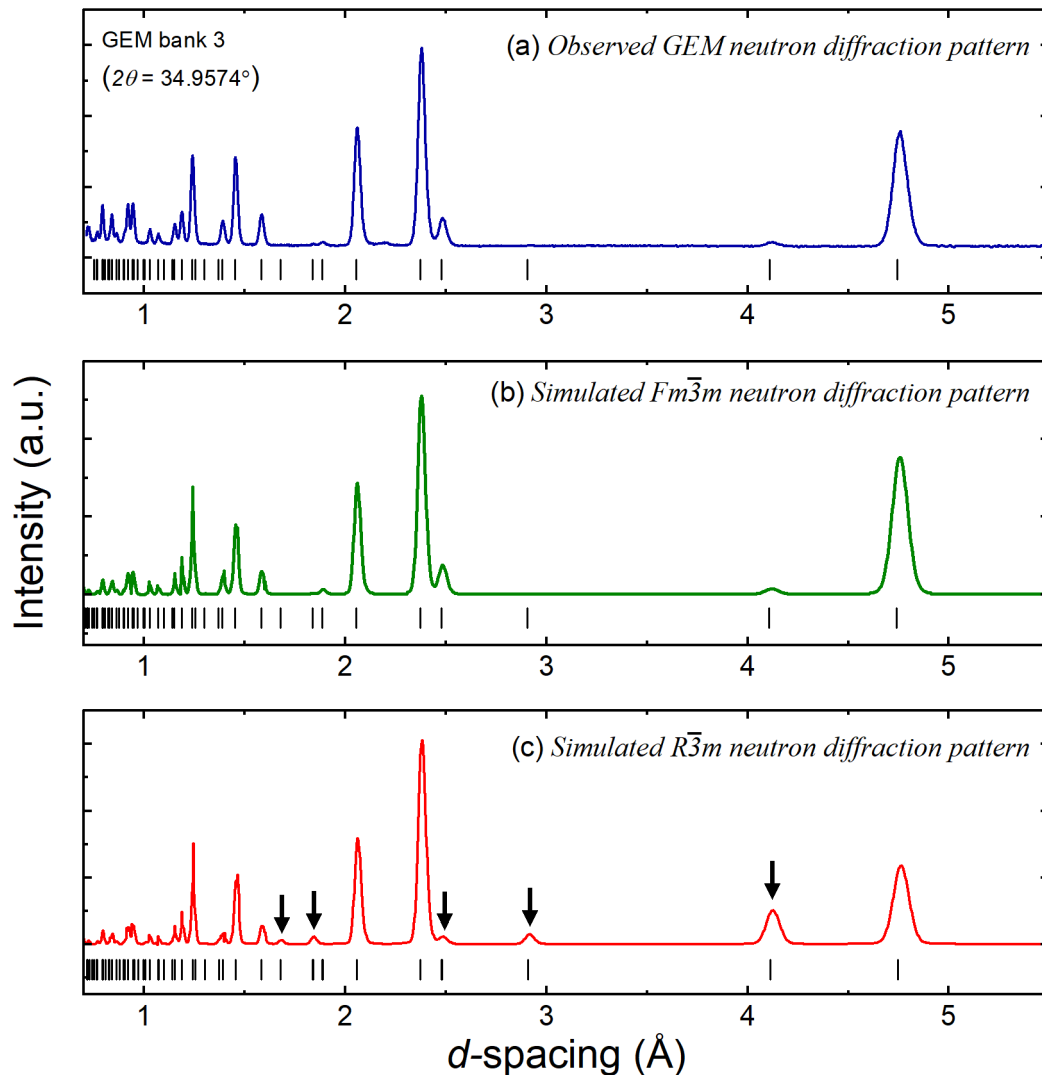


Fig. 3.6 (a) The bank 3 ($2\theta = 34.9574^\circ$) GEM neutron diffraction pattern of $\text{Ba}_2\text{MnTeO}_6$ at 100 K. (b) The simulated neutron diffraction pattern of $\text{Ba}_2\text{MnTeO}_6$ using the $Fm\bar{3}m$ model. (c) The simulated neutron diffraction pattern of $\text{Ba}_2\text{MnTeO}_6$ using the $R\bar{3}m$ model. The simulated pattern $Fm\bar{3}m$ model matched the observed pattern well; whereas there are obvious peak intensity mismatches between the simulated $R\bar{3}m$ and observed neutron diffraction pattern. The $R\bar{3}m$ peaks with large intensity mismatches are indicated using black arrows.

To further prove $\text{Ba}_2\text{MnTeO}_6$ is cubic, the $Fm\bar{3}m$ model was refined using the 100 K neutron data. The refined $Fm\bar{3}m$ model was then transformed to the $R\bar{3}m$ model using one of the four possible transformation matrices provided by the WYCKSPLIT tool on the Bilbao Crystallographic Server.⁶⁴ The chosen matrix is given below:

$$\mathbf{T} = \begin{bmatrix} -1/2 & 0 & 1 \\ 1/2 & -1/2 & 1 \\ 0 & 1/2 & 1 \end{bmatrix} \quad (3.4)$$

The $Fm\bar{3}m$ to $R\bar{3}m$ transformation was performed using the TRANSTRU tool also provided by the Bilbao Crystallographic Server.^{65,66} The $R\bar{3}m$ model obtained was then refined using the same 100 K data. A significant improvement in the fit compared to the $Fm\bar{3}m$ model would support $R\bar{3}m$ symmetry. The refinement was performed in the same way as for the original $Fm\bar{3}m$ model. The Rietveld fits for the $Fm\bar{3}m$ and $R\bar{3}m$ models are shown in Fig. 3.7b and Fig. 3.7c, respectively. Comparing the R -values for the Rietveld fits in Table 3.3 shows there is a minor improvement in the fit when converting to the $R\bar{3}m$ model. Again, the minor improvement results from the additional refineable parameters in the $R\bar{3}m$ model. Therefore, the neutron data does not support $Fm\bar{3}m$ to $R\bar{3}m$ distortion of the O^{2-} positions.

Table 3.3: Comparison of R -values for the $Fm\bar{3}m$ and $R\bar{3}m$ models using the 100 K neutron data in Fig. 3.5.

R-values	$Fm\bar{3}m$ model	$R\bar{3}m$ model
R_{wp}	6.84	6.97
R_p	7.44	7.07
R_{exp}	3.50	3.23
χ^2	3.82	4.66

The refined $R\bar{3}m$ model was then converted back to the $Fm\bar{3}m$ model. From this the percentage rhombohedral distortion in the lattice parameters and oxygen positions could be calculated. The $R\bar{3}m$ lattice parameters (a_R and c_R) were converted to the cubic lattice parameter (a_C) using the ratio relationships in equations 3.5 and 3.6.

$$\frac{a_C}{a_R} \cong \frac{2}{\sqrt{2}} \quad (3.5)$$

$$\frac{a_C}{c_R} \cong \frac{1}{\sqrt{3}} \quad (3.6)$$

Dividing equations 3.5 and 3.6 gives an expression for the percentage rhombohedral lattice distortion:

$$R\bar{3}m \text{ lattice distortion } (\%) = \left(\left[\frac{2\sqrt{3} a_{R(exp)}}{\sqrt{2} c_{R(exp)}} \right] \times 100 \right) - 100 \quad (3.7)$$

The percentage rhombohedral distortion in the oxygen positions was calculated as follows. The $Fm\bar{3}m$ oxygen coordinates ($x, 0, 0$) were converted to the $R\bar{3}m$ ($x, 2x, z$) using the subgroup basis $(-4/3x, -2/3x, 1/3x)$. By reversing this transform, the refined $R\bar{3}m$ oxygen positions could be converted back to the $Fm\bar{3}m$ oxygen parameters. The percentage rhombohedral distortion of the oxygen positions was then calculated using the ratio of the transformed $O_{x_{R\bar{3}m}}$ and $O_{z_{R\bar{3}m}}$ parameters as in equation 3.8.

$$R\bar{3}m \text{ oxygen position distortion } (\%) = \left(\left[\frac{O(x_{R\bar{3}m} \rightarrow x_{Fm\bar{3}m})}{O(z_{R\bar{3}m} \rightarrow x_{Fm\bar{3}m})} \right] \times 100 \right) - 100 \quad (3.8)$$

The percentage rhombohedral distortions of the lattice and oxygen positions are tabulated in Table 3.4. The above calculations were also performed using the $R\bar{3}m$ lattice parameters and oxygen

positions reported in the single crystal X-ray diffraction study of $\text{Ba}_2\text{MnTeO}_6$.²⁹ The percentage lattice and oxygen distortion determined from these values are listed in Table 3.4.

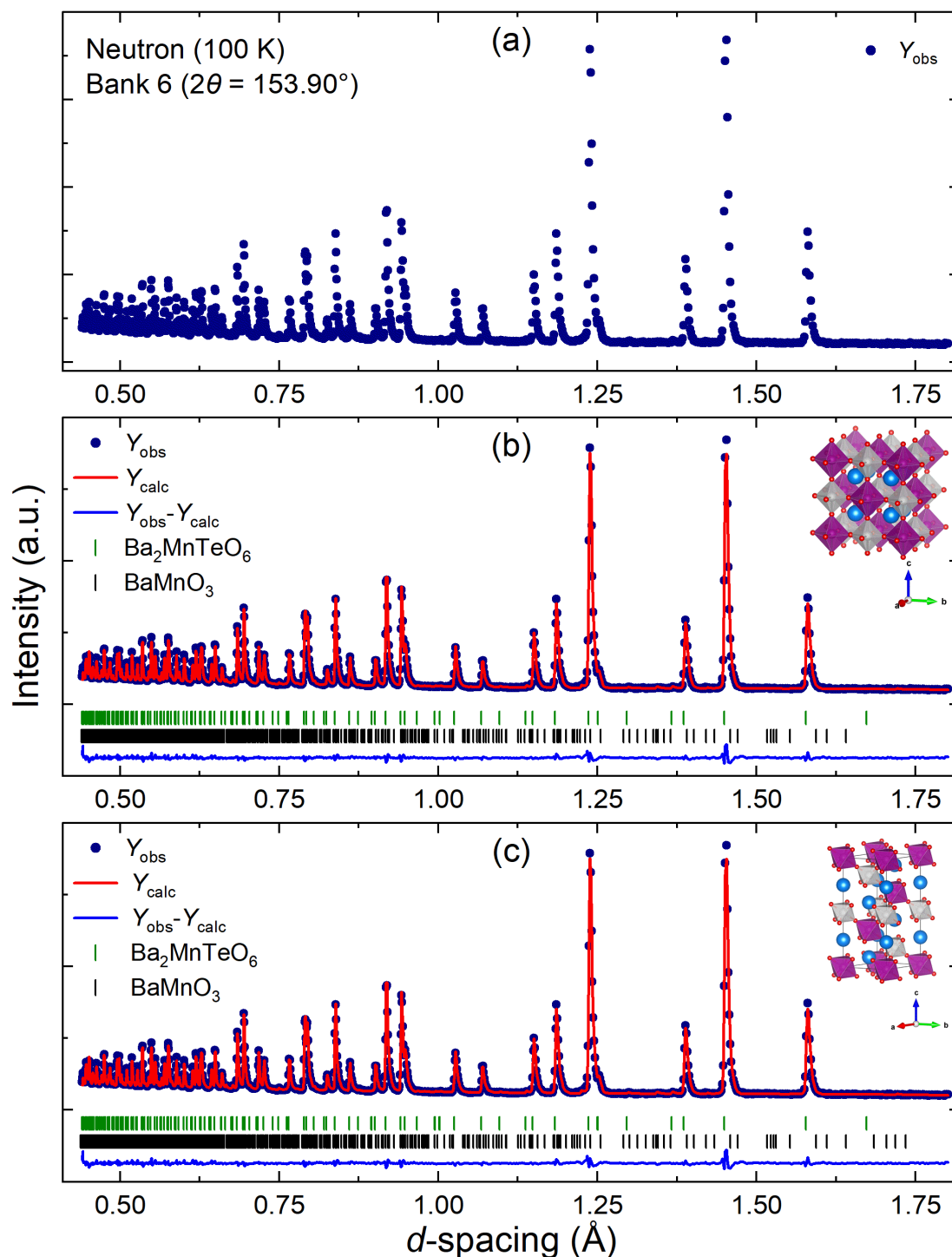


Fig. 3.7 (a) The GEM neutron diffraction pattern of $\text{Ba}_2\text{MnTeO}_6$ at 100 K. The pattern is shown for the highest resolution bank: bank 6 ($2\theta = 153.90^\circ$). (b) Rietveld refinement of the $Fm\bar{3}m$ model using the 100 K neutron diffraction data. (c) Rietveld refinement of the $R\bar{3}m$ model using the 100 K neutron diffraction data.

Table 3.4: Percentage rhombohedral distortion in the lattice and oxygen positions determined from the $R\bar{3}m$ model reported here and $R\bar{3}m$ model reported in the single crystal diffraction study of Ba_2MnTeO_6 in ref.²⁹.

	This work	Single crystal X-ray diffraction study ²⁹
$R\bar{3}m$ lattice distortion (%)	$0.12 \pm 0.017\%$	$0.033 \pm 0.10\%$
$R\bar{3}m$ oxygen position distortion (%)	$0.031 \pm 0.34\%$	$0.57 \pm 0.54\%$

Table 3.4 shows the percentage $R\bar{3}m$ distortion of the lattice and oxygen positions in Ba_2MnTeO_6 are less than 1%. Thus, the structure is cubic within one standard deviation. Furthermore, a number of the distortion percentages in Table 3.4 have large errors. In some cases, the error is an order of magnitude greater than the value. For example, the lattice parameters reported in the single crystal diffraction study are distorted from the *ideal* cubic perovskite structure by 0.033% but there is an error of 0.10%. Similarly, there is a large error associated with the oxygen position in this work. Therefore, the neutron data does not support $Fm\bar{3}m$ to $R\bar{3}m$ distortion of the O^{2-} positions.

In summary, the X-ray and Neutron diffraction data do not support $R\bar{3}m$ symmetry. As per crystallographic convention, Ba_2MnTeO_6 is correctly described using the higher symmetry $Fm\bar{3}m$ model. This agrees with the structure predicted by the tolerance factor. The results from the refinement of the $Fm\bar{3}m$ model using the 100 K and 2 K neutron diffraction data are shown in Table 3.5. The R -values are shown for the highest backscattering bank (bank 6). Using the Ba-O, Mn-O and Te-O bond lengths from the 100 K data, bond valence sums (BVS) were calculated. The BVS values in Table 3.6 are close to the expected oxidation numbers for Ba^{2+} , Mn^{2+} and Te^{6+} .

Table 3.5: Refined $Fm\bar{3}m$ model at 2 K and 100 K for the Ba_2MnTeO_6 neutron diffraction data. The R -values are shown for bank 6 ($2\theta = 153.90^\circ$).

	2 K	100 K
a (Å)	8.2066(3)	8.2106(4)
Ba ($100 \times U_{iso}$ (Å ²))	0.01(4)	0.13(4)
Mn ($100 \times U_{iso}$ (Å ²))	0.00(4)	0.03(4)
Te ($100 \times U_{iso}$ (Å ²))	0.03(3)	0.07(3)
Ox	0.2646(1)	0.2647(1)
O ($100 \times U_{iso}$ (Å ²))	0.22(2)	0.32(2)
BaMnO ₃ (%)	1.0(1)	1.0(1)
R_p (%)	6.61	7.44
R_{wp} (%)	6.47	6.84
R_{exp} (%)	1.89	3.50
χ^2	11.7	3.82

Table 3.6: Bond Valence Sums (BVS) for Ba, Mn and Te in Ba_2MnTeO_6 ($Fm\bar{3}m$) calculated using the 100 K neutron diffraction data.

	Bond Valence Sum (BVS)	Charge
Ba-O	2.244	2+
Mn-O	2.132	2+
Te-O	5.755	6+

The structural results presented here were published in 2020.⁶² Since 2020, there have been subsequent publications on Ba_2MnTeO_6 . Two of these publications have argued the $Fm\bar{3}m$ and $R\bar{3}m$ models are marginally different; therefore either can be used to describe the structure of Ba_2MnTeO_6 .^{57,58} The X-ray and neutron diffraction results here show this is incorrect. $R\bar{3}m$ distortion of the $Fm\bar{3}m$ structure is so small it is non-existent, so the structure can only be assigned as cubic. Nevertheless, Ba_2MnTeO_6 has been described as an example of a two-dimensional triangular lattice using the $R\bar{3}m$ structure. The proposed two-dimensional triangular lattice is shown in Fig. 3.8a. The triangular layers are made by connecting each Mn^{2+} cation to six neighbouring Mn^{2+} cations within the ab plane of the $R\bar{3}m$ structure. The triangular layers are stacked in the c direction.

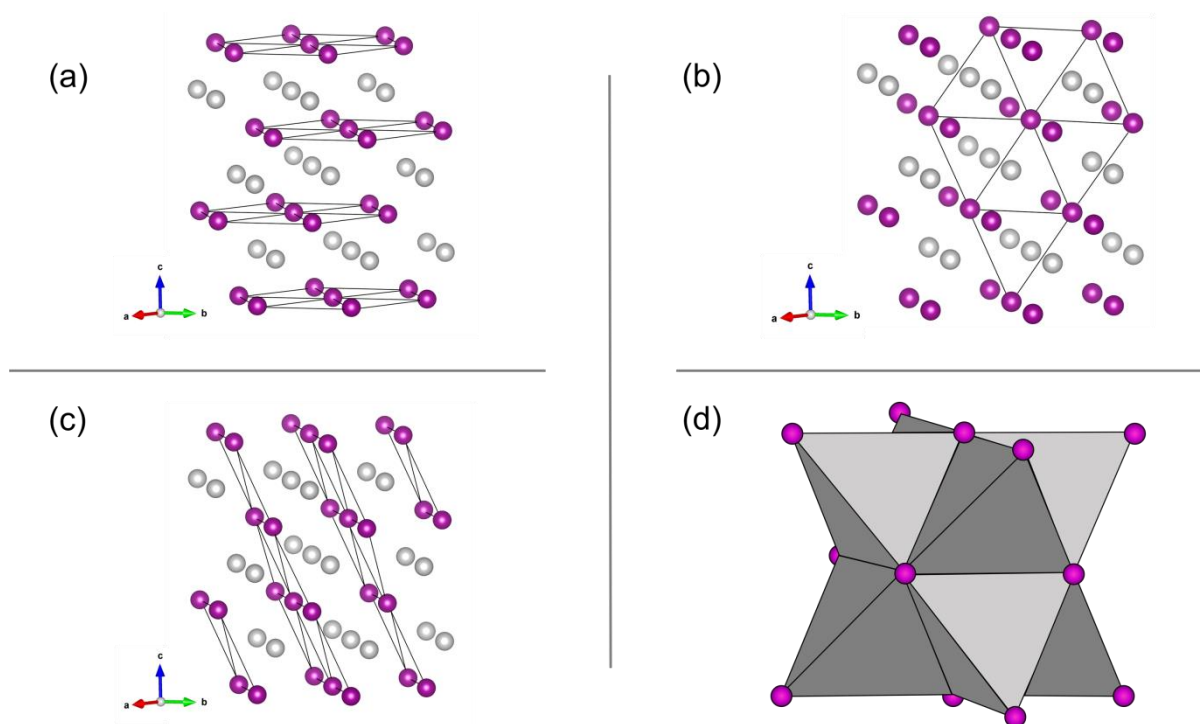


Fig. 3.8 (a) The proposed two-dimensional triangular lattice in the $R\bar{3}m$ structure. The intra-layer connections between the Mn^{2+} - Mn^{2+} in the triangular layers and its six neighbouring Mn^{2+} cations are shown by the solid black lines. (b) and (c) show the symmetry equivalent inter-layer Mn^{2+} - Mn^{2+} connections between the triangular layers. (d) The 3D network of equilateral triangles produced when the connections in (a), (b) and (c) are combined. This 3D network of equilateral triangles is a distinguishing feature of the face-centred cubic lattice.

If the structure in Fig. 3.8a was truly two-dimensional, the inter-layer distance between a Mn^{2+} cation and its six neighbouring Mn^{2+} cations in the adjacent layers along c should be different to the intra-layer distance between the Mn^{2+} cation and its six Mn^{2+} neighbours within the triangular layers in the ab plane. However, these distances are almost identical: inter-layer Mn^{2+} - Mn^{2+} distance = 5.7566(6) Å; and intra-layer Mn^{2+} - Mn^{2+} distance = 5.7533(6) Å.⁶⁰ Similarly, the intra- and inter-layer Mn^{2+} - Mn^{2+} distances were found to be near identical in the $R\bar{3}m$ model reported here: inter-layer Mn^{2+} - Mn^{2+} distance = 5.806(4) Å; and intra-layer Mn^{2+} - Mn^{2+} distance = 5.806(3) Å. When the inter-layer Mn^{2+} - Mn^{2+} connections drawn in Fig. 3.8b and Fig. 3.8c are combined with the intra-layer connections in Fig. 3.8a, the result is a network of equilateral triangles shown in Fig. 3.8d. In three-dimensions, this is the face-centred *cubic* lattice. Hence, the $R\bar{3}m$ structure is only generated by neglecting to consider half of the Mn^{2+} - Mn^{2+} interactions. Neglecting these interactions ignores the three dimensional symmetry equivalence of the Mn^{2+} - Mn^{2+} interactions and hence the true cubic symmetry. Symmetry equivalence is also supported by the values of the exchange interactions. The intra- and inter-layer Mn^{2+} - Mn^{2+} exchange interactions were identical (J (intra-layer) = 0.27 (3) meV and J (inter-layer) = 0.27(3) meV) showing they represent equivalent superexchange pathways.⁶⁰

d. Magnetic structure

Cooling $\text{Ba}_2\text{MnTeO}_6$ to 2K saw the arrival of several additional peaks in the neutron diffraction pattern. The extra peaks were non-coincident with the nuclear peaks of $\text{Ba}_2\text{MnTeO}_6$ and the BaMnO_3 impurity phase (1%). The extra peaks are magnetic Bragg peaks caused by antiferromagnetic ordering. The magnetic Bragg peaks were strongest at 2 K and can clearly be distinguished from the nuclear Bragg peaks by comparing the 2 K and 100 K NPD patterns in Fig. 3.9, where the magnetic Bragg peaks are indicated by an asterisk.

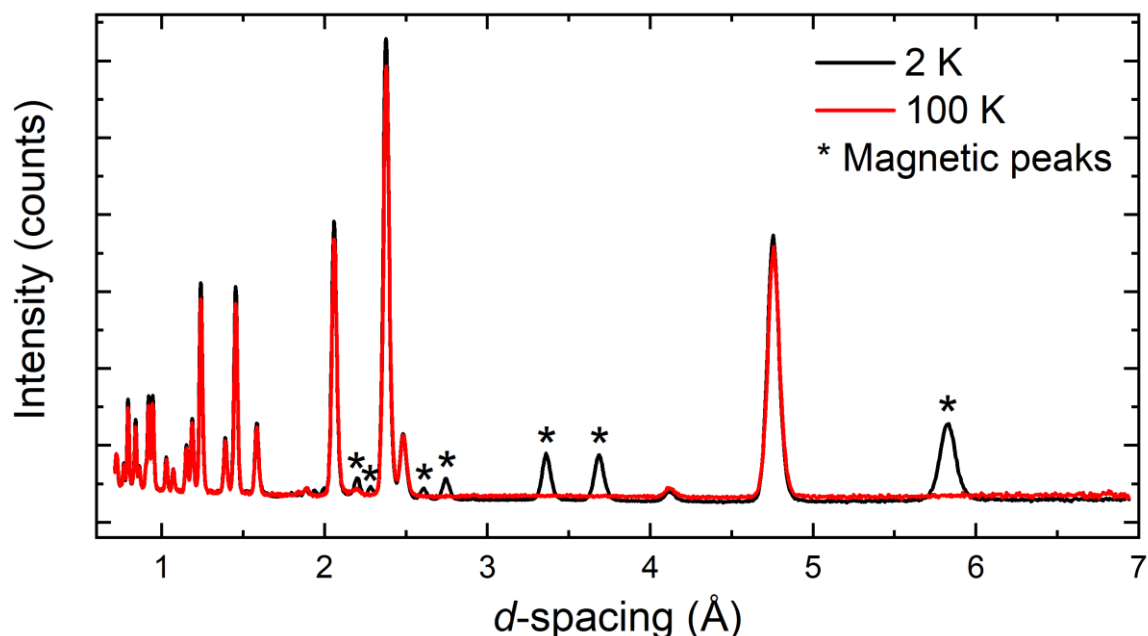


Fig. 3.9 Comparison of the neutron diffraction patterns of $\text{Ba}_2\text{MnTeO}_6$ at 2 K (black) and 100 K (red). The 100 K pattern contains contributions from nuclear scattering only, whereas the 2 K pattern contains additional magnetic Bragg peaks marked with an asterisk (*).

To describe the 2 K data, a two-phase (nuclear phase + magnetic phase) Rietveld refinement was performed. The nuclear phase was the $Fm\bar{3}m$ structure. The magnetic phase was either the type I or type II antiferromagnetic model. The type II antiferromagnetic model failed to describe the magnetic phase. The type I antiferromagnetic phase provided a good description of the magnetic Bragg peaks when the propagation vector was $k = (0,0,1)$. $k = (0,0,1)$ is equivalent to $k = (1,0,0) = (0,1,0)$ in the $Fm\bar{3}m$ structure. Analysis using BASIREPS and SARAh showed there are two symmetry allowed representations for a propagation vector of $k = (0,0,1)$.⁵⁵ In the first representation, the Mn^{2+} moment lies within the ab plane of the ferromagnetic layers. In the second representation, the Mn^{2+} spins point out of the ab plane along c . The second representation fails to describe the intensity of the magnetic Bragg peaks. Conversely, the first representation provides a very good description as demonstrated by the Rietveld plot in Fig. 3.10. It was not possible to determine the exact direction of the magnetic moment in the ab -plane using a powder sample. Conversely, in a single crystal experiment the crystal can be rotated to observe only the magnetisation that is perpendicular Q .

Fig. 3.11a shows the type I antiferromagnetic structure of Ba_2MnTeO_6 , in which the magnetic moment was arbitrarily set to point along the a -axis. At 2 K, the refined Mn^{2+} magnetic moment was determined to be $\mu = 4.34(3) \mu_B$ per Mn^{2+} , close to the expected value for an $Mn^{2+} S = 5/2$ cation. The refined moment is slightly reduced as a result of spin wave excitation (i.e. inelastic scattering) causing collective oscillations of the magnetic moments. The refined Mn^{2+} moment is plotted as a function of temperature in Fig. 3.11b. The refined moment decreases as the temperature increases with the largest changes occurring about 20 K. This agrees well with the T_N determined from DC susceptibility and heat capacity measurements. The refined moment does not decrease as quickly as would be expected above T_N and does not reach zero upon approaching 25 K.

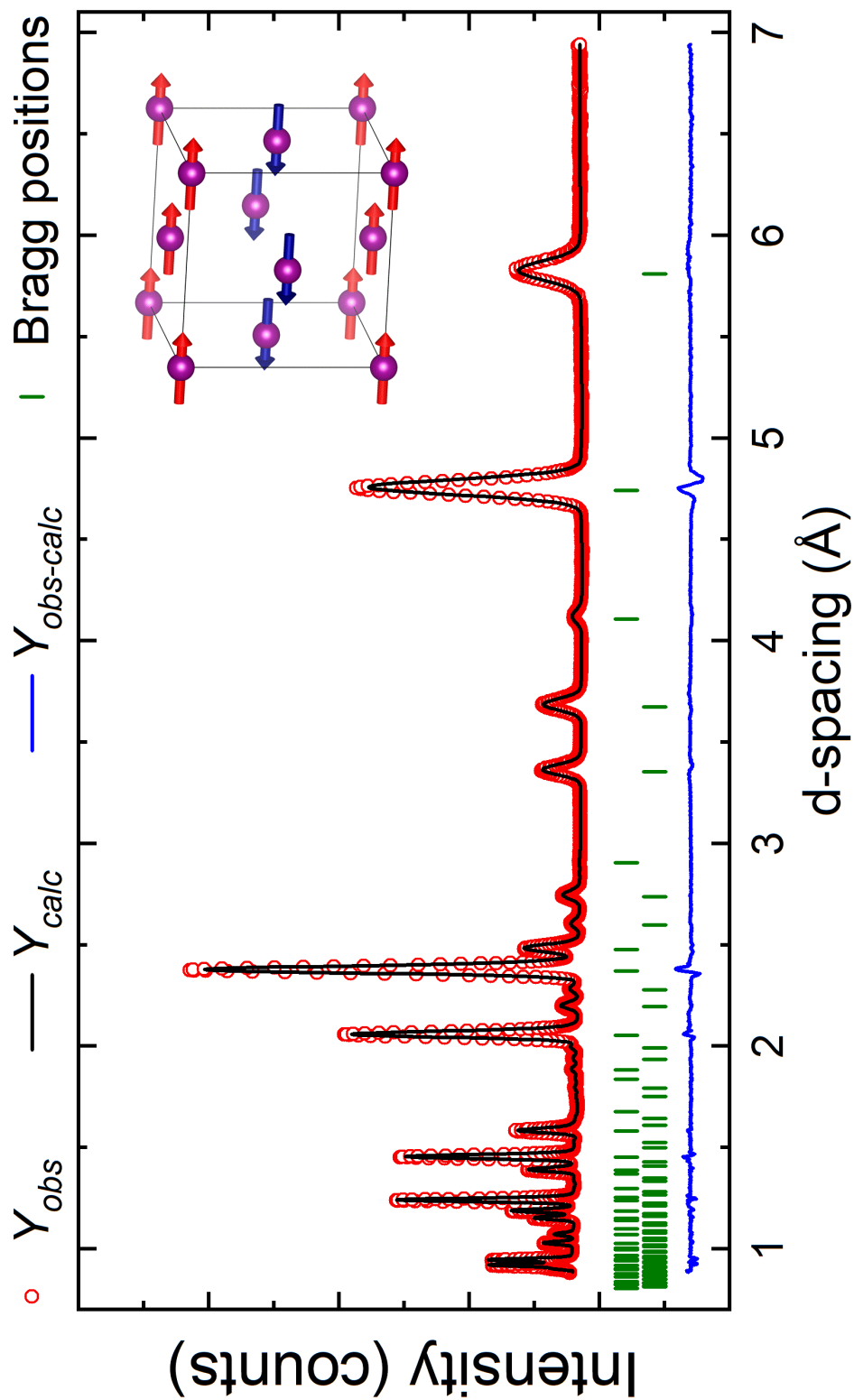


Fig. 3.10 Two-phase (nuclear + magnetic) Rietveld refinement using the 2 K $\text{Ba}_2\text{MnTeO}_6$ neutron diffraction data from bank 3 ($2\theta = 34.9574^\circ$). The nuclear structure was described using the $Fm\bar{3}m$ structure and the magnetic structure the type I antiferromagnetic model.

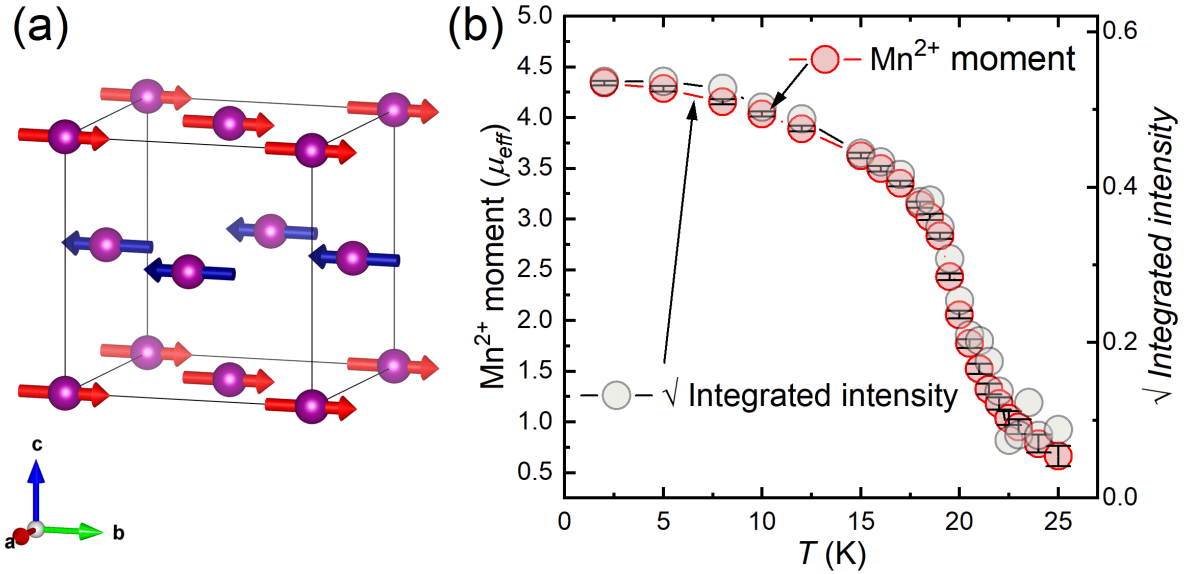


Fig. 3.11 (a) The type I antiferromagnetic structure of Ba_2MnTeO_6 and (b) the refined Mn^{2+} magnetic moment determined from the neutron diffraction data plotted as a function of temperature. In (b), the left axis shows the refined Mn^{2+} moment (μ_{eff}) and the right axis is the square root of the integrated intensity of the main magnetic peak. The refined moment follows the square root of the integrated intensity well showing the refinement provides an accurate estimate of μ_{eff} .

The waterfall plot in Fig. 3.12a shows the evolution of the magnetic Bragg peaks about the transition temperature between 14-25 K. As the temperature approaches ~ 20 K, the magnetic Bragg peaks become sharper, signifying the onset of antiferromagnetic ordering. The decay of the magnetic peaks was also investigated above 20 K. Unexpectedly, the magnetic Bragg peaks do not completely disappear above the transition temperature. This can be seen even more clearly in Fig. 3.12b, where the diffraction patterns at temperatures between 5 to 100 K are overlaid. The magnetic scattering peaks continue to make a visible contribution to the diffraction pattern well above T_N . The intensity of the (001) magnetic peak at ~ 8.3 Å is plotted as a function of temperature in Fig. 3.13. The peak intensity quickly decays above 20 K, but does not plateau to a constant value. Instead, the decrease in the peak intensity is spread out over a wide temperature range. The inset shows the (001) peak at 40 K. The peak is broad indicating diffuse magnetic scattering. Diffuse magnetic scattering suggests the presence of a short-range magnetically ordered state. Diffuse magnetic scattering would explain the gradual decrease of the refined Mn^{2+} moment around the transition temperature. Similar diffuse magnetic scattering at temperatures far greater than T_N has been observed for Ba_2MnWO_6 .¹⁹ Diffuse magnetic scattering is no longer visible at 100 K (see inset in Fig. 3.13) implying Ba_2MnTeO_6 is fully paramagnetic. Inelastic neutron scattering and polarised magnetic scattering measurements were performed to investigate the disordered state above T_N .

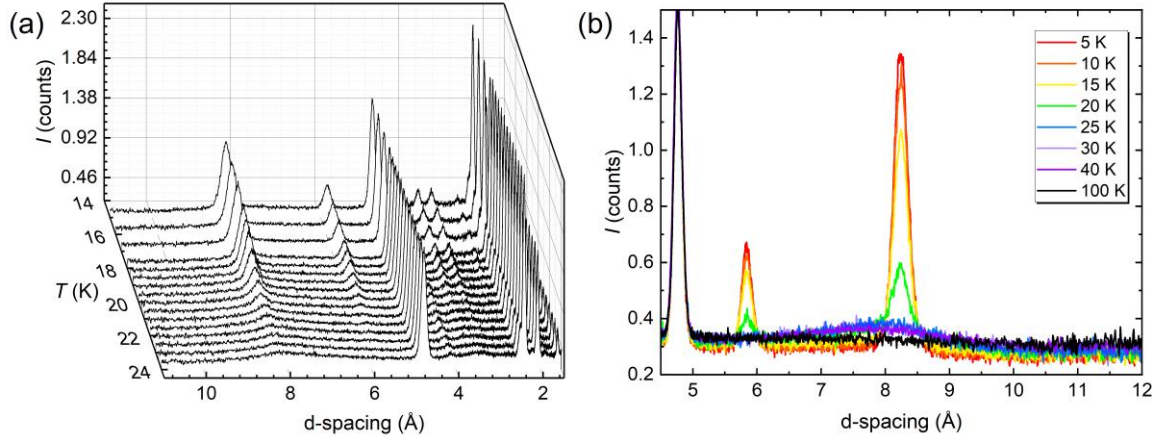


Fig. 3.12 (a) Waterfall plot of the Ba_2MnTeO_6 neutron diffraction patterns between 14 to 25 K. The waterfall plot shows the evolution of the magnetic scattering peaks below and above T_N . (b) Plot overlaying the neutron diffraction patterns at various temperatures between 5-100 K. The intensity of the magnetic peaks decreases as the temperature approaches T_N , but the peaks do not completely disappear above T_N . Broad magnetic scattering peaks are still visible at 40 K (purple line).

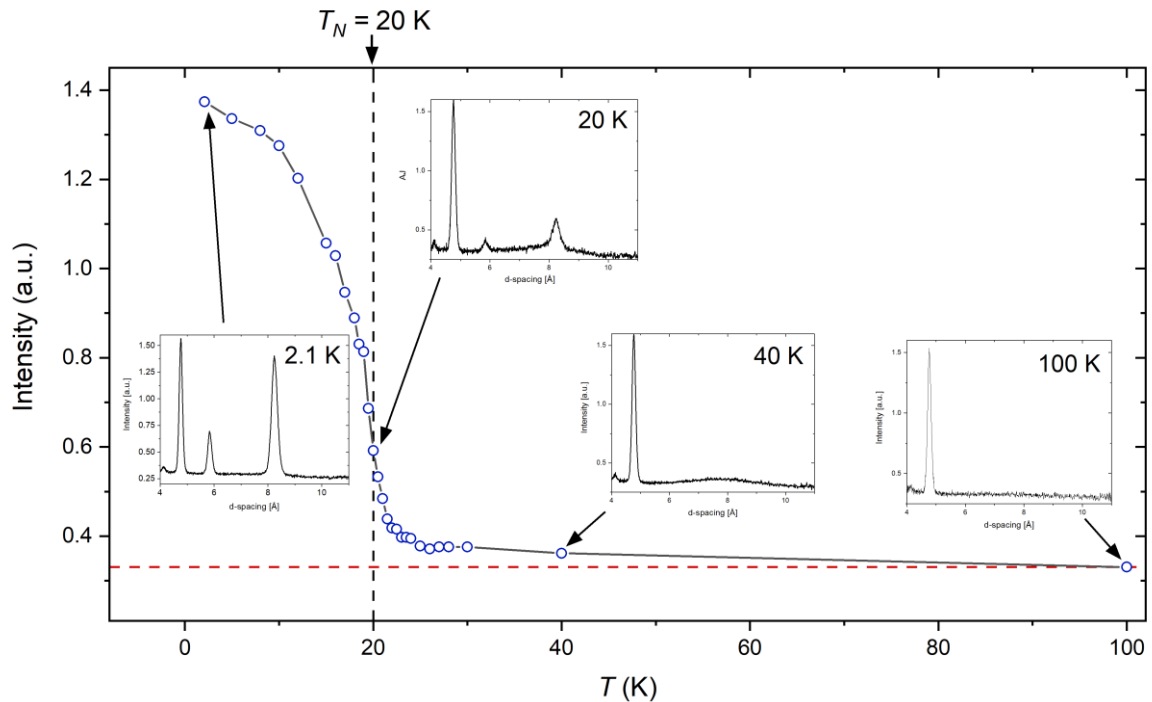


Fig. 3.13 Intensity of the (001) Ba_2MnTeO_6 magnetic reflection at $\sim 8.3 \text{ \AA}$ as a function of temperature. The insets show the neutron diffraction patterns corresponding to the peak intensities at specified temperatures.

e. Inelastic neutron scattering

The inelastic neutron scattering spectra of Ba_2MnTeO_6 was measured below T_N at 6 K, and above T_N at 44 K and 109 K. The spectra are shown in Fig. 3.14. The horizontal yellow band at $E = 0 \text{ meV}$ represents the elastic line (i.e. the diffraction intensity). In the 6 K spectrum (Fig. 3.14a), there are clear excitations above the elastic line. The excitations represent spin-waves. Spin-waves in one dimension are modelled using linear spin-wave theory. SpinW uses linear spin wave theory and classical Monte Carlo methods to solve the spin Hamiltonian for a system and simulate the inelastic neutron scattering spectra.⁶⁷ SpinW was used to simulate the low temperature inelastic neutron

scattering spectrum of $\text{Ba}_2\text{MnTeO}_6$. $\text{Ba}_2\text{MnTeO}_6$ was described using the Heisenberg J_1 - J_2 model for which the spin Hamiltonian is given by equation 3.9.

$$\hat{H} = -J_1 \sum_{\langle ij \rangle} \mathbf{S}_i \cdot \mathbf{S}_j - J_2 \sum_{\langle\langle ij \rangle\rangle} \mathbf{S}_i \cdot \mathbf{S}_j \quad (3.9)$$

Here, J_1 and J_2 are the nearest neighbour (NN) and next-nearest neighbour (NNN) exchange interactions. S_i and S_j are the spins on sites i and j . The simulated inelastic neutron scattering spectrum is shown in Fig. 3.14d. The simulation reproduces the excitation features observed in the 6 K spectrum well showing the excitations are consistent with spin-waves. Vertical slices of the data were summed over different $|Q|$ ranges and plotted as a function of energy transfer (E). Fig. 3.14e shows the vertical cuts for the 6 K spectra (data points) and the simulation (black solid lines). The black solid lines of the simulated data follow the vertical cuts of the 6 K spectra well. The close agreement between the simulated and experimental data allowed extraction of the exchange interactions using equation 3.9. The exchange interactions are consistent with type I ordering: $J_1 = -0.34$ meV and $J_2 = 0.03$ meV ($J_2/J_1 = 0.088$).

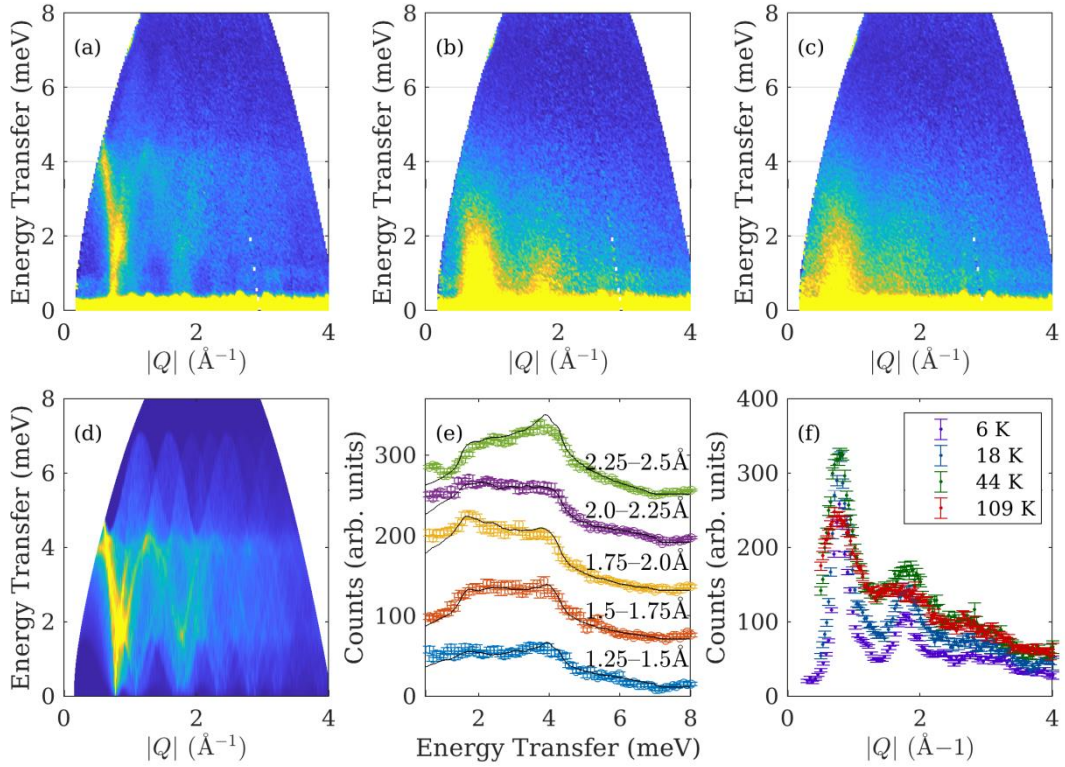


Fig. 3.14 The inelastic neutron scattering spectrum of $\text{Ba}_2\text{MnTeO}_6$ at (a) 6 K, (b) 44 K and (c) 109 K. Inelastic neutron scattering spectra were collected on the MERLIN time-of-flight spectrometer. The simulated 6 K inelastic neutron scattering spectrum of $\text{Ba}_2\text{MnTeO}_6$ produced using SpinW is shown in (d). Panel (e) shows vertical slices of the 6 K data summed over different $|Q|$ ranges. The data points with error bars are the vertical slices through the experimental data and the solid black lines show the vertical slices through the simulated data. The simulated vertical slices follow the experimental vertical slices well as a function of energy transfer (E) allowing determination of the exchange interactions: $J_1 = -0.34$ meV and $J_2 = 0.03$ meV. Panel (f) show horizontal slices through the spectra in (a)-(c) summed over an energy transfer range of $E = 1$ -2 meV. The excitations observed below T_N have the same peak positions and features as the high temperature excitations observed above T_N .

The spectra above T_N at 44 K and 109 K are shown in Fig. 3.14b and Fig. 3.14c. Broad features reminiscent of the spin wave excitations still exist in the 44 K and 109 K spectra. Horizontal slices of the spectra between $E = 1-2$ meV were summed and plotted as a function of $|Q|$ in Fig. 3.14f. The peaks in the horizontal slices of the 44 K and 109 K data have the same peak positions and features as the 6 K data. This indicates the excitations above T_N are magnetic in origin and resemble the magnetically ordered state. The excitations become weaker with temperature but are still discernible at 109 K. This agrees with the neutron diffraction data and shows a short-range magnetic correlated state exists even at $5 \times T_N$. Similar behaviour has been observed in the inelastic neutron spectra of Ba_2MnWO_6 where magnetic excitations are visible at 40 K ($5 \times T_N$). Polarized neutron scattering experiments were performed to investigate the short-range correlated state above T_N .

f. Polarized Neutron Scattering

The diffuse magnetic scattering of $\text{Ba}_2\text{MnTeO}_6$ ($T_N = 20$ K) and Ba_2MnWO_6 ($T_N = 8$ K) at various temperatures above T_N are shown in Fig. 3.15a and 3.16a, respectively. Fig. 3.15a shows the diffuse magnetic scattering of $\text{Ba}_2\text{MnTeO}_6$ consists of two diffuse magnetic peaks at $|Q| \sim 0.78 \text{ \AA}^{-1}$ and $\sim 1.8 \text{ \AA}^{-1}$. These peaks are clearly visible at both 30 K (10 K above T_N) and 100 K ($5 \times T_N$). The position of the diffuse scattering peaks agrees well with the positions of the ordered magnetic Bragg peaks observed below $T_N = 20$ K in the neutron diffraction data at $|Q| = 0.78, 1.71$ and 1.83 \AA^{-1} . Similarly, diffuse magnetic scattering was observed well above T_N for Ba_2MnWO_6 in Fig. 3.16a. Now only one diffuse magnetic peak was clearly visible up to 100 K. The position of this main broad peak was slightly shifted compared to $\text{Ba}_2\text{MnTeO}_6$. This is expected given the different magnetic structures. The peak position at $|Q| \sim 0.68 \text{ \AA}^{-1}$ agrees well with the position of the main magnetic Bragg peak ($|Q| = 0.66 \text{ \AA}^{-1}$) in the neutron diffraction data below $T_N = 8$ K. The close agreement between the positions of the diffuse magnetic peaks and magnetic Bragg peaks provides further evidence that the disordered magnetic state above T_N closely resembles the magnetically ordered state below T_N .

Reverse Monte Carlo modelling using SPINVERT gave the spin-spin correlations between the Mn^{2+} cations. Fig. 3.15b and Fig. 3.16b compare the spin-spin correlations of $\text{Ba}_2\text{MnTeO}_6$ and Ba_2MnWO_6 , respectively. The J_1 and J_2 spin-spin correlations at different temperatures are indicated. The sign of the spin-spin correlations agrees well with the J_1 and J_2 interactions in the type I and type II magnetic structures of $\text{Ba}_2\text{MnTeO}_6$ and Ba_2MnWO_6 . For type I order, the J_1 spin-spin correlation is expected to be negative as $2/3$ of the $\text{NN-}J_1$ spins couple antiferromagnetically while $1/3$ of the $\text{NN-}J_1$ spin couple ferromagnetically. Overall, this produces a dominant antiferromagnetic correlation. The J_2 spin-spin correlation is expected to be positive as all the $\text{NNN-}J_2$ spins couple ferromagnetically. In Fig. 3.15b, the J_1 spin-spin correlation is strongly negative, while J_2 is slightly weaker and positive. This agrees well with the antiferromagnetic $J_1 = -0.34$ meV and ferromagnetic $J_2 = 0.03$ meV interactions observed in type I ordered $\text{Ba}_2\text{MnTeO}_6$.

For type II ordering, the J_1 spin-spin correlation is expected to be zero as there are an equal number of antiferromagnetic and ferromagnetic $\text{NN-}J_2$ interactions. The J_2 spin-spin correlation should be negative as all the NNN interactions are antiferromagnetic. Fig. 3.16b shows the J_2 spin-spin correlation for Ba_2MnWO_6 is negative as expected; but the J_1 spin-spin correlation is also negative and slightly bigger than J_2 . Type II ordering is obtained when the J_2/J_1 ratio is above 0.5.³⁸ For Ba_2MnWO_6 the ratio is close to 1 ($J_2/J_1 = 0.95$) placing Ba_2MnWO_6 on the strong J_1 side of the type II antiferromagnetic phase. Inelastic neutron scattering showed the J_1 interaction is almost equal to the J_2 interaction in the magnetically ordered state: $J_1 = -0.080$ meV and $J_2 = -0.076$ meV.¹⁹ Therefore, the negative J_1 spin-spin correlation results due to the strongly antiferromagnetic J_1 . While these interactions are comparable (in fact J_1 is slightly larger than J_2), type II magnetic ordering still results as it is the strong antiferromagnetic J_2 interaction that drives type II ordering.^{19,38}

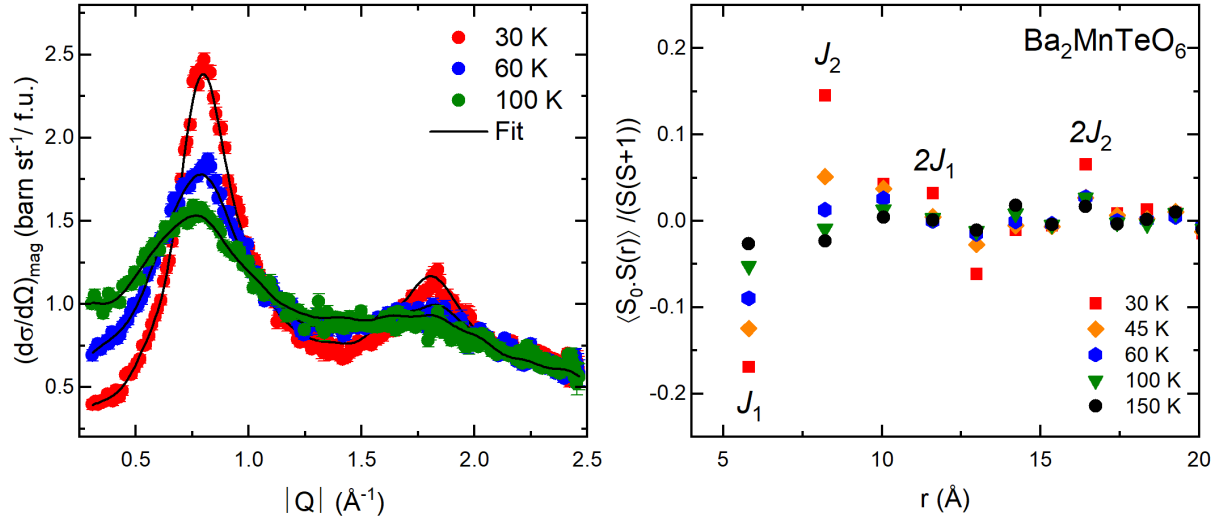


Fig. 3.15 D7 polarized neutron scattering data for $\text{Ba}_2\text{MnTeO}_6$ showing: (a) the diffuse magnetic scattering at various temperatures above T_N ; and (b) the spin-spin correlations between Mn^{2+} spins calculated using SPINVERT between 30 to 150 K. The J_1 and J_2 spin-spin correlations are indicated.

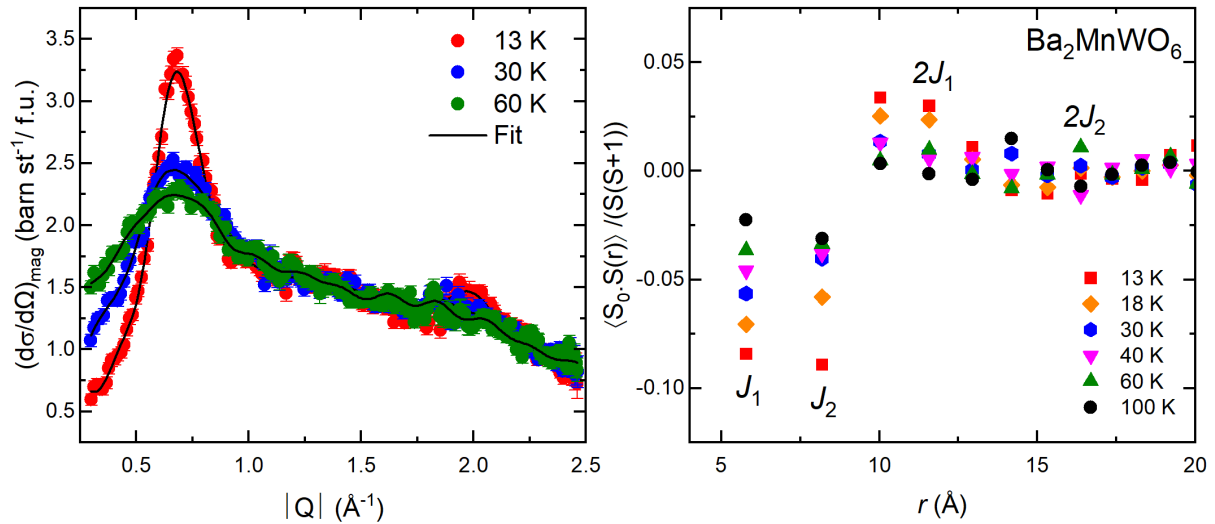


Fig. 3.16 D7 polarized neutron scattering data for Ba_2MnWO_6 showing: (a) the diffuse magnetic scattering at different temperatures above T_N ; and (b) the spin-spin correlations between the Mn^{2+} spins calculated using SPINVERT between 13 to 100 K. The J_1 and J_2 spin-spin correlations are indicated.

g. Density functional theory calculations

Density functional theory (DFT) calculations were performed by O. Mustonen. The electronic structure of $\text{Ba}_2\text{MnTeO}_6$ and Ba_2MnWO_6 was modelled using the DFT+ U method with $U = 7$ eV. The DFT calculations showed how the partial density of states for Ba^{2+} , Mn^{2+} , $\text{Te}^{2+}/\text{W}^{6+}$ and O^{2-} contribute to the total density of states in $\text{Ba}_2\text{MnTeO}_6$ and Ba_2MnWO_6 . The density of states shows the distribution of energy levels that can be occupied by electrons at a given energy.

The total and partial density of states for $\text{Ba}_2\text{MnTeO}_6$ are shown in Fig. 3.17a. The total density of states shows a clear band gap of $E_g = 1.75$ eV, as expected for an antiferromagnetic insulator. The main contributors to the valence band below the Fermi level (shown by the dotted line) are the hybridized Mn^{2+} $3d$ states and the O^{2-} $2p$ states. Above the Fermi level, the empty Mn^{2+} $3d$ states hybridize with the O^{2-} $2p$ states contributing to the conduction band. Te^{6+} barely contributes to the

total density of states. The panel for Te^{6+} shows there is a weak hybridization of the empty $5s$ and $5p$ states with the $\text{O}^{2-} 2p$ or $\text{Mn}^{2+} 3d$ states, but there is no involvement from the filled $4d^{10}$ orbitals. The $\text{Te}^{6+} 4d^{10}$ orbitals are not visible in the plot as they lie far below the Fermi level; so do not contribute to Mn-O-Te-O-Mn superexchange.

Similarly, the total density of states in Fig. 3.17b shows Ba_2MnWO_6 has a comparable band gap of 1.98 eV. Like $\text{Ba}_2\text{MnTeO}_6$, the valence band is composed of the $\text{Mn}^{2+} 3d$ and $\text{O}^{2-} 2p$ states. Comparing Fig. 3.17b to Fig. 3.17a shows clear differences between the Te^{6+} and W^{6+} contributions to the conduction bands in $\text{Ba}_2\text{MnTeO}_6$ versus Ba_2MnWO_6 . While Te^{6+} contributes very little to the conduction band, the partial density of states in Fig. 3.15b show W^{6+} makes a much larger contribution. The empty $5d^0$ states of W^{6+} hybridize strongly with the $\text{O}^{2-} 2p$ orbitals; as well as the $\text{Mn}^{2+} 3d$ orbitals, but to a lesser degree. Unlike $\text{Ba}_2\text{MnTeO}_6$, the empty $\text{W}^{6+} 5d^0$ orbitals are involved in superexchange. These differences in hybridization underpin the d^{10}/d^0 effect and determine whether the dominant exchange interaction is J_1 or J_2 in the J_1 - J_2 Heisenberg model.

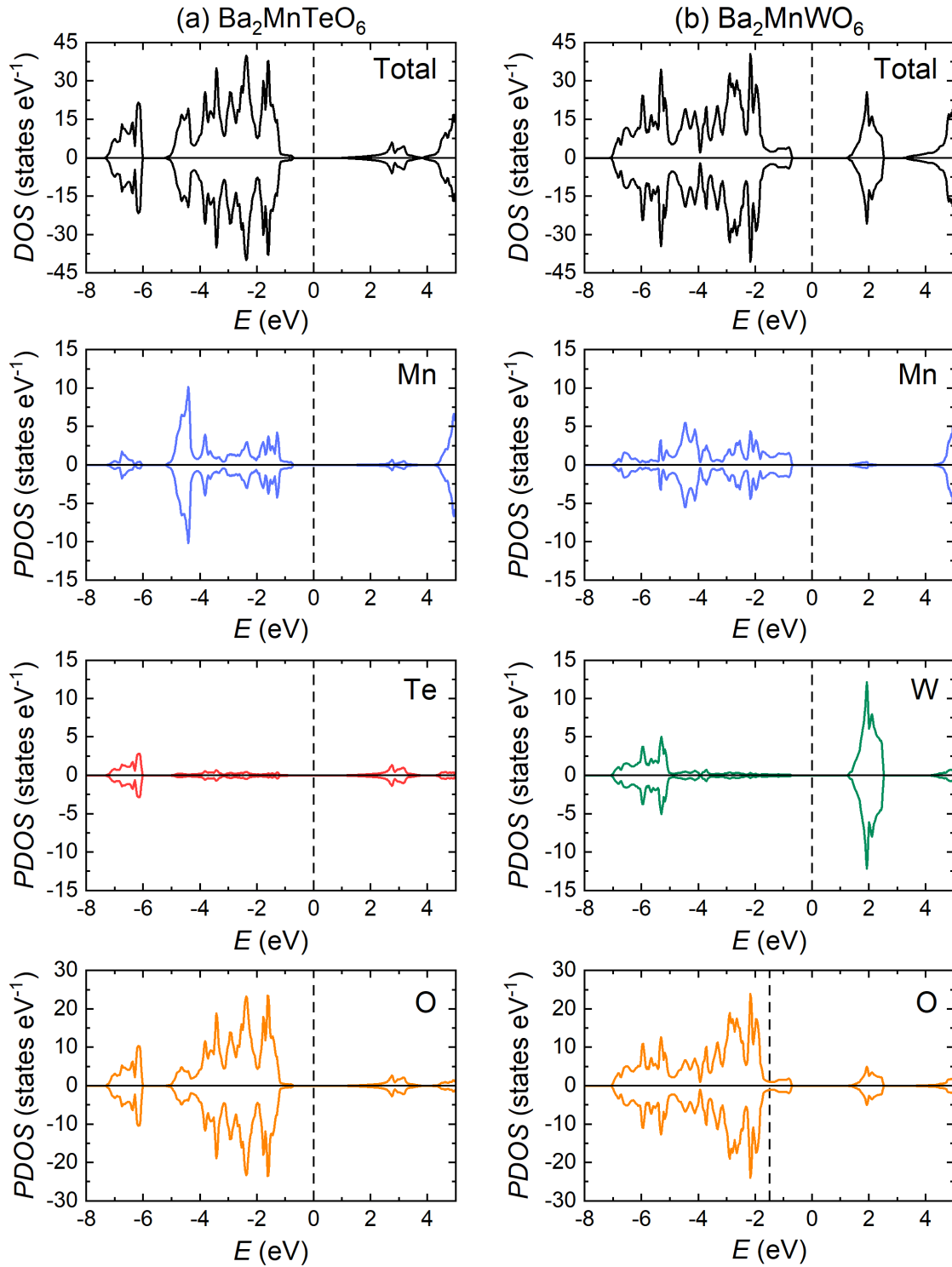


Fig. 3.17 The total and partial density of states of (a) $\text{Ba}_2\text{MnTeO}_6$ and (b) Ba_2MnWO_6 calculated using DFT+U ($U = 7$ eV) methods. The top panels show the total density of states for (a) $\text{Ba}_2\text{MnTeO}_6$ and (b) Ba_2MnWO_6 , respectively. The partial density of states for Mn^{2+} , Te/W^{6+} and O^{2-} are shown below the total density of states. Comparing the partial density of states for $\text{Ba}_2\text{MnTeO}_6$ and Ba_2MnWO_6 , shows Mn^{2+} and O^{2-} hybridize similarly in these compounds. Conversely, Te^{6+} and W^{6+} contribute differently to hybridization with Mn^{2+} 3d and O^{2-} 2p orbitals. The partial density of states of Te^{6+} shows the 5s and 5p orbitals contribute very little to hybridization in Mn-O-Te-O-Mn superexchange. The W^{6+} partial density of states shows the 5d orbitals contribute strongly to Mn-O-W-O-Mn superexchange in Ba_2MnWO_6 . Hence, the W^{6+} participation in extended superexchange is much greater than Te^{6+} .

5. Discussion

Table 3.7 provides a summary comparing the key structural and magnetic properties of $\text{Ba}_2\text{MnTeO}_6$ and Ba_2MnWO_6 .

Table 3.7: Comparison of the crystal structure and magnetic properties of $\text{Ba}_2\text{MnTeO}_6$ and Ba_2MnWO_6 .

		$\text{Ba}_2\text{MnTeO}_6$	Ba_2MnWO_6
Crystal structure	Unit cell parameters (300 K)	$a = 8.21565(2) \text{ \AA}$ Vol. = $554.531(3) \text{ \AA}^3$	$a = 8.18734(6) \text{ \AA}$ Vol. = $548.810(4) \text{ \AA}^3$
	Space group	$Fm\bar{3}m$ (cubic)	$Fm\bar{3}m$ (cubic)
	Bond lengths	2.162(4) \AA (Mn-O) 1.945(4) \AA (Te-O)	2.1711(3) \AA (Mn-O) 1.9225(3) \AA (W-O)
	Bond valence sums	2.24 (Ba^{2+}) 2.13 (Mn^{2+}) 5.56 (Te^{6+})	2.32 (Ba^{2+}) 2.14 (Mn^{2+}) 5.98 (W^{6+})
Magnetic structure	T_N	20 K	8 K
	θ_w	-157(1) K	-64 K
	μ_{eff}	6.31(7) μ_B	6.3(3) μ_B
	Frustration index (f)	8	8
	Magnetic structure	Type I antiferromagnet	Type II antiferromagnet
	Exchange constants	$J_1 = -0.34 \text{ meV}$ $J_2 = 0.03 \text{ meV}$	$J_1 = -0.080 \text{ meV}$ $J_2 = -0.076 \text{ meV}$
	Magnetic excitations above T_N	✓	✓

Comparing the crystal structure data clearly shows $\text{Ba}_2\text{MnTeO}_6$ and Ba_2MnWO_6 are isostructural. Using a combination of X-ray and neutron diffraction, $\text{Ba}_2\text{MnTeO}_6$ was found to be cubic and is described using the same $Fm\bar{3}m$ symmetry as Ba_2MnWO_6 . Furthermore, $\text{Ba}_2\text{MnTeO}_6$ and Ba_2MnWO_6 have very similar lattice parameters and unit cell volumes; and there is little difference between the Mn-O and Te-O vs W-O bond lengths in Table 3.7. The similarity between the Te-O and W-O bond lengths and unit cell parameters is not surprising given the near-identical Te^{6+} and W^{6+} ionic radii ($\text{Te}^{6+} = 0.56 \text{ \AA}$ and $\text{W}^{6+} = 0.60 \text{ \AA}$).³⁵ As a result, the bond valence sums for Ba, Mn and Te/W are all nearly the same for $\text{Ba}_2\text{MnTeO}_6$ and Ba_2MnWO_6 .

The crystal structure similarities do not extend to the magnetic structure. Low temperature neutron diffraction revealed $\text{Ba}_2\text{MnTeO}_6$ has a type I antiferromagnetic structure. This is the same magnetic structure displayed by the $B''=\text{Te}^{6+} A_2\text{Mn}B''\text{O}_6$ compounds in Table 3.1. Inelastic neutron scattering showed type I order results from a strong antiferromagnetic $J_1 = -0.34 \text{ meV}$ and weak ferromagnetic

$J_2 = 0.03$ meV interaction. The $J_2/J_1 = -0.088$ ratio produces a type 1 ordered structure of ferromagnetically coupled layers of Mn^{2+} cations in the (001) planes with antiferromagnetic coupling between layers (as seen in Fig. 3.1a). Conversely, both $J_1 = -0.080$ meV and $J_2 = -0.076$ meV are antiferromagnetic for Ba_2MnWO_6 .¹⁹ $J_2/J_1 = 0.95$ leading to type II antiferromagnetic ordering where ferromagnetic layers are directed along the (111) plane with antiferromagnetic interactions in-between (as seen in Fig. 3.1b). The minor structural differences between $\text{Ba}_2\text{MnTeO}_6$ and Ba_2MnWO_6 means the different exchange interactions must arise from the d^{10}/d^0 effect.

The density functional theory (DFT) calculations reveal the origins of the d^{10}/d^0 effect. Te^{6+} was found to make a very weak contribution towards hybridization in Mn-O-Te-O-Mn superexchange. The filled $4d^{10}$ orbitals do not contribute. Instead, superexchange relies upon the Te^{6+} 5s and 5p orbitals, which hybridize weakly with the Mn^{2+} 3d and O^{2-} 2p orbitals. It is not clear why the 5s and 5p contribution to hybridisation is so weak. It could be that these orbitals are too compact to facilitate good orbital overlap.⁶⁸ As Fig. 3.18 illustrates, the $180^\circ J_2$ interaction passes through the B'' cation. For the J_2 interaction to be significant, a d -orbital contribution is required to facilitate hybridisation with the O^{2-} 2p orbitals in the $180^\circ J_2$ Mn-O- B'' -O-Mn superexchange pathway. Te^{6+} does not have a d -orbital to contribute leading to a near-zero J_2 interaction in $\text{Ba}_2\text{MnTeO}_6$ ($J_2 = 0.03$ meV). The majority of superexchange occurs via the $90^\circ J_1$ NN interaction ($J_1 = -0.34$ meV). At 90° , superexchange between the Mn^{2+} cations can occur through a Mn-O-O-Mn interaction via the O^{2-} 2p orbitals. The 5s and 5p orbitals may contribute, but as the arrow illustrates in Fig. 3.18 a strong J_1 superexchange can be facilitated without Te^{6+} by passing through the O^{2-} anions. The result is type I order.

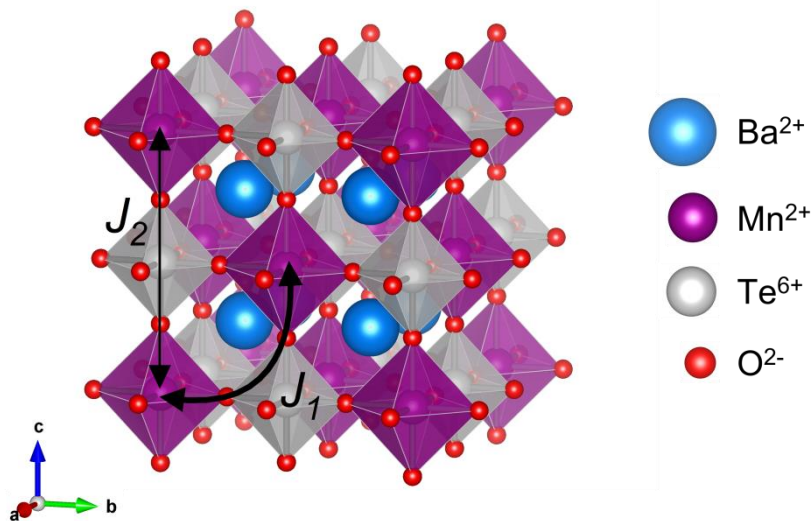


Fig. 3.18 The J_1 and J_2 exchange interactions in the cubic $\text{Ba}_2\text{MnTeO}_6$ structure. The key shows the cation colours in the structure. The exchange interactions are illustrated by the black arrows. In $\text{Ba}_2\text{MnTeO}_6$, the $180^\circ J_2$ interaction along Mn-O-Te-O-Mn is weak as the $4d^{10}$ Te^{6+} cation (shown in grey) cannot provide the d -orbital contribution required to facilitate J_2 superexchange. Instead, dominant exchange occurs through the $90^\circ J_1$ interaction. The thickness of the arrows reflects the relative strength of the exchange interactions. Note, the black arrow for the J_1 interaction does not pass through the Te^{6+} cation. At 90° , J_1 superexchange between the Mn^{2+} cations (shown in purple) can be facilitated via a Mn-O-O-Mn interaction, with minimal involvement from Te^{6+} (shown in grey).

The situation is different for Ba_2MnWO_6 . The empty $5d^0$ orbitals lie close to the Fermi level so can participate in hybridization with the O^{2-} 2p and Mn^{2+} 3d orbitals. This facilitates strong $180^\circ J_2$ superexchange via Mn-O-W-O-Mn leading to type II ordering. One might expect stronger hybridization enhances the J_1 interaction as well. However, while the J_1 and J_2 interactions are

comparable ($J_2/J_1 = 0.95$) in Ba_2MnWO_6 , the strength of the $J_1 (= -0.080 \text{ meV})$ is weak compared to in $\text{Ba}_2\text{MnTeO}_6$ where $J_1 = -0.34 \text{ meV}$. A smaller unit cell volume for Ba_2MnWO_6 would suggest a stronger J_1 from improved orbital overlap. Studies of other non-cubic $B'' = \text{W}^{6+}$ or Te^{6+} double perovskites have found the J_1 interaction is generally suppressed, with superexchange dominated mainly by the J_2 interaction. This has been observed in Sr_2CuWO_6 and Ba_2CuWO_6 .⁶⁸⁻⁷¹ In the former case, the $\text{W}^{6+} 5d^0$ orbitals introduce a ferromagnetic J_1 interaction, in addition to the antiferromagnetic J_1 interaction.⁷⁰ The $5d_{x^2-y^2}$ orbitals form the antiferromagnetic interaction through a sigma (σ)-bonding interaction with the $\text{O}^{2-} 2p$ orbitals. But the $\text{W}^{6+} 5d_{xz}$ and $5d_{yz}$ orbitals also form a ferromagnetic pi (π)-bonding interaction with the $\text{O}^{2-} 2p$ orbitals. The competing ferromagnetic vs antiferromagnetic interactions suppress J_1 exchange. This is expected to be the origin of the suppressed J_1 here, and in other $B'' = \text{W}^{6+}$ or Te^{6+} double perovskites. Suppression of the J_1 interaction explains why the T_N and Weiss constant (θ_w) for Ba_2MnWO_6 are lower compared to $\text{Ba}_2\text{MnTeO}_6$. Despite suppression of J_1 , the strong J_2 interaction still drives type II ordering.

Table 3.8 compares the magnetic properties of a range of $A_2B'B''\text{O}_6$ perovskites with different magnetic B' cations in combination with $B'' = \text{Te}^{6+}$ or W^{6+} . Irrespective of the identity of the magnetic B' cation, Table 3.8 clearly shows that double perovskites where $B'' = \text{Te}^{6+}$ are type I or Néel ordered. Whereas, when $B'' = \text{W}^{6+}$ type II order is observed.

Table 3.8: The magnetic properties of ordered double perovskites with d^0 (Te^{6+}) or d^{10} (W^{6+} , Mo^{6+} , Ti^{4+}) B'' cations in combination with different magnetic B' cations.

Structure	Space group*	T_N (K)	Magnetic structure	J_1 (meV)	J_2 (meV)	J_2/J_1	Ref.
$\text{Ba}_2\text{MnTeO}_6$	$Fm\bar{3}m$	20	Type I	-0.34	0.03	-0.088	62
$\text{Sr}_2\text{MnTeO}_6$	$P2_1/n$	20	Type I	-	-	-	30,31
$\text{Sr}_2\text{CoTeO}_6$	$P2_1/n$	18	Type I	-	-	-	72
$\text{Sr}_2\text{NiTeO}_6$	$P2_1/n$	35	Type I	-	-	-	73,74
$\text{Ba}_2\text{CuTeO}_6$	$I4/m$	-	Néel	-20.22	0.23	-0.01	50,71
$\text{Sr}_2\text{CuTeO}_6$	$I4/m$	29	Néel	-7.18	-0.21	0.03	45,46,48
Ba_2MnWO_6	$Fm\bar{3}m$	8	Type II	-0.080	-0.076	0.95	19
Ba_2CuWO_6	$I4/m$	28	Type II	-1.17	-11.94	10.18	50,71,75
Sr_2MnWO_6	$P2_1/n$	14	Type II	-	-	-	20,21
Sr_2CoWO_6	$P2_1/n$	24	Type II	-	-	-	76
Sr_2NiWO_6	$I4/m$	54	Type II	-0.02	-1.81	90.5	74,77
Sr_2CuWO_6	$I4/m$	24	Type II	-1.2	-7.47	6.23	69,70,78,79
Ca_2MnWO_6	$P2_1/n$	16-17	Type II				22,23
$\text{Ba}_2\text{MnMoO}_6$	$Fm\bar{3}m$	11	Type II	-1.17	-0.87	0.74	24,25,80
$\text{Sr}_2\text{MnMoO}_6$	$P4_2/n$	12-15	Type II				22,24,26
$\text{Sr}_2\text{CoMoO}_6$	$I4/m$	36	Type II				81
$\text{Ba}_2\text{NiMoO}_6$	$Fm\bar{3}m$	64	Type II				82
$\text{Sr}_2\text{NiMoO}_6$	$I4/m$	81	Type II				82,83
$\text{La}_2\text{MnTiO}_6$	$P2_1/n$	9	Type II				84

* Space group at low temperatures.

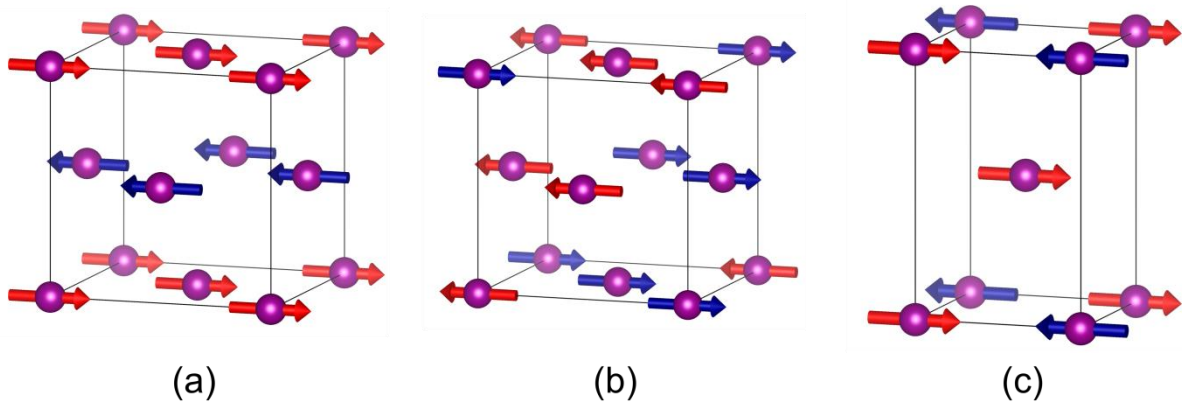


Fig. 3.19 Comparison of (a) Type I antiferromagnetic order; (b) Type II antiferromagnetic order in the cubic unit cell; and (c) Néel order in the tetragonal unit cell.

Fig. 3.19 compares the type I, type II and Néel ordered $A_2B'TeO_6$ structures. Beginning with the $B'' = Te^{6+}$ perovskites, Néel ordering arises for the $B' = Cu^{2+}$ double perovskites. The Jahn-Teller active Cu^{2+} cation elongates the unit cell along c leading to tetragonal symmetry ($I4/m$). Elongation of the unit cell creates a highly two-dimensional magnetic structure. The exchange interactions in the ab plane dominate while the interactions between the ab planes along the c -axis are weak. Generating the Néel ordered structure in Fig. 3.19c in the tetragonal unit cell requires a dominant antiferromagnetic J_1 interaction. This can be facilitated by Te^{6+} as superexchange prefers a strong J_1 and weak J_2 interaction. But not W^{6+} as the $5d^0$ orbital promotes a strong J_2 interaction. Consequently, isostructural $(Sr,Ba)_2CuTeO_6$ are Néel ordered, whereas $(Sr,Ba)_2CuWO_6$ are type II ordered.

In addition to the Jahn-Teller distorted Cu^{2+} perovskites, the d^{10}/d^0 effect can also be observed in the distorted $B' = Mn^{2+}$, Co^{2+} and Ni^{2+} perovskites. These monoclinic and tetragonal $(Sr, Ba)_2B'(Te/W)O_6$ ($B' = Mn^{2+}$, Co^{2+} and Ni^{2+}) perovskites all display the d^{10}/d^0 effect: Te^{2+} - strong J_1 (type II/Néel) and W^{6+} - strong J_2 (type II). Furthermore, the J_2/J_1 ratios for the Te^{6+} and W^{6+} structures in Table 3.8 are similar to the J_2/J_1 ratios determined for cubic Ba_2MnTeO_6 and Ba_2MnWO_6 , respectively. The J_2/J_1 ratio is close to zero in all the $(Sr, Ba)_2B'TeO_6$ ($B' = Mn^{2+}$, Co^{2+} and Ni^{2+}) perovskites. This shows Te^{6+} consistently produces a weak J_2 superexchange interaction, despite the differences in crystal symmetry. This leads to type I order for $(Sr, Ba)_2B'TeO_6$ ($B' = Mn^{2+}$, Co^{2+} and Ni^{2+}). Alternatively, J_2 is enhanced by the W^{6+} d -orbital contribution to NNN exchange in the $(Sr, Ba)_2B'WO_6$ ($B' = Mn^{2+}$, Co^{2+} and Ni^{2+}) perovskites, all of which are type II ordered. Similar to in Ba_2MnWO_6 , the greater W^{6+} $5d^0$ contribution to superexchange does not enhance the J_1 interaction. The J_1 interaction is either significantly smaller (producing a large J_2/J_1 ratio) or of similar magnitude to the J_1 interaction (J_2/J_1 is close to unity). Thus, the difference in Te^{6+} $4d^{10}$ and W^{6+} $5d^0$ orbital hybridization affects the strength of superexchange in a similar manner, even when the superexchange distances and angles are distorted in the non-cubic structures.

Also included in Table 3.8 are the magnetic properties of ordered double perovskites containing Mo^{6+} ($4d^0$) and Ti^{4+} ($3d^0$) cations. Identical to W^{6+} $5d^0$, the Mo^{6+} and Ti^{4+} perovskites exhibit type II antiferromagnetic ordering. As in the case of Ba_2MnWO_6 , the greater hybridization between empty d^0 orbitals and O $2p$ orbitals strengthens the J_2 interaction leading to type II ordering.⁸⁴ This suggests a variety of d^{10} and d^0 cations can be used to manipulate magnetic ordering in a range of double perovskite structures.

Ba_2MnTeO_6 and Ba_2MnWO_6 both show evidence of diffuse magnetic scattering in their inelastic neutron scattering spectra at $5 \times T_N$. The close correspondence between the magnetic excitations above T_N and spin waves below T_N in the inelastic neutron scattering data suggested the disordered

magnetic state resembles the ordered magnetic state. Diffuse magnetic scattering was observed at temperatures $5 \times T_N$ for both $\text{Ba}_2\text{MnTeO}_6$ and Ba_2MnWO_6 . The positions of the diffuse magnetic peaks are close to the position of the magnetic Bragg peaks confirming a close resemblance between the disordered and ordered magnetic structures. The sign of the J_1 and J_2 spin-spin correlations agrees well with type I order for $\text{Ba}_2\text{MnTeO}_6$, with J_1 negative (antiferromagnetic) and J_2 positive (ferromagnetic). The J_1 and J_2 spin-spin correlations are both negative agreeing with type II ordering for Ba_2MnWO_6 . Hence, the disordered magnetic state likely represents decay of the magnetically ordered state. Instead of occurring just above the transition, the magnetic state decays gradually above T_N . J_1 and J_2 spin-spin correlations still persist even at 150 K in the case of $\text{Ba}_2\text{MnTeO}_6$. Such behaviour is not novel to these perovskites. Diffuse magnetic scattering has been observed well above T_N in the double perovskites Ba_2YRuO_6 and Sr_2CuWO_6 .^{69,85} A range of double perovskites could display strong magnetic correlations above T_N . However, studying diffuse magnetic interactions is difficult and requires access to complex instruments, of which there are few. Hence, the low temperature magnetic properties often take precedence.

6. Conclusions

$\text{Ba}_2\text{MnTeO}_6$ and Ba_2MnWO_6 are isostructural, but adopt different antiferromagnetic ordering: $\text{Ba}_2\text{MnTeO}_6$ – type I ($T_N = 20$ K) and $\text{Ba}_2\text{MnTeO}_6$ – type II ($T_N = 8$ K). Differences in magnetic ordering are explained by the d^{10}/d^0 effect. Density functional theory calculations showed the d^{10}/d^0 effect arises from the contrasting Te^{6+} and W^{6+} contributions towards orbital hybridization. $\text{Te}^{6+} 4d^{10}$ is unable to facilitate the $180^\circ J_2$ superexchange interaction required for type II order due to the limited orbital contribution to hybridization. The J_1 interaction can be facilitated without Te^{6+} via a Mn-O-O-Mn interaction. This leads to type I order with a strong J_1 and near zero J_2 . The $\text{W}^{6+} 5d^0$ orbitals do contribute to hybridization leading to type II ordered Ba_2MnWO_6 from the strong J_2 interaction. This established the d^{10}/d^0 effect in an *ideal* cubic perovskite structure, in which there are no complex structural or magnetic influences. The d^{10}/d^0 effect was evaluated in distorted $A_2B'B''O_6$ perovskites containing other magnetic B' cations in combination with Te^{6+} and W^{6+} , as well as Mo^{6+} and Ti^{4+} . The structures containing $d^{10} B''$ cations exclusively adopted type I or Néel ordering, whereas structures containing $d^0 B''$ cations adopted type II ordering. Thus, the d^{10}/d^0 effect can be used to manipulate order in a range of double perovskite structures, where d^{10} (strong J_1) = type I/Néel ordering and d^0 (strong J_2) = type II ordering. The behaviour above the magnetic transition was also investigated. $\text{Ba}_2\text{MnTeO}_6$ and Ba_2MnWO_6 both exhibit evidence of short-range magnetic order at $5 \times T_N$. The results suggest this represents decay of the magnetically ordered state. Other magnetic double perovskites could display similar behaviour above T_N .

7. References

1. Schewe, H. & Schelter, W. Industrial applications of magnetoresistive sensors. *Sensors Actuators A* **59**, 165–167 (1997).
2. Jogschies, L. *et al.* Recent developments of magnetoresistive sensors for industrial applications. *Sensors* **15**, 28665–28689 (2015).
3. Graham, D. L., Ferreira, H. A. & Freitas, P. P. Magnetoresistive-based biosensors and biochips. *Trends Biotechnol.* **22**, 455–462 (2004).
4. Hu, J. M., Li, Z., Chen, L. Q. & Nan, C. W. High-density magnetoresistive random access memory operating at ultralow voltage at room temperature. *Nat. Commun.* **2**, 553 (2011).
5. Ramirez, A. P. Colossal magnetoresistance. *J. Phys. Condens. Matter* **9**, 8171–8199 (1997).
6. Kobayashi, K. I., Kimura, T., Sawada, H., Terakura, K. & Tokura, Y. Room-temperature magnetoresistance in an oxide material with an ordered double-perovskite structure. *Nature* **395**, 677–680 (1998).

7. Yin, H. Q. *et al.* Intra- versus intergranular low-field magnetoresistance of Sr₂FeMoO₆ thin films. *Appl. Phys. Lett.* **75**, 2812–2814 (1999).
8. Kim, T. H., Uehara, M., Cheong, S. W. & Lee, S. Large room-temperature intergrain magnetoresistance in double perovskite SrFe_{1-x}(Mo or Re)_xO₃. *Appl. Phys. Lett.* **74**, 1737–1739 (1999).
9. Nag, A., Jana, S., Middey, S. & Ray, S. The many facets of tunneling magnetoresistance in Sr₂FeMoO₆. *Indian J. Phys.* **91**, 883–893 (2017).
10. Guo, Y., Shi, L., Zhou, S., Zhao, J. & Liu, W. Near room-temperature magnetoresistance effect in double perovskite La₂NiMnO₆. *Appl. Phys. Lett.* **102**, 222401 (2013).
11. Mahato, R. N., Sethupathi, K. & Sankaranarayanan, V. Colossal magnetoresistance in the double perovskite oxide La₂CoMnO₆. *J. Appl. Phys.* **107**, 09D714 (2010).
12. Woodward, P. M. Octahedral Tilting in Perovskites. I. Geometrical Considerations. *Acta Cryst.* **B53**, 32–43 (1997).
13. Woodward, P. M. Octahedral Tilting in Perovskites. II. Structure Stabilizing Forces. *Acta Cryst.* **B53**, 44–66 (1997).
14. Lufaso, M. W. & Woodward, P. M. Jahn-Teller distortions, cation ordering and octahedral tilting in perovskites. *Acta Cryst.* **B60**, 10–20 (2004).
15. Goodenough, J. B. Theory of the role of covalence in the perovskite-type manganites [La,M(II)]MnO₃. *Phys. Rev.* **100**, 564–573 (1955).
16. Goodenough, J. B. An interpretation of the magnetic properties of the perovskite-type mixed crystals La_{1-x}Sr_xCoO_{3-λ}. *J. Phys. Chem. Solids* **6**, 287–297 (1958).
17. Kanamori, J. Superexchange interaction and symmetry properties of electron orbitals. *J. Phys. Chem. Solids* **10**, 87–98 (1959).
18. Khattak, C. P., Cox, D. E. & Wang, F. F. Y. The Magnetic Structure of Ba₂MnWO₆. *J. Solid State Chem.* **17**, 323–325 (1976).
19. Mutch, H. *et al.* Long- and short-range magnetism in the frustrated double perovskite Ba₂MnWO₆. *Phys. Rev. Mater.* **4**, 014408 (2020).
20. Azad, A. K. *et al.* Synthesis, crystal structure, and magnetic characterization of the double perovskite Ba₂MnWO₆. *Mater. Res. Bull.* **36**, 2215–2228 (2001).
21. Faik, A. *et al.* Crystal structures and temperature-induced phase transitions of Sr₂Mn²⁺W⁶⁺O₆, and of its transformation to Sr₂Mn³⁺W⁶⁺O_{6+δ}. *J. Mol. Struct.* **933**, 53–62 (2009).
22. Muñoz, A., Alonso, J. A., Casais, M. T., Martínez-Lope, M. J. & Fernández-Díaz, M. T. Crystal and magnetic structure of the complex oxides Sr₂MnMoO₆, Sr₂MnWO₆ and Ca₂MnWO₆: a neutron diffraction study. *J. Phys. Condens. Matter* **14**, 8817–8830 (2002).
23. Azad, A. K. *et al.* Nuclear and magnetic structure of Ca₂MnWO₆: A neutron powder diffraction study. *Mater. Res. Bull.* **36**, 2485–2496 (2001).
24. Azad, A. K. *et al.* Synthesis, structural and magnetic characterisation of the double perovskite A₂MnMoO₆ (A = Ba, Sr). *J. Alloys Compd.* **364**, 77–82 (2004).
25. Martínez-Lope, M. J., Alonso, J. A. & Casais, M. T. Synthesis, crystal and magnetic structure of the new double perovskite Ba₂MnMoO₆. *Z. Naturforsch* **58b**, 571–576 (2003).

26. Itoh, M., Ohta, I. & Inaguma, Y. Valency pair and properties of 1:1 ordered perovskite-type compounds Sr_2MMoO_6 ($M = \text{Mn, Fe, Co}$). *Mater. Sci. Eng.* **B41**, 55–58 (1996).
27. Poddar, A., Das, S. & Chattopadhyay, B. Effect of alkaline-earth and transition metals on the electrical transport of double perovskites. *J. Appl. Phys.* **95**, 6261–6267 (2004).
28. Djefal, A. *et al.* First-principles prediction of insulating antiferromagnet in ordered double-perovskite $\text{Ca}_2\text{MnMoO}_6$ compound. *Int. J. Comput. Mater. Sci. Eng.* **06**, 1750027 (2017).
29. Wulff, L., Wedel, B. & Müller-Buschbaum, H. Zur kristallchemie von telluraten mit Mn^{2+} im kationischen und anionischen teil der kristallstruktur: $(\text{Mn}_{2,4}\text{Cu}_{0,6})\text{TeO}_6$, $\text{Ba}_2\text{MnTeO}_6$ und $\text{Pb}(\text{Mn}_{0,5}\text{Te}_{0,5})\text{O}_3$. *Z. Naturforsch* **53 b**, 49–52 (1998).
30. Ortega-San Martin, L. *et al.* Structural phase transitions in the ordered double perovskite $\text{Sr}_2\text{MnTeO}_6$. *J. Phys. Condens. Matter* **16**, 3879–3888 (2004).
31. Ortega-San Martin, L. *et al.* Magnetic properties of the ordered double perovskite $\text{Sr}_2\text{MnTeO}_6$. *Eur. J. Inorg. Chem.* **2006**, 1362–1370 (2006).
32. Shan, Y. J., Kanai, Y., Tezuka, K. & Imoto, H. Synthesis and Electromagnetic Properties of Ca_2MTeO_6 ($M = \text{Mn, Co, Mg}$). *Adv. Sci. Technol.* **45**, 2572–2575 (2006).
33. Azad, A. K. *et al.* Structural and magnetic properties of the double perovskite Sr_2MnWO_6 . *J. Magn. Magn. Mater.* **237**, 124–134 (2001).
34. Azad, A. K. & Eriksson, S. G. Formation of a cubic Sr_2MnWO_6 phase at elevated temperature; a neutron powder diffraction study. *Solid State Commun.* **126**, 503–508 (2003).
35. Shannon, R. D. Revised effective ionic radii and systematic studies of interatomic distances in halides and chalcogenides. *Acta Cryst.* **A 32**, 751–767 (1976).
36. Battle, P. D. & Jones, C. W. The Crystal and Magnetic Structures of $\text{Ba}_2\text{LuRuO}_6$, Ba_2YRuO_6 , and $\text{Ba}_2\text{LuRuO}_6$. *J. Solid State Chem.* **78**, 108–116 (1989).
37. Tahir-Kheli, R. A., Callen, H. B. & Jarrett, H. Magnetic ordering in cubic crystals with first and second neighbor exchange. *J. Phys. Chem. Solids* **27**, 23–32 (1966).
38. Sun, N. N. & Wang, H. Y. The J_1 - J_2 model on the face-centered-cubic lattices. *J. Magn. Magn. Mater.* **454**, 176–184 (2018).
39. Kanungo, S., Yan, B., Felser, C. & Jansen, M. Active role of nonmagnetic cations in magnetic interactions for double-perovskite Sr_2BOsO_6 ($B = \text{Y, In, Sc}$). *Phys. Rev. B* **93**, 161116(R) (2016).
40. Paul, A. K. *et al.* Magnetically frustrated double perovskites: Synthesis, structural properties, and magnetic order of Sr_2BOsO_6 ($B = \text{Y, In, Sc}$). *Zeitschrift für Anorg. und Allg. Chemie* **641**, 197–205 (2015).
41. Taylor, A. E. *et al.* Magnetic order and electronic structure of the $5d^3$ double perovskite $\text{Sr}_2\text{ScOsO}_6$. *Phys. Rev. B* **91**, 100406(R) (2015).
42. Feng, H. L., Yamaura, K., Tjeng, L. H. & Jansen, M. The role of nonmagnetic d^0 vs. d^{10} B-type cations on the magnetic exchange interactions in osmium double perovskites. *J. Solid State Chem.* **243**, 119–123 (2016).
43. Vasala, S., Avdeev, M., Danilkin, S., Chmaissem, O. & Karppinen, M. Magnetic structure of Sr_2CuWO_6 . *J. Phys. Condens. Matter* **26**, 496001 (2014).
44. Vasala, S., Cheng, J. G., Yamauchi, H., Goodenough, J. B. & Karppinen, M. Synthesis and characterization of $\text{Sr}_2\text{Cu}(\text{W}_{1-x}\text{Mo}_x)\text{O}_6$: A quasi-two-dimensional magnetic system. *Chem.*

- Mater.* **24**, 2764–2774 (2012).
45. Koga, T. *et al.* Magnetic structure of the $S=1/2$ quasi-two-dimensional square-lattice Heisenberg antiferromagnet $\text{Sr}_2\text{CuTeO}_6$. *Phys. Rev. B* **93**, 054426 (2016).
 46. Babkevich, P. *et al.* Magnetic Excitations and Electronic Interactions in $\text{Sr}_2\text{CuTeO}_6$: A Spin-1/2 Square Lattice Heisenberg Antiferromagnet. *Phys. Rev. Lett.* **117**, 237203 (2016).
 47. Mustonen, O. *et al.* Tuning the $S=1/2$ square-lattice antiferromagnet $\text{Sr}_2\text{Cu}(\text{Te}_{1-x}\text{W}_x)\text{O}_6$ from Néel order to quantum disorder to columnar order. *Phys. Rev. B* **98**, 064411 (2018).
 48. Mustonen, O. *et al.* Spin-liquid-like state in a spin-1/2 square-lattice antiferromagnet perovskite induced by d^{10} - d^0 cation mixing. *Nat. Commun.* **9**, 1085 (2018).
 49. Shiraki, H. *et al.* Ferromagnetic cuprates $\text{CaCu}_3\text{Ge}_4\text{O}_{12}$ and $\text{CaCu}_3\text{Sn}_4\text{O}_{12}$ with A-site ordered perovskite structure. *Phys. Rev. B* **76**, 140403(R) (2007).
 50. Iwanaga, D., Inaguma, Y. & Itoh, M. Crystal Structure and Magnetic Properties of B-Site Ordered Perovskite-type Oxides $\text{A}_2\text{CuB}'\text{O}_6$ ($A = \text{Ba}, \text{Sr}$; $B' = \text{W}, \text{Te}$). *J. Solid State Chem.* **147**, 291–295 (1999).
 51. Marjerrison, C. A. *et al.* Magnetic ground states in the three Os^{6+} ($5d^2$) double perovskites Ba_2MOsO_6 ($M = \text{Mg}, \text{Zn}, \text{and Cd}$) from Néel order to its suppression. *Phys. Rev. B* **94**, 134429 (2016).
 52. Maharaj, D. D. *et al.* Spin gaps in the ordered states of La_2LiXO_6 ($X = \text{Ru}, \text{Os}$) and their relation to the distortion of the cubic double perovskite structure in $4d^3$ and $5d^3$ magnets. *Phys. Rev. B* **98**, 104434 (2018).
 53. Balents, L. Spin liquids in frustrated magnets. *Nature* **464**, 199–208 (2010).
 54. Vasala, S. & Karppinen, M. $\text{A}_2\text{B}'\text{B}''\text{O}_6$ perovskites: A review. *Prog. Solid State Chem.* **43**, 1–36 (2015).
 55. Rodríguez-Carvajal, J. Recent advances in magnetic structure determination by neutron powder diffraction. *Physica B* **192**, 55–69 (1993).
 56. Paddison, J. A. M., Ross Stewart, J. & Goodwin, A. L. Spinvert: A program for refinement of paramagnetic diffuse scattering data. *J. Phys. Condens. Matter* **25**, 454220 (2013).
 57. Doi, Y., Hinatsu, Y., Oikawa, K. ichi, Shimojo, Y. & Morii, Y. Magnetic and neutron diffraction study on the ordered perovskite $\text{Sr}_2\text{HoRuO}_6$. *J. Mater. Chem.* **10**, 797–800 (2000).
 58. Greedan, J. E. Geometrically frustrated magnetic materials. *J. Mater. Chem.* **11**, 37–53 (2001).
 59. Khatua, J. *et al.* Development of short and long-range magnetic order in the double perovskite based frustrated triangular lattice antiferromagnet $\text{Ba}_2\text{MnTeO}_6$. *Sci. Rep.* **11**, 6959 (2021).
 60. Li, L. *et al.* Magnetic ordering and spin dynamics in the $S=5/2$ staggered triangular lattice antiferromagnet $\text{Ba}_2\text{MnTeO}_6$. *Phys. Rev. B* **102**, 094413 (2020).
 61. Huang, H. M. *et al.* Transition of spin gapless semiconductor to semiconductor and half-metal in ferromagnetic $\text{Ba}_2\text{MnTeO}_6$. *Results Phys.* **25**, 104315 (2021).
 62. Mustonen, O. H. J. *et al.* Diamagnetic d -orbitals drive magnetic structure selection in the double perovskite $\text{Ba}_2\text{MnTeO}_6$. *Chem. Mater.* **32**, 7070–7079 (2020).
 63. Howard, C. J., Kennedy, B. J. & Woodward, P. M. Ordered double perovskites - a group-

- theoretical analysis research papers. *Acta Cryst.* **B59**, 463–471 (2003).
64. Kroumova, E., Perez-Mato, J. M. & Aroyo, M. I. WYCKSPLIT: a computer program for determination of the relationships of Wyckoff positions for a group-subgroup pair. *J. Appl. Crystallogr.* **31**, 646 (1998).
 65. Aroyo, M. I. . *et al.* Bilbao Crystallographic Server I: Databases and crystallographic computing programs. *Zeitschrift fuer Krist.* **221**, 15–27 (2006).
 66. Aroyo, M. I., Kirov, A., Capillas, C., Perez-Mato, J. M. & Wondratschek, H. Bilbao Crystallographic Server. II. Representations of crystallographic point groups and space groups. *Acta Cryst.* **A62**, 115–128 (2006).
 67. Toth, S. & Lake, B. Linear spin wave theory for single-Q incommensurate magnetic structures. *J. Phys. Condens. Matter* **27**, 166002 (2015).
 68. Katukuri, V. M. *et al.* Exchange Interactions Mediated by Nonmagnetic Cations in Double Perovskites. *Phys. Rev. Lett.* **124**, 077202 (2020).
 69. Walker, H. C. *et al.* Spin wave excitations in the tetragonal double perovskite Sr₂CuWO₆. *Phys. Rev. B* **94**, 064411 (2016).
 70. Xu, Y. *et al.* Comparative description of magnetic interactions in Sr₂CuTeO₆ and Sr₂CuWO₆. *J. Phys. Condens. Matter* **29**, 105801 (2017).
 71. Mustonen, O. *et al.* Magnetic interactions in the: $S = 1/2$ square-lattice antiferromagnets Ba₂CuTeO₆ and Ba₂CuWO₆: Parent phases of a possible spin liquid. *Chem. Commun.* **55**, 1132–1135 (2019).
 72. Ortega-San Martin, L. *et al.* Factors determining the effect of Co(II) in the ordered double perovskite structure: Sr₂CoTeO₆. *J. Mater. Chem.* **15**, 183–193 (2005).
 73. Orayech, B. *et al.* The effect of partial substitution of Ni by Mg on the structural, magnetic and spectroscopic properties of the double perovskite Sr₂NiTeO₆. *Dalt. Trans.* **45**, 14378–14393 (2016).
 74. Iwanaga, D., Inaguma, Y. & Itoh, M. Structure and magnetic properties of Sr₂NiAO₆ (A = W, Te). *Mater. Res. Bull.* **35**, 449–457 (2000).
 75. Todate, Y. Antiferromagnetism and frustration in Ba₂CuWO₆. *J. Phys. Soc. Japan* **70**, 337–340 (2001).
 76. Viola, M. C. *et al.* Structure and magnetic properties of Sr₂CoWO₆: An ordered double perovskite containing Co²⁺(HS) with unquenched orbital magnetic moment. *Chem. Mater.* **15**, 1655–1663 (2003).
 77. Rezaei, N. *et al.* Ab initio investigation of magnetic ordering in the double perovskite Sr₂NiWO₆. *Phys. Rev. B* **99**, 104411 (2019).
 78. Vasala, S., Avdeev, M., Danilkin, S., Chmaissem, O. & Karppinen, M. Magnetic structure of Sr₂CuWO₆. *J. Phys. Condens. Matter* **26**, 496001 (2014).
 79. Vasala, S. *et al.* Characterization of magnetic properties of Sr₂CuWO₆ and Sr₂CuMoO₆. *Phys. Rev. B* **89**, 134419 (2014).
 80. Lv, S., Liu, X., Li, H., Wu, Z. & Meng, J. Magnetic and electronic structures of Ba₂MnMoO₆ from first-principles calculations. *Comput. Mater. Sci.* **49**, 266–269 (2010).
 81. Ivanov, S. A., Eriksson, S. G., Tellgren, R., Rundlöf, H. & Tsegai, M. The magnetoelectric

- perovskite $\text{Sr}_2\text{CoMoO}_6$: An insight from neutron powder diffraction. *Mater. Res. Bull.* **40**, 840–849 (2005).
82. Martínez-Lope, M. J., Alonso, J. A. & Casais, M. T. Synthesis, crystal and magnetic structure of the double perovskites A_2NiMoO_6 ($\text{A} = \text{Sr}, \text{Ba}$): A neutron diffraction study. *Eur. J. Inorg. Chem.* **6**, 2839–2844 (2003).
 83. Eriksson, A. K. *et al.* High temperature phase transition of the magnetoelectric double perovskite $\text{Sr}_2\text{NiMoO}_6$ by neutron diffraction. *Mater. Res. Bull.* **41**, 144–157 (2006).
 84. Arciniegas Jaimes, D. M. *et al.* Effect of B -Site Order-Disorder in the Structure and Magnetism of the New Perovskite Family $\text{La}_2\text{MnB}'\text{O}_6$ with $B' = \text{Ti}, \text{Zr},$ and Hf . *Inorg. Chem.* **60**, 4935–4944 (2021).
 85. Nilsen, G. J., Thompson, C. M., Ehlers, G., Marjerrison, C. A. & Greedan, J. E. Diffuse magnetic neutron scattering in the highly frustrated double perovskite Ba_2YRuO_6 . *Phys. Rev. B* **91**, 054415 (2015).

Chapter 4: Site-selective W^{6+} (d^0) substitution in $Ba_2CuTe_{1-x}W_xO_6$

Contents

1. Abstract
2. Introduction
3. Experimental
4. Results
 - a. Laboratory X-ray diffraction
 - b. Synchrotron X-ray diffraction
 - c. Extended X-ray Absorption Fine Structure (EXAFS)
 - d. Neutron diffraction
5. Discussion
6. Conclusions
7. References
8. Appendix

1. Abstract

Chapter 3 introduced the d^{10}/d^0 effect in double perovskites. Different types of magnetic order resulted when $B'' = d^{10}$ (Te^{6+}) versus $B'' = d^0$ (W^{6+} , Mo^{6+}). Recently, mixtures of d^{10} and d^0 cations have been found to destabilise magnetic ordering in double perovskites. Examples include the $Sr_2CuTe_{1-x}W_xO_6$ solid solution. The aim in this chapter was to determine whether similar behaviours could be induced by introducing competing d^{10}/d^0 interactions in more complex perovskite structures, such as hexagonal perovskites. The hexagonal perovskite Ba_2CuTeO_6 was an excellent structure for this investigation. It possesses a more complex crystal and magnetic structure compared to Sr_2CuTeO_6 , whilst bearing an analogous Cu^{2+} magnetic geometry. A $Ba_2CuTe_{1-x}W_xO_6$ solid solution was prepared between $0 \leq x \leq 0.3$. A strong site-selectivity for W^{6+} substitution at the corner-sharing site was identified. The result was site-selective d^{10}/d^0 tuning of the intra-ladder interactions in the Cu^{2+} spin ladder structure of $Ba_2CuTe_{1-x}W_xO_6$. The effect on the magnetic interactions is investigated in chapter 5.

2. Introduction

The following two chapters are concerned with mixtures of d^{10} and d^0 cations in perovskite systems. One example is the $Sr_2CuTe_{1-x}W_xO_6$ solid solution between the isostructural antiferromagnetic Sr_2CuTeO_6 and Sr_2CuWO_6 double perovskites. The competition between the d^{10} -strong J_1 and d^0 -strong J_2 exchange interactions destabilizes antiferromagnetic order and tunes $Sr_2CuTe_{1-x}W_xO_6$ into a magnetically disordered state.¹⁻³ The ground state of $Sr_2CuTe_{0.5}W_{0.5}O_6$ ($x = 0.5$) closely resembles a quantum spin liquid, an exotic quantum magnetic state that has evoked much interest since its proposal in the 1970s.^{2,4-6} The Ba analogue of Sr_2CuTeO_6 possesses a hexagonal perovskite structure. The mixture of corner- and face-sharing creates a more complex structure compared to the purely corner-sharing Sr_2CuTeO_6 double perovskite. Despite these structural differences, Ba_2CuTeO_6 possesses structural features similar to in Sr_2CuTeO_6 , including a similar structural magnetic motif and the same type of magnetic ordering. Partial W^{6+} substitution of Te^{6+} in Ba_2CuTeO_6 to form

$\text{Ba}_2\text{CuTe}_{1-x}\text{W}_x\text{O}_6$ creates an ideal system to investigate d^{10}/d^0 mixtures in more complex perovskite structures.

There are suggestions that the d^{10}/d^0 effect has a wide-ranging effect on the magnetic interactions, even in non-perovskite structures. For example, the ordering temperature in the inverse-trirutile $\text{Cr}_2(\text{Te}_{1-x}\text{W}_x)\text{O}_6$ structure is highly dependent on the W^{6+} (d^0) vs Te^{6+} (d^{10}) concentration.⁷ Magnetic ordering observed for Cr_2TeO_6 and Cr_2WO_6 is retained across the $\text{Cr}_2(\text{Te}_{1-x}\text{W}_x)\text{O}_6$ solution, but the ordering temperature decreases to a minimum at $x = 0.7$, whereupon the Cr_2TeO_6 and Cr_2WO_6 magnetic states co-exist. Examples of the d^{10}/d^0 effect in perovskites include the cubic perovskite $\text{CaCu}_3\text{B}_4\text{O}_{12}$ ($B = \text{Ge}, \text{Ti}$ and Sn), and the $\text{Sr}_2\text{CuTeO}_6$ and Sr_2CuWO_6 double perovskites and their aforementioned solid solution $\text{Sr}_2\text{CuTe}_{1-x}\text{W}_x\text{O}_6$. In the former case, different types of magnetic order are observed when $B = \text{Ge}^{4+}$ or Sn^{4+} (d^{10}) (ferromagnetic) vs $B = \text{Ti}^{4+}$ (d^0) (antiferromagnetic). In line with the d^{10}/d^0 effect, different types of ordering result as Ti^{4+} $3d^0$ possesses the necessary vacant d -orbitals required for antiferromagnetic superexchange.⁸ The d^{10}/d^0 effect in the latter case has even more interesting effects on the magnetic behaviour of $\text{Sr}_2\text{CuTe}_{1-x}\text{W}_x\text{O}_6$.

The $\text{Sr}_2\text{CuTe}_{1-x}\text{W}_x\text{O}_6$ solid solution is formed by W^{6+} substitution for Te^{6+} in $\text{Sr}_2\text{CuTeO}_6$ or vice versa for Sr_2CuWO_6 . Magnetism in $\text{Sr}_2\text{CuTeO}_6$ and Sr_2CuWO_6 is highly two-dimensional owing to Jahn-Teller distortion of CuO_6 .⁹ Jahn-Teller distortion elongates the unit cell along the c -axis. As a result, the magnetic interactions along a , b and c are not equivalent. The magnetic structure is described as a square lattice Heisenberg antiferromagnet and consists of square lattices of Cu^{2+} cations in the ab plane of the tetragonal unit cell. The square lattice planes are stacked along the c -axis as shown in Fig. 4.1. Within the ab square lattice planes, Cu^{2+} cations communicate via extended superexchange through O^{2-} and Te/W^{6+} to form two in-plane J_1 and J_2 Cu-O-(Te/W)-O-Cu interactions. There are inter-plane interactions, J_3 and J_4 , along c between the square planes. The inter-plane interactions are weak. Magnetism is dominated by the square lattice J_1 and J_2 interactions leading to quasi-two-dimensional magnetism.^{10,11}

Different ordering results depending on whether Cu-O-(Te/W)-O-Cu superexchange involves Te^{6+} or W^{6+} . In line with the d^{10}/d^0 effect, Te^{6+} does not participate in extended superexchange leading to a weak J_2 (-0.21 meV). Instead, superexchange occurs mainly via the dominant J_1 (-7.18 meV) interaction via Cu-O-O-Cu leading to Néel ordering for $\text{Sr}_2\text{CuTeO}_6$.^{2,12-14} Conversely, the empty $5d^0$ orbitals allow W^{6+} to contribute towards Cu-O-W-O-Cu extended superexchange via J_2 . The result is columnar ordering for Sr_2CuWO_6 due to the weak J_1 (-1.2 meV) and strong J_2 (-9.5 meV).^{15,16} The different types of magnetic ordering for $\text{Sr}_2\text{CuTeO}_6$ and Sr_2CuWO_6 are depicted in Fig. 4.1.

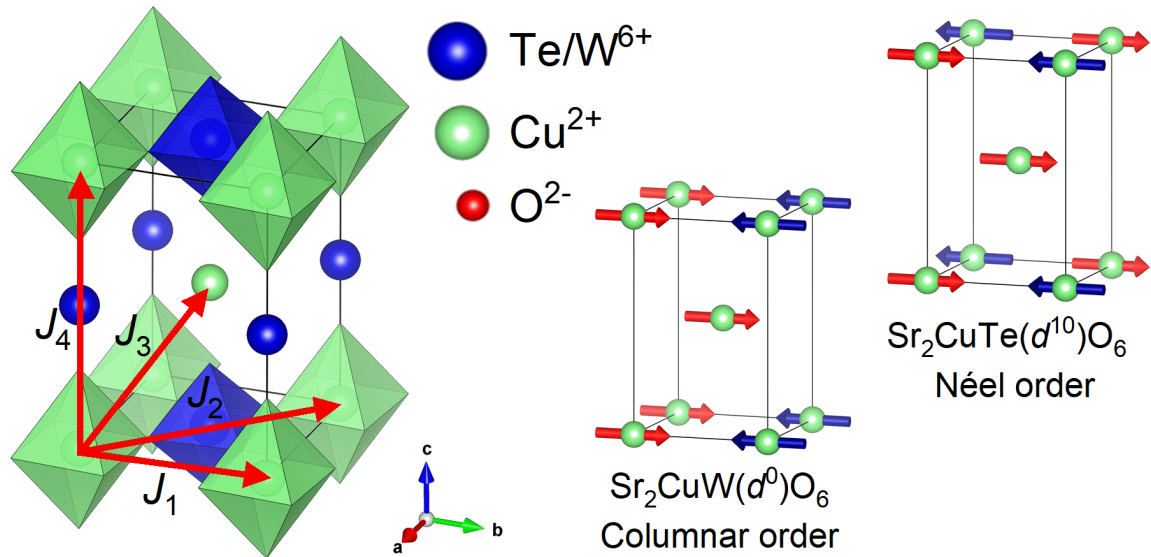


Fig. 4.1 The magnetic interactions in the tetragonal $\text{Sr}_2\text{Cu}(\text{Te}/\text{W})\text{O}_6$ structure. The Cu^{2+} interactions within the square planes form a Heisenberg square lattice antiferromagnet with two J_1 and J_2 in-plane interactions between the Cu^{2+} cations in green. Between square planes there are two J_3 and J_4 inter-plane interactions. Depending on whether the B'' (cation shown in blue) is Te^{6+} or W^{6+} , different types of magnetic order result. As depicted in the figure, the strong J_1 leads to Néel order for $\text{Sr}_2\text{CuTe}(d^{10})\text{O}_6$, whereas a strong J_2 generates columnar order for $\text{Sr}_2\text{CuW}(d^0)\text{O}_6$.

In the $\text{Sr}_2\text{CuTe}_{1-x}\text{W}_x\text{O}_6$ solution, the contrasting strong J_2 (W^{6+}) vs strong J_1 (Te^{6+}) interactions destabilises magnetic ordering.³ For $\text{Sr}_2\text{CuTeO}_6$, the competition introduced by W^{6+} substitutions levels as low as $x = 0.05$ are sufficient to prevent formation of the Néel ordered state.^{17,18} No magnetic order is detected in the muon spin relaxation spectrum of $\text{Sr}_2\text{CuTe}_{0.95}\text{W}_{0.05}\text{O}_6$.¹⁸ It has been suggested even lower W^{6+} concentrations of $x = 0.025$ are enough to prevent ordering.¹⁷ As x increases, the J_1 vs J_2 competition escalates and the interactions become increasingly frustrated.¹ Disorder induced frustration leads to a quantum spin-liquid like state for $x = 0.5$.² A quantum spin-liquid is a non-magnetically ordered state where magnetic moments remain dynamic even at zero Kelvin, and are often characterized by a continuum of spin excitations known as a gapless system.^{5,19,20} Evidence to suggest spin-liquid behaviour includes muon spin relaxation measurements, where the local magnetism in $\text{Sr}_2\text{CuTe}_{0.5}\text{W}_{0.5}\text{O}_6$ is dynamic even at 19 mK.² A linear low temperature heat capacity and a broad spectrum of excitations in the inelastic neutron scattering data also points towards a quantum spin liquid-like state.¹⁴ Beyond $x = 0.6$, the stronger J_2 interaction of W^{6+} ($J_2 = -9.5$ meV) (c.f. the J_1 interaction of Te^{6+} ($J_1 = -7.18$ meV)) leads to columnar ordering for $0.7 \leq x \leq 1$.^{1,17} Therefore, higher Te^{6+} concentrations are required to destabilise magnetic ordering in Sr_2CuWO_6 . Through the d^{10}/d^0 effect, $\text{Sr}_2\text{CuTe}_{1-x}\text{W}_x\text{O}_6$ is tuned from magnetic order to quantum disorder then back to magnetic order across the solution series between $x = 0$ to 1.

d^{10}/d^0 tuning in $\text{Sr}_2\text{CuTe}_{1-x}\text{W}_x\text{O}_6$ provided the first identification of spin-liquid like behaviour in a $S = \frac{1}{2}$ square-lattice Heisenberg antiferromagnet. Realization of unusual quantum magnetic states such as quantum spin-liquids is experimentally challenging therefore the discovery in 2018 generated significant interest. There have been numerous subsequent studies to further understand the magnetic ground state of $\text{Sr}_2\text{CuTe}_{0.5}\text{W}_{0.5}\text{O}_6$.²¹⁻²³ It also raises the question: can d^{10}/d^0 mixtures be applied to other perovskite structures? Furthermore, can they be applied in perovskite structures with more complex magnetic geometries than the square-lattice? Demonstrating both would

highlight the d^{10}/d^0 effect as an experimental tool for tuning magnetic ground states across the perovskite family.

The Ba analogue of $\text{Sr}_2\text{CuTeO}_6$ is an excellent structure for these investigations. While Ba_2CuWO_6 possesses the same double perovskite structure as $\text{Sr}_2\text{CuTeO}_6$ and Sr_2CuWO_6 , $\text{Ba}_2\text{CuTeO}_6$ has a hexagonal perovskite structure at atmospheric pressure. The double perovskite structure consists of purely corner-sharing octahedra; whereas, the hexagonal perovskite structure has both corner- and face-sharing octahedra. The corner- and face-sharing stacking sequence creates a more complex structure where the shorter face-sharing cation-cation distance can garner different magnetic behaviours to purely corner-sharing structures.²⁴ The $\text{Ba}_2\text{CuTeO}_6$ 12R hexagonal structure is shown in Fig. 4.2a. Here, trimers of face-sharing $[\text{CuO}_6\text{-TeO}_6\text{-CuO}_6]$ octahedra are linked by corner-sharing TeO_6 octahedra. This creates two-leg spin ladders of Cu^{2+} cations (Fig. 4.2b). In an analogous manner to $\text{Sr}_2\text{CuTe}_{1-x}\text{W}_x\text{O}_6$, the Cu^{2+} cations in the spin ladder are linked by extended Cu-O-Te-O-Cu superexchange via the intra-ladder J_{leg} and J_{rung} interactions indicated by the red arrows. There are additional inter-ladder interactions, of which the most dominant is the J_{inter} interaction indicated by the blue arrow through the face-sharing TeO_6 octahedra.²⁵ The resulting Cu^{2+} spin ladders illustrated by the solid lines in Fig. 4.2c run along the b -axis and are stacked in the ab plane.

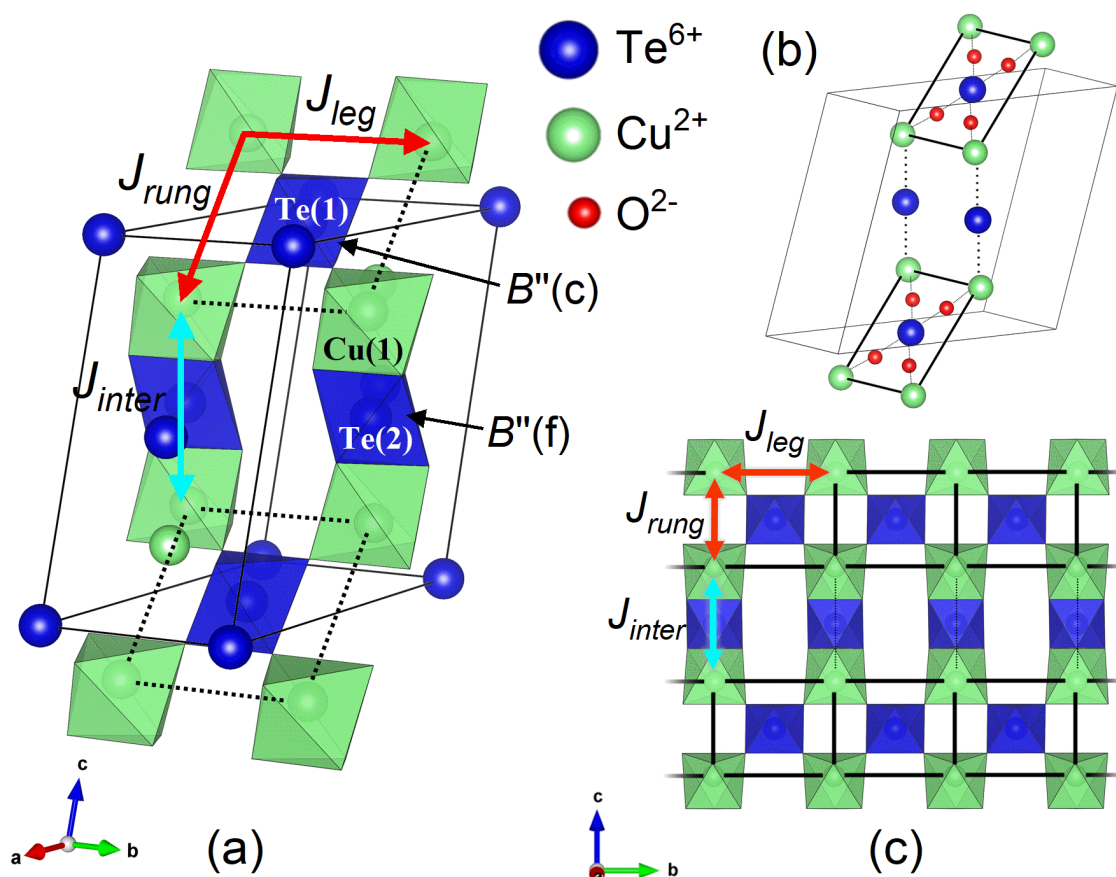


Fig. 4.2 (a) The room temperature structure of $\text{Ba}_2\text{CuTeO}_6$ (monoclinic, $C2/m$) showing the hexagonal stacking sequence of face-sharing $[\text{CuO}_6\text{-TeO}_6\text{-CuO}_6]$ trimers linked by corner-sharing TeO_6 octahedra. Extended super-exchange between the Cu^{2+} cations in green via Te^{6+} (blue) and O^{2-} (red) creates the intra-ladder (J_{leg} and J_{rung}) interactions (red arrows) and dominant inter-ladder interaction (J_{inter}) along the face-sharing trimer (blue arrow). (b) Ball-and-stick diagram of the two-leg Cu^{2+} spin ladders in the monoclinic unit cell. (c) Cu^{2+} spin ladders in $\text{Ba}_2\text{CuTeO}_6$ viewed from looking down the a -axis. The spin ladders rung along b and are stacked in the ab plane.

Whilst exhibiting different magnetic geometries, there are similarities between $\text{Sr}_2\text{CuTeO}_6$ and $\text{Ba}_2\text{CuTeO}_6$ that make them excellent structures for comparison. $\text{Sr}_2\text{CuTeO}_6$ and $\text{Ba}_2\text{CuTeO}_6$ both have a Néel ordered ground state below 29 K and 14 K, respectively.^{1,26} They also have highly two-dimensional magnetic structures with similar $\text{Cu}^{2+} \cdots \text{Cu}^{2+}$ superexchange environments. As illustrated in Fig. 4.3, the intra-ladder J_{leg} and J_{rung} interactions in $\text{Ba}_2\text{CuTeO}_6$ resemble the J_1 and J_2 interactions in the square lattice of $\text{Sr}_2\text{CuTeO}_6$. In both structures, the Cu^{2+} geometry features four Cu^{2+} cations interacting by extended Cu-O-Te-O-Cu superexchange in a square. Given these similarities, W^{6+} substitution in $\text{Ba}_2\text{CuTeO}_6$ might suppress magnetic ordering in a similar manner to in the $\text{Sr}_2\text{CuTe}_{1-x}\text{Te}_x\text{O}_6$ solution. Furthermore, the hexagonal structure offers two sites for W^{6+} substitution: (1) the corner-sharing TeO_6 site; and (2) the face-sharing TeO_6 . The two sites are labelled as the $B'(c)$ and $B'(f)$ site, respectively, where c denotes corner-sharing and f denotes face-sharing. If W^{6+} substitution were to favour one site, then the intra-ladder interactions could be tuned independently of the intra-ladder interactions or vice versa. This would demonstrate the d^{10}/d^0 effect can also be applied site-selectively to tune specific magnetic interactions in a material.

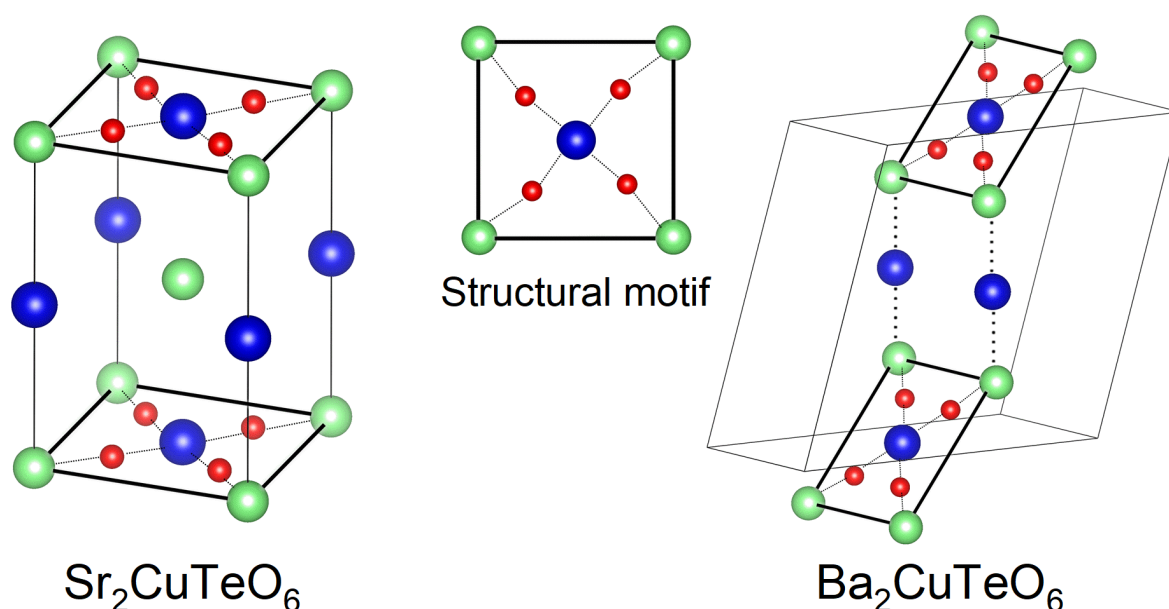


Fig. 4.3 Comparison of the $\text{Sr}_2\text{CuTeO}_6$ and $\text{Ba}_2\text{CuTeO}_6$ structures. The structures are drawn as a ball-and-stick model. Both structures possess the same structural motif of four corner Cu^{2+} cations linked by extended Cu-O-B''-O-Cu superexchange.

To investigate, a $\text{Ba}_2\text{CuTe}_{1-x}\text{W}_x\text{O}_6$ solid solution ($0 \leq x \leq 0.3$) solid solution was prepared using solid state techniques. This chapter presents the results from structural characterization of the $\text{Ba}_2\text{CuTe}_{1-x}\text{W}_x\text{O}_6$ solid solution using a combination of laboratory X-rays, synchrotron X-rays, neutron diffraction and EXAFS. This identified a strong site preference for W^{6+} to reside on the $B'(c)$ site versus the $B'(f)$ site. The next chapter investigates how this affects magnetic behaviour of $\text{Ba}_2\text{CuTe}_{1-x}\text{W}_x\text{O}_6$ compared to $\text{Ba}_2\text{CuTeO}_6$.

3. Experimental

Synthesis

Polycrystalline samples of $x = 0, 0.05, 0.1, 0.2$ and 0.3 were prepared by thoroughly grinding stoichiometric quantities of high purity BaCO_3 (99.997%), CuO (99.9995%), TeO_2 (99.995%) and WO_3 (99.998%) in an agate mortar. The reactant mixture was pressed into a pellet using a load of 1 tonne,

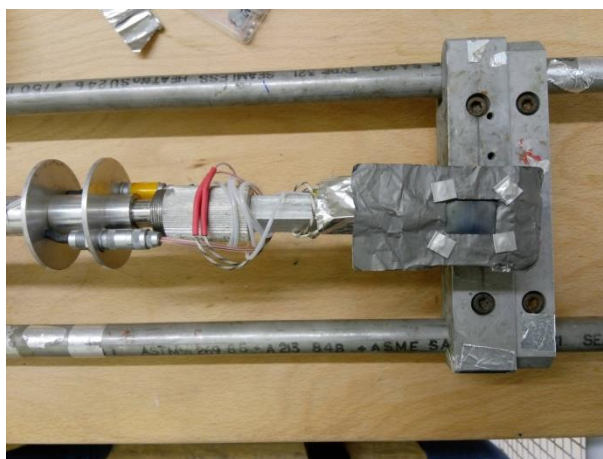
before calcination at 900 °C in air for 12 hours. The calcined pellets were broken, re-ground and pressed again, after which they were heated at reaction temperatures between 1000-1100 °C. Samples were repeatedly heated in 24 hour periods with re-grinding and pressing in between each heating. Between 72-120 hours was required to achieve phase purity in all samples, where upon the synthesis was stopped. Higher temperatures and longer reaction times were required to obtain single-phase samples as the W^{6+} content increased.

Laboratory X-ray diffraction

Laboratory X-ray diffraction was performed using a Rigaku Miniflex diffractometer ($Cu\ K\alpha_1/K\alpha_2$ ($\lambda = 1.5405$ and 1.5443 Å)). Powder diffraction patterns were collected at 300 K between each 24 hour heating to monitor phase purity during the reaction. Upon achieving phase purity, long scan X-ray diffraction patterns were collected for Rietveld refinement. Rietveld refinement was performed using the Ba_2CuTeO_6 monoclinic $C2/m$ structural model in GSAS-2.^{27,28}

Neutron diffraction

The High-Resolution Powder Diffractometer (HRPD) at the ISIS Neutron and Muon source was used to collect high-resolution neutron diffraction patterns of the $x = 0.1$ and 0.3 samples.²⁹ Al-alloy slab cans were loaded with ~ 8 g of powder and sealed using vanadium windows. Picture 4.1 below shows the slab-can mounted onto the sample rod. The can was covered in highly absorbing Gd and Cd foils to ensure only the ‘transparent’ vanadium windows of the can were exposed to the neutron flux. The slab-can was aligned perpendicular to the neutron beam and cooled to 2 K using a close cycle cryostat. Time-of-flight neutron powder diffraction patterns were collected between 2-300 K. The data were normalized against the vanadium standard and corrected for sample absorption. Rietveld refinement was performed in GSAS-2 using the data from all three neutron banks (bank 1 - $2\theta = 168.567^\circ$, bank 2 - $2\theta = 90.6161^\circ$ and bank 3 - $2\theta = 29.6304^\circ$).^{27,28} Bank 1 is the highest resolution bank on HRPD.



Picture 4.1 Image of the neutron slab can mounted onto the sample rod and covered with absorbing Gd and Cd foils.

Synchrotron X-ray diffraction

Synchrotron X-ray diffraction experiments were performed using the PETRA III X-ray radiation source at the German Electron Synchrotron (DESY). The $x = 0.1$, 0.2 and 0.3 samples were loaded into glass capillaries 0.6 mm in diameter. Capillaries were placed 1169.45 mm away from the Perkin Elmer XRD1621 2D detector on the P02.1 beamline. Room temperature (300 K) synchrotron X-ray diffraction patterns were collected while the capillary was spun using an X-ray wavelength of $\lambda = 0.20742$ Å. The collected 2D data was processed using DAWN Science to produce 1D diffraction

patterns.³⁰ Refinements were performed in GSAS-II.^{27,28} The neutron and X-ray (laboratory and synchrotron) diffraction experiments were performed using samples from the same batch.

Extended X-ray fine structure (EXAFS)

Extended X-ray Absorption Fine Structure (EXAFS) measurements were performed at the National Synchrotron Light Source II (NSLS-II) on the Beamline for Materials Measurement (6-BM). The $x = 0.3$ sample was finely ground and dispersed in polyethylene to create a sheet with a thickness of one absorption length. Room temperature (300 K) X-ray absorption spectra (XAS) were collected near the W L_3 edge. Ionization chambers filled with mixtures of He and N₂ to achieve a stable I/V curve were used to measure the intensity of the incident and transmitted beam. The internal energy was calibrated using a tungsten foil reference with the first inflection point in the W L_3 edge. This defined the initial X-ray absorption energy as $E_0 = 10206.8$ eV. A combination of the Athena, Artemis and Hephaestus programmes were used to perform the data reduction and analysis.³¹ Athena produced the EXAFS data which was examined using the ATOM and FEFF software in Artemis.

4. Results

a. Laboratory X-ray diffraction

Laboratory X-ray powder diffraction patterns collected for samples $x = 0, 0.05, 0.1, 0.2$ and 0.3 were all single phase, with no impurities detected in any pattern. Synthesis of richer W⁶⁺ compositions beyond $x = 0.3$ were attempted. But when $x \geq 0.3$, significant W⁶⁺ impurities (BaWO₄) were present. Te⁶⁺ substitution for W⁶⁺ was also attempted from the Ba₂CuWO₆ side of the phase diagram. Even with low Te⁶⁺ concentrations where $x = 0.9$, two separate Ba₂CuTeO₆ and Ba₂CuWO₆ phases were observed. The phases remained immiscible after prolonged heating at 1100 °C and 1150 °C. Heating beyond 1150 °C was not possible because of tellurium evaporation. Therefore, the Ba₂CuTe_{1-x}W_xO₆ solid solution is narrower ($0 \leq x \leq 0.3$) than the Sr₂CuTe_{1-x}W_xO₆ ($0 \leq x \leq 1$). The difference in solubility is not surprising given Sr₂CuTeO₆ and Sr₂CuWO₆ belong to the same crystal class, whereas Ba₂CuTeO₆ (monoclinic ($C2/m$)) and Ba₂CuWO₆ (tetragonal ($I4/m$)) belong to different crystal classes.³²⁻³⁴ Although, it was surprising that Ba₂CuWO₆ completely rejected Te⁶⁺ doping given their near identical ionic radii (Te⁶⁺ (0.56 Å) and W⁶⁺ (0.6 Å)) and identical 6+ charge.³⁵ The explanation for this is discussed later.

The X-ray powder diffraction patterns of Ba₂CuTe_{1-x}W_xO₆ $x = 0, 0.05, 0.1, 0.2$ and 0.3 are well described using the monoclinic ($C2/m$) structural model showing the symmetry of the Ba₂CuTeO₆ structure is retained. The Rietveld plot for $x = 0.1$ is shown as an example in Fig. 4.4 to demonstrate the excellent agreement between the monoclinic model and experimental diffraction pattern. The inset in Fig. 4.4 shows the unit cell volume as a function of x in Ba₂CuTe_{1-x}W_xO₆. The lattice parameters decrease linearly with x in agreement with Vegard's Law. This demonstrates Te⁶⁺ was successfully substituted for W⁶⁺ between $x = 0$ to 0.3 .

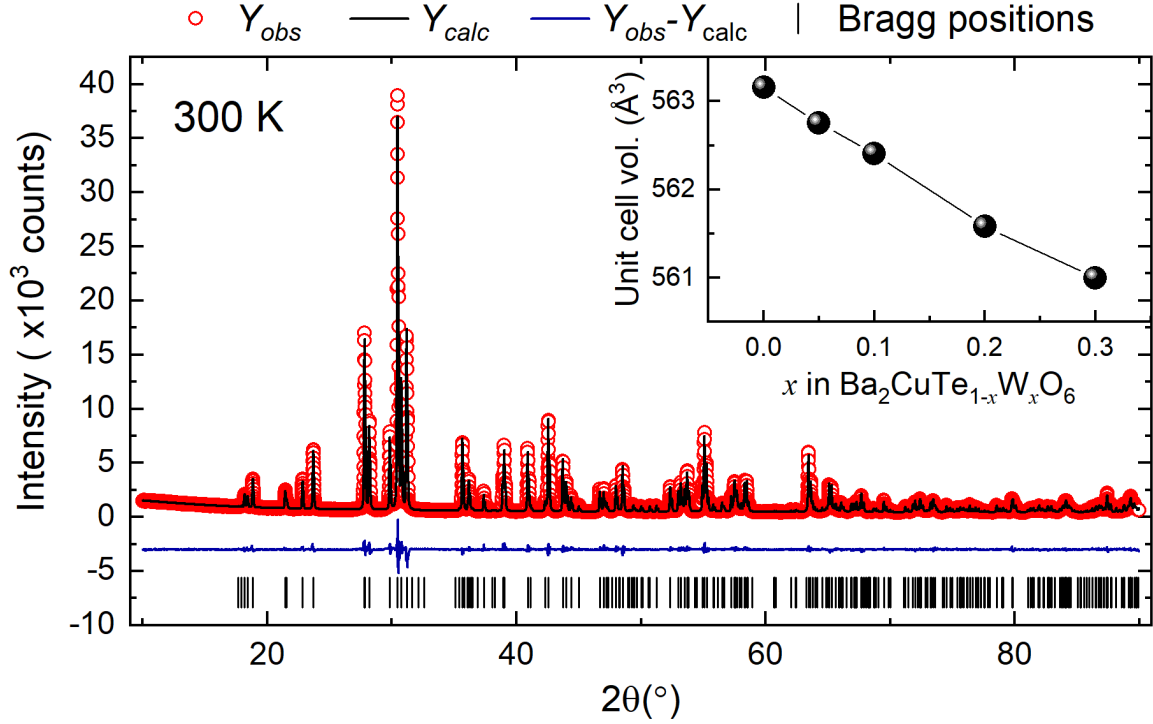


Fig. 4.4 The laboratory X-ray diffraction pattern of $x = 0.1$ recorded at 300 K using the Rigaku Miniflex diffractometer ($\text{Cu } K\alpha_1/K\alpha_2$ ($\lambda = 1.5405$ and 1.5443 \AA)). The inset shows a linear unit cell volume change as a function of x in $\text{Ba}_2\text{CuTe}_{1-x}\text{W}_x\text{O}_6$ across the $0 \leq x \leq 0.3$ solid solution.

b. Synchrotron X-ray diffraction

Synchrotron X-ray diffraction patterns were collected at 300 K for $x = 0.1, 0.2$ and 0.3 to determine the W^{6+} and Te^{6+} distribution across the $B''(\text{c})$ and $B''(\text{f})$ sites. There are three possible scenarios for W^{6+} substitution: 1) W^{6+} substitutes Te^{6+} exclusively on the $B''(\text{c})$ site; 2) W^{6+} substitutes Te^{6+} exclusively on the $B''(\text{f})$ site; and 3) Te^{6+} is substituted for W^{6+} on both the $B''(\text{c})$ and $B''(\text{f})$ sites. In model (3) W^{6+} was assumed to be equally distributed (50:50) across the two sites. The three site occupancy models were refined using the synchrotron diffraction data for each composition. The results of the Rietveld refinement are compared in Table 4.1.

Table 4.1: The final R_{wp} and χ^2 values obtained from refinement of the three different W^{6+} site occupancy models using the $x = 0.1, 0.2$ and 0.3 synchrotron X-ray diffraction data. Note, R_{wp} and χ^2 are consistently lowest for model (1).

R-values	Model (1) W^{6+} on $B''(\text{c})$ site	Model (2) W^{6+} on $B''(\text{f})$ site	Model (3) W^{6+} on $B''(\text{c})$ and $B''(\text{f})$ sites
R_{wp} (%) ($x = 0.1$)	1.54	2.03	1.65
χ^2 ($x = 0.1$)	3.42	5.86	3.88
R_{wp} (%) ($x = 0.2$)	1.76	3.10	2.07
χ^2 ($x = 0.2$)	4.58	14.29	6.35
R_{wp} (%) ($x = 0.3$)	2.65	4.81	3.14
χ^2 ($x = 0.3$)	10.69*	35.28	14.98

* The larger χ^2 for $x = 0.3$ reflects a longer counting time compared to the $x = 0.1$ and 0.2 samples.

The R_{wp} and χ^2 values in Table 4.1 are consistently lowest when model (1) is used to describe the crystal structure of $x = 0.1, 0.2$ and 0.3 . The example refinement for $x = 0.2$ in Fig. 4.5 shows model (1) reproduces the observed diffraction pattern very well. This reflects a strong preference for W^{6+} to occupy the corner-sharing $B''(c)$ site instead of the face-sharing $B''(f)$ site. The $B''(c)$ and $B''(f)$ site fractions of model (1) were refined within the stoichiometric constraints for each composition. The constraints ensured the total site-fraction (s.f.) of W^{6+} and Te^{6+} across the $B''(c)$ and $B''(f)$ sites did not exceed 1 (i.e. W^{6+} s.f. ($B''(c)$) + W^{6+} s.f. $B''(f)$ = 1 and Te^{6+} s.f. ($B''(c)$) + Te^{6+} s.f. $B''(f)$ = 1). Upon refinement, a small amount of W^{6+} shifted from the $B''(c)$ site to the $B''(f)$ site. Table 4.2 shows the W^{6+} site occupancy on the $B''(f)$ site increases linearly with x to a maximum value of $\sim 3\%$ for $x = 0.3$. By dividing the $B''(f)$ W^{6+} site occupancy by the total W^{6+} $B''(c)$ + $B''(f)$ site occupancy, it was possible to determine the percentage W^{6+} residing on the $B''(f)$ site in each composition. In $x = 0.1, 0.2$ and 0.3 , the majority $\sim 95\%$ of the total W^{6+} present in the composition resides on the $B''(c)$ site, while a minor $\sim 5\%$ resides on the $B''(f)$ site. The minor 5% occupancy of the $B''(f)$ site led to a slight, but noticeable improvement in the quality of the Rietveld fit. Comparing the R -values in Table 4.1 for model (1), when the site fractions were not refined, to those in Table 4.2, where the site fractions were refined, shows a slight reduction in the value of R_{wp} and χ^2 upon 5% occupation of the $B''(f)$ site. The strong site preference was confirmed by refining the site occupancies in model (2) where all the W^{6+} initially resides on the $B''(f)$ site. The refinement converged to the same result as when the model (1) site-occupancies were refined.

Table 4.2: The refined site occupancies for the $B''(c)$ and $B''(f)$ sites obtained when model (1) is refined using the $x = 0.1, 0.2$ and 0.3 synchrotron X-ray diffraction data. The percentage of W^{6+} in each composition residing on the $B''(f)$ site was calculated by dividing the W^{6+} $B''(f)$ site fraction by the total W^{6+} $B''(c)$ + $B''(f)$ site fraction. Also shown in the far column are the R -values obtained when the site occupancies are refined for the different compositions. Note, the improved $R_{wp}(\%)$ and χ^2 compared to with model (1) in Table 4.1.

	$B''(c)$		$B''(f)$		Percentage W^{6+} on $B''(f)$ site	R -values	
	Te(1)	W(1)	Te(2)	W(2)		R_{wp} (%)	χ^2
$x = 0.1$	0.809(1)	0.191(1)	0.991(1)	0.009(1)	4.5(2)%	1.54	3.39
$x = 0.2$	0.618(1)	0.382(1)	0.982(1)	0.018(1)	4.5(2)%	1.75	4.54
$x = 0.3$	0.430(1)	0.570(1)	0.970(1)	0.030(1)	5.0(2)%	2.60	10.50*

* The larger χ^2 for $x = 0.3$ reflects a longer counting time compared to the $x = 0.1$ and 0.2 samples.

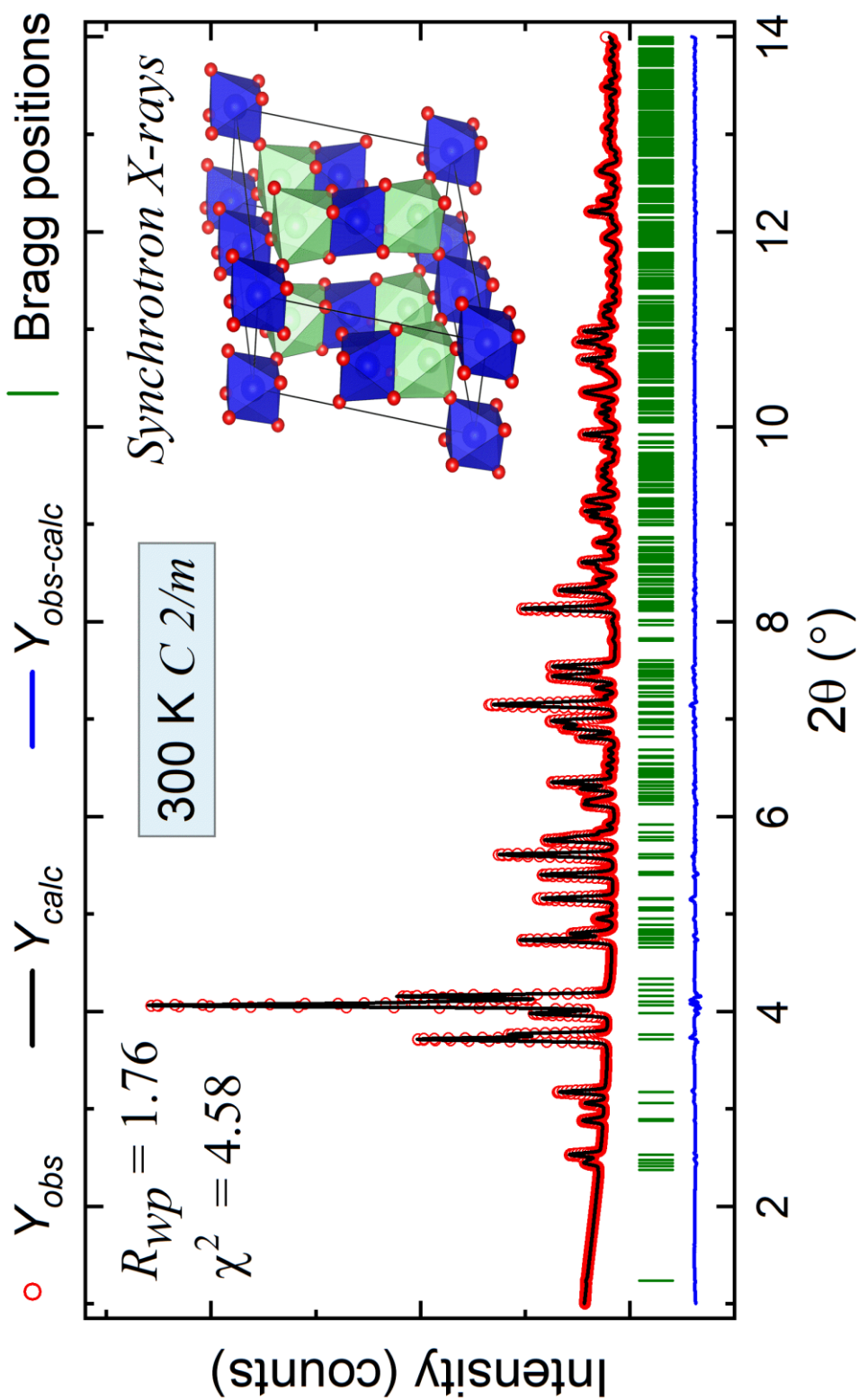


Fig. 4.5 Rietveld fit obtained for $Ba_2CuTe_{0.8}W_{0.2}O_6$ using the DESY synchrotron X-ray diffraction data collected using a X-ray wavelength of $\lambda = 0.20742 \text{ \AA}$ at 300 K. The refined structural model was model (1), where W^{6+} resided exclusively on the $B''(c)$ site. For this fit the $R_{wp} = 1.76 \%$ and $\chi^2 = 4.58$.

c. Extended X-ray Absorption Fine Structure (EXAFS)

The strong $B''(c)$ site preference was further investigated using Extended X-ray Absorption Fine Structure (EXAFS). Using the EXAFS data, it was possible to locally probe the W^{6+} environment within the $Ba_2CuTe_{0.7}W_{0.3}O_6$ structure. The EXAFS data collected for $x = 0.3$ was analysed using two site occupancy models: (1) W^{6+} fully substitutes Te^{6+} on the $B''(c)$ site; and (2) W^{6+} fully substitutes Te^{6+} on the $B''(f)$ site. Fully substituted models were used as the Artemis programme does not easily accommodate structural models with fractional site occupancies.

Fig. 4.6 compares the fits to the EXAFS data using (a) model (1) and (b) model (2). At low radial distances, models (1) and (2) describe the first shell $W^{6+}-O^{2+}$ scattering well and both provide a reasonable W-O bond distance of 1.900(7) Å and 1.90(15) Å, respectively. These are close to the average Te/W-O bond length on the $Te/W(1)O_6$ site (1.920(5) Å) determined from the 300 K neutron diffraction data. At radial distances beyond 2 Å, model (1) continues to provide a good description of the EXAFS data across the whole fitting range between $1.15 < R(\text{Å}) < 4.0$ in Fig. 4.6a. Table 4.3 shows the path lengths and Debye Waller factors for the fit in Fig. 4.6a are all reasonable and positive. Therefore, model (1) provides a plausible description of the W^{6+} environment. Conversely, the fit using model (2) fails to describe the second shell scattering well beyond 2 Å, with noticeable discrepancies between the fit and experimental data in Fig. 4.6b. Consequently, the R -factor for model (2) is significantly higher compared to model (1): R -factor = 1.18% (model (1)) vs R -factor = 9.07% (model (2)). Table 4.4 shows model (2) does not provide a plausible W^{6+} environment and has several paths with negative Debye-Waller factors. In good agreement with the synchrotron X-ray data, this supports dominant substitution for W^{6+} at the $B''(c)$ site.

Table 4.3: The refined parameters for model (1) where W^{6+} fully substitutes the $B''(c)$ site using the $Ba_2CuTe_{0.7}W_{0.3}O_6$ EXAFS data. The scattering paths were generated using the ATOMS algorithm in Artemis.³⁰ In the table, R is the refined path length of the specified path and σ^2 is the EXAFS Debye-Waller factor; N is the path degeneracy, which corresponds to the co-ordination number in the first shell. The global parameters are: S_0^2 , the passive electron reduction factor; the energy alignment factor, ΔE_0 ; the number of independent data points, according to the Nyquist criterion, N_{idp} ; and the number of variables in the model, N_{var} . The fit ranges were $3.0 < k < 11.0$, with a Hanning window of $dk = 1.0 \text{ Å}^{-1}$; and $1.15 < R < 4.0$.

Shell	Path	N	$R(\text{Å})$	$\sigma^2(\text{Å}^2)$	Global parameters
1	W(Te1)...O3.1 (single scattering)	6	1.900(7)	0.002(1)	$S_0^2 = 0.76(6)$ $\Delta E_0 = 7.3(1.0) \text{ eV}$ $N_{idp} = 14$ $N_{var} = 8$ $R(\%) = 1.18$
2	W(Te1)...O3.1...O4.1 (double scattering)	20	3.24(13)	0.003(2)	
2	W(Te1)...Ba2.1 (single scattering)	8	3.61(14)	0.007(3)	
2	W(Te1)...O3.1 (hinge)	24	3.80(15)	0.001(1)	
2	W(Te1)...O4.1 (forward though absorber)	4	3.82(15)	0.002(5)	
2	W(Te1)...O4.1...Cu1.1 (forward scattering)	8	3.85(15)	0.008(2)	
2	W(Te1)...O4.1...Cu1.1...O4.1 (double forward scattering)	4	3.85(15)	0.006(3)	

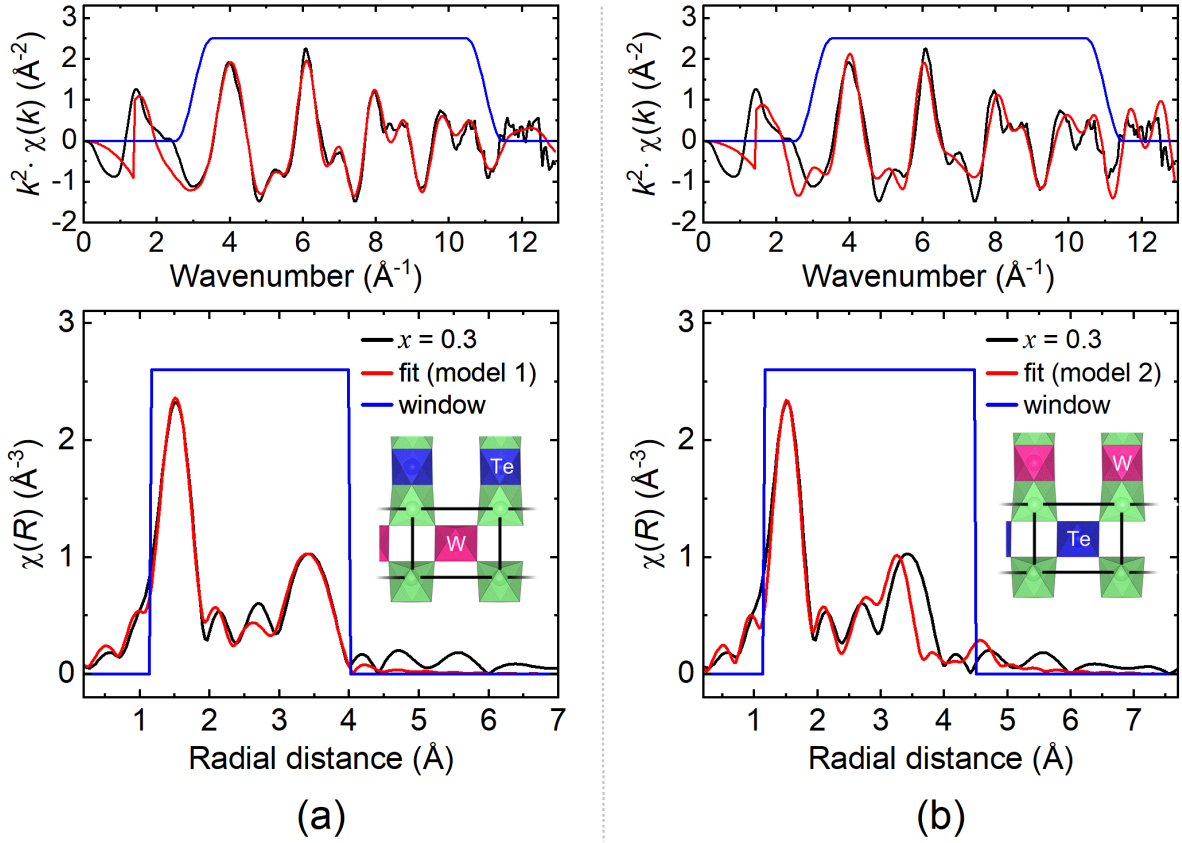


Fig. 4.6 Fits to the k -space and R -space $W L_3$ edge EXAFS data for $Ba_2CuTe_{0.7}W_{0.3}O_6$ using the two different structural models. The solid black lines represent the experimental data; the solid red lines represent the fit; and the solid blue lines are the fitting window. (a) The $k^2\chi(k)$ and $\chi(R)$ EXAFS data with model (1), where W^{6+} is placed on the $B''(c)$ site. (b) The $k^2\chi(k)$ and $\chi(R)$ EXAFS data with model (2) where W^{6+} is oppositely placed on the $B''(f)$ site. Sections of the crystal structure depicting the different structural models are shown in the $\chi(R)$ vs radial distance plots. Here, W^{6+} is pink, Te^{6+} blue and the Cu^{2+} spin ladder cations are green.

Attempts were made to capture the 5% occupancy of the $B''(f)$ site suggested by the synchrotron X-ray data. This involved employing a linear constraint to fit the EXAFS data using contributions from model (1) and model (2). However, the minor occupation of the $B''(f)$ site meant it was not possible to stabilise the fit and the number of variables approached the number of data points. Closely examining the fits suggests signatures of W^{6+} occupation of the $B''(f)$ site are captured in the data. Comparing the fits in the range $2.0 < R < 3.0$ shows there is a slight intensity mismatch between the fit and experimental data in model (1) about the peaks at ~ 2.1 and ~ 2.7 Å in Fig. 4.6a. Conversely, these same peaks are described quite well by model (2) in Fig. 4.6b. This suggests the slight intensity mismatch observed between $2.0 < R < 3.0$ in the fit for model (1) represents the contribution from the $B''(f)$ site which could not be stabilized in the fit.

Table 4.4: The refined parameters for model (2) where W^{6+} fully substitutes the $B''(f)$ site using the $Ba_2CuTe_{0.7}W_{0.3}O_6$ EXAFS data. The scattering paths were generated using the ATOMS algorithm in Artemis.³⁰ In the table, R is the refined path length of the specified path and σ^2 is the EXAFS Debye-Waller factor; N is the path degeneracy, which corresponds to the co-ordination number in the first shell. The global parameters are: S_0^2 , the passive electron reduction factor; the energy alignment factor, ΔE_0 ; the number of independent data points, according to the Nyquist criterion, N_{idp} ; and the number of variables in the model, N_{var} . The fitted ranges were $3.0 < k < 11.0$, with a Hanning window of $dk = 1.0 \text{ \AA}^{-1}$; and $1.15 < R < 4.5$.

Shell	Path	N	$R(\text{\AA})$	$\sigma^2(\text{\AA}^2)$	Global parameters
1	W(Te1)...O1.1 (single scattering)	6	1.90(15)	-0.0004(25)	$S_0^2 = 0.62(13)$ $\Delta E_0 = 7.6(2.3) \text{ eV}$ $N_{idp} = 14$ $N_{var} = 8$ $R(\%) = 9.07$
2	W(Te1)...Cu1.1 (double scattering)	2	2.69(21)	0.03(10)	
2	W(Te1)...O1.1...O2.1 (double scattering)	16	3.24(26)	-0.006(12)	
2	W(Te1)...Ba1.1 (single scattering)	4	3.45(27)	0.03(0.16)	
2	W(Te1)...O1.1 (forward though absorber)	6	3.80(30)	-0.012(3)	
2	W(Te1)...O2.1...Ba2.2 (non-forward linear)	8	4.69(37)	0.008(0.012)	

d. Neutron diffraction

Variable temperature neutron diffraction experiments were performed to investigate structural changes on cooling. A clear picture of the low temperature structure is important in low dimensional systems, where unusual magnetic behaviour often occurs due to the weaker magnetic interactions. Given the similar neutron scattering lengths of W^{6+} and Te^{6+} , it was not possible to determine the $B'''(c)$ and $B''(f)$ site occupancies using neutrons. Ion migration becomes less energetically favourable on cooling making it highly unlikely for there to be any site-occupancy changes between 300 to 2 K. Therefore, it was accurate to use the site occupancies determined from the 300 K synchrotron X-ray data to analyse the low temperature neutron diffraction data.

Variable temperature neutron diffraction – structural transition on cooling

Variable temperature neutron diffraction patterns were collected for the $x = 0.1$ and 0.3 samples between 300 to 2 K. The 300 K structural models from the synchrotron X-ray diffraction data were used as the initial models. The data were sequentially refined on cooling from 300 to 2 K. For both the $x = 0.1$ and 0.3 data, a point was reached where the $C2/m$ model failed to describe the observed powder pattern. The rise in the R_{wp} and χ^2 values below 240 K ($x = 0.1$) and 120 K ($x = 0.3$) can be seen in plots (c) and (d) in Fig. 4.7. Below these temperatures, the powder pattern is better described using triclinic symmetry. The triclinic $P\bar{1}$ space group provided a significantly improved fit for the low temperature crystal structure as seen in the Rietveld fits for $x = 0.3$ at (a) 1.44 K ($P\bar{1}$) and (b) 300 K ($C2/m$) in Fig. 4.8. The refined low temperature (~ 2 K) $C2/m$ and high temperature (300 K) $P\bar{1}$ structures for $x = 0.1$ and $x = 0.3$ are presented in Tables 4.5-4.8.

The same $C2/m$ to $P\bar{1}$ transition is observed for Ba_2CuTeO_6 close to room temperature at 287 K. The transition to lower symmetry can also be observed from the introduction of additional reflections in the powder diffraction patterns on cooling. The waterfall plots in Fig. 4.7a and Fig. 4.7b show the evolution of peak splitting with temperature. This places the structural transition between 235-240 K for $x = 0.1$ and 100-120 K for $x = 0.3$. The reduction in the structural transition temperature (T_{trans}) with larger x is a result of the increasing cation disorder introduced by W^{6+} substitution. It is expected T_{trans} will be reduced in the $x = 0.05$ and 0.2 samples and follow a decreasing trend across the solution as W^{6+} doping (and hence cation disorder) increases.

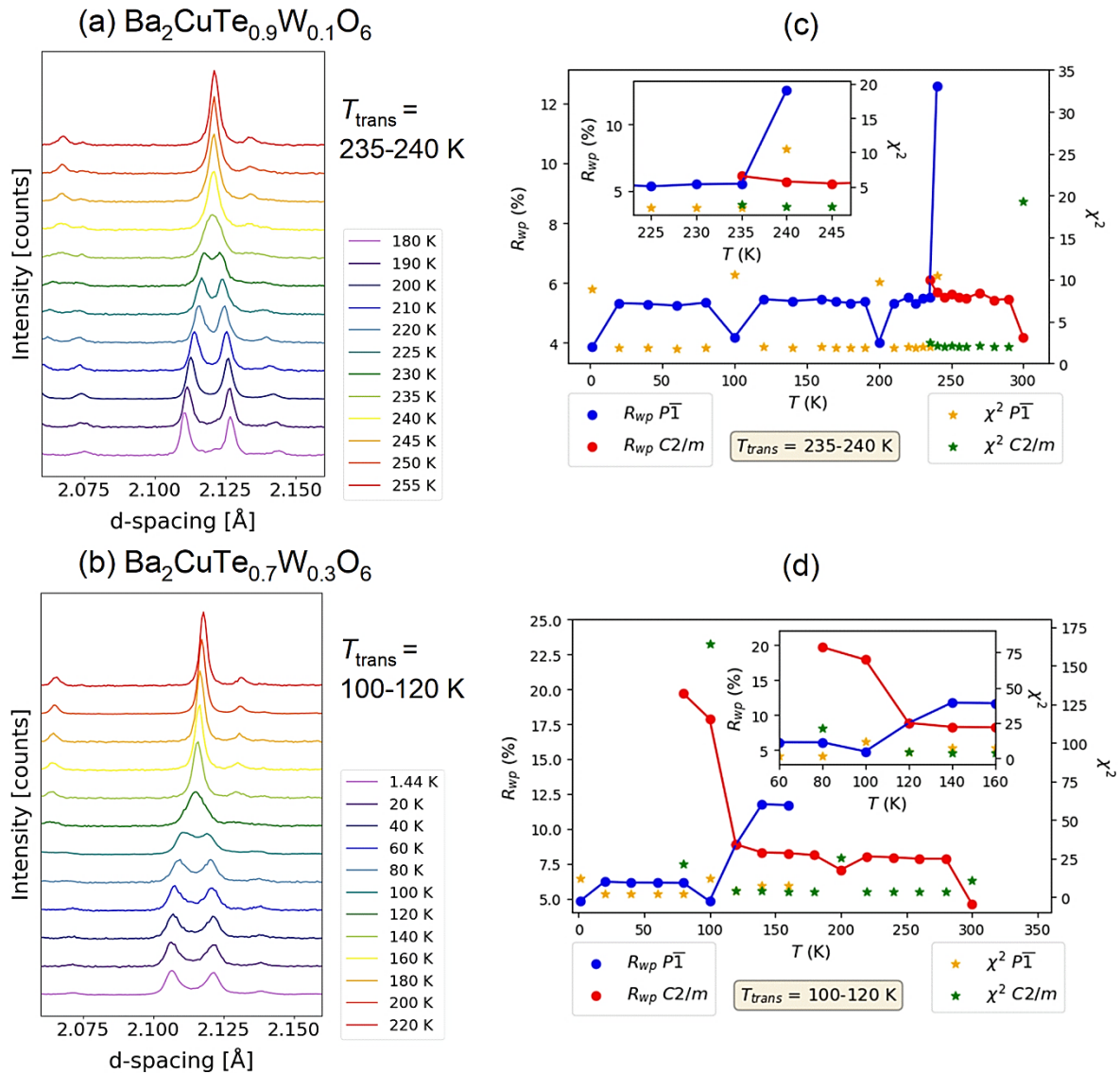


Fig. 4.7 Monoclinic to triclinic distortion in the variable temperature HRPD data of $x = 0.1$ and $x = 0.3$. (a) and (b) are waterfall plots showing the evolution of peak splitting for $Ba_2CuTe_{0.9}W_{0.1}O_6$ and $Ba_2CuTe_{0.7}W_{0.3}O_6$, respectively. (c) R_{wp} and χ^2 as a function of temperature, T , for $Ba_2CuTe_{0.9}W_{0.1}O_6$. (d) R_{wp} and χ^2 as a function of T for $Ba_2CuTe_{0.7}W_{0.3}O_6$. The position of T_{trans} is determined from the point at which the R_{wp} and χ^2 values for the $C2/m$ model increase, after which the $P\bar{1}$ model becomes a better description of the crystal structure. The low R_{wp} and χ^2 values for the 2 K, 100 K, 200 K and 300 K data in plots (c) and (d) represents the longer counting time used for these datasets.

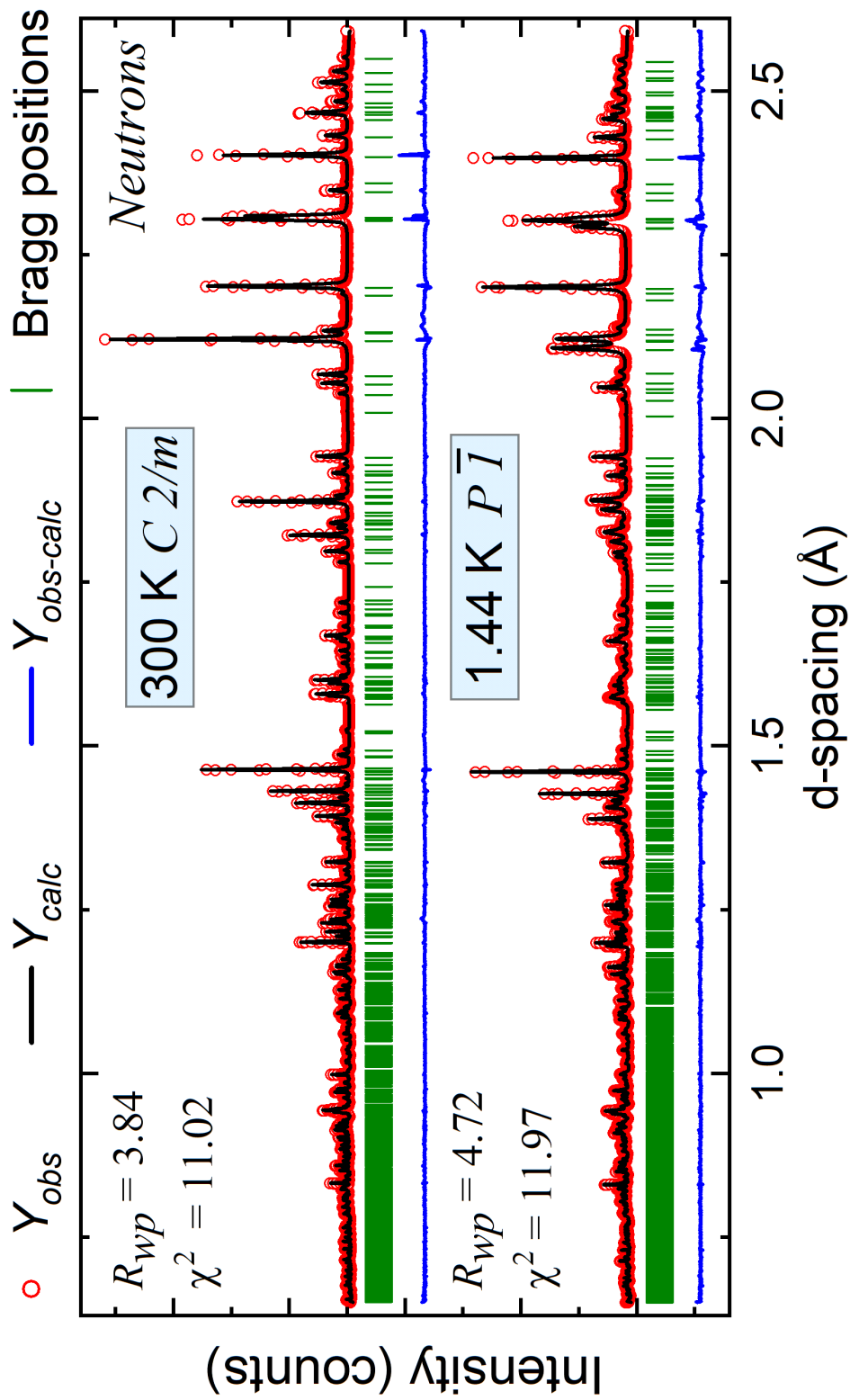


Fig. 4.8 Rietveld fits of the $Ba_2CuTe_{0.7}W_{0.3}O_6$ structure using the $P\bar{1}$ structural model for the 1.44 K HRPD data and the $C2/m$ structural model for the 300 K HRPD data.

Table 4.5: The refined $C2/m$ crystal structure of $Ba_2CuTe_{0.9}W_{0.1}O_6$ at 300 K.

Space Group: $C2/m$, No. 12, 300 K						
R_p (%) = 3.10, R_{wp} (%) = 3.85, R_{exp} (%) = 1.22, χ^2 = 19.10, var. 86						
a = 10.2278(2) Å, b = 5.72160(4) Å, c = 10.0958(2) Å, β = 107.9556(5)°						
Vol. = 562.03(1) Å ³						
Site	Wyckoff Position	x	y	z	Site fraction	Uiso (Å ²)
Ba1	4i	0.12823(18)	0	0.37994(18)	1.0	0.00553(46)
Ba2	4i	0.28256(19)	0	0.84900(18)	1.0	0.01041(50)
Te1	2a	0	0	0	0.809*	0.00704(57)
W1	2a	0	0	0	0.191*	0.00704(57)
Te2	2d	0	0.5	0.5	0.991*	0.00761(56)
W2	2d	0	0.5	0.5	0.009*	0.00761(56)
Cu1	4i	0.90579(13)	0.5	0.21445(11)	1.0	0.00981(41)
O1	4i	0.13295(17)	0.5	0.40048(18)	1.0	0.01445(50)
O2	8j	0.89497(11)	0.72871(21)	0.36907(11)	1.0	0.01020(36)
O3	4i	0.31753(19)	0.5	0.87535(19)	1.0	0.01884(54)
O4	8j	0.04970(14)	0.76066(27)	0.88914(13)	1.0	0.01698(40)

* $B''(c)$ and $B''(f)$ site fractions determined from synchrotron X-ray diffraction data.

Table 4.6: The refined $P\bar{1}$ crystal structure of $Ba_2CuTe_{0.9}W_{0.1}O_6$ at 1.55 K.

Space Group: $P\bar{1}$, No. 2, 1.44 K						
R_p (%) = 3.45, R_{wp} (%) = 3.97%, R_{exp} (%) = 1.66%, χ^2 = 8.94, 111 var.						
a = 5.7065(2) Å, b = 5.8490(2) Å, c = 10.2555(7) Å						
α = 108.464(1)°, β = 107.0747(8)°, γ = 60.7373(3)°						
Vol. = 279.233(5) Å ³						
Site	Wyckoff Position	x	y	z	Site fraction	Uiso (Å ²)
Ba1	2i	0.13093(40)	0.12213(35)	0.38101(19)	1.0	0.00192(32)
Ba2	2i	0.27722(40)	0.28124(34)	0.85036(18)	1.0	0.0019
Te1	1a	0	0	0	0.809*	0.00403(53)
W1	1a	0	0	0	0.191*	0.00403
Te2	1h	0.5	0.5	0.5	0.991*	0.00388(56)
W2	1h	0.5	0.5	0.5	0.009*	0.00388(56)
Cu1	2i	0.41345(26)	0.40522(25)	0.21466(12)	1.0	0.0055(38)
O1	2i	0.62858(35)	0.58280(40)	0.37455(17)	1.0	0.00619(47)
O2	2i	0.16934(33)	0.57361(38)	0.36287(19)	1.0	0.00551(45)
O3	2i	0.35992(37)	0.86776(31)	0.59887(18)	1.0	0.00793(48)
O4	2i	0.79881(42)	0.78944(41)	0.90323(18)	1.0	0.00710(44)
O5	2i	0.26919(41)	0.78131(40)	0.87853(19)	1.0	0.00631(49)
O6	2i	0.20133(42)	0.76452(33)	0.12686(18)	1.0	0.00790(48)

* $B''(c)$ and $B''(f)$ site fractions determined from synchrotron X-ray diffraction data.

Table 4.7: The refined $C2/m$ crystal structure of $Ba_2CuTe_{0.7}W_{0.3}O_6$ at 300 K.

Space Group: $C2/m$, No. 12, 300 K						
$R_p = 3.35\%$, $R_{wp} = 3.84\%$, $R_{exp} = 1.74\%$, $\chi^2 = 11.02$, var. 86						
$a = 10.2118(3) \text{ \AA}$, $b = 5.71745(5) \text{ \AA}$, $c = 10.0866(3) \text{ \AA}$, $\beta = 107.9193(6)^\circ$						
Vol. = $560.35(1) \text{ \AA}^3$						
Site	Wyckoff Position	x	y	z	Site fraction	Uiso (Å^2)
Ba1	4i	0.12841(23)	0	0.38015(22)	1.0	0.00394(55)
Ba2	4i	0.28318(25)	0	0.84944(23)	1.0	0.01013(63)
Te1	2a	0	0	0	0.43*	0.00850(75)
W1	2a	0	0	0	0.57*	0.00850(75)
Te2	2d	0	0.5	0.5	0.97*	0.00865(70)
W2	2d	0	0.5	0.5	0.03*	0.00865(70)
Cu1	4i	0.90545(17)	0.5	0.21486(14)	1.0	0.01123(51)
O1	4i	0.13336(23)	0.5	0.39967(23)	1.0	0.01726(64)
O2	8j	0.89457(14)	0.72904(27)	0.36959(14)	1.0	0.01200(45)
O3	4i	0.31705(24)	0.5	0.87607(23)	1.0	0.01712(65)
O4	8j	0.04946(17)	0.76007(34)	0.88959(16)	1.0	0.01577(48)

* $B''(c)$ and $B''(f)$ site fractions determined from synchrotron X-ray diffraction data.

Table 4.8: The refined $P\bar{1}$ crystal structure of $Ba_2CuTe_{0.7}W_{0.3}O_6$ at 1.44 K.

Space Group: $P\bar{1}$, No. 2, 1.44 K						
$R_p = 4.18\%$, $R_{wp} = 4.72\%$, $R_{exp} = 1.75\%$, $\chi^2 = 11.97$, 111 var.						
$a = 5.7008(4) \text{ \AA}$, $b = 5.8402(5) \text{ \AA}$, $c = 10.223(1) \text{ \AA}$						
$\alpha = 108.250(2)^\circ$, $\beta = 106.693(2)^\circ$, $\gamma = 60.7631(6)^\circ$						
Vol. = $278.328(9) \text{ \AA}^3$						
Site	Wyckoff Position	x	y	z	Site fraction	Uiso (Å^2)
Ba1	2i	0.13036(72)	0.12442(51)	0.38204(29)	1.0	0.00091(45)
Ba2	2i	0.28212(74)	0.28020(49)	0.85115(27)	1.0	0.00091(45)
Te1	1a	0	0	0	0.43*	0.00363(78)
W1	1a	0	0	0	0.57*	0.00363(78)
Te2	1h	0.5	0.5	0.5	0.97*	0.00354(79)
W2	1h	0.5	0.5	0.5	0.03*	0.00354(79)
Cu1	2i	0.40939(45)	0.4028(38)	0.21492(18)	1.0	0.00605(54)
O1	2i	0.62719(60)	0.58563(71)	0.37253(29)	1.0	0.00537(76)
O2	2i	0.16580(58)	0.57569(67)	0.36446(31)	1.0	0.00490(73)
O3	2i	0.36352(71)	0.86942(46)	0.59997(28)	1.0	0.01037(70)
O4	2i	0.80705(75)	0.78764(76)	0.89856(34)	1.0	0.00751(74)
O5	2i	0.28312(74)	0.78123(74)	0.88446(36)	1.0	0.00682(79)
O6	2i	0.19415(73)	0.76774(51)	0.12851(27)	1.0	0.00822(73)

* $B''(c)$ and $B''(f)$ site fractions determined from synchrotron X-ray diffraction data.

Jahn-Teller distortion

The transition from $C2/m$ to $P\bar{1}$ symmetry arises from enhanced Jahn-Teller (J-T) distortion of the CuO_6 octahedra on cooling. J-T distortion was measured empirically as a function of temperature (T) using the J-T distortion parameter (σ_{JT}):³⁶

$$\sigma_{JT} = \sqrt{\frac{1}{6} \sum_i [(B - O)_i - \langle B - O \rangle]^2} \quad (4.1)$$

σ_{JT} is calculated by averaging the sum of the difference between each of the six individual Cu-O bond lengths ($(B - O)_i$) on the i -Cu(1) O_6 site and the mean Cu-O bond length ($\langle B - O \rangle$). σ_{JT} is plotted as a function of temperature (T) in Fig. 4.9. As expected, σ_{JT} is non-zero and large at 300 K. The CuO_6 octahedra display the classic axial J-T distortion with two of the Cu-O bonds elongated in the direction of the d_{z^2} orbital. Uncharacteristically, elongation is uneven with the Cu-O(1) bond extending further than the Cu-O(6) bond to accommodate both corner- and face-sharing with the connecting TeO_6 octahedra. The equatorial bond lengths are approximately equal at all temperatures between 2-300 K.

The plot of σ_{JT} vs T shows as the temperature decreases, distortion gradually increases in both $x = 0.1$ and $x = 0.3$, until reaching a plateau at 100 K. This indicates both structures possess the same distortion limit. There are no large discontinuities about T_{trans} . This reflects a weak structural transition, with no major changes in bond length or angle. The $C2/m$ to $P\bar{1}$ transition in $\text{Ba}_2\text{CuTeO}_6$ has also been identified as weak with only minor changes in bond angles and bond lengths.

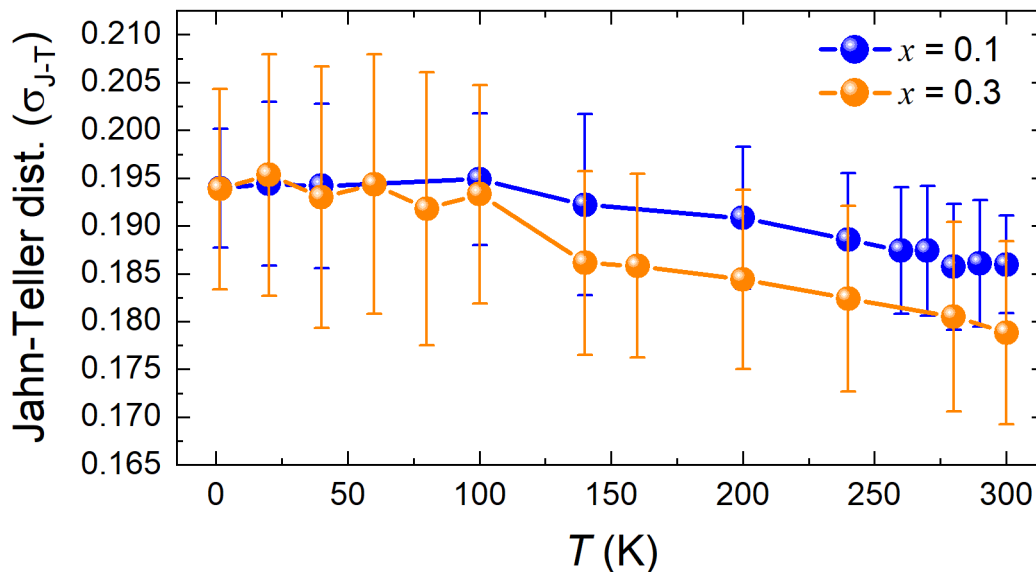


Fig. 4.9 The Jahn-Teller distortion parameter, σ_{JT} , as a function of temperature for $\text{Ba}_2\text{CuTe}_{0.1}\text{W}_{0.9}\text{O}_6$ ($x = 0.1$) and $\text{Ba}_2\text{CuTe}_{0.3}\text{W}_{0.7}\text{O}_6$ ($x = 0.3$). σ_{JT} was calculated using the Cu-O bond lengths determined from the neutron diffraction data.

The weak $C2/m$ to $P\bar{1}$ transition means the spin ladder structure is retained upon the transition to lower symmetry. Fig. 4.10 compares the high temperature monoclinic and low temperature triclinic unit cells. Enhanced J-T distortion of the CuO_6 octahedra is noticeable in the low temperature triclinic structure. But, the 12R stacking sequence remains the same. The Cu^{2+} cations still communicate via $B'-\text{O}-B''-\text{O}-B'$ superexchange via the $B''(\text{c})$ and $B''(\text{f})$ octahedra as they do in the monoclinic unit cells forming the intra- and inter-ladder interactions depicted by the arrows in Fig.

4.10. The monoclinic and triclinic unit cells can therefore be regarded as almost the same. The close structural similarity is advantageous as it allows the low temperature $\text{Ba}_2\text{CuTeO}_6$ magnetic interactions to be modelled within the monoclinic unit cell, greatly simplifying calculations.³⁷

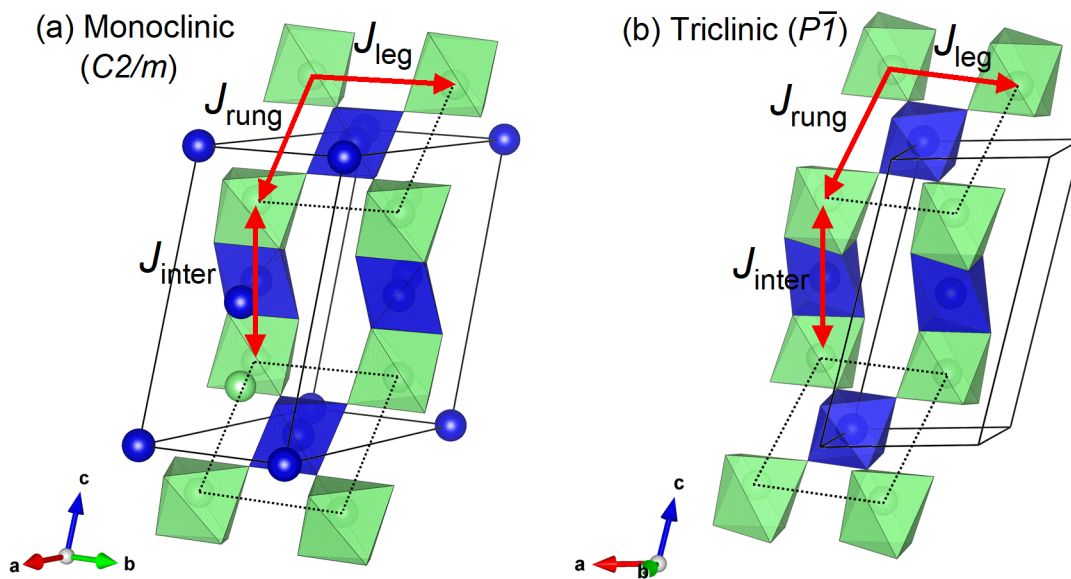


Fig. 4.10 The Cu^{2+} spin ladder structure in (a) the high temperature monoclinic unit cell and (b) the low temperature triclinic unit cell. Comparing (a) and (b) shows the spin ladder geometry remains unchanged upon the transition to lower symmetry. The main difference is increased distortion of the CuO_6 octahedra on cooling, which is notable when comparing the shape of the CuO_6 octahedra (shown in green) in the (a) and (b) structures.

It is notable in the σ_{JT} vs T plot in Fig. 4.9 that the CuO_6 octahedra are less distorted in the $x = 0.3$ structure compared to in the $x = 0.1$. The σ_{JT} values for $x = 0.3$ are consistently lower in the monoclinic phase. The individual Cu-O bond lengths agree with this observation. There is less elongation of the axial Cu-O bonds and an overall smaller variance in the Cu-O bond lengths on the i - $\text{Cu}(1)\text{O}_6$ site in $x = 0.3$. The almost identical Te^{6+} and W^{6+} cation size makes differences in metal oxygen bonding involving d^{10} versus d^0 cations the most probable cause. The filled d^{10} orbitals of Te^{6+} are likely to promote a more covalent bonding nature leading to improved orbital overlap and enhanced J-T distortion. Conversely, empty d^0 orbitals promote ionic bonding due to the greater d -orbital contribution. This reduces J-T distortion by diluting the covalent bonding nature as more Te^{6+} is substituted for W^{6+} with increasing x . While noticeable, the difference in σ_{JT} is small and there are reasonably large errors associated with the σ_{JT} values. Hence, except for the different structural transition temperatures, it is accurate to assume a minor difference between the $x = 0.3$ and $x = 0.1$ structures.

Lattice parameters and unit cell volume

The unit cell volumes (V_{cell}) within the high temperature $C2/m$ and low temperature $P\bar{1}$ structures are plotted as a function of temperature (T) in Fig. 4.11. V_{cell} is linear within the $C2/m$ structure (see Fig. 4.11a and Fig. 4.11b). This occurs due to linear reduction of the a , b , c and β lattice parameters as the temperature decreases. The $C2/m$ lattice parameters are plotted for $x = 0.1$ and $x = 0.3$ in appendix Fig. A4.1 and A4.2. Conversely, the unit cell volume change within the $P\bar{1}$ phase is non-linear. Below T_{trans} , V_{cell} increasingly deviates from linear behaviour (see Fig 4.11c and Fig. 4.11d). The lattice parameters also behave non-linearly. Instead of decreasing, c , α , and β increased on cooling to 2 K. The low temperature unit cell behaviour is the same for $x = 0.1$ and $x = 0.3$.

Therefore, only the $P\bar{1}$ lattice parameters for $x = 0.1$ are shown as an example in Fig. 4.12. The $P\bar{1}$ lattice parameters for $x = 0.3$ are shown in appendix Fig. A4.3.

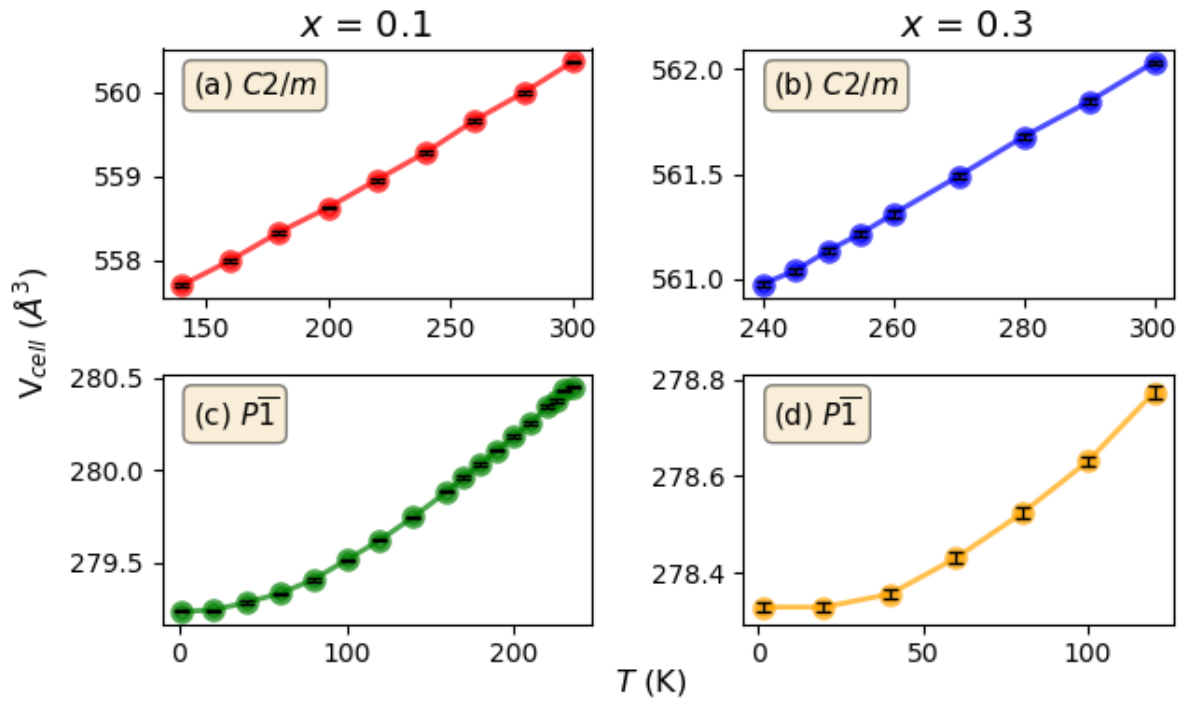


Fig. 4.11 The unit cell volumes V_{cell} as a function of temperature in the high temperature $C2/m$ and low temperature $P\bar{1}$ structures of $\text{Ba}_2\text{CuTe}_{0.1}\text{W}_{0.9}\text{O}_6$ ($x = 0.1$) and $\text{Ba}_2\text{CuTe}_{0.3}\text{W}_{0.7}\text{O}_6$ ($x = 0.3$). Plots (a) and (c) show the unit cell volume change for $x = 0.1$ in the $C2/m$ and $P\bar{1}$ structure, respectively. Plots (b) and (d) show the unit cell volume change for $x = 0.3$ in the $C2/m$ and $P\bar{1}$ structure, respectively.

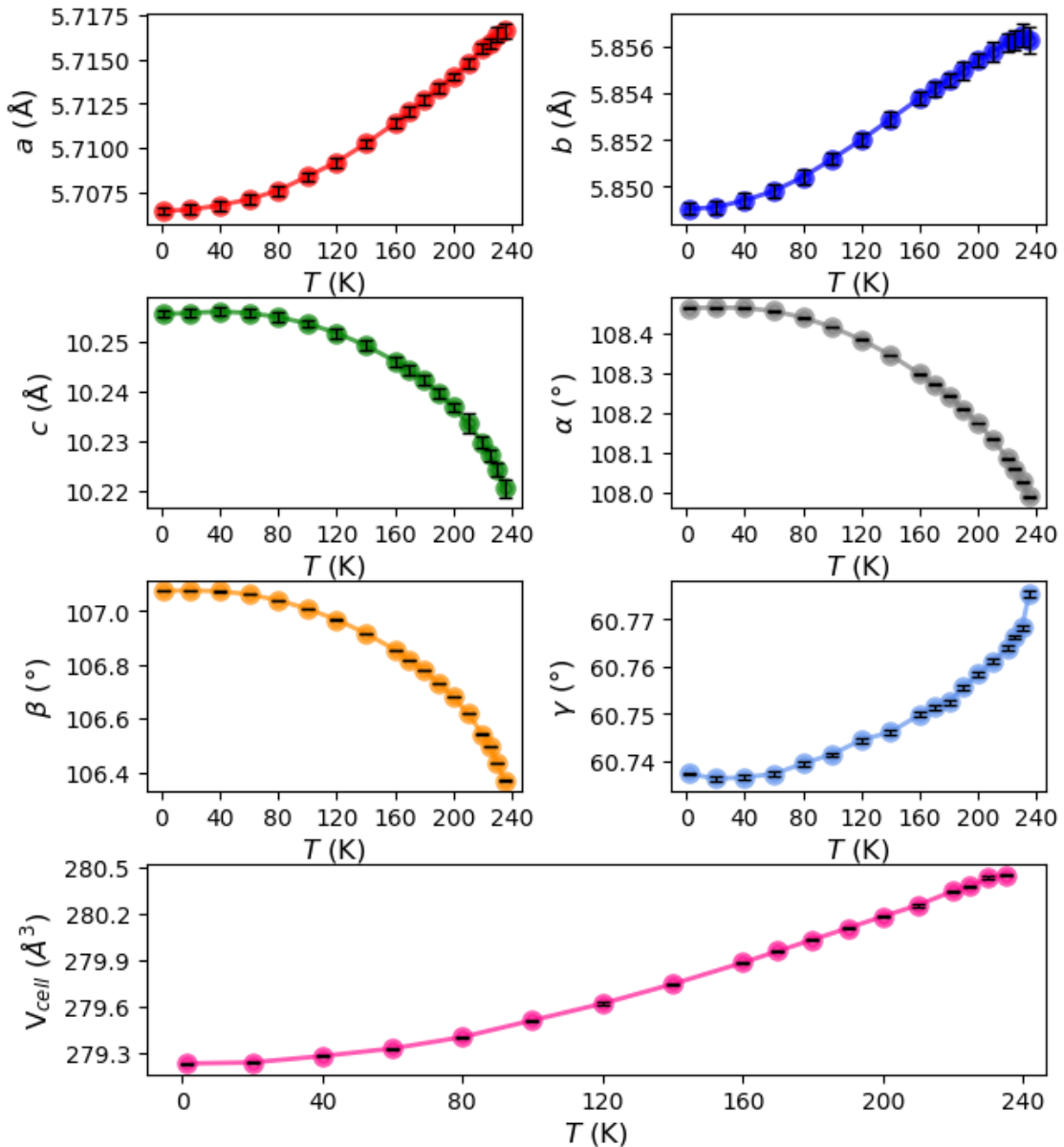


Fig. 4.12 The lattice parameters as a function of temperature (T) within the low temperature triclinic $P\bar{1}$ unit cell of $Ba_2CuTe_{0.1}W_{0.9}O_6$ ($x = 0.1$). The resulting non-linear unit cell volume (V_{cell}) change is shown in the bottom panel.

The non-linear unit cell volume change in the $P\bar{1}$ structure arises due to hexagonal stacking. As illustrated in Fig. 4.10, 12R hexagonal stacking is identical in the $P\bar{1}$ and $C2/m$ structures. In both structures, the face-sharing $\text{Cu}-B''(\text{f})-\text{Cu}$ trimers are aligned along the c -axis and are bridged by TeO_6 octahedra. Plotting the $\text{Cu}-B''(\text{f})$ distance in the trimer as a function of temperatures reveals there is very little change in the overall length of the $\text{Cu}-B''(\text{f})-\text{Cu}$ trimer with temperature (see Appendix Fig. A4.4 and A4.5). Face-sharing places the positively charged Cu^{2+} and Te^{6+} cations in close proximity. Further reducing the $\text{Cu}-B''(\text{f})$ trimer distance brings the positive cations even closer. This is electrostatically unfavourable so the $\text{Cu}-B''(\text{f})-\text{Cu}$ distance resists reduction along c . Instead, the a and b unit cell lengths are reduced by decreasing the $B''(\text{c})-\text{O}-\text{Cu}$ angles within the corner-sharing linkers (see Appendix Fig. A4.6 ($x = 0.1$) and Fig. A4.7 ($x = 0.3$)). The $B''(\text{c})-\text{O}-\text{Cu}$ bond angles do not alter by the same amount, with the $B''(\text{c})-\text{O}(4, 5)-\text{Cu}$ angles decreasing more than the $B''(\text{c})-\text{O}(6)-\text{Cu}$ angle. This reduces γ but increases β and α as the temperature lowers. This can be viewed as pushing the ab planes at the top and bottom of the unit cell up and down, respectively. While this

occurs, the unit cell is expanded along c . The net effect is still a decrease in V_{cell} with reduced T . But the decrease in V_{cell} is non-linear due to the competition between reduction of the unit cell along a and b versus expansion along c .

5. Discussion

Using a combination of structural techniques, site-selective W^{6+} substitution for Te^{6+} in Ba_2CuTeO_6 was identified in the $Ba_2CuTe_{1-x}W_xO_6$ $0 \leq x \leq 0.3$ solid solution. In both the synchrotron X-ray diffraction and neutron diffraction data, the structural model providing the best description of the experimental data was the one in which W^{6+} resides almost exclusively on the corner-sharing $B''(c)$ site. Specifically, only 5% of the total W^{6+} in each composition resided on the face-sharing $B''(f)$ site in the $x = 0.1, 0.2$ and 0.3 samples, while the remaining 95% resided on the $B''(c)$ site. The EXAFS data agreed with the diffraction results. A plausible fit to the EXAFS data was only obtained when the model place W^{6+} on the $B''(c)$ site.

The strong preference for W^{6+} substitution at the $B''(c)$ site initially appears surprising. W^{6+} and Te^{6+} have the same charge and near-identical ionic radii: Te^{6+} (0.56 Å) and W^{6+} (0.6 Å).³⁵ As a result, the Goldschmidt tolerance factors (t) for Ba_2CuTeO_6 and Ba_2CuWO_6 are almost identical: $t = 1.04$ (Ba_2CuTeO_6) and $t = 1.03$ (Ba_2CuWO_6). There are only small changes in the bond lengths and bond angles upon W^{6+} substitution that lead to minor differences in J-T distortion between $x = 0.1$ and $x = 0.3$. The only major difference is the reduction of the monoclinic to triclinic distortion temperature. The position of T_{trans} is reduced from 287 K ($x = 0$) to 100-120 K ($x = 0.3$) due to the increasing B'' cation disorder. Based on this knowledge, it might be expected that W^{6+} and Te^{6+} would be randomly distributed across the $B''(c)$ and $B''(f)$ sites.

The strong site preference can only be explained by considering structural influences other than ionic radii. Reviews of perovskite structures have found W^{6+} and $Mo^{6+}(d^0)$ containing perovskites exclusively form double perovskite structures.³⁸ Whereas, $Te^{6+}(d^{10})$ containing perovskites can also form hexagonal perovskites.³⁸ The inability for W^{6+} and Mo^{6+} perovskites to form hexagonal structures stems from differences in metal-oxygen ($M-O$) bonding involving d^{10} vs d^0 cations.

$M-O$ bonding in isolated TeO_6 octahedra relies on a significant p^0 orbital contribution as a result of the filled $4d^{10}$ orbital. The Te^{6+} p^0 orbitals overlap with the oxygen $2p$ forming $Te-O$ bonds through a σ -bonding interaction. σ -bonding directs the electron density towards the oxide anions and away from the surface of the $[TeO_6]^{6-}$ octahedra.³⁸ Directional $Te-O$ bonding helps to minimize repulsion between Te^{6+} and the neighbouring similarly charged cations. This allows Te^{6+} to accommodate close cation-cation distances, such as the face-sharing sites in hexagonal perovskites. The converse is true for W^{6+} and Mo^{6+} perovskites. W^{6+} and Mo^{6+} both have empty d -orbitals to contribute to $M-O$ bonding. The dominant d^0 contribution to $M-O$ bonding generates σ - and π -bonding interactions. As a result, $M-O$ bonding is less directional and the $[W/MoO_6]^{6-}$ units are highly regular with a spherical charge distribution.³⁹ The $[W/MoO_6]^{6-}$ octahedra prefer to maximize their distance from identically charged neighbouring cations. W^{6+} and Mo^{6+} only assume corner-sharing sites, where the cation-cation distances are greater than at face-sharing sites. Therefore, W^{6+} and Mo^{6+} are unable to form hexagonal structures, but Te^{6+} can adopt either the double or hexagonal perovskite structures.

The strong dislike for W^{6+} to occupy face-sharing sites explains why the majority of W^{6+} resides on the $B''(c)$ site in $Ba_2CuTe_{1-x}W_xO_6$. The Cu^{2+} - B''^{6+} cation distance is significantly smaller within the face-sharing $Cu-B''(f)$ - Te trimer compared to within the corner-sharing $Cu-B''(c)$ - Cu linkers. For example, the $B''(c)$ - Cu^{2+} distance is 3.962(2) Å and the $B''(f)$ - Cu^{2+} distance is 2.738(1) Å in the $x = 0.3$ structure at 300 K. Similar B''^{6+} - Cu^{2+} cation distances are observed in the $x = 0.1$ structure. The

difference between the cation-cation distances at the $B''(c)$ and $B''(f)$ sites is the same in the triclinic structure. Hence, the strong site-selectivity is observed at all temperatures from 300 to 2 K, irrespective of the structural transition. The strong dislike for W^{6+} to adopt the face-sharing site explains why the $Ba_2CuTe_{1-x}W_xO_6$ solution is limited to $0 \leq x \leq 0.3$. The synchrotron X-ray diffraction data suggests the W^{6+} $B''(f)$ site occupancy reaches $\sim 3\%$ in the $x = 0.3$ sample. Significant W^{6+} impurities are observed beyond $x = 0.3$ indicating the structure cannot accommodate further electrostatically unfavourable W^{6+} substitution onto the $B''(f)$ site. Furthermore, the strong corner-sharing preference explains why Ba_2CuTeO_6 and Ba_2CuWO_6 adopt different structures. The Goldschmidt tolerance factor predicts either hexagonal or tetragonal symmetry.⁴⁰ For Ba_2CuWO_6 , the purely corner-sharing tetragonal structure is formed to maximize the W^{6+} - Cu^{2+} cation distance. Alternatively, Te^{6+} can accommodate the closer Te^{6+} - Cu^{2+} cation distance to form tetragonal or hexagonal Ba_2CuTeO_6 . The hexagonal structure is formed at ambient pressures, whereas high pressure synthesis generates the tetragonal structure.

6. Conclusions

Site-selective W^{6+} substitution of Te^{6+} has been demonstrated in the spin ladder structure of hexagonal Ba_2CuTeO_6 . Across the $Ba_2CuTe_{1-x}W_xO_6$ solution, 95% of the total W^{6+} in each x composition resided on the corner-sharing $B''(c)$ site within the hexagonal structure. The strong selectivity for corner-sharing is a result of the differences in metal-oxygen bonding between Te^{6+} $4d^{10}$ and W^{6+} $5d^0$ with the O^{2-} $2p$ orbitals in $[(Te/W)O_6]^{6-}$. The $[WO_6]^{6-}$ units have a more spherical charge distribution compared to $[TeO_6]^{6-}$. The spherical charge distribution maximizes cation-cation repulsions. As a result, W^{6+} strongly dislikes the close $B''(f)$ - Cu^{2+} cation distance at the face-sharing site. Instead, W^{6+} prefers to reside on the corner-sharing site where the $B''(c)$ - Cu^{2+} distance is larger. The strong W^{6+} selectivity for the $B''(c)$ site means the J_{leg} and J_{rung} intra-ladder interactions will be directly modified by the d^0 orbitals. This is illustrated in the summary figure in Fig. 4.13. The next chapter investigates how the mixture of d^0 and d^{10} orbitals at the $B''(c)$ site affects the intra-ladder interactions and the magnetic behaviour compared to Ba_2CuTeO_6 .

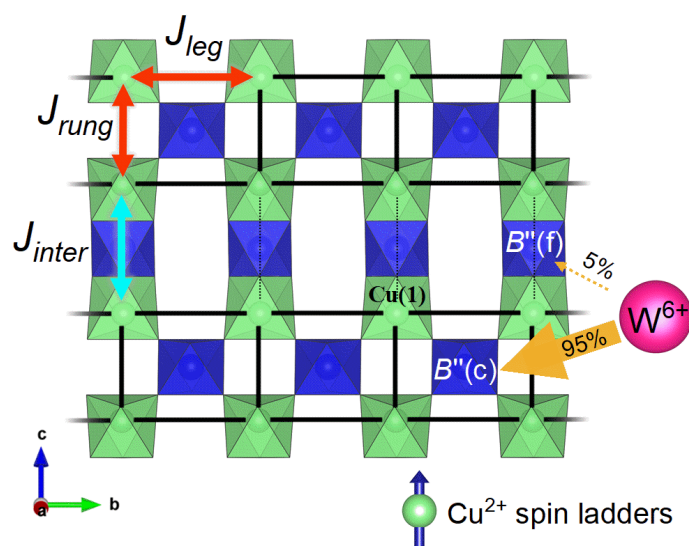


Fig. 4.13 Summary figure illustrating site-selective W^{6+} substitution in the $Ba_2CuTe_{1-x}W_xO_6$ solid solution. The orange arrows show Te^{6+} was almost exclusively substituted for W^{6+} at the corner-sharing $B''(c)$ site, in preference to the face-sharing $B''(f)$ site. Synchrotron X-ray diffraction showed 95% of the total W^{6+} in each composition was located at the $B''(c)$ site, while the remaining 5% went to the $B''(f)$ site. The strong site-selectivity means the intra-ladder interactions in the Cu^{2+} spin ladders will be most affected by the W^{6+} d^0 orbitals.

7. References

1. Mustonen, O. *et al.* Tuning the $S=1/2$ square-lattice antiferromagnet $\text{Sr}_2\text{Cu}(\text{Te}_{1-x}\text{W}_x)\text{O}_6$ from Néel order to quantum disorder to columnar order. *Phys. Rev. B* **98**, 064411 (2018).
2. Mustonen, O. *et al.* Spin-liquid-like state in a spin-1/2 square-lattice antiferromagnet perovskite induced by d^{10} - d^0 cation mixing. *Nat. Commun.* **9**, 1085 (2018).
3. Watanabe, M. *et al.* Valence-bond-glass state with a singlet gap in the spin-1/2 square-lattice random J^1 - J^2 Heisenberg antiferromagnet $\text{Sr}_2\text{CuTe}_{1-x}\text{W}_x\text{O}_6$. *Phys. Rev. B* **98**, 054422 (2018).
4. Balents, L. Spin liquids in frustrated magnets. *Nature* **464**, 199–208 (2010).
5. Savary, L. & Balents, L. Quantum spin liquids: A review. *Reports Prog. Phys.* **80**, 016502 (2017).
6. Chamorro, J. R., McQueen, T. M. & Tran, T. T. Chemistry of Quantum Spin Liquids. *Chem. Rev.* **121**, 2898–2934 (2021).
7. Zhu, M. *et al.* Tuning the magnetic exchange via a control of orbital hybridization in $\text{Cr}_2(\text{Te}_{1-x}\text{W}_x)\text{O}_6$. *Phys. Rev. Lett.* **113**, 076406 (2014).
8. Shiraki, H. *et al.* Ferromagnetic cuprates $\text{CaCu}_3\text{Ge}_4\text{O}_{12}$ and $\text{CaCu}_3\text{Sn}_4\text{O}_{12}$ with A-site ordered perovskite structure. *Phys. Rev. B* **76**, 140403(R) (2007).
9. Iwanaga, D., Inaguma, Y. & Itoh, M. Crystal Structure and Magnetic Properties of B-Site Ordered Perovskite-type Oxides $\text{A}_2\text{CuB}'\text{O}_6$ ($A = \text{Ba}, \text{Sr}$; $B' = \text{W}, \text{Te}$). *J. Solid State Chem.* **147**, 291–295 (1999).
10. Walker, H. C. *et al.* Spin wave excitations in the tetragonal double perovskite Sr_2CuWO_6 . *Phys. Rev. B* **94**, 064411 (2016).
11. Xu, Y. *et al.* Comparative description of magnetic interactions in $\text{Sr}_2\text{CuTeO}_6$ and Sr_2CuWO_6 . *J. Phys. Condens. Matter* **29**, 105801 (2017).
12. Koga, T. *et al.* Magnetic structure of the $S=1/2$ quasi-two-dimensional square-lattice Heisenberg antiferromagnet $\text{Sr}_2\text{CuTeO}_6$. *Phys. Rev. B* **93**, 054426 (2016).
13. Babkevich, P. *et al.* Magnetic Excitations and Electronic Interactions in $\text{Sr}_2\text{CuTeO}_6$: A Spin-1/2 Square Lattice Heisenberg Antiferromagnet. *Phys. Rev. Lett.* **117**, 237203 (2016).
14. Katukuri, V. M. *et al.* Exchange Interactions Mediated by Nonmagnetic Cations in Double Perovskites. *Phys. Rev. Lett.* **124**, 077202 (2020).
15. Vasala, S., Avdeev, M., Danilkin, S., Chmaissem, O. & Karppinen, M. Magnetic structure of Sr_2CuWO_6 . *J. Phys. Condens. Matter* **26**, 496001 (2014).
16. Vasala, S., Cheng, J. G., Yamauchi, H., Goodenough, J. B. & Karppinen, M. Synthesis and characterization of $\text{Sr}_2\text{Cu}(\text{W}_{1-x}\text{Mo}_x)\text{O}_6$: A quasi-two-dimensional magnetic system. *Chem. Mater.* **24**, 2764–2774 (2012).
17. Hong, W. *et al.* Extreme Suppression of Antiferromagnetic Order and Critical Scaling in a Two-Dimensional Random Quantum Magnet. *Phys. Rev. Lett.* **126**, 037201 (2021).
18. Yoon, S. *et al.* Quantum disordered state in the J_1 - J_2 square-lattice antiferromagnet $\text{Sr}_2\text{Cu}(\text{Te}_{0.95}\text{W}_{0.05})\text{O}_6$. *Phys. Rev. Mater.* **5**, 014411 (2021).
19. Balents, L. Spin liquids in frustrated magnets. *Nature* **464**, 199–208 (2010).
20. Wen, J., Yu, S. L., Li, S., Yu, W. & Li, J. X. Experimental identification of quantum spin liquids.

- npj Quantum Mater.* **4**, 1–9 (2019).
21. Liu, L., Shao, H., Lin, Y. C., Guo, W. & Sandvik, A. W. Random-Singlet Phase in Disordered Two-Dimensional Quantum Magnets. *Phys. Rev. X* **8**, 041040 (2018).
 22. Uematsu, K. & Kawamura, H. Randomness-induced quantum spin liquid behavior in the $S=1/2$ random J_1 - J_2 Heisenberg antiferromagnet on the square lattice. *Phys. Rev. B* **98**, 134427 (2018).
 23. Ren, H. Da, Xiong, T. Y., Wu, H. Q., Sheng, D. N. & Gong, S. S. Characterizing random-singlet state in two-dimensional frustrated quantum magnets and implications for the double perovskite $\text{Sr}_2\text{CuTe}_{1-x}\text{W}_x\text{O}_6$. *arXiv:2004.02128* 1–11 (2020).
 24. Nguyen, L. T. & Cava, R. J. Hexagonal Perovskites as Quantum Materials. *Chem. Rev.* **121**, 2935–2965 (2021).
 25. Gibbs, A. S. *et al.* $S=1/2$ quantum critical spin ladders produced by orbital ordering in $\text{Ba}_2\text{CuTeO}_6$. *Phys. Rev. B* **95**, 104428 (2017).
 26. Glamazda, A. *et al.* Quantum criticality in the coupled two-leg spin ladder $\text{Ba}_2\text{CuTeO}_6$. *Phys. Rev. B* **95**, 184430 (2017).
 27. Toby, B. H. & Von Dreele, R. B. GSAS-II: the genesis of a modern open-source all purpose crystallography software package. *J. Appl. Cryst.* **46**, 544–549 (2013).
 28. Mccusker, L. B., Dreele, R. B. Von, Cox, D. E., Loue, D. & Scardi, P. Rietveld refinement guidelines. *J. Appl. Cryst.* **32**, 36–50 (1999).
 29. Cussen, E. J., Gibbs, A. S., Mustonen, O. H. J. & Pughe, C. E. Structural Distortion and Magnetic Transitions in Spin Ladder Compounds $\text{Ba}_2\text{CuTe}_{1-x}\text{W}_x\text{O}_6$. <https://doi.org/10.5286/ISIS.E.RB2000100>
 30. Filik, J. *et al.* Processing two-dimensional X-ray diffraction and small-angle scattering data in DAWN 2. *J. Appl. Crystallogr.* **50**, 959–966 (2017).
 31. Ravel, B. & Newville, M. ATHENA, ARTEMIS, HEPHAESTUS: Data analysis for X-ray absorption spectroscopy using IFEFFIT. *J. Synchrotron Radiat.* **12**, 537–541 (2005).
 32. Kohl, P. & Reinen, D. Structural and Spectroscopic Investigations on $\text{Ba}_2\text{CuTeO}_6$. *Zeitschrift für Anorg. Und Allg. Chemie* **409**, 257–272 (1974).
 33. Todate, Y. Antiferromagnetism and frustration in Ba_2CuWO_6 . *J. Phys. Soc. Japan* **70**, 337–340 (2001).
 34. Mustonen, O. *et al.* Magnetic interactions in the: $S=1/2$ square-lattice antiferromagnets $\text{Ba}_2\text{CuTeO}_6$ and Ba_2CuWO_6 : Parent phases of a possible spin liquid. *Chem. Commun.* **55**, 1132–1135 (2019).
 35. Shannon, R. D. Revised effective ionic radii and systematic studies of interatomic distances in halides and chalcogenides. *Acta Cryst.* **A 32**, 751–767 (1976).
 36. Cussen, E. J. *et al.* Control of magnetic ordering by Jahn-Teller distortions in $\text{Nd}_2\text{GaMnO}_6$ and $\text{La}_2\text{GaMnO}_6$. *J. Am. Chem. Soc.* **123**, 1111–1122 (2001).
 37. Macdougall, D. *et al.* Spin dynamics of coupled spin ladders near quantum criticality in $\text{Ba}_2\text{CuTeO}_6$. *Phys. Rev. B* **98**, 174410 (2018).
 38. Flores, A. V. *et al.* Comparison of the crystal chemistry of tellurium (VI), molybdenum (VI), and tungsten (VI) in double perovskite oxides and related materials. *Prog. Solid State Chem.*

- 56, 100251 (2019).
39. Day, B. E. *et al.* Structures of ordered tungsten- or molybdenum-containing quaternary perovskite oxides. *J. Solid State Chem.* **185**, 107–116 (2012).
40. Vasala, S. & Karppinen, M. $A_2B'B''O_6$ perovskites: A review. *Prog. Solid State Chem.* **43**, 1–36 (2015).

8. Appendix

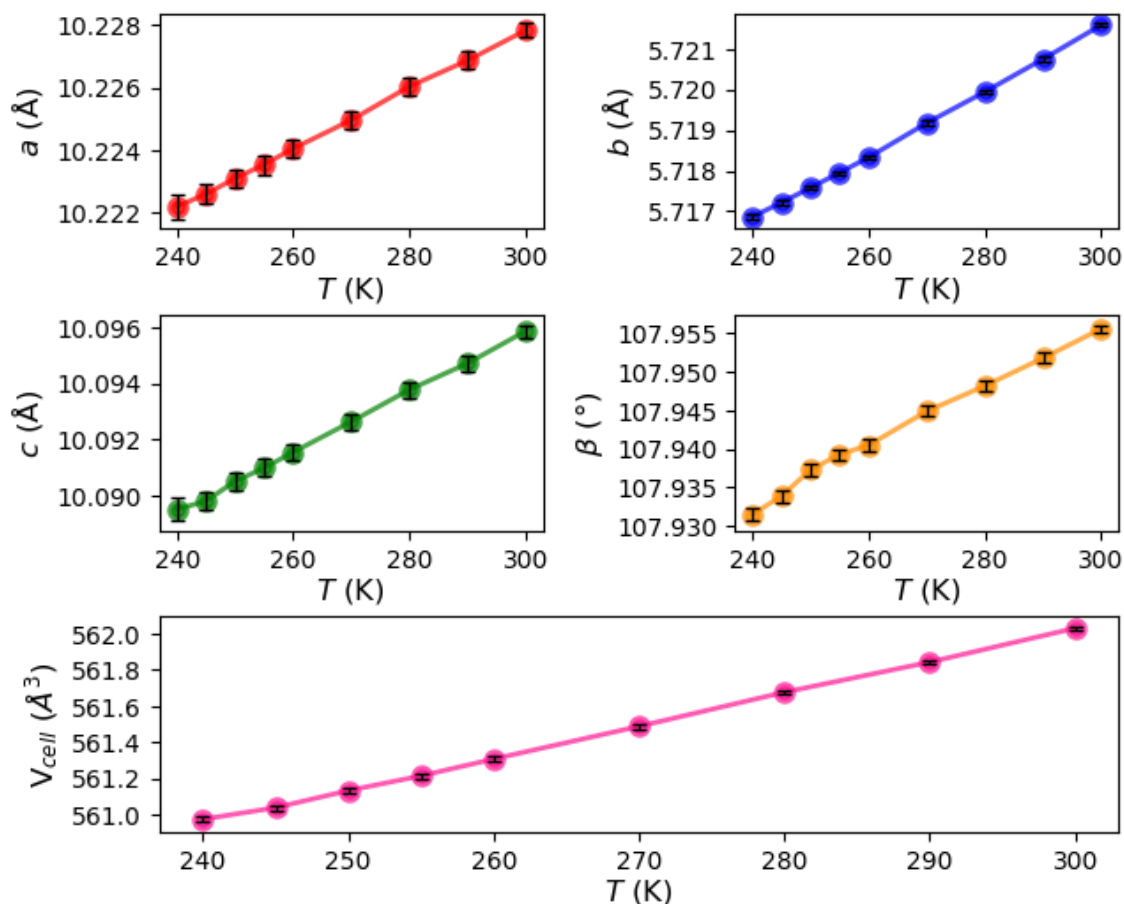


Fig. A4.1 Unit cell parameters of $Ba_2CuTe_{0.9}W_{0.1}O_6$ in the monoclinic ($C2/m$) phase between 240–300 K.

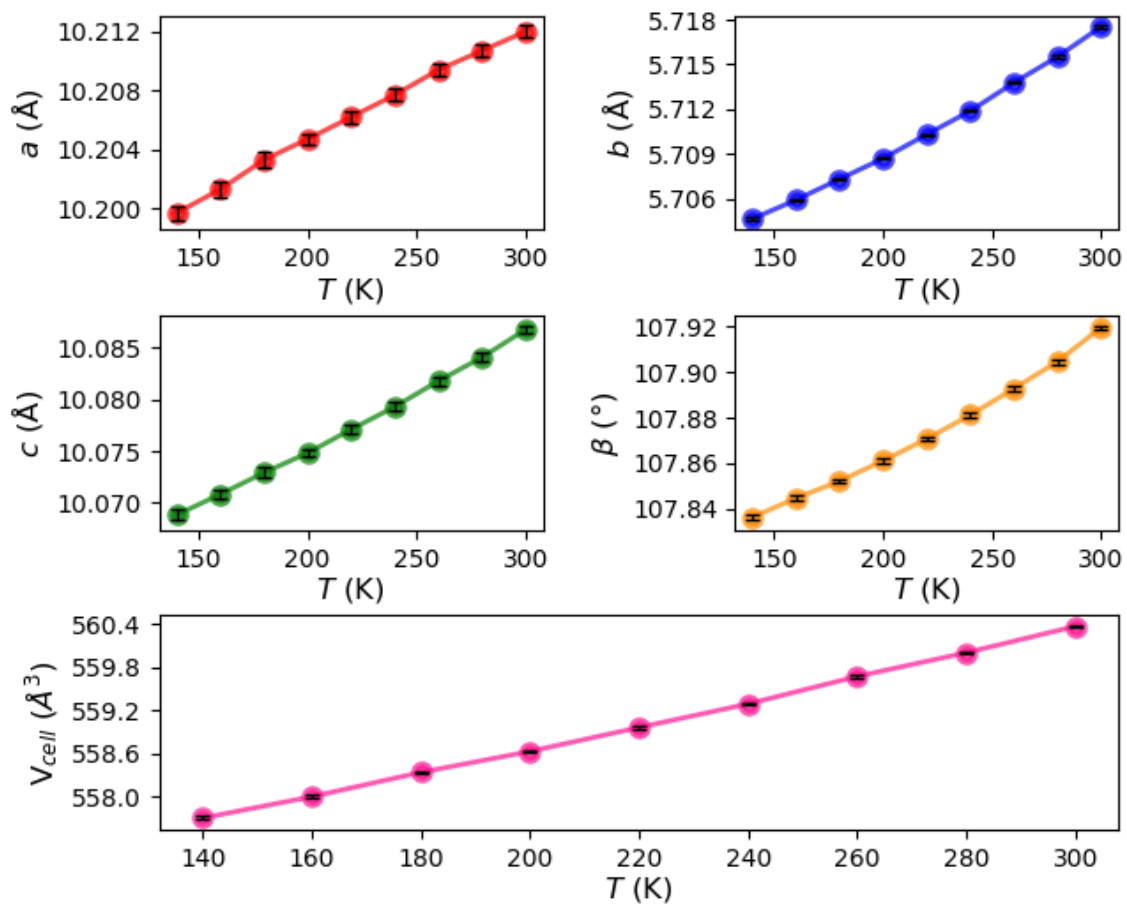


Fig. A4.2 Unit cell parameters of $Ba_2CuTe_{0.7}W_{0.3}O_6$ in the monoclinic ($C2/m$) phase between 140-300 K.

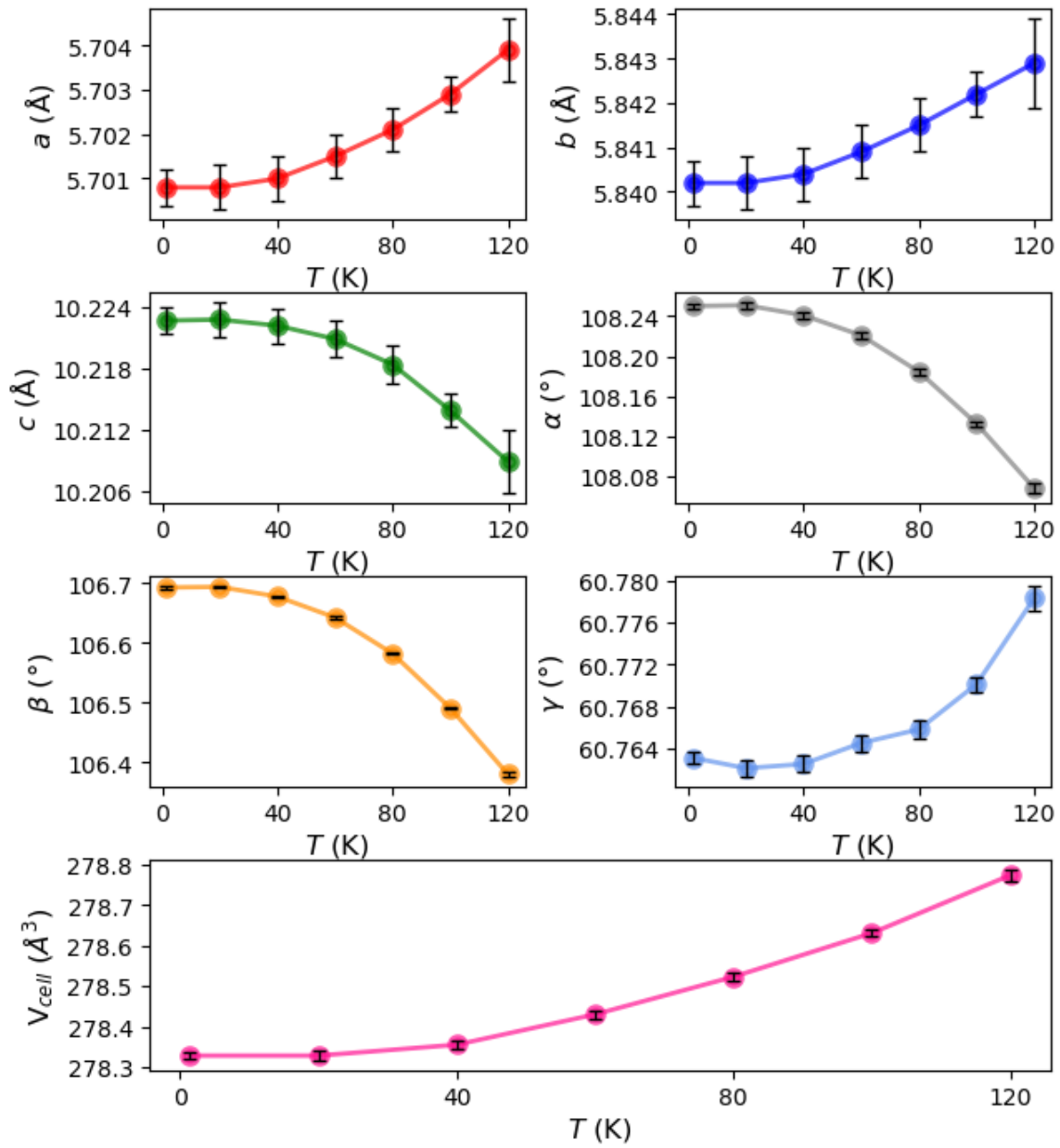


Fig. A4.3 Unit cell parameters of $Ba_2CuTe_{0.7}W_{0.3}O_6$ in the triclinic ($P\bar{1}$) phase between 1.44-120 K.

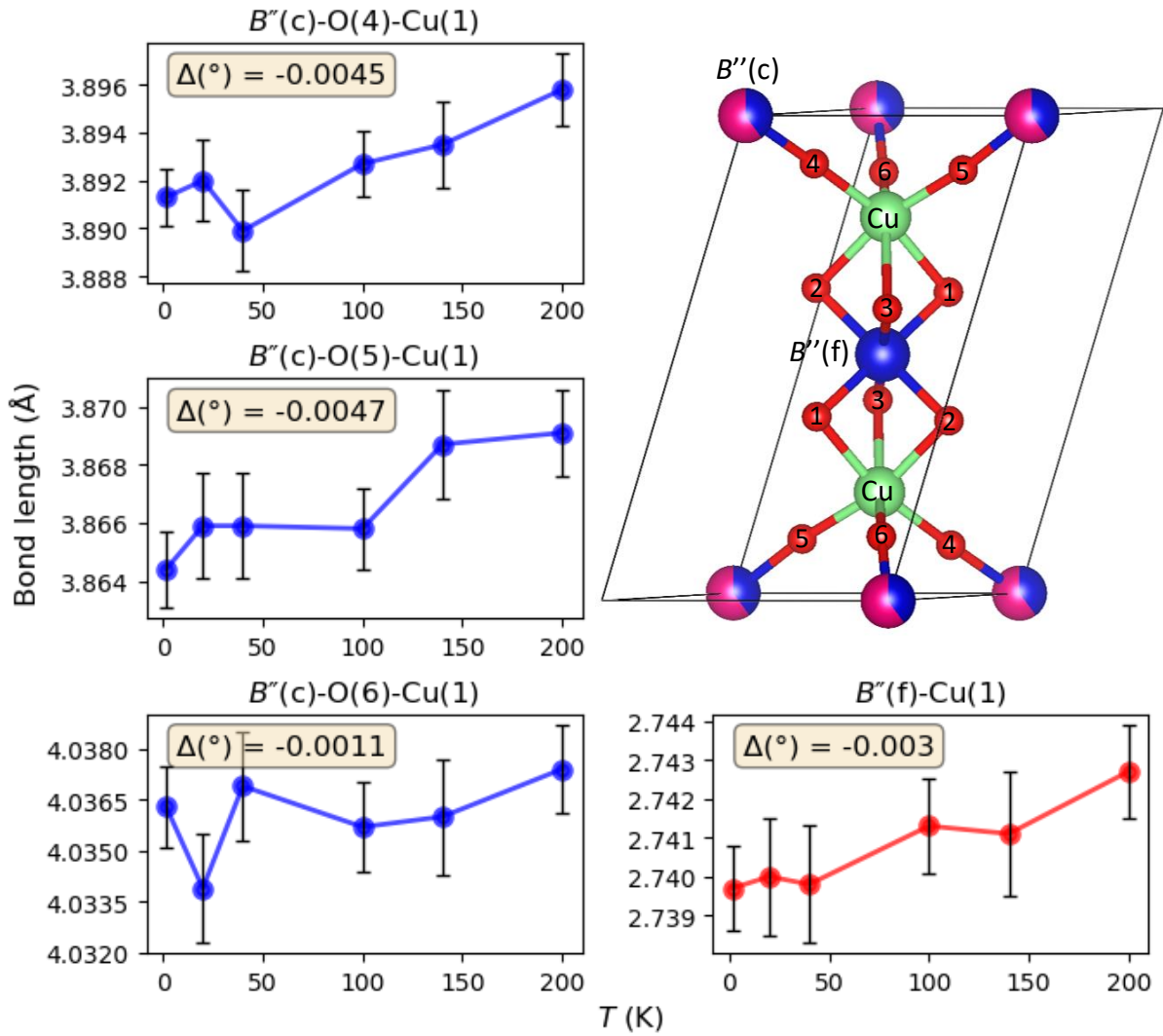


Fig. A4.4 The $B''(c)-O(5-6)-Cu$ bond lengths and the $B''(f)-Cu$ bond lengths in $Ba_2CuTe_{0.9}W_{0.1}O_6$ in the triclinic ($P\bar{1}$) phase between 1.5-200 K. The illustration of the triclinic structure shows the atom positions and measured bond lengths.

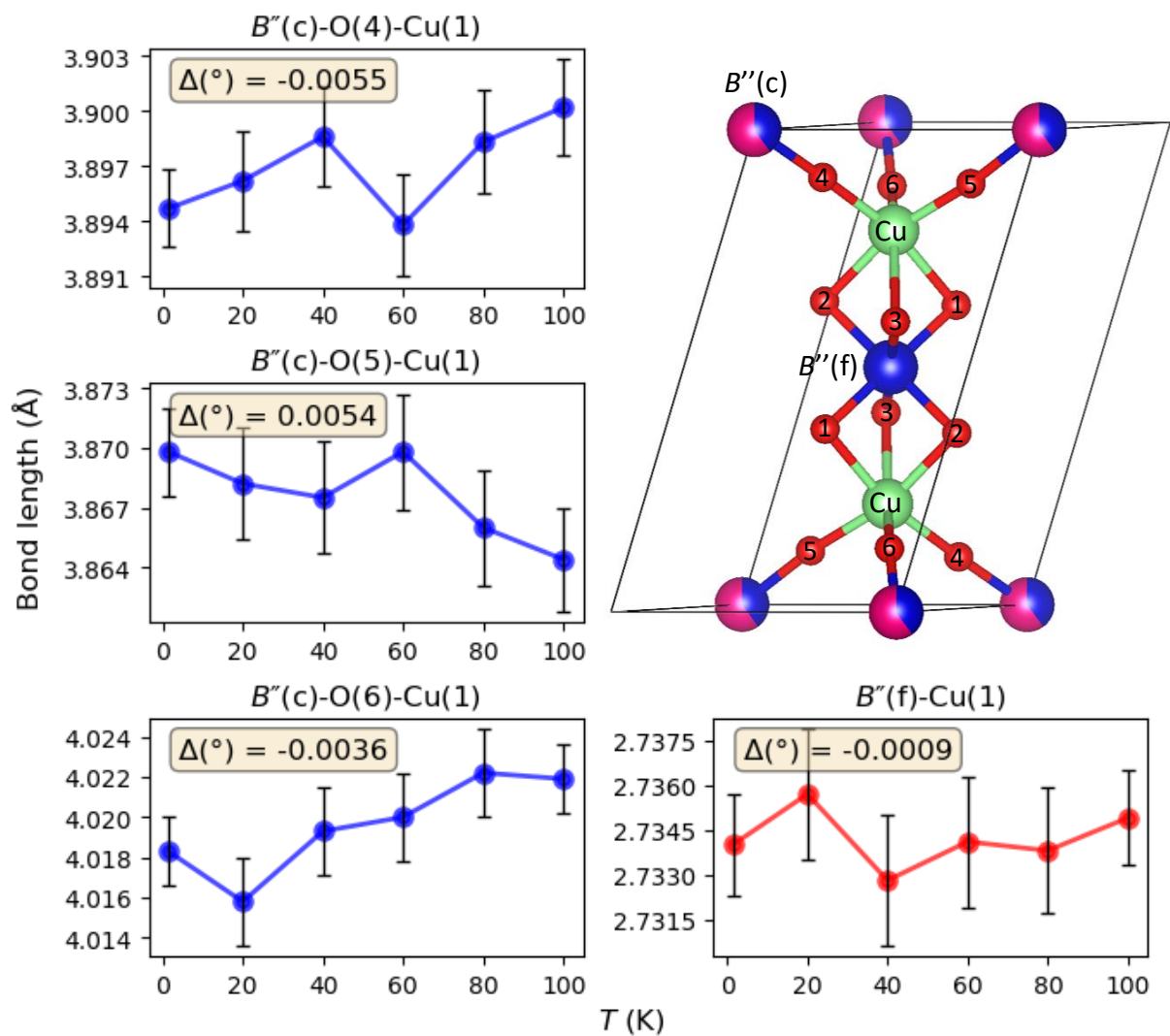


Fig. A4.5 The $B''(c)-O(5-6)-Cu$ bond lengths and the $B''(f)-Cu$ bond lengths in $Ba_2CuTe_{0.7}W_{0.3}O_6$ in the triclinic ($P\bar{1}$) phase between 1.44-100 K. The illustration of the triclinic structure shows the atom positions and measured bond lengths.

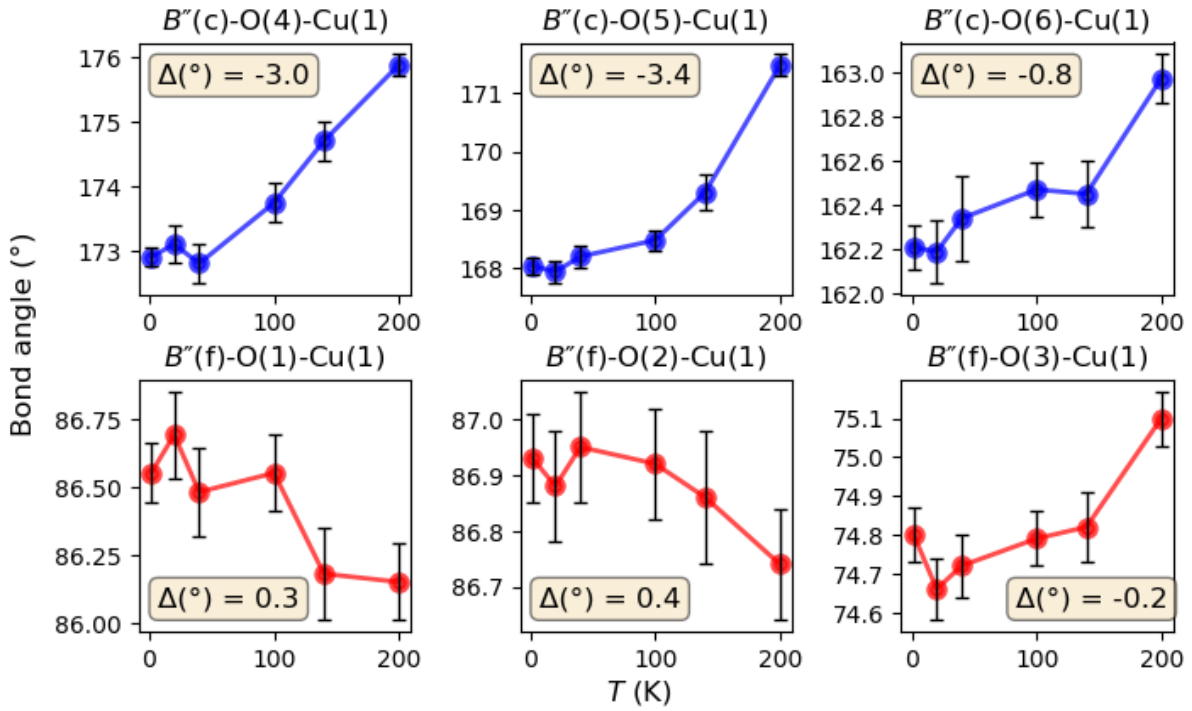


Fig. A4.6 The $B''(c)-O(4-6)-Cu$ and $B''(f)-O(1-3)-Cu$ bond angles in $Ba_2CuTe_{0.9}W_{0.1}O_6$ in the triclinic ($P\bar{1}$) phase between 1.5-200 K.

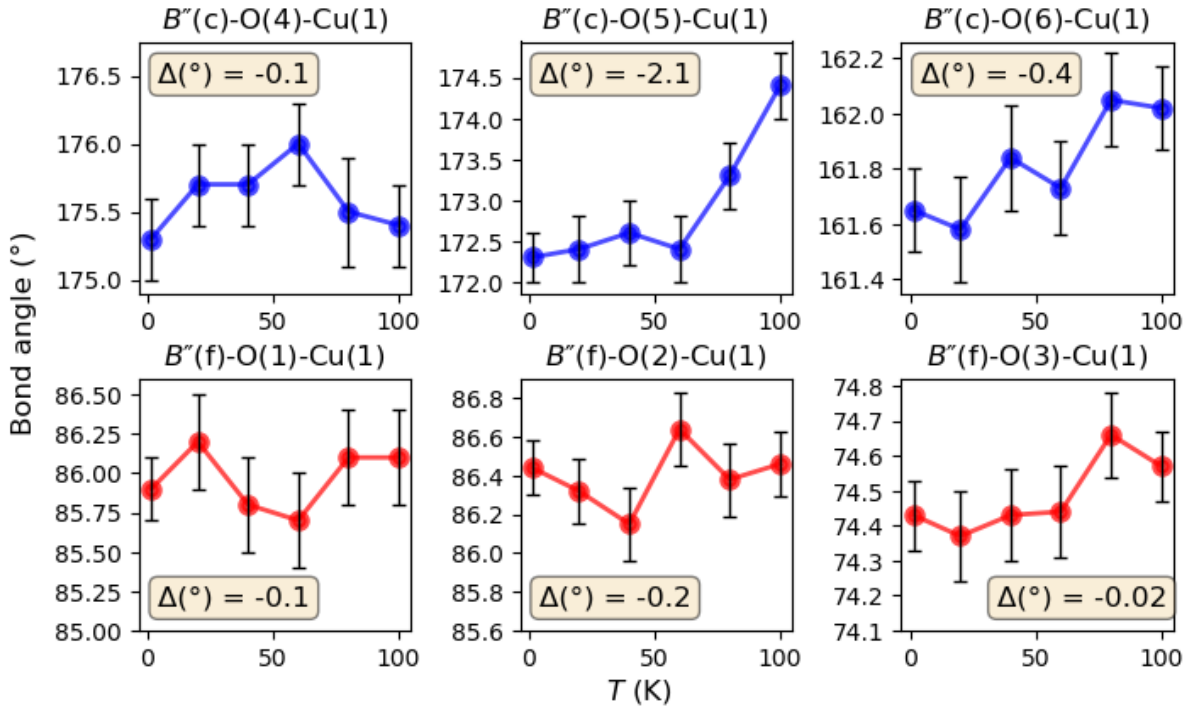


Fig. A4.7 The $B''(c)-O(4-6)-Cu$ and $B''(f)-O(1-3)-Cu$ bond angles in $Ba_2CuTe_{0.7}W_{0.3}O_6$ in the triclinic ($P\bar{1}$) phase between 1.44-100 K.

Chapter 5: Effects of site-selective W^{6+} substitution on the magnetic properties of $Ba_2CuTe_{1-x}W_xO_6$

Contents

1. Abstract
2. Introduction
3. Experimental
4. Results
 - a. DC magnetic susceptibility
 - b. AC susceptibility
 - c. Modelling the DC susceptibility data
 - d. Heat capacity
 - e. Muon Spin Relaxation (μ SR)
5. Discussion
6. Conclusions
7. References
8. Appendix

1. Abstract

This chapter characterizes the magnetic properties of $Ba_2CuTe_{1-x}W_xO_6$ to investigate the effect of site-selective W^{6+} substitution. Bulk characterization showed a clear change in the magnetic behaviour compared to Ba_2CuTeO_6 . By modelling the DC magnetic susceptibility data, it was possible to quantify the effect of W^{6+} on the intra-ladder interactions. The J_{rung}/J_{leg} ratio decreases from near unity for $x = 0$, towards zero for $x = 0.3$. This showed the d^{10}/d^0 effect tunes the system from a spin ladder towards a spin chain. Muon spin relaxation experiments confirm the $0.05 \leq x \leq 0.3$ $Ba_2CuTe_{1-x}W_xO_6$ samples do not exhibit long-range magnetic order. Inelastic neutron scattering experiments are required to determine the exact nature of the ground state, which is likely to be a disorder induced quantum magnetic state, possibly similar to that observed in $Sr_2CuTe_{1-x}W_xO_6$. Meanwhile, this shows d^0 and d^{10} cations are powerful tools for tuning the magnetic interactions in double and hexagonal perovskites.

2. Introduction

The strong site-selectivity for the corner-sharing site in $Ba_2CuTe_{1-x}W_xO_6$ means the intra-ladder interactions will be most affected by W^{6+} substitution. The competition between the $Te^{6+} d^{10}$ and $W^{6+} d^0$ interactions could have a range of effects on the magnetic behaviour. A likely scenario is suppressed magnetic ordering, as observed from the disorder induced frustration in $Sr_2CuTe_{1-x}W_xO_6$.¹⁻³ Before investigating the magnetic interactions in $Ba_2CuTe_{1-x}W_xO_6$, the magnetic properties of Ba_2CuTeO_6 will first be discussed to observe how they are affected by W^{6+} .

The Cu^{2+} spin ladder in $\text{Ba}_2\text{CuTeO}_6$ is described by the two-leg $S = \frac{1}{2}$ spin ladder model. The two-leg spin ladder model is formed when spin chains of Cu^{2+} cations interact. The interaction between spin chains creates a two-leg spin ladder in which each Cu^{2+} is connected to three neighbours via two J_{leg} and one J_{rung} interaction.⁴ This magnetic geometry resembles a chain of square lattice plaquettes. As noted in chapter 4, the square plaquettes resemble the Heisenberg square lattice J_1 and J_2 interactions in $\text{Sr}_2\text{CuTe}_{1-x}\text{W}_x\text{O}_6$. The two-leg spin ladders interact via the inter-ladder J_{inter} interaction. The magnitude of the J_{inter} interaction determines where the system lies on the magnetic phase diagram shown in Fig. 5.1.

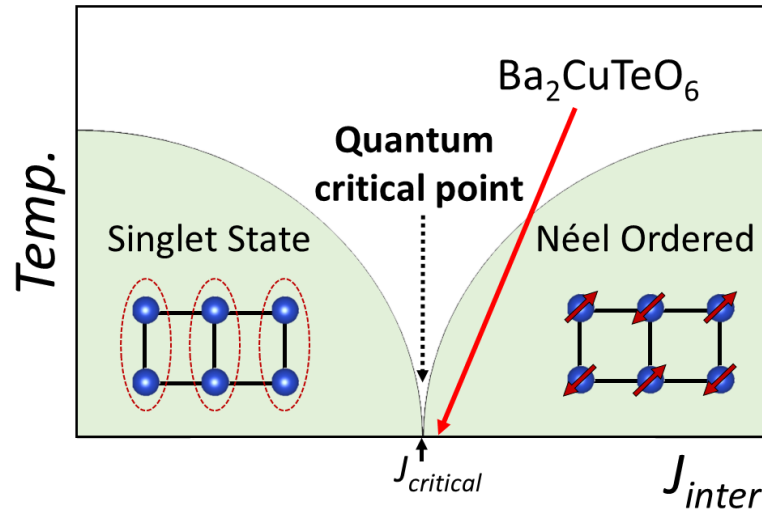


Fig. 5.1 The magnetic phase diagram of a two-leg spin ladder. The ground state is tuned between the Néel ordered phase and singlet phase by varying the inter-ladder interaction J_{inter} . The two phases are separated by the quantum critical point, which $\text{Ba}_2\text{CuTeO}_6$ lies close to.

The magnetic phase diagram consists of a spin singlet phase and Néel ordered phase separated by a quantum critical point.^{5,6} A quantum critical point (QCP) is an electronic phase transition at absolute zero.⁷ There are no thermal fluctuations at zero Kelvin, therefore quantum critical transitions are brought about by non-thermal influences such as pressure, magnetic fields, or magnetic interactions that create quantum fluctuations.⁸ Strictly, the QCP is only present at absolute zero, but the effects of the quantum fluctuations associated with the QCP can be observed at temperatures above absolute zero.^{9,10} Quantum critical transitions are present in phase diagrams of many quantum materials including superconductors, insulators and semiconductors.

The QCP is reached by tuning the inter-ladder J_{inter} interaction towards the critical value (J_c). The value of J_c depends on the ratio of the intra-ladder interactions. When the intra-ladder interactions are equal ($J_{\text{leg}} = J_{\text{rung}} = J$), the value of the critical inter-ladder coupling is $J_c = 0.314J$.¹¹ Below $J_c = 0.314J$, the two-leg spin ladder forms the spin singlet phase.^{9,12,13} Fig. 5.1 provides an illustration of the singlet state, which consists of an array of spins that have paired (or dimerized) to form singlets with their spins aligned antiparallel so the spins cancel to give a total spin of $|S| = \frac{1}{2} + -\frac{1}{2} = 0$. The singlet state is represented by $\frac{1}{\sqrt{2}}(|\uparrow\downarrow\rangle - |\downarrow\uparrow\rangle)$ in Dirac notation.

Evidence for the spin singlet state is obtained from quantum excitations. At a specific energy, the singlet state ($|S| = 0$) is excited to the triplet state ($|S| = \frac{1}{2} + \frac{1}{2} = 1$).^{9,12} Excitations can be observed using inelastic neutron scattering. Excitation features are observed when the neutron energy

matches the singlet-triplet energy gap.¹³ Inelastic neutron scattering can also be used to identify the Néel ordered state. The Néel state is observed when J_{inter} is strong and above the critical value of $J_C = 0.314J$. The spins on the corners of the square plaquettes in the ladder align antiparallel with respect to on another, resulting in long-range antiferromagnetic ordering.^{5,14} This leads to spin waves in the inelastic neutron scattering spectrum.

For $\text{Ba}_2\text{CuTeO}_6$, the value of J_{inter} when $J_{\text{leg}} = J_{\text{rung}}$ has been calculated as $J_{\text{inter}} = 0.58J$.⁶ This is larger than the critical value of $J_C = 0.314J$ placing $\text{Ba}_2\text{CuTeO}_6$ in the Néel ordered phase. While Néel ordered, a variety of experimental techniques have shown $\text{Ba}_2\text{CuTeO}_6$ lies very close to the quantum critical point.^{6,15,16} There is no clear indication of antiferromagnetic ordering in the magnetic susceptibility, heat capacity, or neutron diffraction data (where magnetic Bragg peaks might be expected). Instead, a weak Néel transition at $T_N \sim 14$ K has been detected by probing the local magnetism using muon spin relaxation (μSR) techniques.¹⁵ Inelastic neutron scattering has also been used to demonstrate magnetic ordering. Spin waves representing Néel order are observed below T_N .⁶ The weak transition indicates the value of J_{inter} is just large enough to induce magnetic ordering and there are strong fluctuations in the magnetic interactions. Strong quantum fluctuations imply $\text{Ba}_2\text{CuTeO}_6$ lies close to the quantum critical point.

W^{6+} substitution could modify the J_{inter} interaction between the two-leg spin ladders and tune the ground state towards the QCP. However, W^{6+} substitution occurs almost exclusively at the corner-sharing site within the ladder. Hence, the d^0 effect on the J_{inter} interaction is likely to be minor. It can be assumed that the W^{6+} d^0 orbitals directly affect the J_{leg} and J_{rung} interactions, while J_{inter} is mostly unaffected. The d^{10}/d^0 effect shows the W^{6+} and Te^{6+} cations produce different dominant interactions in a square plaquette geometry. W^{6+} $5d^0$ promotes a strong diagonal J_2 interaction and suppresses J_1 . Alternatively, Te^{6+} $4d^{10}$ promotes a strong nearest neighbour J_1 interaction and near zero J_2 . The square plaquette geometry of four Cu^{2+} cations in the $\text{Ba}_2\text{CuTeO}_6$ spin ladder is similar to the square lattice J_1 - J_2 interactions in $\text{Ba}_2\text{Mn}(\text{Te}/\text{W})\text{O}_6$ and $\text{Sr}_2\text{Cu}(\text{Te}/\text{W})\text{O}_6$. Hence, it is more likely that W^{6+} substitution tunes the J_{leg} and J_{rung} interactions through the d^0/d^{10} competition. If $J_{\text{leg}} \neq J_{\text{rung}}$, this would place $\text{Ba}_2\text{CuTe}_{1-x}\text{W}_x\text{O}_6$ on an alternate phase diagram to that of the isolated two-leg spin ladder shown in Fig. 5.1.

To investigate how W^{6+} influences the J_{leg} and J_{rung} interactions magnetic characterization was performed on the $\text{Ba}_2\text{CuTe}_{1-x}\text{W}_x\text{O}_6$ samples. The following presents the results and comparison to $\text{Ba}_2\text{CuTeO}_6$. There is clear evidence showing d^{10}/d^0 tuning of the spin ladder interactions.

3. Experimental

Magnetic susceptibility

A Quantum Design MPMS3 SQUID magnetometer was used to perform magnetic susceptibility measurements on the $x = 0, 0.05, 0.1, 0.2$ and 0.3 $\text{Ba}_2\text{CuTe}_{1-x}\text{W}_x\text{O}_6$ samples. The sample was prepared using the same method described in chapter 3. Zero-field cooled (ZFC) and field-cooled (FC) measurements were performed between 2-300 K using an external field of 0.1 T. The AC susceptibility (χ'_{AC}) of the $x = 0.1$ and $x = 0.3$ samples was measured between 2-100 K. To improve the signal, a weak DC field of 25 Oe was applied during the AC measurement. The AC field was 5 Oe producing AC frequencies in the range of 10 to 467 Hz.

Heat capacity

Measurements were performed on the $\text{Ba}_2\text{CuTe}_{1-x}\text{W}_x\text{O}_6$ ($0 \leq x \leq 0.3$) samples using a Quantum Design PPMS instrument. The samples were prepared by mixing the polycrystalline powders with silver (99.99%) in a 1:1 gravimetric ratio. The silver helped to improve the thermal conductivity between the sample and the sample holder at low temperatures. The $\text{Ba}_2\text{CuTe}_{1-x}\text{W}_x\text{O}_6:\text{Ag}$ powder was then pressed into a pellet and the pellet broken into shards. Shards weighing ~ 10 mg were placed onto the sample puck. The heat capacity of each sample was measured using the thermal relaxation method between 2-120 K. In the thermal relaxation method, the time dependence of the temperature is monitored after applying a heat pulse. The heat capacity is determined from the temperature difference before and after the pulse and the relaxation time. By subtracting the silver contribution from the total heat capacity, the sample heat capacity was obtained. The silver contribution was modelled using heat capacity measurements of the pure silver powder.

Muon Spin Relaxation (μSR)

Muon Spin Relaxation (μSR) measurements were performed using the HIFI and MUSR beamlines at the ISIS Neutron and Muon Source. Polycrystalline powders (ca. 3 g) were sealed inside silver foil packets. The silver foil packet was placed onto the sample rod and inserted into a closed cycle helium cryostat. On the HIFI beamline the cryostat has an operating range between 2-300 K. The μSR measurements were performed on the $x = 0, 0.05, 0.1, 0.2$ and 0.3 samples down to the minimum temperature of 2 K on the HIFI beamline. Measurements below 2 K were performed using the MUSR beamline equipped with a helium dilution fridge to obtain temperatures down to 50 mK. To improve the thermal conductivity between the sample and sample holder, the polycrystalline powders were mixed with GE varnish. μSR measurements were performed on the $x = 0.05$ and $x = 0.1$ samples down to 90 mK and 50 mK, respectively. The μSR measurements included zero-field (ZF), transverse-field (TF) and longitudinal-field (LF) measurements. The data were analysed using MANTID.

4. Results

a. DC magnetic susceptibility

Fig. 5.2 shows the DC magnetic susceptibility (χ) of the $x = 0, 0.05, 0.1, 0.2$ and 0.3 samples between 2-400 K. The behaviour above 35 K is the same with a broad maximum at $T_{max} \sim 70$ K. Broad features are common in low dimensional magnetic systems and indicate the establishment of short-range ladder interactions. Table 5.1 shows T_{max} shifts to lower temperatures as x increases, implying W^{6+} weakens the short-range ladder interactions. Below T_{max} , the susceptibility of all samples decreases. In the case of $x = 0$, χ decreases before leading onto a small upturn beyond $T_{min} \sim 14$ K. This behaviour has been previously observed in the χ vs T curve of $\text{Ba}_2\text{CuTeO}_6$.^{16,17} The low temperature upturn is not a classical indication of antiferromagnetic order, where a sharp peak about a maximum would be expected. Hence, the upturn alone does not show antiferromagnetic order, but is thought to be related to the transition from spin ladder behaviour to the Néel ordered state.¹⁶ Hence, DC magnetic susceptibility (χ) cannot confirm antiferromagnetic order, and advanced muon techniques were required to determine the T_N of 14.1 K.¹⁵ The close agreement between the position of $T_N = 14.1$ K and the upturn at $T_{min} \sim 14$ K is a coincidence.

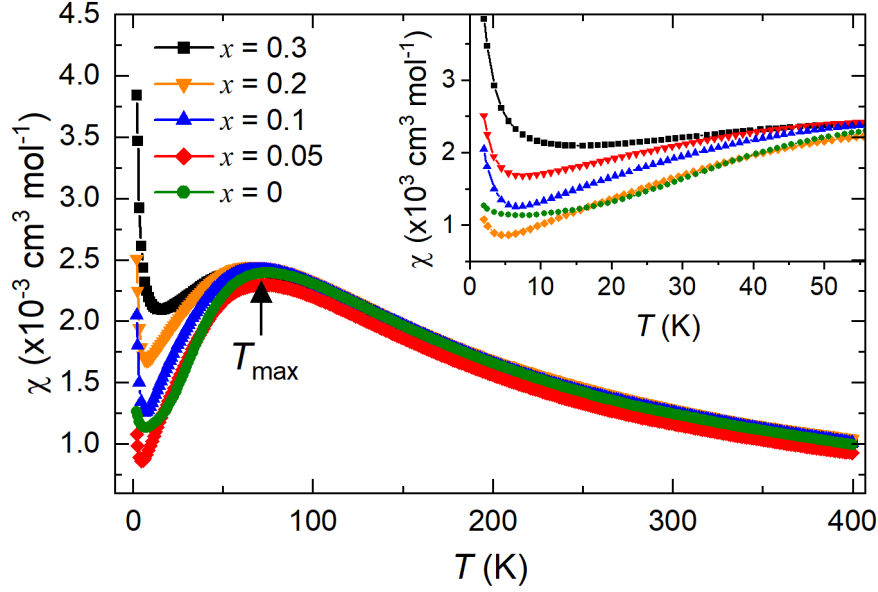


Fig. 5.2 The DC magnetic susceptibility data of $Ba_2CuTe_{1-x}W_xO_6$ $x = 0, 0.05, 0.1, 0.2$ and 0.3 plotted as a function of temperature (T) between 2-400 K. The broad T_{max} feature is indicated in the plot. The expansion shows the low temperature susceptibility data between 2 – 50 K, where the upturn in the $x = 0$ data and growing Curie-tails in the $x = 0.05, 0.1, 0.2$ and 0.3 samples are more visible.

Table 5.1: Results from analysis of the DC magnetic susceptibility data of $Ba_2CuTe_{1-x}W_xO_6$.

x	0	0.05	0.1	0.2	0.3
T_{max} (K)	73.9	72.3	70.5	67.1	63.8
C ($cm^3 K mol^{-1}$)	0.5018(4)	0.4582(3)	0.5189(2)	0.5450(5)	0.5048(4)
θ_W (K)	-102.9(3)	-94.2(1)	-113.4(1)	-124.1(2)	-102.0(2)
μ_{eff} (μ_B per Cu^{2+})	2.003(9)	1.914(2)	2.037(1)	2.088(3)	2.009(2)

Upon substitution of Te^{6+} for W^{6+} , the upturn feature becomes stronger with increasing x . The upturn is strongest for the $x = 0.3$ sample, at which point the low temperature behaviour resembles a ‘Curie-tail’. A Curie-tail is a sharp almost linear rise in the low temperature susceptibility, indicating paramagnetic-like behaviour. The susceptibility measurements were performed on various sample batches. The ‘Curie-tail’ like feature does not change between sample batches, indicating the feature is intrinsic to the sample and not representative of an impurity. The Curie-tails also show no field dependence when measuring the susceptibility in a higher DC field of 1 T. There was no divergence between the ZFC and FC curves for any of the samples.

The high temperature χ vs T data between 200-400 K were fitted using the inverse Curie-Weiss law. Panel (a) in Fig. 5.3 provides an example Curie-Weiss fit to the $x = 0.1$ χ vs T data. The Curie-Weiss fits for the other samples are shown in the Appendix. Panels (c) and (d) show the value of θ_W and μ_{eff} as a function of x in $Ba_2CuTe_{1-x}W_xO_6$. The values of θ_W in Table 1 are negative for all samples showing the interactions are antiferromagnetic and the strength remains approximately constant as W^{6+} increases. The values of μ_{eff} shown in Table 5.1 and panel (d) are close to the previously reported value for Cu^{2+} in Ba_2CuTeO_6 , where μ_{eff} was $1.96 \mu_B$ per Cu^{2+} .

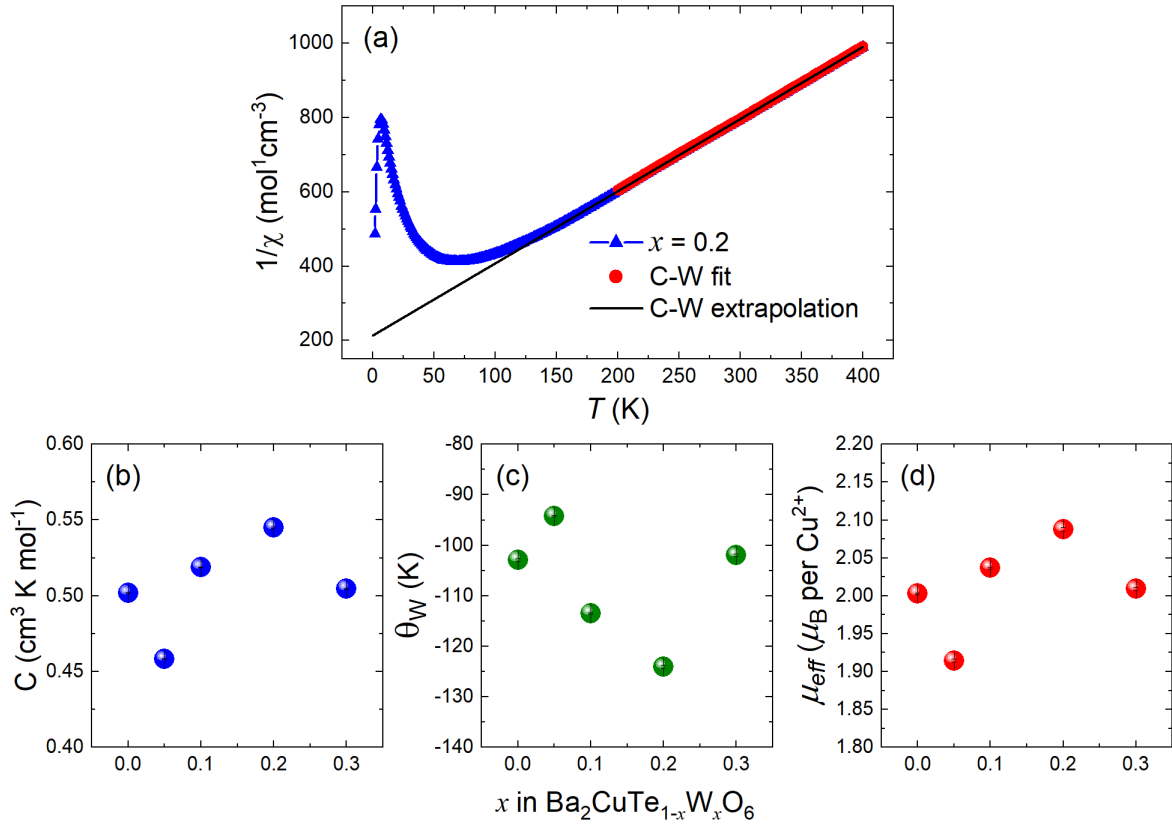


Fig. 5.3 (a) Curie-Weiss fit to the inverse $1/\chi$ vs T data of $x = 0.2$ between 200-400 K. The Curie-Weiss fit shown by the red line describes the $1/\chi$ vs T data well in this region. The black line shows an extrapolation of the Curie-Weiss fit. Panel (b) shows the Curie constant (C) as a function of x in $Ba_2CuTe_{1-x}W_xO_6$. Panel (c) shows the Weiss constant (θ_W) as a function of x in $Ba_2CuTe_{1-x}W_xO_6$. Panel (d) shows the effective magnetic moment μ_{eff} as a function of x in $Ba_2CuTe_{1-x}W_xO_6$.

b. AC susceptibility

The AC susceptibility curves of $x = 0.1$ and $x = 0.3$ are shown in Fig. 5.4. Neither dataset shows the characteristic shift in the χ'_{AC} vs T data associated with spin glass behaviour. Further evidence to support no spin glass behaviour is shown by the imaginary component (χ''_{AC}) of the AC susceptibilities in panels (c) and (d) of Fig. 5.4. There are no peaks in the χ''_{AC} vs T data which would be expected if $Ba_2CuTe_{1-x}W_xO_6$ was a spin glass.

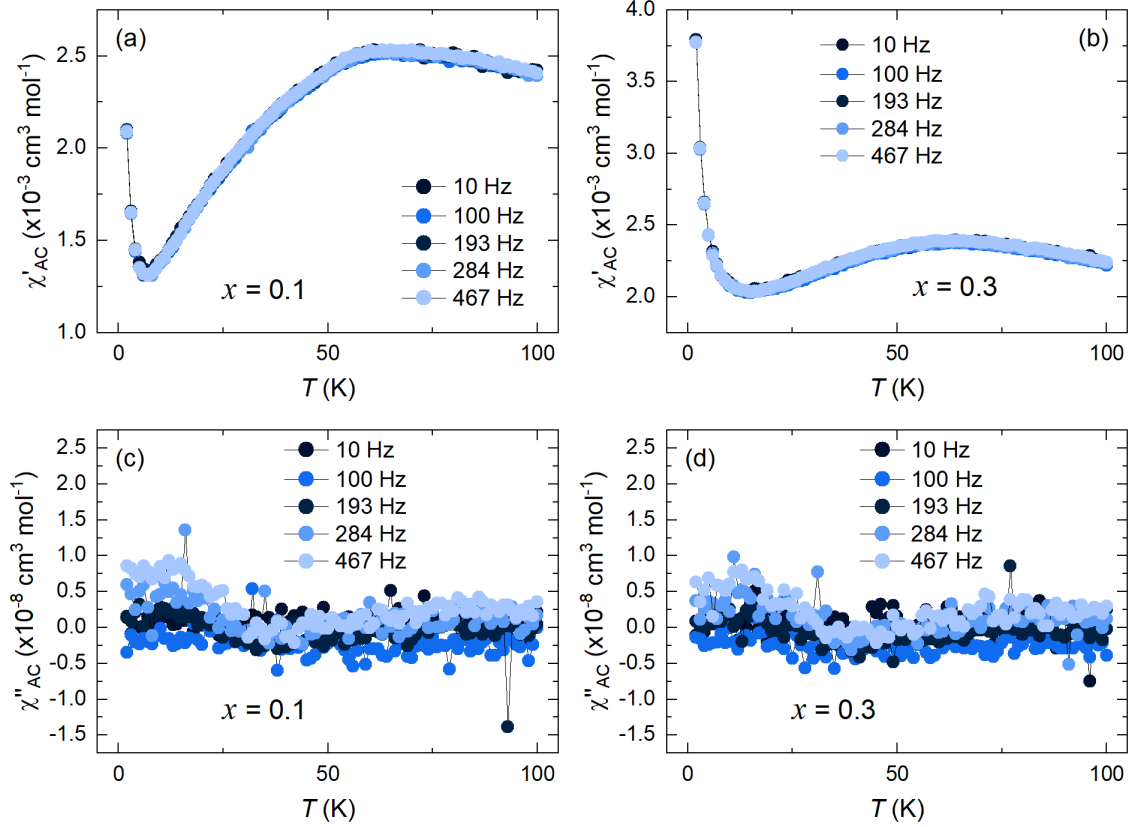


Fig. 5.4 The AC magnetic susceptibility data (χ'_{AC} vs T) of (a) $x = 0.1$ and (b) $x = 0.3$. No frequency dependent shift is observed in panels (a) and (b). Panels (c) and (d) show the imaginary component of the AC susceptibility (χ''_{AC}) as a function of temperature (T). There are no peaks in the χ''_{AC} vs T plots of $x = 0.1$ or $x = 0.3$ in panels (c) and (d), respectively. This confirms the $Ba_2CuTe_{1-x}W_xO_6$ samples are not spin glasses.

c. Modelling the DC susceptibility data

The DC susceptibility data between 35 to 300 K was modelled using the isolated two-leg spin ladder model. The isolated two-leg spin ladder model has been used to model Ba_2CuTeO_6 previously and is based on Quantum Monte Carlo (QMC) simulations of an isolated two-leg spin ladder.^{13,16} The model is valid when $J_{rung}/J_{leg} \leq 1$, where J_{rung}/J_{leg} is the ratio of the intra-ladder interactions. The equations for the isolated two-leg spin ladder model are shown in the Appendix. The main equation for the molar magnetic susceptibility is shown below:¹³

$$\chi(T) = \frac{N_A g^2 \mu_B^2 e^{-\frac{\Delta}{T}}}{4k_B T} P_6^6 \left(\frac{T}{J_{leg}} \right) + \chi_0 \quad \text{Where, } \Delta = 0.4030 \left(\frac{J_{rung}}{J_{leg}} \right) + 0.0989 \left(\frac{J_{rung}}{J_{leg}} \right)^3 \quad (5.1)$$

There are three fitting parameters: the intra-ladder J_{leg} interaction, the J_{rung}/J_{leg} ratio, and the Landé g -factor. The plots in Fig. 5.5 show fitting of the isolated two-leg spin ladder model to the (a) $x = 0$, (b) $x = 0.05$, (c) $x = 0.1$, (d) $x = 0.2$ and (e) $x = 0.3$ DC susceptibility data. Table 5.2 displays the values of J_{leg} , J_{rung}/J_{leg} and g determined for each x composition. The plots in Fig. 5.5 show the isolated spin ladder model depicted in panel (f) describes the magnetic susceptibility of all samples well. The J_{rung}/J_{leg} ratio obtained for $x = 0$ was near unity showing the intra-ladder J_{leg} and J_{rung} interactions are almost equal. The values of J_{leg} and J_{rung}/J_{leg} are similar to the values obtained when $x = 0$ was modelled using the spin ladder model previously: $J_{rung}/J_{leg} = 0.98(2)$ and $J_{leg} =$

$J_{rung} = 7.07 \text{ meV} = 82.04 \text{ K}$.¹⁶ These values were used to model the inelastic neutron spectra and provide a good description supporting $J_{rung}/J_{leg} \sim 1$.

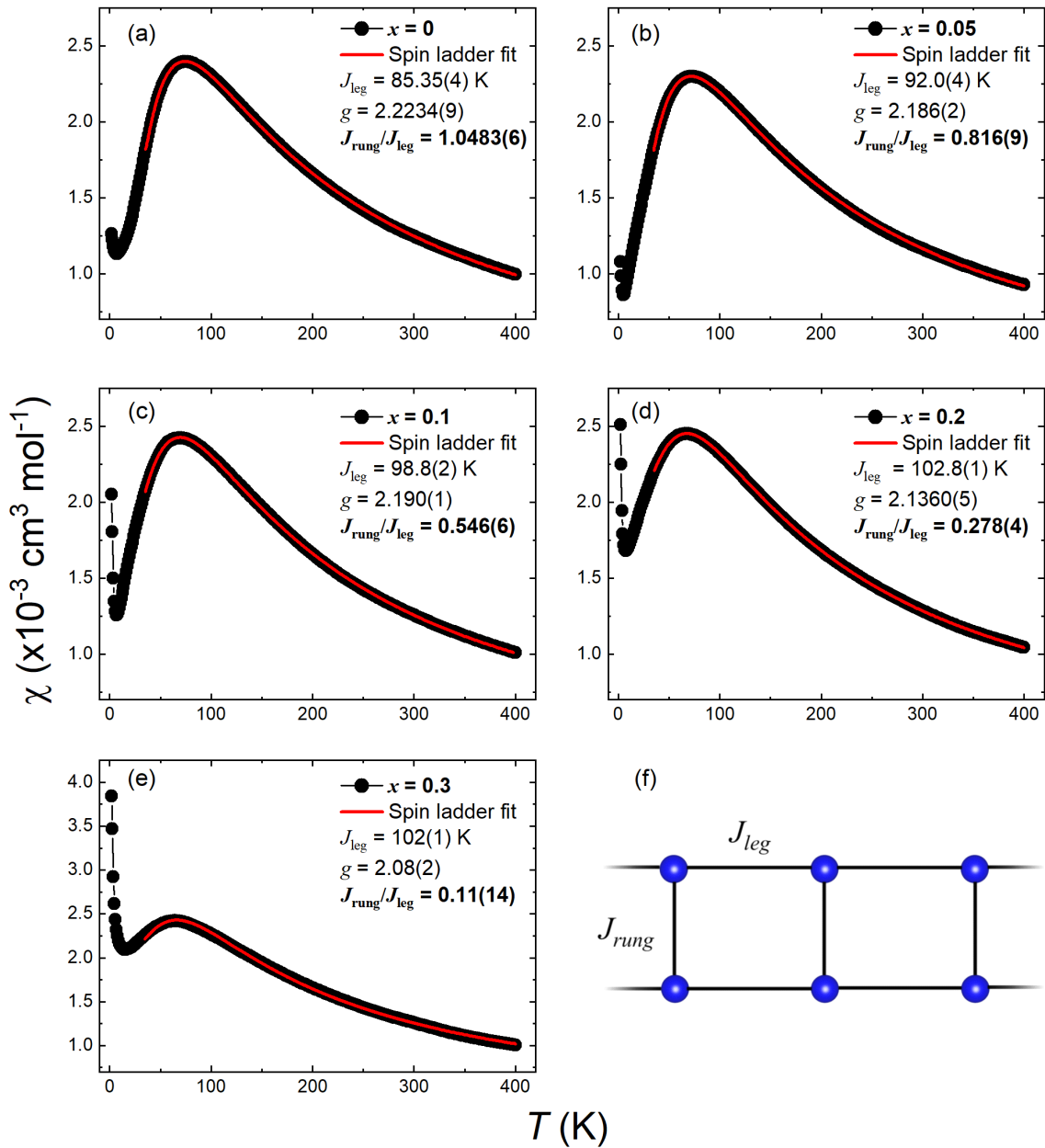


Fig. 5.5 Modelling the $\text{Ba}_2\text{CuTe}_{1-x}\text{W}_x\text{O}_6$ susceptibility data using the isolated two-leg spin ladder model. The fits to the (a) $x = 0$, (b) $x = 0.05$, (c) $x = 0.1$, (d) $x = 0.2$ and (e) $x = 0.3$ susceptibility data are shown by the red line. The legend in the plots show the values obtained for the fitting parameters: J_{leg} , J_{rung}/J_{leg} and g . Panel (f) is a depiction of the spin ladder model.

Table 5.2: The values of the J_{leg} , J_{rung}/J_{leg} and g parameters determined from fitting the $Ba_2CuTe_{1-x}W_xO_6$ susceptibility data using the isolated two-leg spin ladder model.

x	0	0.05	0.1	0.2	0.3
J_{leg} (K)	85.35(4)	92.0(4)	98.8(2)	102.8(1)	102(1)
J_{rung}/J_{leg}	1.0483(6)	0.816(9)	0.546(6)	0.278(4)	0.11(14)
g	2.2234(9)	2.186(2)	2.190(1)	2.1360(5)	2.08(2)

Table 5.2 shows W^{6+} substitution at the corner-sharing site decreases the value of the J_{rung}/J_{leg} ratio from $J_{rung}/J_{leg} \sim 1$ for $x = 0$ to a value of $J_{rung}/J_{leg} = 0.11(14)$ upon reaching $x = 0.3$. The slight increase in the value of J_{leg} with increasing x is too small to account for the large reduction in J_{rung}/J_{leg} ; suppression of the J_{rung} interaction must also contribute. The decrease in J_{rung}/J_{leg} is caused by slight strengthening of J_{leg} and strong suppression of J_{rung} by W^{6+} . As the illustration depicts in Fig. 5.6, weakening of the J_{rung} interaction causes the magnetic geometry to increasingly resemble a spin chain rather than a ladder as x increases. To assess this, the magnetic susceptibility data was also modelled using the Heisenberg spin chain model defined in equation 5.2.^{18,19}

$$\chi = \frac{N\mu_B^2}{k_B} \frac{0.25 + 0.14995\left(\frac{J_{chain}}{T}\right) + 0.30094\left(\frac{J_{chain}}{T}\right)^2}{1 + 1.9862\left(\frac{J_{chain}}{T}\right) + 0.68854\left(\frac{J_{chain}}{T}\right)^2 + 6.0626\left(\frac{J_{chain}}{T}\right)^3} + \chi_0 \quad (5.2)$$

The fitting parameters in the spin chain model are the Landè g -factor and the chain interaction (J_{chain}). The plots in Fig. 5.7 show the Heisenberg spin chain fits to the magnetic susceptibility data. Comparing the spin chain and spin ladder fits in Fig. 5.5 and Fig. 5.7, respectively, shows both models adequately describe the high temperature susceptibility. Differences between the models occur at lower temperatures, about the broad T_{max} feature. Panels (a) to (c) show the spin chain fit provides a poor description of the $x = 0, 0.05$ and 0.1 susceptibility curves about T_{max} . However, beyond $x = 0.1$ the spin chain model depicted in panel (f) begins to describe the T_{max} feature well as the J_{rung}/J_{leg} ratio decreases and T_{max} becomes broader.

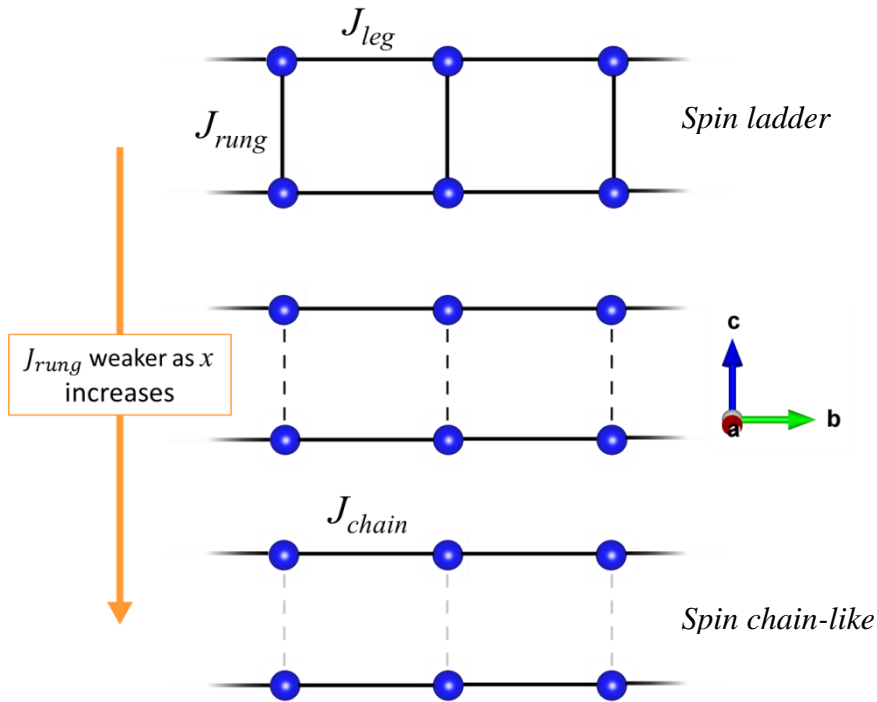


Fig. 5.6 Illustration depicting suppression of the J_{rung} interaction as x in $Ba_2CuTe_{1-x}W_xO_6$ increases. Suppression of the J_{rung} interaction leads to a gradual transition from a spin ladder towards a spin chain-like magnetic geometry on approaching $x = 0.3$.

These observations are in agreement with the calculated features of the spin ladder and spin chain models. The isolated two-leg spin ladder model and Heisenberg spin chain models are similar at high temperatures. But at low temperatures the spin ladder model has a sharp, asymmetric T_{max} feature when $J_{rung}/J_{leg} = 1$. Alternatively, the Heisenberg spin chain produces a more symmetric, broader T_{max} feature. The magnetic susceptibility of the isolated two-leg spin ladder model has also been calculated using different J_{rung}/J_{leg} ratios.¹³ As the J_{rung}/J_{leg} ratio decreases, the calculated T_{max} feature becomes broader and symmetric i.e. more like the spin chain model. The observation of this behaviour in the experimental magnetic susceptibility curves in Fig. 5.5 and Fig. 5.7 supports the decrease in J_{rung}/J_{leg} .

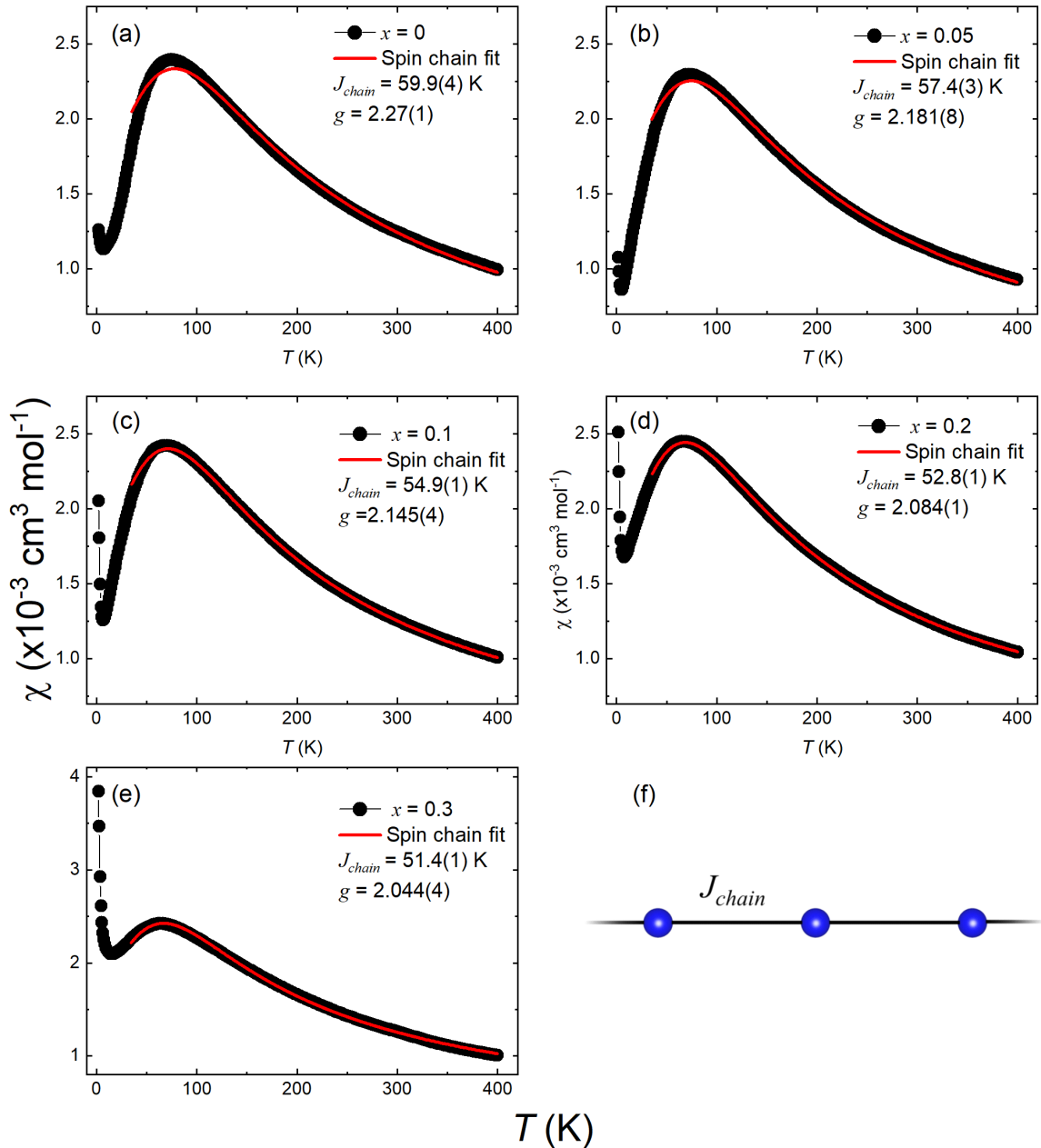


Fig. 5.7 Modelling of the $\text{Ba}_2\text{CuTe}_{1-x}\text{W}_x\text{O}_6$ susceptibility data using the Heisenberg spin chain model. The fits to the (a) $x = 0$, (b) $x = 0.05$, (c) $x = 0.1$, (d) $x = 0.2$ and (e) $x = 0.3$ susceptibility data are shown by the red line. The legend in the plots show the values obtained for the fitting parameters: J_{chain} and g . Panel (f) is a depiction of the spin ladder model.

To illustrate further, the spin ladder fits with $J_{rung}/J_{leg} = 1$ and spin chain fits for $x = 0$ and $x = 0.2$ are compared in Fig. 5.8. The spin ladder fit shown in red clearly provides the best description of the $x = 0$ susceptibility data, but fails to adequately describe the $x = 0.2$ data. The model produces a T_{max} feature that is sharper than that experimentally observed for $x = 0.2$. The reverse occurs for the spin chain fits shown in blue. Now, the spin chain model describes the sharp T_{max} feature of $x = 0$ poorly, while the fit to the $x = 0.2$ data is superior to the spin ladder. The broad, symmetric T_{max} feature is reproduced almost exactly, and the description of the high temperature susceptibility is also improved. This further supports a shift in the magnetic geometry from spin ladder towards a spin chain as a result of site-selective W^{6+} substitution.

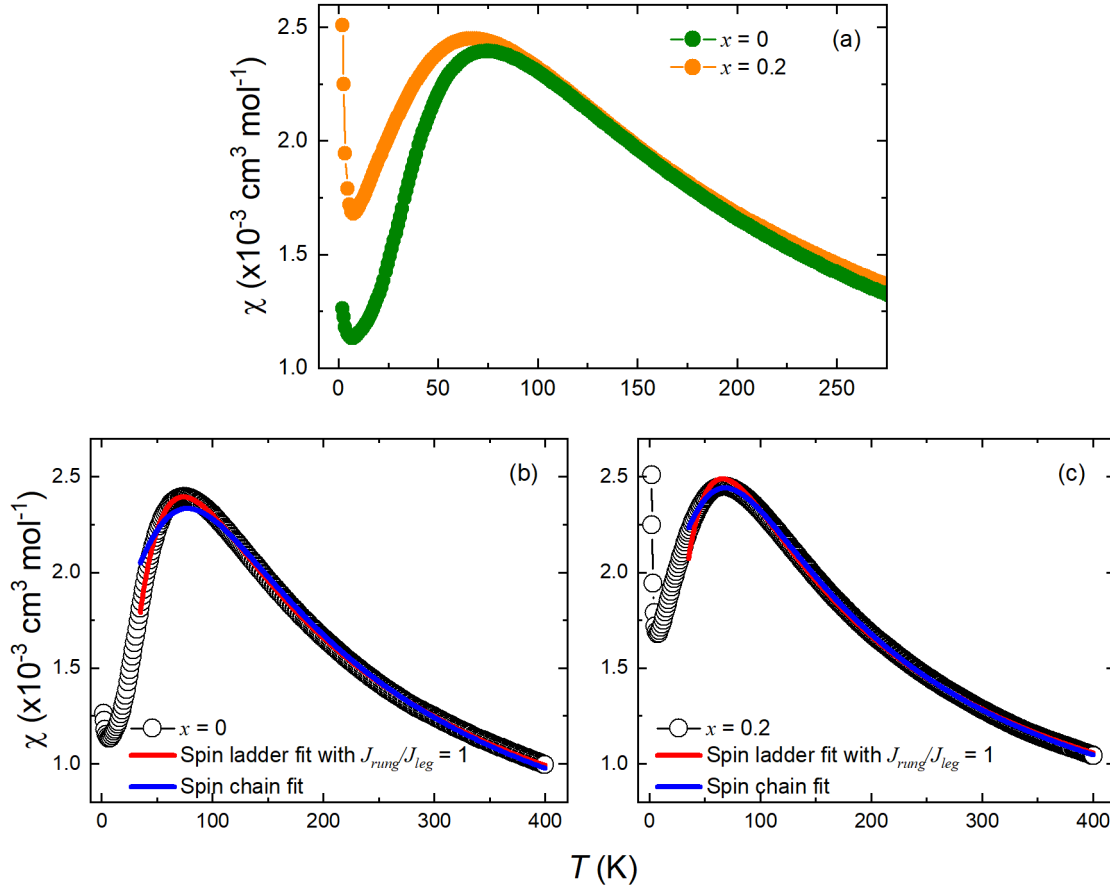


Fig. 5.8 Comparison of the spin ladder and spin chain fits to the Ba_2CuTeO_6 ($x = 0$) and $Ba_2CuTe_{0.8}W_{0.2}O_6$ ($x = 0.2$) susceptibility data. Panel (a) compares the DC magnetic susceptibility data of $x = 0$ and $x = 0.2$ about the position of T_{max} . The T_{max} peak is broader and more symmetric in the $x = 0.2$ data compared to the $x = 0$. Panel (b) compares the spin ladder fit with $J_{rung}/J_{leg} = 1$ (red line) and the spin chain (blue line) to the $x = 0$ susceptibility data. The spin ladder model provides a much better description of the sharper, asymmetric T_{max} peak. Panel (c) shows the corresponding spin ladder with $J_{rung}/J_{leg} = 1$ and spin chain fit to the $x = 0.2$ susceptibility data. Now, the broader, symmetric T_{max} peak is best described by the spin chain model (blue line), instead of the spin ladder (red line).

d. Heat capacity

Fig. 5.9a shows the zero-field heat capacity C_p of the $x = 0, 0.05, 0.1, 0.2$ and 0.3 samples. The C_p/T vs T curve for $x = 0$ shown in green possesses no lambda peak to indicate magnetic ordering. The inset shows an expansion of the low temperature data. There are no features to indicate a transition about the known position of T_N at ~ 14 K. This agrees with previous heat capacity measurements of Ba_2CuTeO_6 .^{16,17} Unless a very small temperature step is used, heat capacity measurements are insensitive to the Néel ordering transition in Ba_2CuTeO_6 as the large quantum fluctuations spread out the magnetic entropy making it difficult to distinguish a clear lambda peak.^{6,15-17}

The C_p/T vs T curve for $x = 0$ was compared to the W^{6+} substituted $Ba_2CuTe_{1-x}W_xO_6$ samples. The shape of the curves are similar, and there are no clear signatures of a lambda ordering peak in the $x = 0.05, 0.1, 0.2$ and 0.3 data. There appears to be a trend in the heat capacity data at high temperatures. The high temperature heat capacity generally decreases with increasing x , with the

exception of $x = 0.2$, where the high temperature heat capacity is higher than the other samples. This behaviour arises from the silver contribution to the heat capacity. At high temperatures, the silver contribution to the heat capacity dominates over the sample contribution. This makes the silver correction at high temperatures less accurate leading to variations in the high temperature data. The low temperature data is not affected as the silver contribution is much smaller.

The expansion of the low temperature C_p/T vs T^2 data in Fig. 5.9b shows the heat capacity of the W^{6+} substituted samples does not tend towards zero, unlike the Ba_2CuTeO_6 sample. This implies a non-zero magnetic entropy exists at zero Kelvin. The linear data can be fitted using the Debye-Einstein model in equation 5.3. The Debye-Einstein model combines the Debye model and Einstein models to describe the lattice (phonon) and electronic contributions to the heat capacity of a material, where γ is the electronic contribution to C_p and β_D is the phonon contribution.

$$C_p = \gamma T + \beta_D T^3 \quad (5.3)$$

The γ contribution to C_p was calculated from the intercept of the fit to the C_p/T vs T^2 data plotted in Fig. 5.9b. The values of γ are plotted as a function of x in $Ba_2CuTe_{1-x}W_xO_6$ in Fig. 5.9c. γ for $x = 0$ is almost zero, as expected for an antiferromagnetic insulator. As x increases, the value of γ increases from near zero to a value of $29.6(2) \text{ mJ mol}^{-1} \text{ K}^{-2}$ for the $x = 0.3$ sample. A significant γ contribution was observed in the $Sr_2CuTe_{1-x}W_xO_6$ samples. The γ value for $x = 0.3$ is over 50% of the value determined for $Sr_2CuTe_{0.5}W_{0.5}O_6$, where $\gamma = 54.2(5) \text{ mJ mol}^{-1} \text{ K}^{-2}$. The polycrystalline $Ba_2CuTe_{1-x}W_xO_6$ samples are all yellow implying a significant band gap. The colour changes from a light yellow to darker yellow as x increases suggesting W^{6+} modifies the band gap. Therefore, the $Ba_2CuTe_{1-x}W_xO_6$ samples can be regarded as insulators. For an insulator, the electronic contribution to the heat capacity must originate from magnetic excitations, and not conduction electrons.

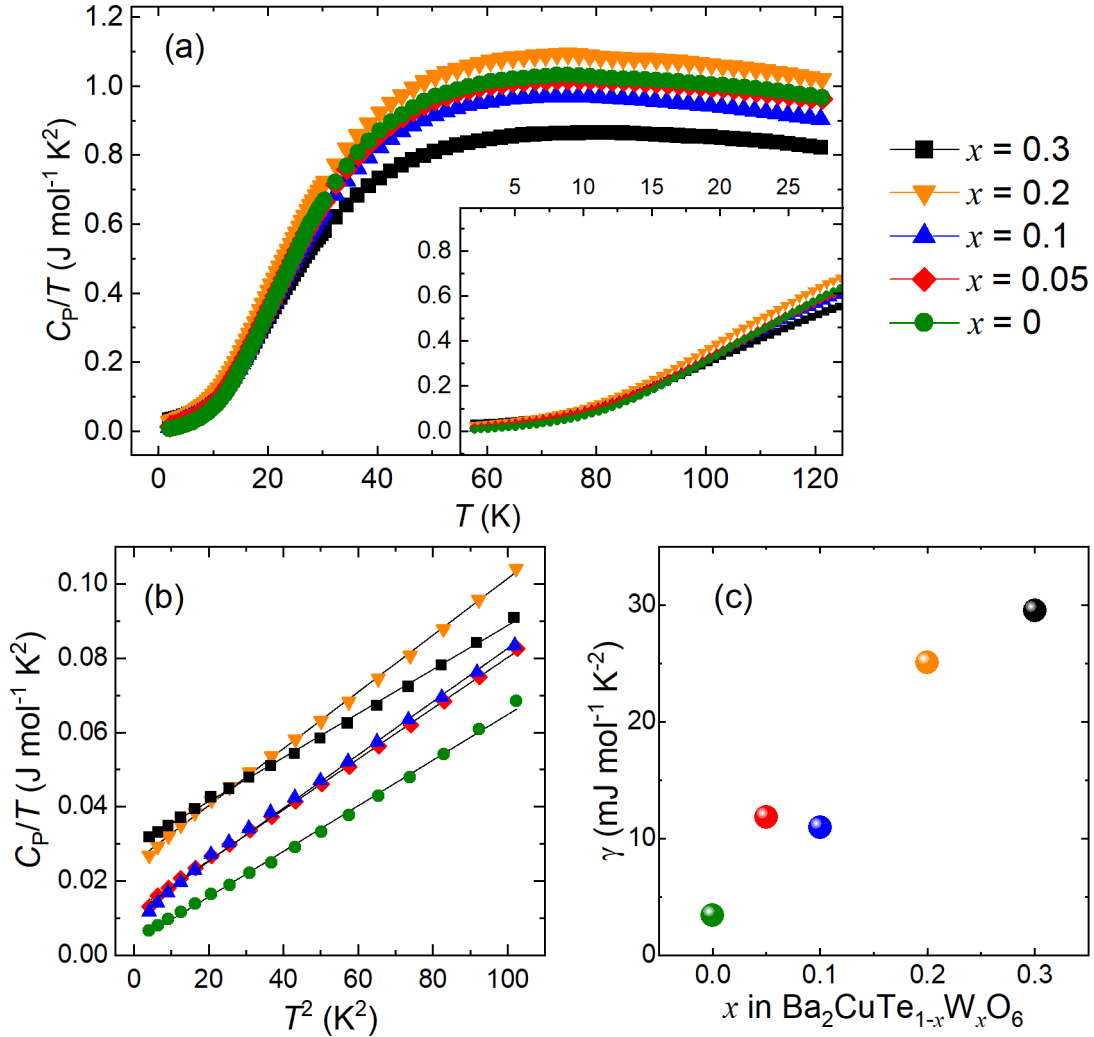


Fig. 5.9 The heat capacity data of the $\text{Ba}_2\text{CuTe}_{1-x}\text{W}_x\text{O}_6$ $x = 0, 0.05, 0.1, 0.2$ and 0.3 samples. Panel (a) shows the C_p/T vs T data from 2-120 K. The inset is an expansion of the low temperature heat capacity. There is no evidence of a lambda peak in any of the $\text{Ba}_2\text{CuTe}_{1-x}\text{W}_x\text{O}_6$ samples, including $x = 0$. Panel (b) shows the C_p/T vs T^2 data of all samples. The C_p/T vs T^2 data is linear and can be fitted using the Debye-Einstein model. The Debye-Einstein fits are shown by the black lines. From the Debye-Einstein fits it was possible to determine the electronic contribution (γ) to the heat capacity which is plotted as a function of x in $\text{Ba}_2\text{CuTe}_{1-x}\text{W}_x\text{O}_6$ in panel (c).

e. Muon Spin Relaxation (μSR)

Bulk magnetic characterisation is mostly insensitive to antiferromagnetic ordering in $\text{Ba}_2\text{CuTeO}_6$. Zero-field (ZF)- μSR experiments were one of the key techniques that confirmed magnetic order.¹⁵ Therefore, muon experiments were performed on the $\text{Ba}_2\text{CuTe}_{1-x}\text{W}_x\text{O}_6$ samples. ZF- μSR experiments were performed using the HIFI muon beamline. The ZF- μSR measurement of $x = 0$ at 2 K are shown in Fig. 5.10a. There are clear oscillations that can be fitted using a similar function to that employed by Ref.¹⁵ previously. The muon polarization function ($P(t)$) in equation 5.4 combines an exponentially relaxing cosine with an exponential relaxation function; with an additional A_{bkgd} term to describe the background.

$$P(t) = A_L e^{-\lambda_L t} + A_T e^{-\lambda_T t} \cos(2\pi f t + \phi) + A_{bkgd} \quad (5.4)$$

A_L and A_T are the asymmetry of the longitudinal and transverse muon polarization at time zero, respectively. λ_L and λ_T are the longitudinal and transverse muon polarization relaxation rates, respectively. f is the frequency and ϕ the phase of the oscillation. The fit to the 2 K ZF- μ SR data is shown by the red line in Fig. 5.10a. The ZF muon polarization is described well using this function and produces values of $\lambda_T = 1.40(5) \mu\text{s}^{-1}$ and $f = 3.815(5) \text{ MHz}$. These are close to the values reported previously where $\lambda_T \sim 1.7 \mu\text{s}^{-1}$ and $f \sim 4 \text{ MHz}$.¹⁵

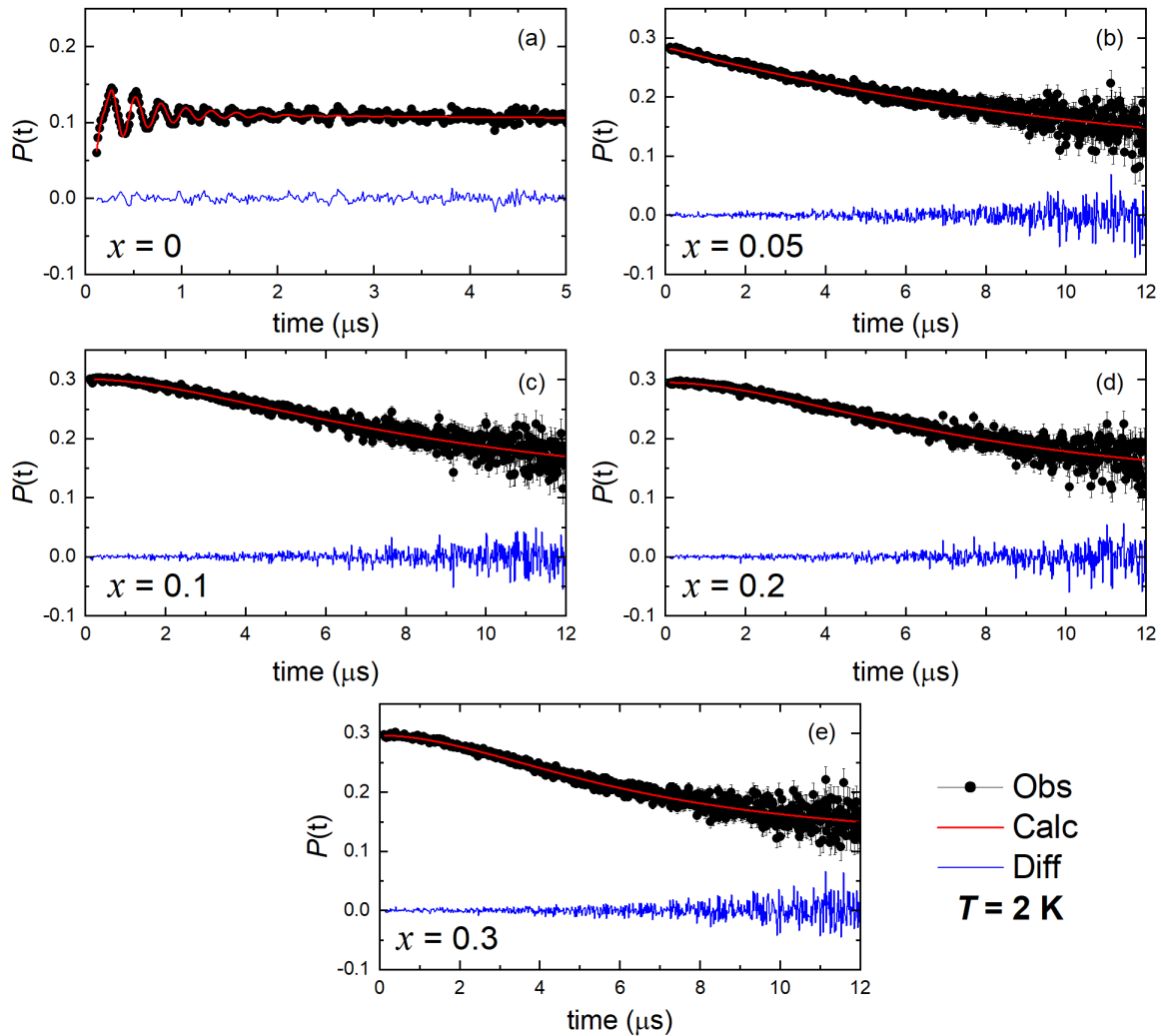


Fig. 5.10 The HIFI ZF- μ SR measurements of (a) $\text{Ba}_2\text{CuTeO}_6$ ($x = 0$), (b) $\text{Ba}_2\text{CuTe}_{0.95}\text{W}_{0.05}\text{O}_6$ ($x = 0.05$), (c) $\text{Ba}_2\text{CuTe}_{0.9}\text{W}_{0.1}\text{O}_6$ ($x = 0.1$), (d) $\text{Ba}_2\text{CuTe}_{0.8}\text{W}_{0.2}\text{O}_6$ ($x = 0.2$) and (e) $\text{Ba}_2\text{CuTe}_{0.7}\text{W}_{0.3}\text{O}_6$ ($x = 0.3$) at 2 K. In panel (a) there are clear oscillations indicating magnetic order for $x = 0$. In contrast, there are no oscillations in panels (b) to (e) to indicate magnetic ordering in the $x = 0.05$ to $x = 0.3$ samples. The red lines in the plots are the fits to the experimentally measured muon polarization. The $x = 0$ ZF- μ SR data was fitted using an exponential relaxation function combined with an exponentially relaxing cosine function. The $x = 0.05$ to 0.3 data were all fitted using the dynamic Kubo-Toyabe function. The blue lines show the difference between the experimental data and the calculated fit.

The ordering temperature of $x = 0$ was determined using transverse-field (TF)- μ SR experiments. In a 90 G TF field, paramagnetic behaviour was observed at 20 K. The muons precessed in the direction of the external TF field generating an oscillatory signal. The initial TF asymmetry of the oscillation was maintained on cooling until the magnetic transition temperature was reached. At the transition,

the TF oscillations began to dampen as the muons coupled to the internal magnetic field. Dampening of the TF oscillations is observed by comparing the TF- μ SR measurements at 20 K and 2 K in Fig. 5.11a and 5.11b, respectively. The TF oscillations were fitted using equation 5.4 to determine how the normalized transverse asymmetry ($A_T(T)/A_T(45\text{ K})$) evolved with temperature (T). $A_T(T)/A_T(45\text{ K})$ is plotted as a function of T in Fig. 5.11c. Dampening of $A_T(T)/A_T(45\text{ K})$ occurs between 14-15 K; in agreement with the $T_N = 14.1\text{ K}$ obtained for $\text{Ba}_2\text{CuTeO}_6$ using ZF- μ SR measurements.¹⁵

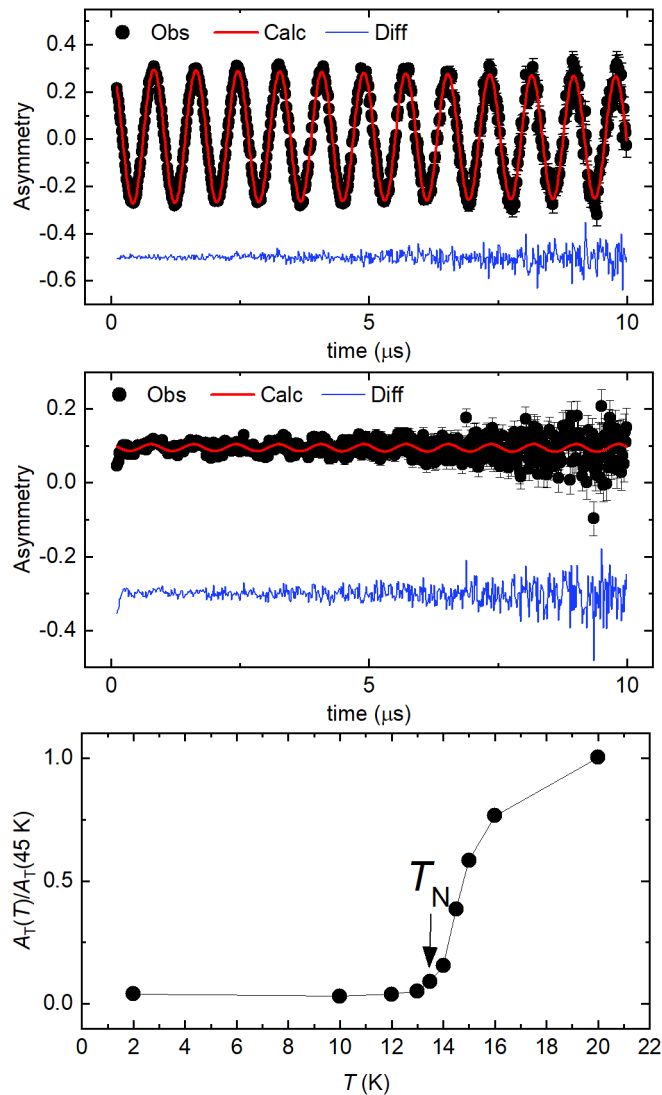


Fig. 5.11 (a) The TF- μ SR measurements of $\text{Ba}_2\text{CuTeO}_6$ ($x = 0$) at 20 K. The muon senses a paramagnetic environment and precesses around the externally applied transverse magnetic field of 90 G. (b) The TF- μ SR measurement of $x = 0$ at 2 K. Now, long-range ordering causes the muon spin to couple to the internal magnetic field, thus dampening the transverse asymmetry (A_T). Panel (c) plots the normalized $A_T(T)/A_T(45\text{ K})$ as a function of temperature.

In Fig. 5.10 the 2 K ZF- μ SR measurements of $x = 0.05, 0.1, 0.2$ and 0.3 in panels (b) to (e) are compared to the 2 K ZF- μ SR measurement of $x = 0$ in panel (a). There is a clear difference between the muon polarization of the $\text{Ba}_2\text{CuTeO}_6$ and $\text{Ba}_2\text{CuTe}_{1-x}\text{W}_x\text{O}_6$ samples ($x > 0$). There are no oscillations present in the $x = 0.05, 0.1, 0.2$ and 0.3 ZF- μ SR data. Instead, the muon polarization

resembles the dynamic Kubo-Toyabe function. The red line in the plots in panels (b)-(e) are the fits to the ZF- μ SR data using the dynamic Kubo-Toyabe function in equation 5.5.

$$P_z(t) = p_z(t) + v \int_0^t p_z(t') P_z(t-t') dt' \quad (5.5)$$

The dynamic Kubo-Toyabe function is examined between time t and t' and contains the static Kubo-Toyabe function, $p_z(t)$ and the fluctuation rate, v . The dynamic Kubo-Toyabe function provided a good description of the $x = 0.05, 0.1, 0.2$ and 0.3 ZF- μ SR data showing the muon spins experience a dynamic magnetic environment down to 2 K.

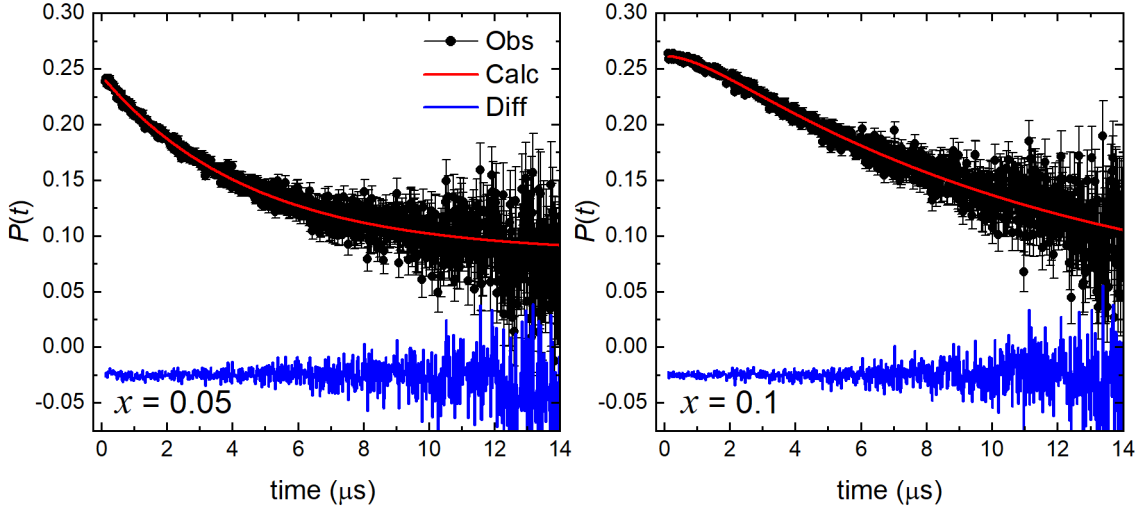


Fig. 5.12 The MUSR ZF- μ SR measurements of (a) $Ba_2CuTe_{0.95}W_{0.05}O_6$ ($x = 0.05$) and (b) $Ba_2CuTe_{0.9}W_{0.1}O_6$ ($x = 0.1$) at 90 mK and 50 mK, respectively. For $x = 0.05$, the muon polarization relaxes faster at short times cf. $x = 0.1$. The $x = 0.05$ ZF muon polarization can be described using an exponential muon decay function (goodness of fit, $\chi^2 = 1.170$). The $x = 0.1$ muon polarization is described using the Keren function (goodness of fit, $\chi^2 = 1.161$). The red lines in the plots are the calculated fits to the observed muon polarization.

The $x = 0.05$ and $x = 0.1$ samples were further investigated in a helium dilution fridge experiment on the MUSR beamline. Fig. 5.12 compares the ZF- μ SR measurements of $x = 0.05$ and $x = 0.1$ at 90 mK and 50 mK, respectively. Neither contains oscillations to suggest long-range order; and there is no $1/3$ recovery of the initial polarization to suggest a static local field. Panel (b) in Fig. 5.10 shows the muon polarization for $x = 0.05$ relaxes faster at low times compared to the other samples in panels (c) to (e). In Fig. 5.12a at 90 mK, the faster ZF relaxation is accentuated. The $x = 0.05$ muon polarization is exponential and could be fitted using the $P(t)$ function in equation 5.6.

$$P(t) = Ae^{-\lambda t} + A_{bkgd} \quad (5.6)$$

Here, λ is the decay rate of the initial muon polarization, A . A faster muon relaxation at low times suggests there is more electronic relaxation compared to nuclear. Both nuclear and electronic spins contribute to muon depolarization, but the effect of nuclear spins is weaker. ZF- μ SR measurements performed at higher temperatures in Fig. 5.13a were fitted using equation 5.6. The value of λ derived from the fits is plotted as a function of temperature in Fig. 5.13b. λ increases as the temperature decreases, implying slowing down of the spin fluctuations. Faster relaxation occurs as the dynamics slow down at lower temperatures. This causes the muon to experience less of an

average field and more of the fluctuating magnetic field resulting in faster muon relaxation. The decay rate plateaus to a constant value of $\lambda \sim 0.21 \mu\text{s}^{-1}$ below 1.25 K. Plateauing of λ is a common feature observed in the ZF- μSR of a quantum spin liquid. Therefore, the behaviour of $x = 0.05$ is dynamic down to 90 mK and resembles a quantum spin liquid.^{1,20}

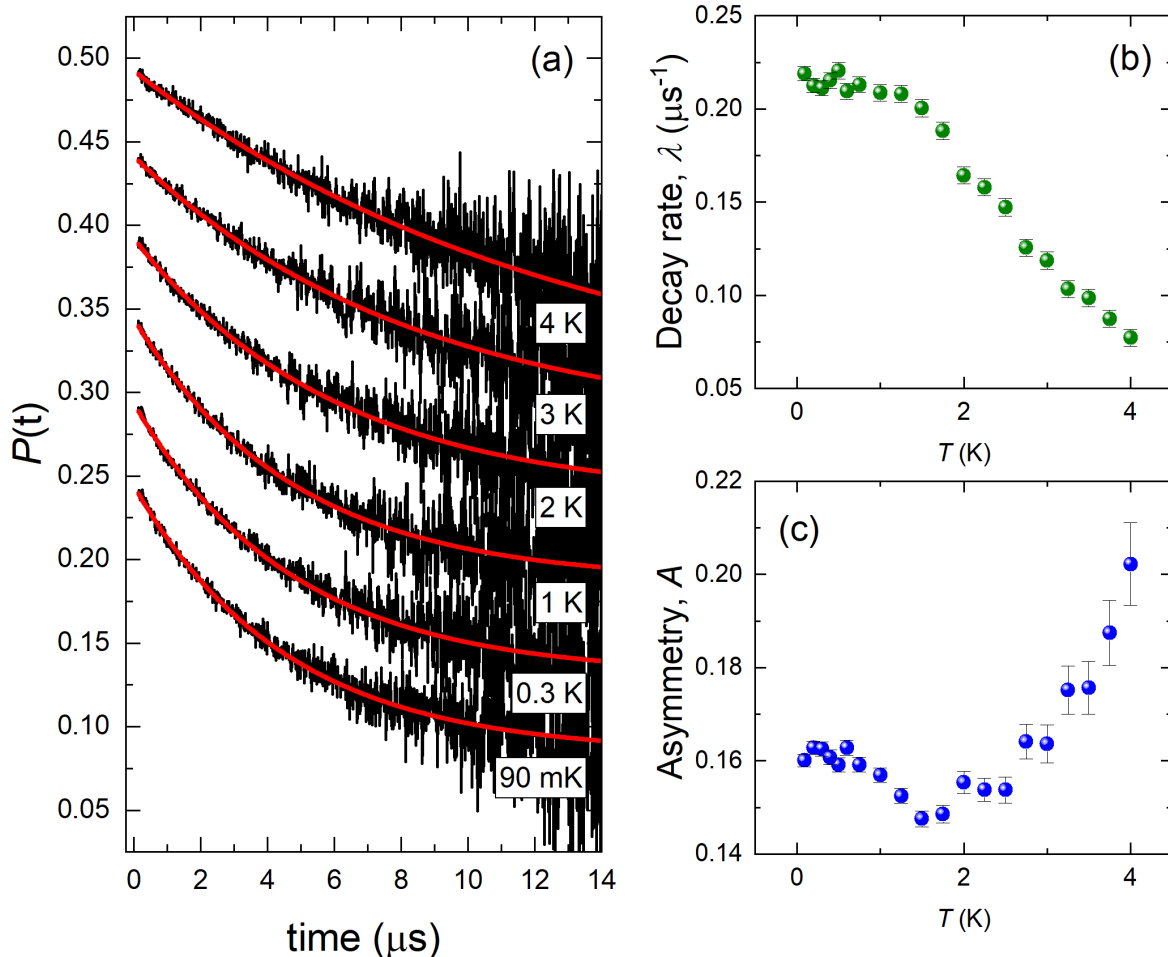


Fig. 5.13 (a) The μSR ZF- μSR measurements of $\text{Ba}_2\text{CuTe}_{0.95}\text{W}_{0.05}\text{O}_6$ ($x = 0.05$) at various temperatures between 90 mK and 4 K. The data have been offset to observe the changes clearly. The red lines show the fits to the ZF data using the function in equation 5.6. (b) The muon relaxation rate (λ) plotted as a function of temperature. (c) The initial asymmetry (A) as a function of temperature.

The low time muon relaxation for $x = 0.1$ does not decay as quickly as $x = 0.05$ (see Fig. 5.12). Longitudinal-field (LF) measurements were performed to determine the field strength required to repolarize the ZF muon polarization. Fig. 5.14 compares the LF- μSR data of (a) $x = 0.05$ and (b) $x = 0.1$ at fields between 20 to 1000 G. Only 20 G was required to repolarize the muon spins in $x = 0.1$ (Fig. 5.14b). Conversely, repolarization of the muon spin in $x = 0.05$ was more gradual and required larger fields (Fig. 5.14a). Decoupling of the muon spin from electronic fields requires larger fields. This implies muon relaxation of $x = 0.05$ has a greater dynamic electronic contribution. Whereas, slower muon relaxation in $x = 0.1$ implies a suppressed dynamic electronic contribution. Relaxation in $x = 0.1$ is likely to occur from a static nuclear and weak dynamic electronic contribution. The static nuclear contribution is generated by static random nuclear fields which depolarize the muon spin.

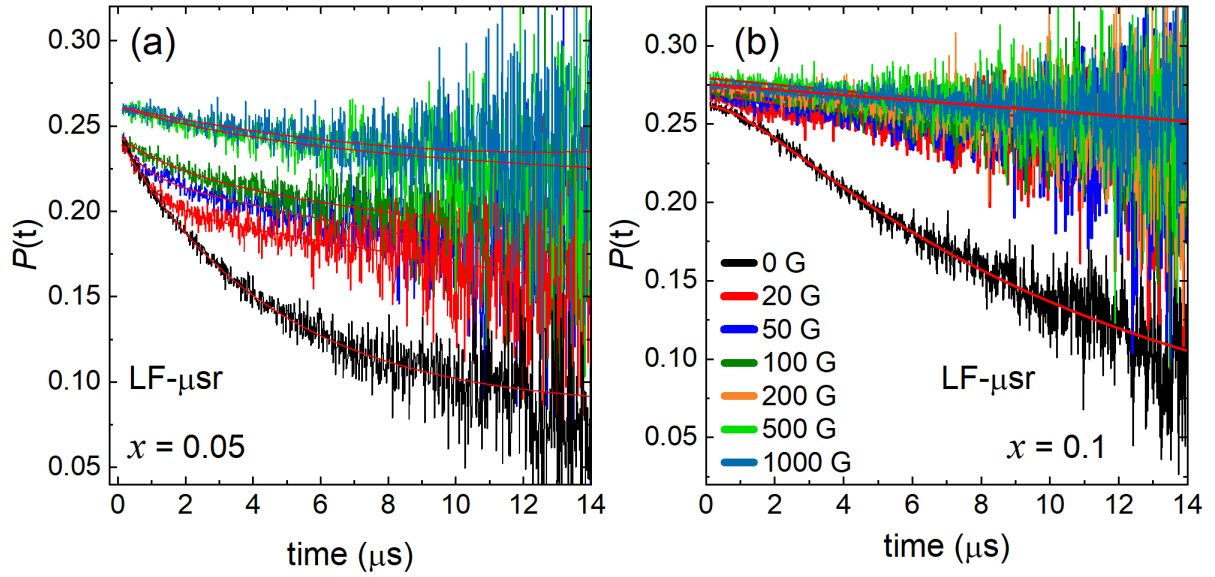


Fig. 5.14 The LF- μ SR measurements of (a) $Ba_2CuTe_{0.95}W_{0.05}O_6$ ($x = 0.05$) at 90 mK and (b) $Ba_2CuTe_{0.9}W_{0.1}O_6$ ($x = 0.1$) at 50 mK. The plot shows the muon polarization when longitudinal-fields between 20 – 1000 G were applied in the direction of the incoming muon beam. For comparison, the ZF- μ SR measurements in a 0 G field are also shown.

The $x = 0.1$ ZF- μ SR data was fitted using the combination of a static Kubo-Toyabe and exponential relaxation to describe the respective static nuclear and dynamic electronic contributions to the muon depolarization. The fit to the 50 mK ZF- μ SR data using the function in equation 5.7 is shown in Fig. 5.15a. δ is the decay rate of the muon polarization. This function provides an adequate description of the muon polarization at long times, but overestimates the initial asymmetry at short times.

$$P(t) = Ae^{-\lambda t} \left(\frac{1}{3} + \frac{2}{3} e^{-\frac{1}{2}\delta^2 t^2} (1 - \delta^2 t^2) \right) + A_{bkgd} \quad (5.7)$$

Instead, fitting was performed using a function known as the Keren function. The Keren function is designed to describe muon environments where both dynamic and static fields contribute to the muon relaxation.²¹ The Keren function is shown in equation 5.8.

$$P_z(t) = A \exp[-\Gamma(t)t] \quad (5.8)$$

Where, $\Gamma(t)$ is the relaxation rate given by:

$$\Gamma(t)t = 2\Delta^2 \frac{\{(\omega_L^2 + v^2)vt + (\omega_L^2 - v^2)(1 - e^{-vt} \cos(\omega_L t)) - 2v\omega_L e^{-vt} \sin(\omega_L t)\}}{(\omega_L^2 + v^2)^2} \quad (5.9)$$

The expression for the relaxation rate contains the muon fluctuation rate (v) the width of the distribution of local fields (Δ) and the Larmor precession frequency of the muon spin (ω_L). The fit using the Keren function is shown in Fig. 5.15b. The Keren function provides a much better description of the $x = 0.1$ ZF- μ SR data at short times. The Keren function also describes the high temperature data well. Fig. 5.16a shows the Keren function fits to the ZF- μ SR muon polarization up to 2 K. The fit quality reduces above 2 K indicating a change in the behaviour towards the dynamic Kubo-Toyabe behaviour observed in the HIFI data. From the fits in Fig. 5.16a, the values of v and Δ

were determined. The distribution width of the local fields is ~ 0.2 MHz (Fig. 5.16c) and is approximately constant between 50 mK to 2 K. The fluctuation rate increases as the system becomes more dynamic with increasing temperature (Fig. 5.16d). The value of ν does not reach zero showing a dynamic component still exists at 50 mK.

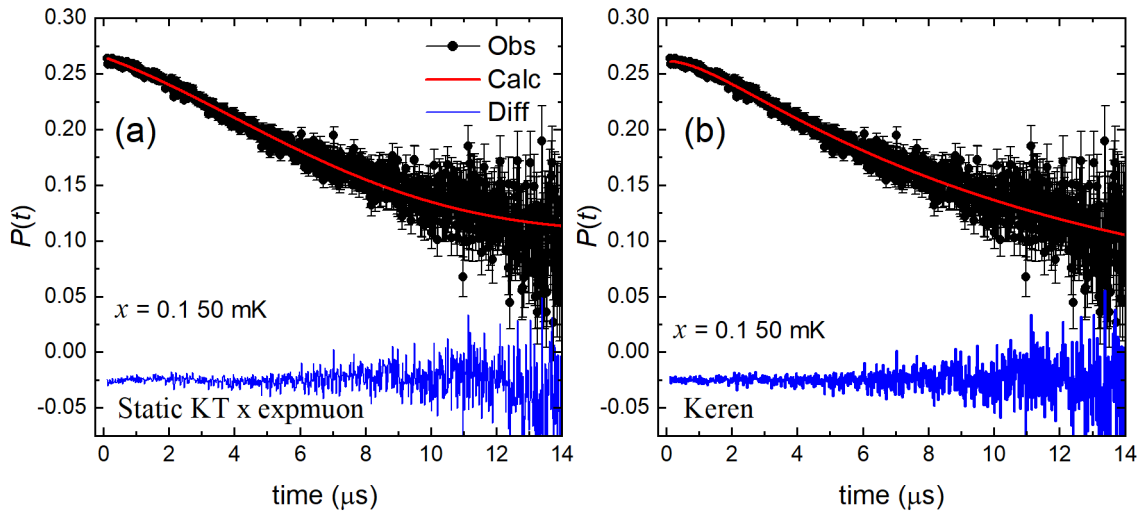


Fig. 5.15 (a) The ZF- μ SR data of $Ba_2CuTe_{0.9}W_{0.1}O_6$ ($x = 0.1$) at 50 mK in which the muon polarization is described using the combination of a static Kubo-Toyabe function multiplied by an exponential muon decay function. (b) Fitting of the same ZF- μ SR data for $x = 0.1$ at 50 mK using the Keren function. The fits are shown by the red lines. The fit using the Keren function provides a much better description of the relaxation at low times and provides the best fit. The goodness of fit in panel (a) was $\chi^2 = 1.269$ (static KT x expmuon) and in panel (b) $\chi^2 = 1.161$ (Keren).

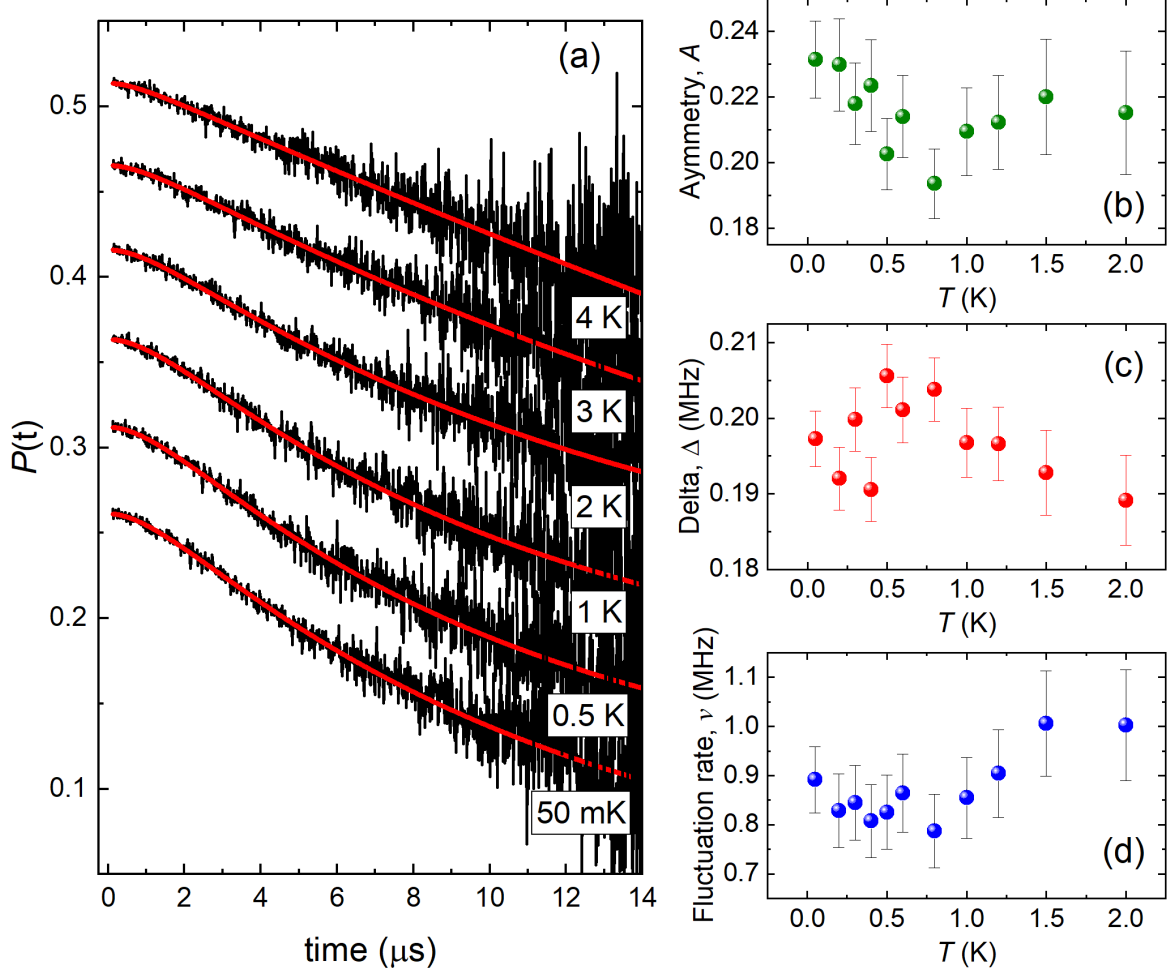


Fig. 5.16: (a) The ZF- μ SR measurements of $\text{Ba}_2\text{CuTe}_{0.9}\text{W}_{0.1}\text{O}_6$ ($x = 0.1$) between 50 mK and 2 K. The red lines in the plot are the fits to the muon relaxation using the Keren function.²⁰ Panels (b) to (c) plot the Keren function parameters determined from the fits: (b) The initial asymmetry (A) of the ZF muon relaxation as a function of temperature; (c) The width of the local field distribution (Δ) as a function of temperature; and (d) The muon fluctuation rate (ν) as a function of temperature.

5. Discussion

Modelling the DC magnetic susceptibility data shows W^{6+} substitution at the corner-sharing site directly modified the intra-ladder interactions. J_{leg} was slightly strengthened, while J_{rung} was strongly suppressed causing the $J_{\text{rung}}/J_{\text{leg}}$ ratio to decrease from near unity for $x = 0$ ($J_{\text{rung}}/J_{\text{leg}} = 1.0483(6)$) to nearly zero for $x = 0.3$ ($J_{\text{rung}}/J_{\text{leg}} = 0.11(14)$). This tuned the magnetic interactions from a spin ladder towards a spin chain. Weakening of the J_{rung} interaction agrees with the shift in the position of T_{max} . As x increases, T_{max} shifts from ~ 74 K to ~ 64 K. Given strong suppression of J_{rung} , the decrease in T_{max} might be expected to be more significant. Also, the Weiss constant does not suggest weakening of the magnetic interactions and remains approximately constant across the $\text{Ba}_2\text{CuTe}_{1-x}\text{W}_x\text{O}_6$ solid solution. The small shift in T_{max} is explained by considering the number of J_{rung} and J_{leg} interactions per Cu^{2+} site in the two-leg spin ladder model. Each Cu^{2+} cation is connected to three other Cu^{2+} cations via one J_{rung} and two J_{leg} interactions. Although J_{rung} is strongly suppressed, the net effect is moderate weakening of the overall intra-ladder interactions as twice the number of J_{leg} interactions are slightly strengthened. It is unclear why the Weiss constant does not increase with

the decreasing $J_{\text{rung}}/J_{\text{leg}}$ ratio. One possibility could be strong quantum fluctuations, combined with overall moderate weakening of the intra-ladder interactions that could obscure detection of minor changes in θ_W .

Introduction of W^{6+} produced a marked change in the DC susceptibility data. The upturn feature at 14 K gradually transitioned into a large Curie-tail like feature as x increased. This suggests W^{6+} doping produces a different ground state to Néel ordered $\text{Ba}_2\text{CuTeO}_6$. The AC susceptibility data showed no evidence of spin glass behaviour. The heat capacity data shows no evidence of a lambda peak to indicate magnetic ordering; however, the large quantum fluctuations make detection of a lambda ordering peak unlikely. A notable electronic contribution to the heat capacity was observed for the $\text{Ba}_2\text{CuTe}_{1-x}\text{W}_x\text{O}_6$ ($0.05 \leq x \leq 0.3$) samples, that was not present for $x = 0$. The large electronic contribution is similar to that observed for $\text{Sr}_2\text{CuTe}_{1-x}\text{W}_x\text{O}_6$ and must arise from free spins.

The HIFI and MUSR muon spin relaxation results confirmed suppressed Néel ordering. No oscillations were observed in the 2 K ZF- μ SR HIFI data of $x = 0.05, 0.1, 0.2$ and 0.3 . The MUSR ZF- μ SR data of $x = 0.05$ at 50 mK and $x = 0.1$ at 90 mK contained no oscillations or 1/3 recovery of the initial muon polarization to suggest long-range or static ordering. Hence, substituting 5% Te^{6+} for W^{6+} prevented Néel ordering. This is similar to $\text{Sr}_2\text{CuTe}_{1-x}\text{W}_x\text{O}_6$ where W^{6+} concentrations of $x = 0.025$ and $x = 0.05$ prevent Néel ordering.^{22,23} Hence, despite the differences in magnetic geometry, the disorder introduced by a small degree of competing $W^{6+} d^0$ vs $\text{Te}^{6+} d^{10}$ interactions has a powerful effect on the magnetic behaviour in these perovskites.

To summarise, the results show the main characteristics of the magnetic behaviour in $\text{Ba}_2\text{CuTe}_{1-x}\text{W}_x\text{O}_6$ are:

- (1) A large Curie tail-like feature in the DC magnetic susceptibility.
- (2) Large reduction in the $J_{\text{rung}}/J_{\text{leg}}$ ratio with increasing x showing tuning of the system from a spin ladder towards a spin chain.
- (3) No frequency dependent shift in the AC susceptibility.
- (4) Significant electronic contribution to the heat capacity of the $0.05 \leq x \leq 0.3$ samples.
- (5) No evidence of any oscillations or 1/3 recovery of the initial asymmetry in the muon spin relaxation data of the $x = 0.05, 0.1, 0.2$ and 0.3 samples.
- (6) Small electronic contribution to depolarization of the $x = 0.1$ muon spin relaxation.

The question remains: what type of ground state is created in $\text{Ba}_2\text{CuTe}_{1-x}\text{W}_x\text{O}_6$? One might theorize that W^{6+} substitution pushes $\text{Ba}_2\text{CuTeO}_6$ through the quantum critical point and into the spin singlet phase in Fig. 5.1. The spin singlet phase is consistent with a number of the observations above. For example, the large Curie tails observed in the DC susceptibility data could represent 'orphan spins' left over from singlet formation. The large electronic contribution to the heat capacity suggests low energy spin excitations, which could be singlet excitations. Formation of singlet dimers in an antiparallel orientation results in spin cancellation, thus reducing the magnitude of the dynamic electronic fields felt by the muon. This is consistent with the slow relaxation in the $x = 0.1$ ZF- μ SR data. However, the singlet state is reached by tuning of the J_{inter} ladder interaction in the two-leg spin ladder phase diagram. The two-leg spin ladder model phase diagram shown in Fig. 5.1 is only consistent for $J_{\text{leg}} = J_{\text{rung}}$. Suppression of the $J_{\text{rung}}/J_{\text{leg}}$ ratio towards a spin chain-like system puts $\text{Ba}_2\text{CuTe}_{1-x}\text{W}_x\text{O}_6$ on a different phase diagram to $\text{Ba}_2\text{CuTeO}_6$. Even if the intra-ladder interactions were unaffected and $J_{\text{rung}}/J_{\text{leg}} \sim 1$, the minor 5% occupancy of the face-sharing $B''(f)$ site makes it

unlikely that W^{6+} suppresses J_{inter} enough for $\text{Ba}_2\text{CuTe}_{1-x}\text{W}_x\text{O}_6$ to pass through the QCP into the singlet state.

Some of the magnetic behaviours observed for $\text{Ba}_2\text{CuTe}_{1-x}\text{W}_x\text{O}_6$ are similar to $\text{Sr}_2\text{CuTe}_{1-x}\text{W}_x\text{O}_6$. Recently, the spin-liquid like behaviour observed for $\text{Sr}_2\text{CuTe}_{1-x}\text{W}_x\text{O}_6$ has been ascribed as disorder induced.^{24,25} The disorder introduced from the competing $W^{6+} d^0$ and $\text{Te}^{6+} d^{10}$ interactions in $\text{Sr}_2\text{CuTe}_{1-x}\text{W}_x\text{O}_6$ forms a ground state with dynamic and partially frozen spins. The partially frozen spins are arranged in random networks with both Néel and columnar magnetic correlations creating a short-range ordered random bond state.²⁴ To unambiguously determine if this state forms in $\text{Ba}_2\text{CuTe}_{1-x}\text{W}_x\text{O}_6$, inelastic neutron scattering experiments are required. For a partially short-range ordered ground state, dispersive spin-wave like excitations would be expected in the inelastic neutron scattering spectra at low temperatures.

Alternatively, disorder could form a random singlet state (RSS). Simply viewed, the random singlet state consists of a random lattice covering of singlet dimers.²⁶ Singlet dimers are distance indifferent so can form between both neighbouring spins and spins further away. Singlet dimers can be isolated or form resonating singlet dimer clusters containing the superposition of more than one singlet dimer configurations. Singlet formation results in a fraction of disentangled (so called 'orphan spins') as a result of incomplete dimerization. Orphan spins can also be incorporated in resonating singlets. Therefore, each spin site in an RSS belongs to one of three possible spin configurations: isolated singlet, resonating singlet or orphan spin. The ground state consists of a mixture of all three spin configurations, with the proportion of each spin state varying.

The defining characteristics of a random singlet state are: T -linear low temperature heat capacity, Curie tails in the magnetic susceptibility data and a continuum of excitations in the inelastic neutron scattering spectra. The T -linear heat capacity originates from low energy singlet excitations and the Curie tails from the orphan spins. A continuum of excitations is expected as RSS formation leads to a distribution of exchange couplings resulting in gapless singlet-triplet excitations. There are no predictions of the RSS in a two-leg spin ladder. But, the random singlet state has been observed or predicted in a variety of frustrated lattices including the Kagomè^{27,28}, triangular²⁹, honeycomb lattice³⁰ and square lattice²⁵. A RSS state induced by W^{6+}/Te^{6+} disorder was predicted to be the ground state behind quantum spin liquid-like behaviour in $\text{Sr}_2\text{CuTe}_{1-x}\text{W}_x\text{O}_6$, but was ruled out because of the lack of any continuous excitations in the inelastic neutron spectra.^{24,25,31,32} Two of the features for an RSS state are observed for $\text{Ba}_2\text{CuTe}_{1-x}\text{W}_x\text{O}_6$, but conclusive proof requires inelastic neutron scattering.

6. Conclusions

The effect of W^{6+} substitution on the magnetic behaviour of $\text{Ba}_2\text{CuTeO}_6$ was investigated using bulk magnetic characterization techniques, susceptibility modelling and muon spin relaxation experiments. Modelling the DC susceptibility data showed site-selective W^{6+} substitution modified the intra-ladder magnetic interactions, tuning the system from a spin ladder towards a spin chain. Muon spin relaxation experiments showed this prevented Néel ordering. Site-specific tuning of the intra-ladder interactions means $\text{Ba}_2\text{CuTe}_{1-x}\text{W}_x\text{O}_6$ lies on a different phase diagram to the two-leg spin ladder. Disorder introduced by the mixture of W^{6+} and Te^{6+} cations might induce a random bond partially ordered state, as observed for $\text{Sr}_2\text{CuTe}_{1-x}\text{W}_x\text{O}_6$. A number of the magnetic behaviours observed for $\text{Ba}_2\text{CuTe}_{1-x}\text{W}_x\text{O}_6$ are also consistent with the characteristics of a random singlet state.

Inelastic neutron scattering experiments are required to determine the exact nature of the ground state. While the nature of the ground state is still unclear, it is clear that W^{6+} substitution levels as low as 5% are enough to prevent magnetic ordering through site-selective tuning of the spin ladder interactions. Quantifying the ratio of the intra-ladder interactions ($J_{\text{rung}}/J_{\text{leg}}$) conclusively proved the d^{10}/d^0 effect can modify the magnetic interactions in double *and* hexagonal perovskites.

7. References

1. Mustonen, O. *et al.* Spin-liquid-like state in a spin-1/2 square-lattice antiferromagnet perovskite induced by d^{10} - d^0 cation mixing. *Nat. Commun.* **9**, 1085 (2018).
2. Katukuri, V. M. *et al.* Exchange Interactions Mediated by Nonmagnetic Cations in Double Perovskites. *Phys. Rev. Lett.* **124**, 077202 (2020).
3. Watanabe, M. *et al.* Valence-bond-glass state with a singlet gap in the spin-1/2 square-lattice random J_1 - J_2 Heisenberg antiferromagnet $\text{Sr}_2\text{CuTe}_{1-x}\text{W}_x\text{O}_6$. *Phys. Rev. B* **98**, 054422 (2018).
4. Chitov, G. Y., Ramakko, B. W. & Azzouz, M. Quantum criticality in dimerized spin ladders. *Phys. Rev. B* **77**, 224433 (2008).
5. Furuya, S. C., Dupont, M., Capponi, S., Laflorencie, N. & Giamarchi, T. Dimensional modulation of spontaneous magnetic order in quasi-two-dimensional quantum antiferromagnets. *Phys. Rev. B* **94**, 144403 (2016) (2016).
6. Macdougall, D. *et al.* Spin dynamics of coupled spin ladders near quantum criticality in $\text{Ba}_2\text{CuTeO}_6$. *Phys. Rev. B* **98**, 174410 (2018).
7. Sachdev, S. Quantum magnetism and criticality. *Nat. Phys.* **4**, 173–185 (2008).
8. Vojta, M. Frustration and quantum criticality. *Reports Prog. Phys.* **81**, 064501 (2018).
9. Troyer, M. & Zhitomirsky, M. Nearly critical ground state of $\text{LaCuO}_{2.5}$. *Phys. Rev. B* **55**, R6117–R6120 (1997).
10. Sachdev, S. & Keimer, B. Quantum criticality. *Phys. Today* **64**, 29–35 (2011).
11. Matsumoto, M., Yasuda, C., Todo, S. & Takayama, H. Ground-state phase diagram of quantum Heisenberg antiferromagnets on the anisotropic dimerized square lattice. *Phys. Rev. B* **65**, 014407 (2001).
12. Barnes, T., Dagotto, E., Riera, J. & Swanson, E. S. Excitation spectrum of Heisenberg spin ladders. *Phys. Rev. B* **47**, 3196–3203 (1993).
13. Johnston, D. C. *et al.* Magnetic Susceptibilities of Spin-1/2 Antiferromagnetic Heisenberg Ladders and Applications to Ladder Oxide Compounds. *arXiv:cond-mat/0001147 [cond-mat]* (2000).
14. Imada, M. & Iino, Y. Scaling Properties of Antiferromagnetic Transition in Coupled Spin Ladder Systems Doped with Nonmagnetic Impurities. *J. Phys. Soc. Japan* **66**, 568–571 (1997).
15. Glamazda, A. *et al.* Quantum criticality in the coupled two-leg spin ladder $\text{Ba}_2\text{CuTeO}_6$. *Phys. Rev. B* **95**, 184430 (2017).
16. Gibbs, A. S. *et al.* $S=1/2$ quantum critical spin ladders produced by orbital ordering in $\text{Ba}_2\text{CuTeO}_6$. *Phys. Rev. B* **95**, 104428 (2017).

17. Rao, G. N. *et al.* Tellurium-bridged two-leg spin ladder in Ba₂CuTeO₆. *Phys. Rev. B* **93**, 104401 (2016).
18. Bonner, J. C. & Fisher, M. E. Linear Magnetic Chains with Anisotropic Coupling. *Phys. Rev.* **135**, A640-658 (1964).
19. Hatfield, W. E., Weller, R. R. & Hall, J. W. Exchange Coupling in the Sulfur-Bridged Quasi-Linear-Chain Compound Bis(dimethyldithiocarbamate)copper(II). Observations on Exchange in Sulfur-Bridged Copper(II) Compounds. *Inorg. Chemistry* **19**, 3825–3828 (1980).
20. Balz, C. *et al.* Physical realization of a quantum spin liquid based on a complex frustration mechanism. *Nat. Phys.* **12**, 942–949 (2016).
21. Keren, A. Generalization of the Abragam relaxation function to a longitudinal field. *Phys. Rev. B* **50**, 10039–10042 (1994).
22. Hong, W. *et al.* Extreme Suppression of Antiferromagnetic Order and Critical Scaling in a Two-Dimensional Random Quantum Magnet. *Phys. Rev. Lett.* **126**, 037201 (2021).
23. Yoon, S. *et al.* Quantum disordered state in the J_1 - J_2 square-lattice antiferromagnet Sr₂Cu(Te_{0.95}W_{0.05})O₆. *Phys. Rev. Mater.* **5**, 014411 (2021).
24. Fogh, E. *et al.* Randomness and Frustration in a $S = 1/2$ Square-Lattice Heisenberg Antiferromagnet. *arXiv:2112.03312v2 [cond-mat.str-el]* 1–7 (2022).
25. Uematsu, K. & Kawamura, H. Randomness-induced quantum spin liquid behavior in the $S = 1/2$ random J_1 - J_2 Heisenberg antiferromagnet on the square lattice. *Phys. Rev. B* **98**, 134427 (2018).
26. Kawamura, H. & Uematsu, K. Nature of the randomness-induced quantum spin liquids in two dimensions. *J. Phys. Condens. Matter* **31**, 504003 (2019).
27. Kawamura, H., Watanabe, K. & Shimokawa, T. Quantum spin-liquid behavior in the spin-1/2 random-bond Heisenberg antiferromagnet on the kagome lattice. *J. Phys. Soc. Japan* **83**, 103704 (2014).
28. Shimokawa, T., Watanabe, K. & Kawamura, H. Static and dynamical spin correlations of the $S = 1$ random-bond antiferromagnetic Heisenberg model on the triangular and kagome lattices. *Phys. Rev. B* **92**, 134407 (2015).
29. Watanabe, K., Kawamura, H., Nakano, H. & Sakai, T. Quantum spin-liquid behavior in the spin-1/2 random Heisenberg antiferromagnet on the triangular lattice. *J. Phys. Soc. Japan* **83**, 034714 (2014).
30. Uematsu, K. & Kawamura, H. Randomness-Induced Quantum Spin Liquid Behavior in the $S = 1/2$ Random J_1 - J_2 Heisenberg Antiferromagnet on the Honeycomb Lattice. *J. Phys. Soc. Japan* **86**, 044704 (2017).
31. Ren, H. Da, Xiong, T. Y., Wu, H. Q., Sheng, D. N. & Gong, S. S. Characterizing random-singlet state in two-dimensional frustrated quantum magnets and implications for the double perovskite Sr₂CuTe_{1-x}W_xO₆. *arXiv:2004.02128* 1–11 (2020).
32. Liu, L., Shao, H., Lin, Y. C., Guo, W. & Sandvik, A. W. Random-Singlet Phase in Disordered Two-Dimensional Quantum Magnets. *Phys. Rev. X* **8**, 041040 (2018).

8. Appendix

A1. Curie-Weiss fits of the $Ba_2CuTe_{1-x}W_xO_6$ DC susceptibility data

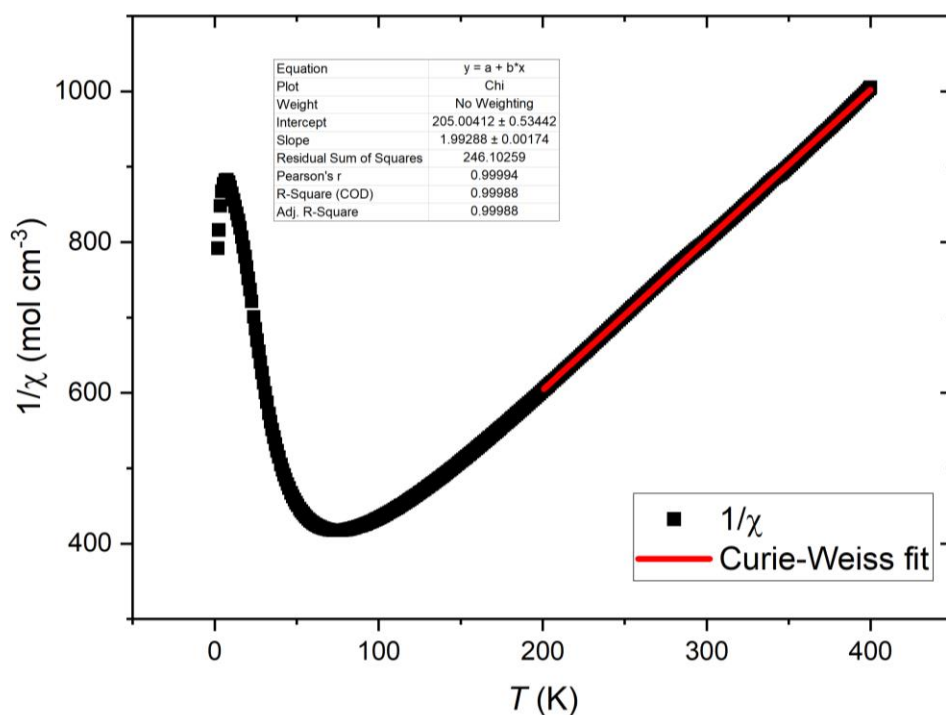


Fig. A5.1 Curie-Weiss fit of Ba_2CuTeO_6 ($x = 0$) between 200-400K.

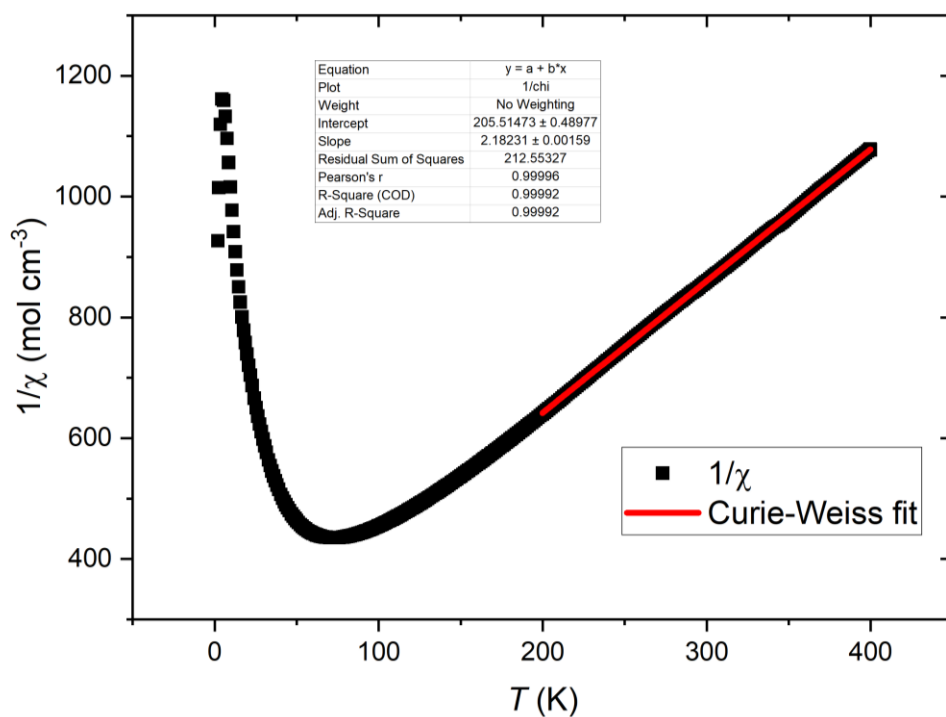


Fig. A5.2 Curie-Weiss fit of $Ba_2CuTe_{0.95}W_{0.05}O_6$ ($x = 0.05$) between 200-400 K.

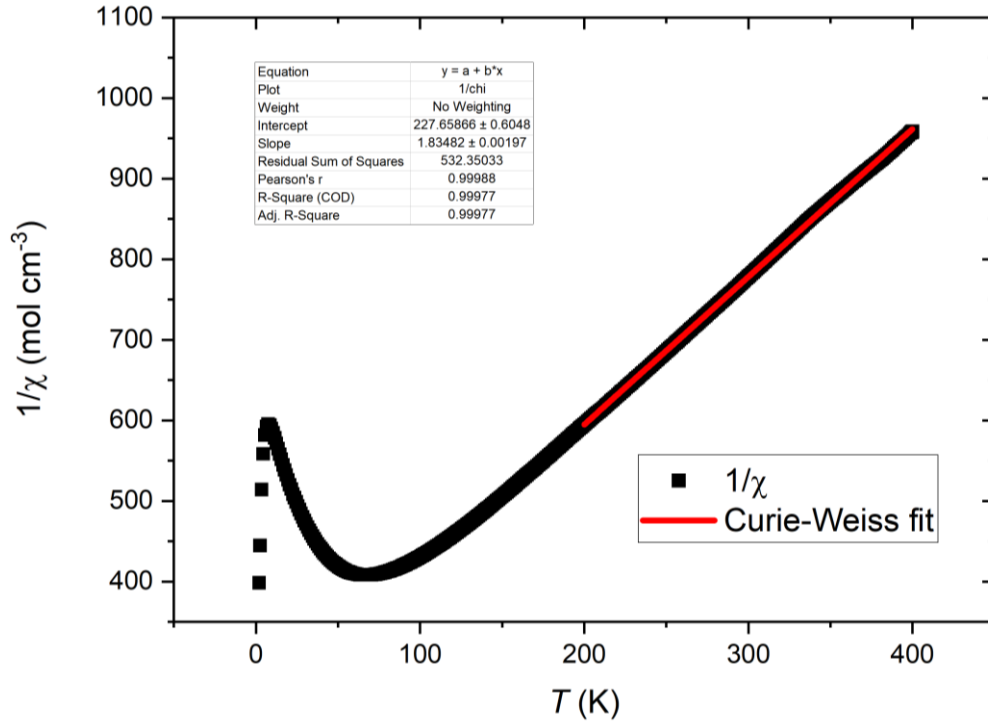


Fig. A5.3 Curie-Weiss fit of $Ba_2CuTe_{0.8}W_{0.2}O_6$ ($x = 0.2$) between 200-400 K.

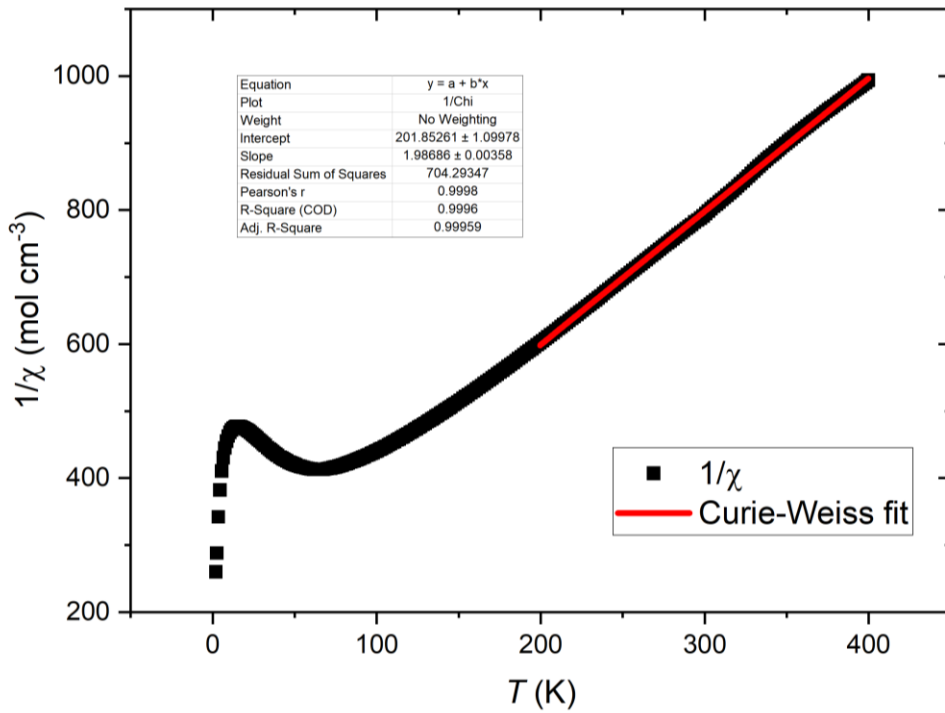


Fig. A5.4 Curie-Weiss fit of $Ba_2CuTe_{0.7}W_{0.3}O_6$ ($x = 0.3$) between 200-400 K.

A2. Isolated two-leg spin ladder model

The full equations for the isolated two-leg spin ladder model from ref. ¹³ are presented below. The model has three fitting parameters: J_{leg} , J_{rung}/J_{leg} and g and defines the molar magnetic susceptibility as:

$$\chi(T) = \frac{N_A g^2 \mu_B^2 e^{-\frac{\Delta}{T}}}{4k_B T} P_6^6 \left(\frac{T}{J_{leg}} \right) + \chi_0 \quad (1A)$$

where,

$$\Delta = 0.4030 \left(\frac{J_{rung}}{J_{leg}} \right) + 0.0989 \left(\frac{J_{rung}}{J_{leg}} \right)^3 \quad (2A)$$

and

$$P_6^6 \left(\frac{T}{J} \right) = \frac{1 + \frac{N_1}{\left(\frac{T}{J_{leg}}\right)} + \frac{N_2}{\left(\frac{T}{J_{leg}}\right)^2} + \frac{N_3}{\left(\frac{T}{J_{leg}}\right)^3} + \frac{N_4}{\left(\frac{T}{J_{leg}}\right)^4} + \frac{N_5}{\left(\frac{T}{J_{leg}}\right)^5} + \frac{N_6}{\left(\frac{T}{J_{leg}}\right)^6}}{1 + \frac{D_1}{\left(\frac{T}{J_{leg}}\right)} + \frac{D_2}{\left(\frac{T}{J_{leg}}\right)^2} + \frac{D_3}{\left(\frac{T}{J_{leg}}\right)^3} + \frac{D_4}{\left(\frac{T}{J_{leg}}\right)^4} + \frac{D_5}{\left(\frac{T}{J_{leg}}\right)^5} + \frac{D_6}{\left(\frac{T}{J_{leg}}\right)^6}} \quad (3A)$$

and

$$N_n = N_{n0} + N_{1n1} \left(\frac{J_{rung}}{J_{leg}} \right) + N_{1n2} \left(\frac{J_{rung}}{J_{leg}} \right)^2 + N_{1n3} \left(\frac{J_{rung}}{J_{leg}} \right)^3 \quad (4A)$$

and

$$D_n = D_{n0} + D_{1n1} \left(\frac{J_{rung}}{J_{leg}} \right) + D_{1n2} \left(\frac{J_{rung}}{J_{leg}} \right)^2 + D_{1n3} \left(\frac{J_{rung}}{J_{leg}} \right)^3 + D_{1n4} \left(\frac{J_{rung}}{J_{leg}} \right)^4 + D_{1n5} \left(\frac{J_{rung}}{J_{leg}} \right)^5 + D_{1n6} \left(\frac{J_{rung}}{J_{leg}} \right)^6 + D_{1n7} \left(\frac{J_{rung}}{J_{leg}} \right)^7 + D_{1n8} \left(\frac{J_{rung}}{J_{leg}} \right)^8 + D_{1n9} \left(\frac{J_{rung}}{J_{leg}} \right)^9 \quad (5A)$$

The values of the N_n and D_n coefficients were obtained from Table VII in ref [4] cited in ref. ¹³. The powers of J_{rung}/J_{leg} up to 6 and 9 are only needed for D_2 with and D_3 , respectively. In these equations, the ladder interactions (J_{rung} and J_{leg}) are expressed in units of Kelvin, K.

Chapter 6: Non-magnetic Zn^{2+} cations in $\text{Ba}_2\text{Cu}_{1-x}\text{Zn}_x\text{TeO}_6$

Contents

1. Abstract
2. Introduction
3. Experimental
4. Results
 - a. Crystal structure
 - b. DC susceptibility
 - c. AC susceptibility
 - d. Muon Spin Relaxation (μSR)
 - e. Heat capacity
5. Discussion
6. Conclusions
7. References

1. Abstract

Continuing working with the $\text{Ba}_2\text{CuTeO}_6$ structure, this chapter investigates substitution of the magnetic Cu^{2+} cation with a non-magnetic B' cation. Non-magnetic cations such as Zn^{2+} have been investigated in two-leg spin ladders with singlet ground states, but not in the Néel ordered $\text{Ba}_2\text{CuTeO}_6$ ground state. Cu^{2+} was substituted for Zn^{2+} forming a $\text{Ba}_2\text{Cu}_{1-x}\text{Zn}_x\text{TeO}_6$ solid solution between $0 \leq x \leq 0.6$ with monoclinic ($C2/m$) symmetry. Magnetic characterization using magnetic susceptibility and muon measurements show Zn^{2+} changes the magnetic behaviour compared to $\text{Ba}_2\text{CuTeO}_6$. Further work is needed to determine whether the Cu^{2+} spin ladder structure is retained upon Zn^{2+} substitution.

2. Introduction

Substitution of non-magnetic d^{10} and d^0 cations at the B'' site has been investigated in detail in double and hexagonal $A_2B'B''O_6$ perovskites. This chapter investigates substitution of the magnetic B' cations with non-magnetic $B' = d^{10}$ cations in the $\text{Ba}_2\text{CuTeO}_6$ spin ladder. Substitution of the magnetic Cu^{2+} cations is expected to produce a different magnetic response to $B'' = d^0$ substitution at the $B''(c)$ site. Hence, demonstrating the spin ladder behaviour can be altered by substitution at either the magnetic B' and non-magnetic B'' site. Nonmagnetic impurities have been shown to induce unexpected magnetic behaviours in other two-leg spin ladder systems. Such behaviours might be expected for $\text{Ba}_2\text{Cu}_{1-x}\text{Zn}_x\text{TeO}_6$.

Non-magnetic Zn^{2+} ($3d^{10}$) impurities have been studied in the two-leg spin ladder system $\text{Sr}(\text{Cu}_{1-x}\text{Zn}_x)_2\text{O}_3$. The ladder structure of $\text{Sr}(\text{Cu}_{1-x}\text{Zn}_x)_2\text{O}_3$ differs to that of $\text{Ba}_2\text{CuTeO}_6$. The two-leg ladders are parallel with respect to one another, but the rungs of Cu^{2+} cations in adjacent ladders are offset by half the J_{leg} distance forming a 'trellis' layered structure.¹ The intra-ladder interactions are approximately equal in magnitude ($J_{\text{rung}}/J_{\text{rung}} \sim 1$). Staggering of the ladders in the trellis structure

weakens the inter-ladder interaction (J_{inter}) so the two-leg ladders are ‘isolated’. Referring to the two-leg spin ladder magnetic phase diagram in Fig. 6.1, this places $\text{Sr}(\text{Cu}_{1-x}\text{Zn}_x)_2\text{O}_3$ in the singlet phase. It was expected ‘free spins’ would be generated as the $\text{Cu}^{2+}\cdots\text{Cu}^{2+}$ singlet dimers are broken by Zn^{2+} . At high temperatures, the magnetic susceptibility has a paramagnetic tail indicating free spins.² However, at low temperatures, the material unexpectedly long-range antiferromagnetically orders, even when the Zn^{2+} substitution level is as low as 1%.^{3,4}

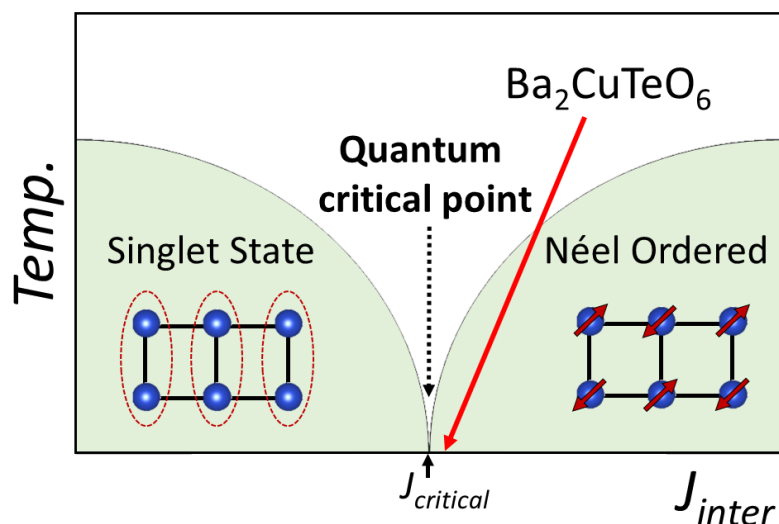


Fig. 6.1 The two-leg spin ladder magnetic phase diagram.

Zn^{2+} impurities have been studied in other two-leg spin ladder systems with gapped singlet ground states. Examples include $\text{Bi}(\text{Cu}_{1-x}\text{Zn}_x)_2\text{PO}_6$ and $(\text{C}_7\text{H}_{10}\text{N})_2\text{Cu}_{1-x}\text{Zn}_x(\text{Br}/\text{Cl})_4$.⁵⁻⁸ BiCu_2PO_6 differs from $\text{Sr}(\text{Cu}_{1-x}\text{Zn}_x)_2\text{O}_3$ because the inter-ladder coupling is not negligible. The spin ladders are not completely isolated, but J_{inter} is still weak enough for BiCu_2PO_6 to reside on the singlet side of the quantum critical point. Muon spin relaxation experiments suggest 2% Zn^{2+} induces static ordering and is believed to represent the formation of antiferromagnetic clusters.⁸ The interactions in $(\text{C}_7\text{H}_{10}\text{N})_2\text{Cu}_{1-x}\text{Zn}_x\text{Cl}_4$ also differ to $\text{Sr}(\text{Cu}_{1-x}\text{Zn}_x)_2\text{O}_3$. In this two-leg ladder structure, 1% Zn^{2+} substitution does not induce antiferromagnetic ordering. Alternatively, the muon data suggests faster relaxation of the muon spins due to fluctuation of the ‘free’ Cu^{2+} spins generated by the Zn^{2+} impurity.⁷ The ‘free’ Cu^{2+} spins are thought to be generated in the vicinity of the Zn^{2+} impurity and create an induced magnetic moment. Theoretical calculations show induced Cu^{2+} moments in these gapped two-leg spin ladders interact in three dimensions and generate antiferromagnetic correlations.⁸ The antiferromagnetic correlations are independent of geometry and the spin gap so can drive impurity induced antiferromagnetic ordering.

The $\text{Ba}_2\text{CuTeO}_6$ spin ladder lies on the Néel ordered side of the two-leg spin ladder phase diagram as J_{inter} is above the critical value. Information on the effects of non-magnetic impurities in a Néel ordered two-leg spin ladder is lacking. In the gapped two-leg spin ladders discussed above, the Zn^{2+} impurity affected the nearby Cu^{2+} spin singlets. Calculations have shown the extended Cu^{2+} spin ladder interactions are unaffected.⁹ Therefore, the spin ladder interactions are not destroyed by Zn^{2+} doping, but segmented. The extended Cu^{2+} ladder structure is expected to remain intact upon Zn^{2+} substitution; except for at the substitution site where the Zn^{2+} impurity breaks the local Cu^{2+} intra-ladder interactions creating unpaired spins. This is illustrated in Fig. 6.2. The free spins would lead to a paramagnetic contribution to the susceptibility. As the Zn^{2+} concentration increases, the spin

ladders would be increasingly segmented. Eventually, the Cu^{2+} interactions will be too segmented to resemble a spin ladder, at which point clusters of short-range correlated Cu^{2+} spins are expected. However, before this occurs, it might be possible to tune the spin ladder length based on Zn^{2+} concentration if the extended Cu^{2+} spin ladder interactions are unaffected by Zn^{2+} doping. This would allow the magnetic behaviour to be studied as a function of ladder length.

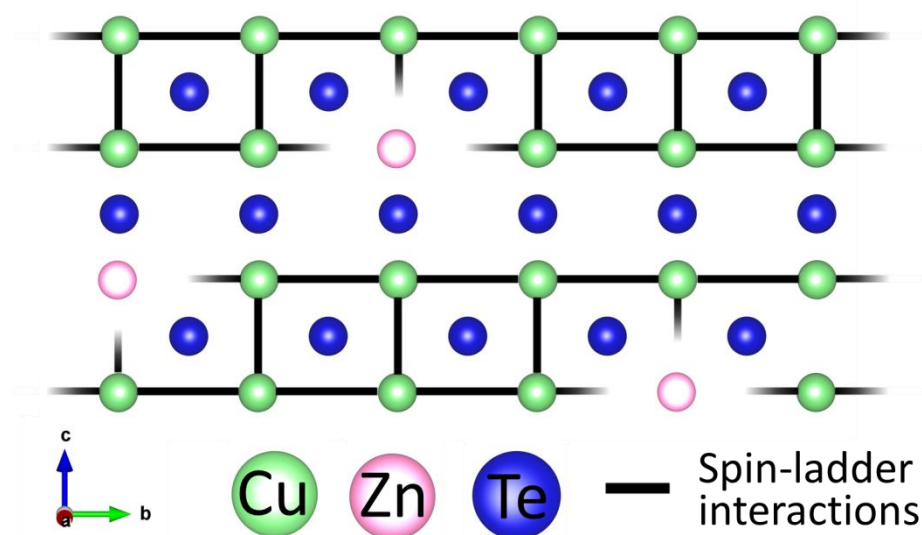


Fig. 6.2 Illustration of the proposed effect of Zn^{2+} substitution in the $\text{Ba}_2\text{CuTeO}_6$ spin ladder structure. Replacing magnetic $S = \frac{1}{2}$ Cu^{2+} cations (green) with non-magnetic Zn^{2+} cations (pink) is predicted to segment the local intra-ladder interactions (solid black lines) producing unpaired Cu^{2+} spins. The Zn^{2+} cation effects the Cu^{2+} interactions in the vicinity of the non-magnetic impurity, with the extended two-leg spin ladder structure remaining intact below a given Zn^{2+} concentration.

To investigate, $\text{Ba}_2\text{Cu}_{1-x}\text{Zn}_x\text{TeO}_6$ samples were prepared using solid state methods. Synthesis and brief structural characterization of $\text{Ba}_2\text{Cu}_{1-x}\text{Zn}_x\text{TeO}_6$ has been reported previously¹⁰, but not magnetic characterization. The monoclinic ($C2/m$) $\text{Ba}_2\text{CuTeO}_6$ structure was observed between $0 \leq x \leq 0.6$.¹⁰ The laboratory X-rays and neutron diffraction results presented here agreed with previous analysis. Magnetic characterization was performed using DC and AC magnetic susceptibility, followed by muon spin relaxation experiments. As discussed in the previous chapter, muon spin relaxation experiments are essential for the $\text{Ba}_2\text{CuTeO}_6$ system and its substituted structures due to the weak Cu^{2+} moment and large quantum fluctuations.^{11,12} This chapter presents the results and discusses further work required to fully understand the effects of Zn^{2+} impurities in $\text{Ba}_2\text{CuTeO}_6$.

3. Experimental

Synthesis

Polycrystalline samples of $\text{Ba}_2\text{Cu}_{1-x}\text{Zn}_x\text{TeO}_6$ between $0 \leq x \leq 1$ (in incremental steps of $x = 0.1$) were prepared using the 'shake n' bake' method. Stoichiometric quantities of high purity BaCO_3 (99.997%), CuO (99.9995%), ZnO (99.99%) and TeO_2 (99.995%) were ground in an agate mortar. The pellets were pressed (load 1 tonne) and calcined in air at 900 °C for 12 hours. The calcined pellets were then re-ground and pressed, before heating at reaction temperatures between 1050 – 1100 °C

whilst under a flow of oxygen to speed up oxidation of Te^{4+} . Reaction times between 48-96 hours were required to reach phase purity in all $0 \leq x \leq 1$ samples.

Laboratory X-ray Diffraction

Laboratory X-ray diffraction was performed using a Rigaku Miniflex diffractometer ($\text{Cu } K\alpha_1/K\alpha_2$ ($\lambda = 1.5405$ and 1.5443 Å)). The Rigaku Miniflex was used to monitor sample purity and obtain a final diffraction pattern of the phase pure sample. Analysis was performed using GSAS-2.^{13,14}

Neutron Diffraction

Neutron diffraction was performed on the $x = 0.5$ sample using the Polaris time-of-flight (TOF) diffractometer at the ISIS Neutron and Muon source. ~ 3 g of sample was loaded into a cylindrical vanadium canister (8 mm diameter). The canister was mounted into a carousel sample holder and aligned with the neutron beam. Time-of-flight neutron diffraction patterns were recorded at 300 K. The data were corrected for sample absorption and analysed using GSAS-2.^{13,14}

Magnetic susceptibility

Measurements were performed using a Quantum Design MPMS3 SQUID magnetometer. Sample preparation was identical to in chapter 5. The zero-field cooled (ZFC) and field cooled (FC) DC susceptibility (χ vs T) was measured between 2- 300 K in an external field of 0.1 T. Magnetization (M vs H) measurements were performed by measuring the DC magnetization (M) as a function of applied field (H) between -5 T to 5 T at a fixed temperature of 2 K. The AC susceptibility (χ'_{AC}) of the $x = 0.1$, $x = 0.2$ and $x = 0.3$ samples was measured between 2-100 K. The DC field was 25 Oe and the AC field was 5 Oe producing AC frequencies in the range of 10 to 467 Hz.

Muon Spin Relaxation (μSR)

Muon spin relaxation experiments were performed on samples $x = 0, 0.1, 0.2$ and 0.3 using the GPS muon beamline at the Paul Scherrer Institut (PSI). The polycrystalline powder (~ 1 g) was sandwiched into a square silver foil packet and secured onto the fork sample holder. The sample holder was inserted into the muon beamline and cooled using a cryostat to a temperature of ~ 1.5 K. The muon spin relaxation was measured in zero-field (ZF), transverse-field (TF) and longitudinal-field (LF) geometries at base temperature and on warming. The data were analysed using the web based version of MUSRFIT, which can be found at <http://musruser.psi.ch/cgi-bin/musrfit.cgi>.

4. Results

a. Crystal structure

The monoclinic ($C2/m$) $\text{Ba}_2\text{CuTeO}_6$ structural model was used to refine the $\text{Ba}_2\text{Cu}_{1-x}\text{Zn}_x\text{TeO}_6$ structure using the laboratory X-ray diffraction data. Fig. 6.3 provides an example of the Rietveld fit to the $x = 0.3$ experimental data. The monoclinic model (red line) provides a good description of the observed diffraction peaks, showing $C2/m$ symmetry is retained upon Zn^{2+} substitution. $C2/m$ symmetry was observed between $0 \leq x \leq 0.6$. Beyond $x = 0.6$, the diffraction profile changed indicating a change in symmetry. Between $x = 0.7$ to $x = 1$, the rhombohedral ($R\bar{3}m$) $\text{Ba}_2\text{ZnTeO}_6$ structure is adopted.¹⁵ The structural phase diagram illustrated in Fig. 6.4 is identical to previous structural characterization.¹⁰ The main focus is the monoclinic phase ($0 \leq x \leq 0.6$), wherein the effect of increasing Zn^{2+} dilution on the Cu^{2+} spin ladders of $\text{Ba}_2\text{CuTeO}_6$ can be observed.

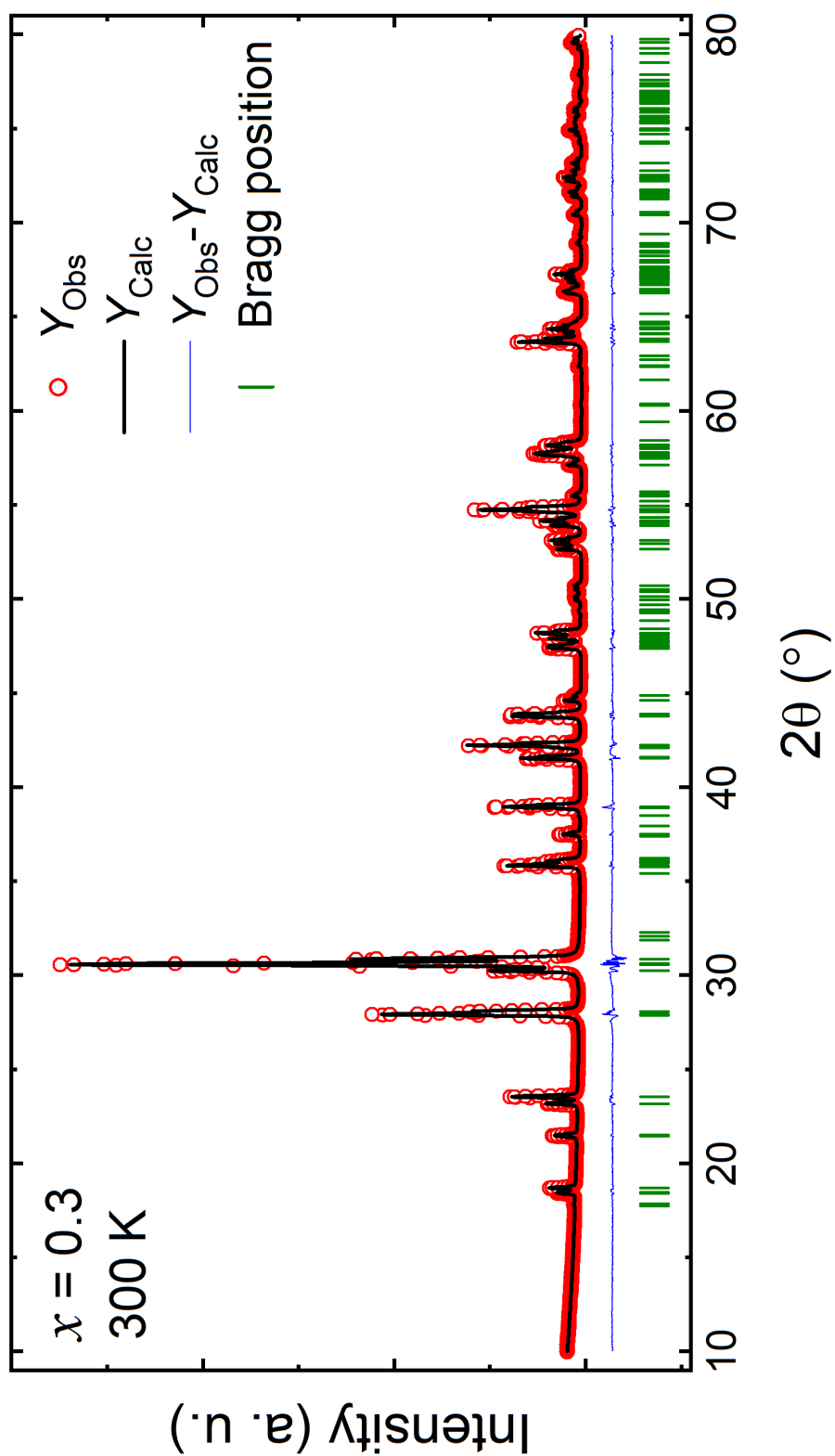


Fig. 6.3 Example Rietveld refinement using the monoclinic structural model. The plot shows the Rietveld fit to the $Ba_2Cu_{0.7}Zn_{0.3}TeO_6$ ($x = 0.3$) laboratory X-ray diffraction data ($R_{wp} = 6.40$, $\chi^2 = 5.38$).

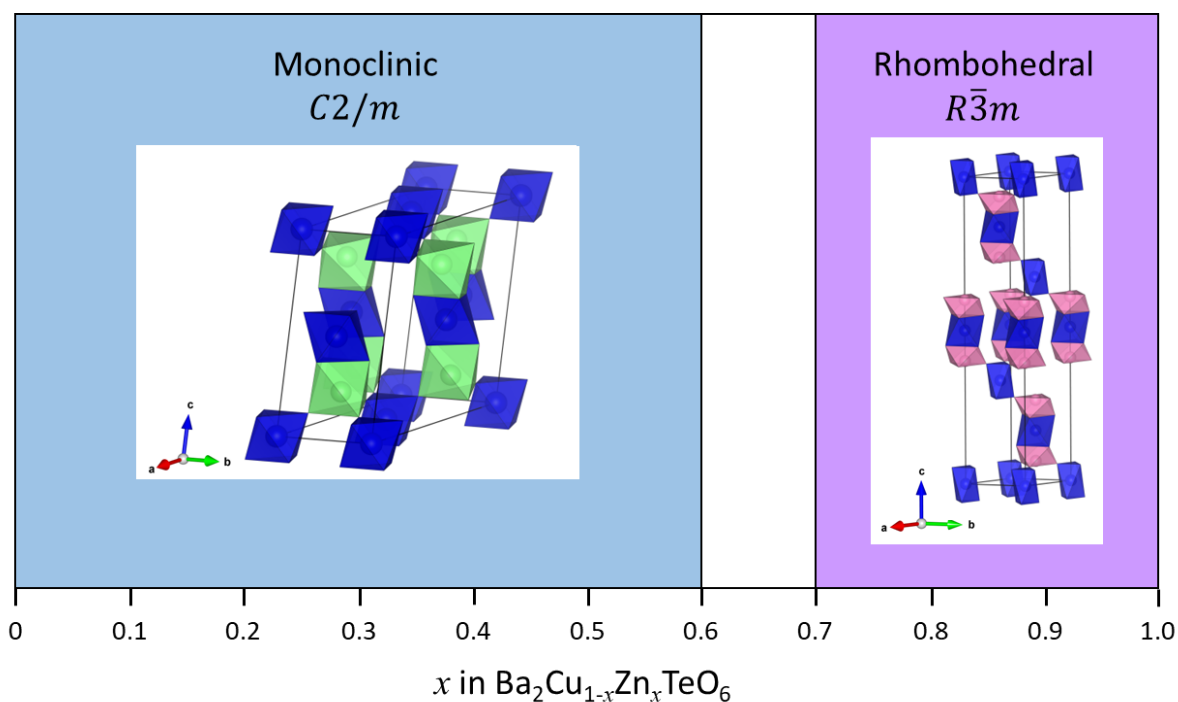


Fig. 6.4 The structural phase diagram of the $Ba_2Cu_{1-x}Zn_xTeO_6$ solid solution in which the transition from the monoclinic to rhombohedral phase occurs between $x = 0.6$ and $x = 0.7$.

The unit cell volume (V_{cell}) of the monoclinic unit cell as a function of x in $Ba_2Cu_{1-x}Zn_xTeO_6$ is shown in Fig. 6.5b. Between $0 \leq x \leq 0.3$, V_{cell} decreases linearly. Between $x = 0.3$ and $x = 0.4$, V_{cell} remains approximately constant, before linearly decreasing again between $x = 0.4$ and $x = 0.6$. A similar deviation between $x = 0.3$ and $x = 0.4$ is observed in the a , b , c and β lattice parameters in panels (c)-(f) of Fig. 6.5. A likely cause of the deviation in V_{cell} is the large change in Jahn-Teller distortion that occurs as Cu^{2+} is increasingly substituted for Zn^{2+} . Using the Cu-O(1-4) bond lengths (indicated in Fig. 6.6a) determined using the X-ray diffraction data, the Jahn-Teller distortion parameter (σ_{JT}) was calculated using equation 6.1 and plotted as a function of x in Fig. 6.6b.¹⁶

$$\sigma_{JT} = \sqrt{\frac{1}{6} \sum_i [(B - O)_i - \langle B - O \rangle]^2} \quad (6.1)$$

As x in $Ba_2Cu_{1-x}Zn_xTeO_6$ increases towards $x = 0.5$, the magnitude of σ_{JT} is approximately halved. This shows replacing half the amount of Cu^{2+} for Jahn-Teller inactive Zn^{2+} in $x = 0$, halves the distortion of the CuO_6 octahedra in $x = 0.5$. The Cu-O(1-4) bond lengths plotted in panels (c) to (f) agree with reduced Jahn-Teller distortion. The axial Cu/Zn-O(1) and Cu/Zn-O(3) bonds become shorter as x increases, while the slight compression of the equatorial Cu/Zn-O(2) and Cu/Zn-O(4) bonds is reduced. There is a similar deviation in the σ_{JT} vs x in $Ba_2Cu_{1-x}Zn_xTeO_6$ data between $x = 0.3$ and $x = 0.4$ to that observed for V_{cell} vs x and in the lattice parameters. This suggests the deviation in V_{cell} is linked to the large changes in Cu/ZnO₆ distortion that occur between $x = 0.3$ and $x = 0.4$.

While Zn^{2+} substitution reduced distortion of the (Cu/Zn)O₆ octahedra, the value of σ_{JT} is still substantial. Given Zn^{2+} is Jahn-Teller inactive, substitution of Zn^{2+} for Cu^{2+} might result in symmetry breaking as Zn^{2+} is unable to assume the highly distorted (Cu/Zn)O₆ site. No additional peaks were detected in the X-ray diffraction data to suggest symmetry breaking. However, the atomic number of Cu ($Z = 29$) and Zn^{2+} ($Z = 30$) differ by one unit. Hence, it was not possible to differentiate between

the Cu^{2+} and Zn^{2+} scattering contributions using X-rays. Neutron diffraction was performed due to the improved contrast between the neutron scattering lengths of Cu^{2+} and Zn^{2+} .

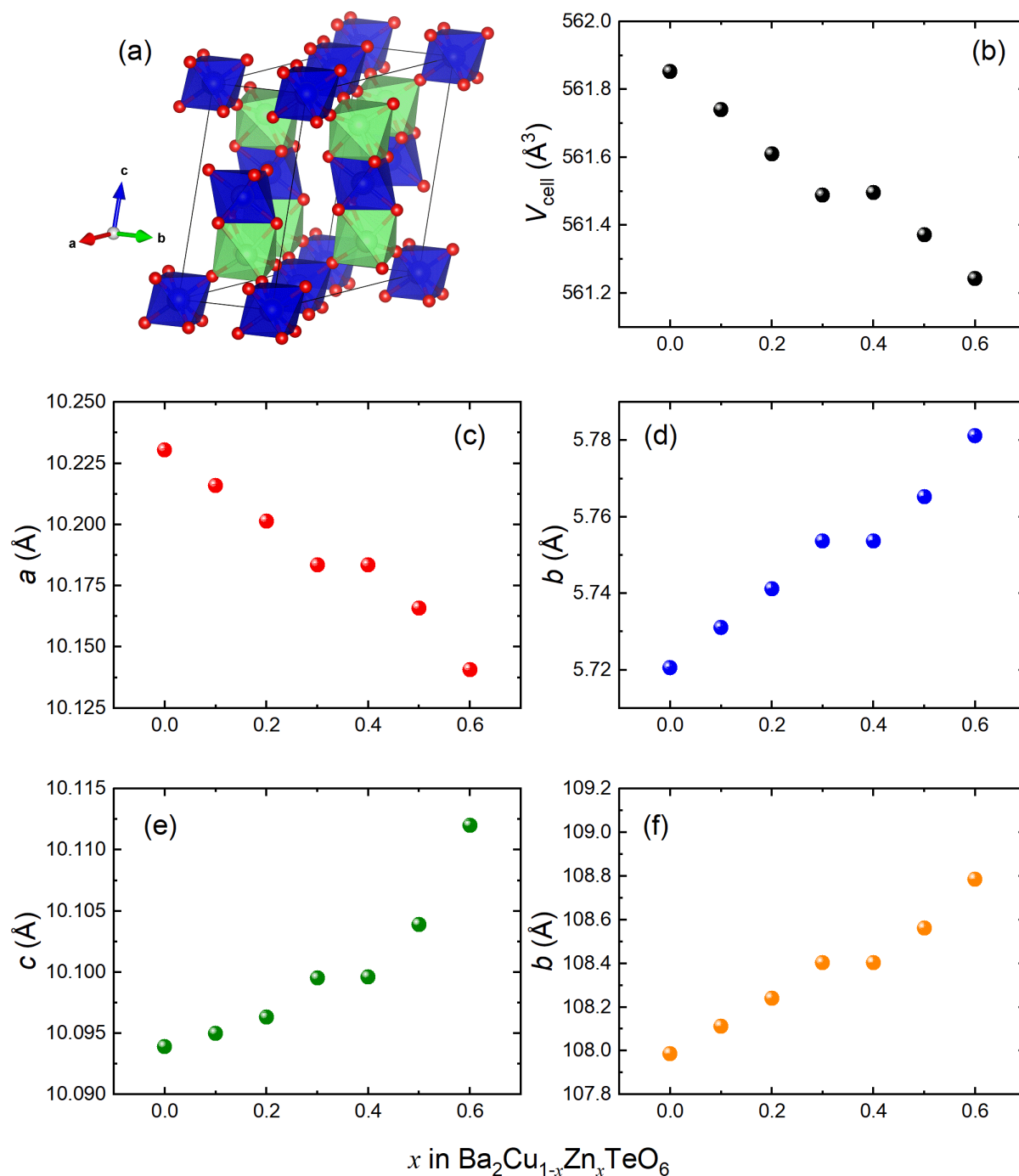


Fig. 6.5 The lattice parameters and unit cell volumes determined from refinement of the monoclinic $C2/m$ structural model shown in panel (a). The atom colours are: green/grey ($\text{Cu}^{2+}/\text{Zn}^{2+}$), blue (Te^{6+}) and red (O^{2-}). Panel (b) shows the unit cell volume as a function of x in $\text{Ba}_2\text{Cu}_{1-x}\text{Zn}_x\text{TeO}_6$. Panels (c) – (f) show the monoclinic lattice parameters (a , b , c and β) as a function of x in $\text{Ba}_2\text{Cu}_{1-x}\text{Zn}_x\text{TeO}_6$.

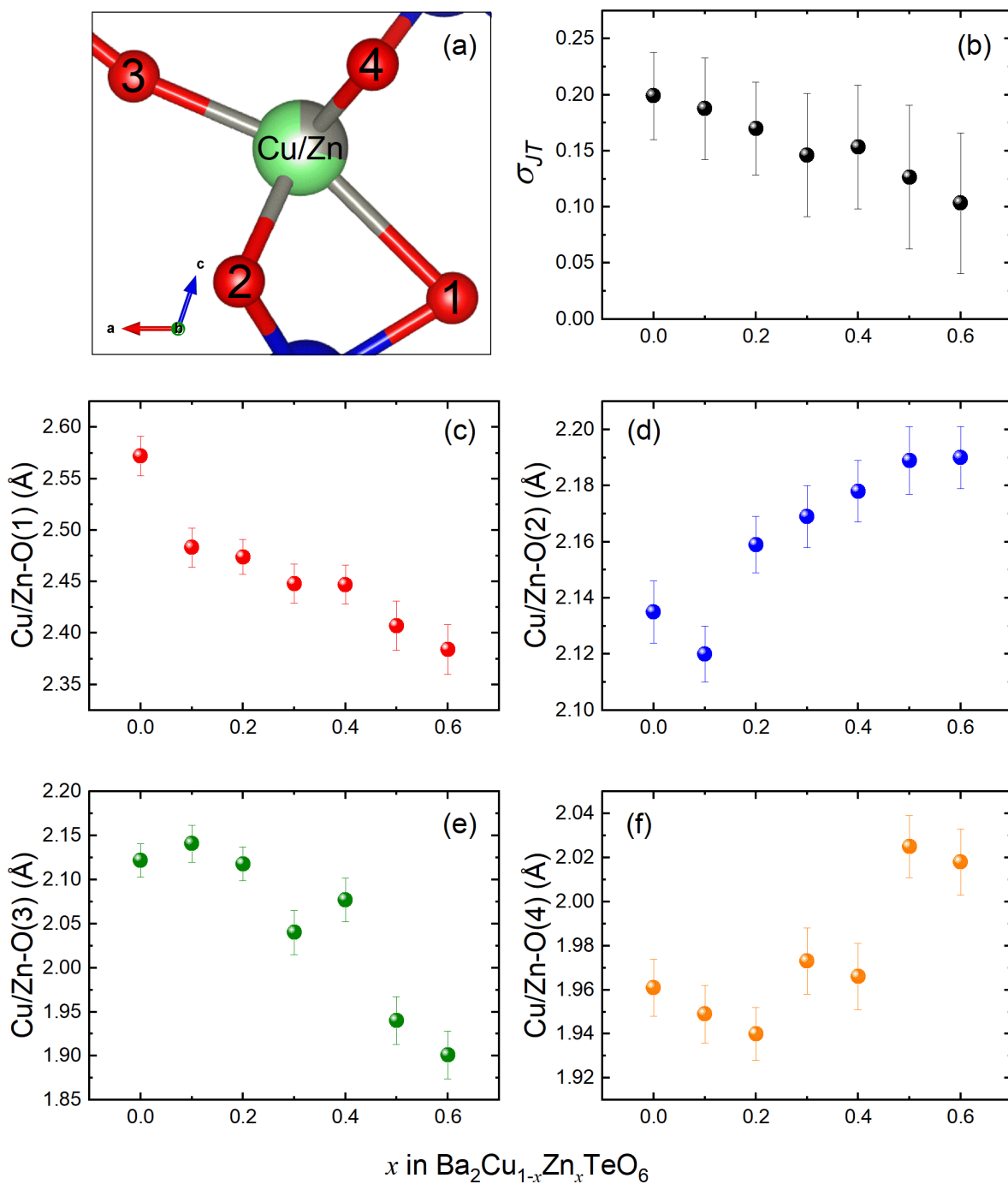


Fig. 6.6 Geometry of the $(\text{Cu/Zn})\text{O}_6$ octahedra in the monoclinic $\text{Ba}_2\text{Cu}_{1-x}\text{Zn}_x\text{TeO}_6$ ($0 \leq x \leq 0.6$) structure. Panel (a) shows an image of the $(\text{Cu/Zn})\text{O}_6$ octahedral geometry, in which asymmetric elongation of the axial $\text{Cu/Zn-O}(3)$ and $\text{Cu/Zn-O}(1)$ bonds is clearly visible. The Cu/Zn-O bond lengths plotted in panels (c)-(f) are indicated in the structural image. Panel (b) plots the Jahn-Teller distortion parameter (σ_{JT}) as a function of x in $\text{Ba}_2\text{Cu}_{1-x}\text{Zn}_x\text{TeO}_6$. Panels (c) to (f) show how the Cu/Zn-O bond lengths used to calculate σ_{JT} change as a function of x in $\text{Ba}_2\text{Cu}_{1-x}\text{Zn}_x\text{TeO}_6$.

The neutron diffraction pattern of $x = 0.5$ was measured at 300 K on Polaris and used to refine the $C2/m$ structural model. Fig. 6.7 shows the resulting Rietveld refinement. The $C2/m$ model agrees well with the observed diffraction pattern, with no additional Bragg peaks to suggest symmetry breaking. Instead of being equivalent for the same site, the positions of Cu^{2+} and Zn^{2+} were allowed

to refine. There was a negligible difference between the x and z positions of Cu^{2+} and Zn^{2+} upon refinement. Table 6.1 shows the refined $\text{Ba}_2\text{Cu}_{0.5}\text{Zn}_{0.5}\text{TeO}_6$ structure without and with Cu^{2+} and Zn^{2+} x and z positions refined. Hence, it is accurate to assume Cu^{2+} and Zn^{2+} occupy the same $\text{Cu/Zn}(1)\text{O}_6$ site across the $\text{Ba}_2\text{Cu}_{1-x}\text{Zn}_x\text{TeO}_6$ $0 \leq x \leq 0.6$ solid solution.

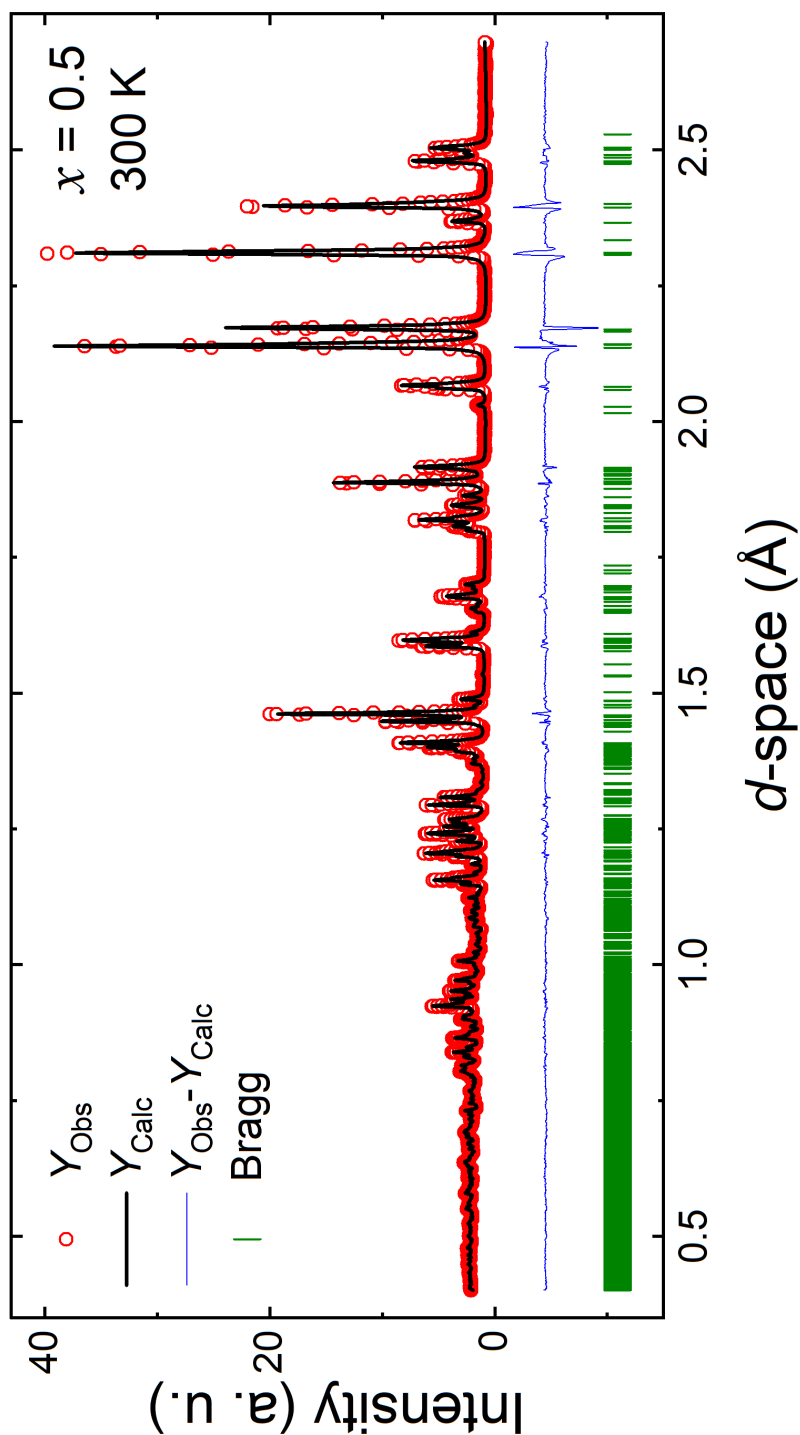


Fig. 6.7 Rietveld fit to the $x = 0.5$ $\text{Ba}_2\text{Cu}_{0.5}\text{Zn}_{0.5}\text{TeO}_6$ Polaris neutron diffraction data from bank 5 ($2\theta = 146.942^\circ$) ($R_{wp} = 3.19$, $\chi^2 = 12.25$).

Table 6.1: Refined structure of $Ba_2Cu_{0.5}Zn_{0.5}TeO_6$ obtained using the Polaris neutron diffraction data. The table shows the refined Cu^{2+} and Zn^{2+} site fractions. The refined Cu^{2+} and Zn^{2+} x and z positions are marked by an asterisk (*).

Space Group: $C2/m$, No. 12, 300 K						
R_p (%) = 3.78, R_{wp} (%) = 3.19, R_{exp} (%) = 1.03, χ^2 = 12.25, var. 79						
a = 10.1404(6) Å, b = 5.78117(11) Å, c = 10.1123(6) Å, β = 108.7862(13)°						
Vol. = 561.233(31) Å ³						
Site	Wyckoff Position	x	y	z	Site fraction	Uiso (Å ²)
Ba1	4i	0.12795(21)	0	0.38118(14)	1.0	0.00316(22)
Ba2	4i	0.28159(24)	0	0.84489(15)	1.0	0.00635(29)
Te1	2a	0	0	0	1	0.00025(24)
Te2	2d	0	0.5	0.5	1	0.00144(26)
Cu1	4i	-0.09746(15) -0.09746(15)*	0.5	0.21105(10) 0.21105(10)*	0.5	0.00452(20)
Zn1	4i	-0.09746(15) -0.09745(15)*	0.5	0.21105(10) 0.21104(10)*	0.5	0.00452(20)
O1	4i	0.12419(19)	0.5	0.39104(18)	1.0	0.0111(4)
O2	8j	-0.11081(11)	0.72873(21)	0.37391(11)	1.0	0.00894(22)
O3	4i	0.30922(20)	0.5	0.87878(22)	1.0	0.0127(4)
O4	8j	0.04409(16)	0.76549(27)	0.88591(14)	1.0	0.01260(23)

b. DC susceptibility

The DC susceptibility data (χ vs T) of the $x = 0, 0.1, 0.2, 0.3, 0.5$ and 0.6 samples are shown in Fig. 6.8. Introduction of Zn^{2+} has a profound effect upon the susceptibility curve of $x = 0$. As described in chapter 5, the $x = 0$ χ vs T curve possesses a broad $T_{max} \sim 74$ K feature representing the short-range ladder interactions. Below T_{max} , the susceptibility decreases and deviates from ladder behaviour leading onto a small upturn feature about $T_{min} \sim 14$ K. Introduction of 10% Zn^{2+} changes the upturn feature. When $x > 0$, there is a sharp rise in the low temperature upturn, resulting in a paramagnetic tail-like feature. Panel (b) shows an expansion of the $x = 0.1$ low temperature susceptibility. Looking closely at the paramagnetic tail in the expansion shows there is a 'kink' at ~ 10 K; close to the position of the T_{min} upturn in the $x = 0$ data. This kink disappears in the $x = 0.2$ data as the expansion between 0-50 K in panel (c) shows. The paramagnetic tail continues to grow and dominates over the T_{max} feature which is no longer visible beyond $x \geq 0.3$ in panel (d). Beyond $x = 0.3$, the susceptibility curve resembles that of a paramagnet with no deviations or kinks in the curve. Instead, the susceptibility rises gradually on cooling from 300 K, before sharply rising below 50 K to form the large paramagnetic tail.

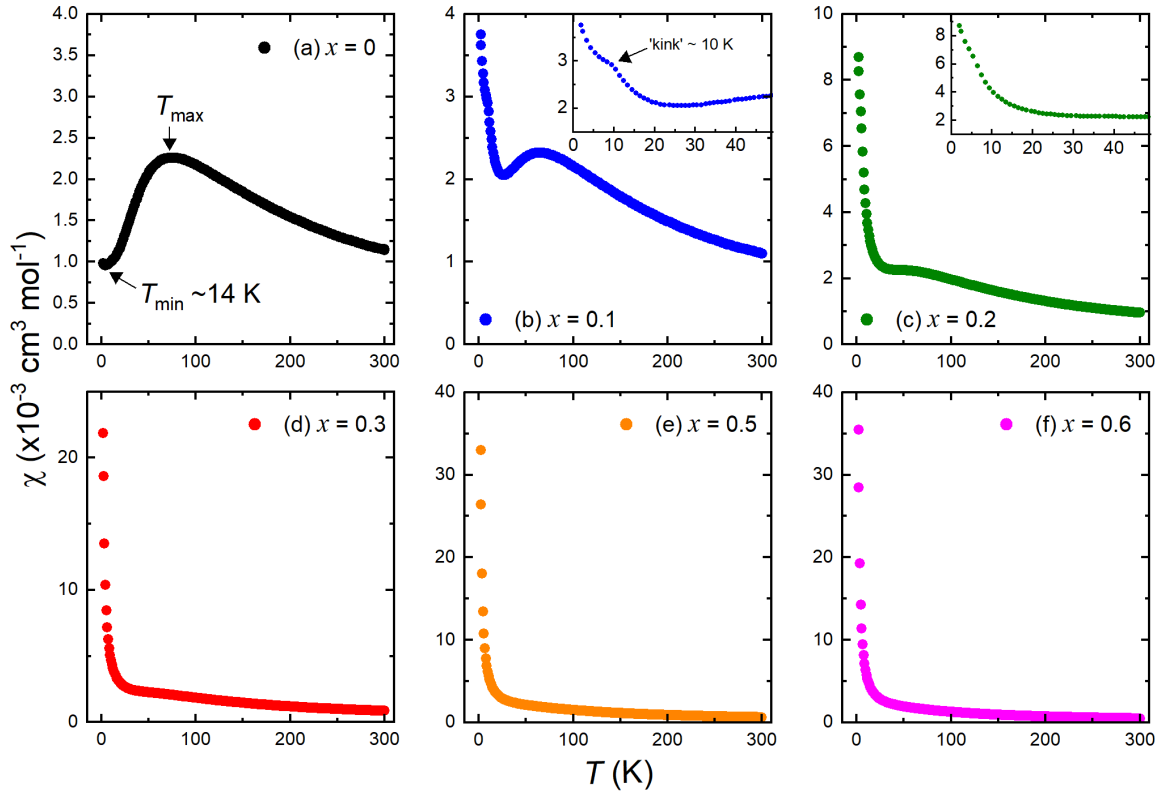


Fig. 6.8 The DC susceptibility data of the $\text{Ba}_2\text{Cu}_{1-x}\text{Zn}_x\text{TeO}_6$ (a) $x = 0$, (b) $x = 0.1$, (c) $x = 0.2$, (d) $x = 0.3$, (e) $x = 0.5$ and (f) $x = 0.6$ samples. In panels (b) and (c), there are expansions of the low temperature data between 0 and 50 K. The DC susceptibility data of $x = 0.4$ was near-identical to the $x > 0.3$ samples.

The $0 \leq x \leq 0.6$ $1/\chi$ vs T data was linear between 150-300 K and could be fitted using the inverse Curie-Weiss law. Table 6.2 shows the values of the Curie constant (C), Weiss constant (θ_W) and effective magnetic moment (μ_{eff}) for each x composition. The values for $x = 0$ are similar to that obtained from $\text{Ba}_2\text{CuTeO}_6$ in chapter 5, confirming consistency between sample batches. Table 6.2 shows there are large changes in C , θ_W and μ_{eff} as x increases. The values of C , θ_W and μ_{eff} are plotted as a function of x in $\text{Ba}_2\text{Cu}_x\text{Zn}_{1-x}\text{TeO}_6$ in Fig. 6.9. Fig. 6.9 shows C decreases linearly with increasing x . The changes in θ_W and μ_{eff} are also linear. θ_W increases linearly from -89.3(4) K for $x = 0$ towards zero reaching a value of -9.9(5) K upon reaching $x = 0.6$. Hence, Zn^{2+} greatly weakens the antiferromagnetic interactions. T_{max} in Table 6.2 also decreased between $x = 0$ to $x = 0.2$ implying weakening of the interactions. The value of μ_{eff} is similar for all compositions and close to the previously reported value for $\text{Ba}_2\text{CuTeO}_6$ and $\text{Ba}_2\text{CuTe}_{1-x}\text{W}_x\text{TeO}_6$.^{11,17} The value of μ_{eff} slightly decreases with increasing x supporting weakening of the Cu^{2+} interactions.

Table 6.2: Results from analysis of the DC susceptibility data of $\text{Ba}_2\text{Cu}_x\text{Zn}_{1-x}\text{TeO}_6$

x	T_{max} (K)	C ($\text{cm}^3 \text{K mol}^{-1}$)	θ_W (K)	μ_{eff} (μ_B per Cu^{2+})
0	73.7	0.4450(7)	-89.3(4)	1.890(5)
0.1	64	0.4219(6)	-84.0(4)	1.936(2)
0.2	~57	0.3551(3)	-71.7(2)	1.8840(8)
0.3	-	0.3056(3)	-58.6(3)	1.869(1)
0.4	-	0.2574(2)	-44.3(2)	1.852(1)
0.5	-	0.2107(1)	-36.5(1)	1.835(1)
0.6	-	0.1500(3)	-9.9(5)	1.732(2)

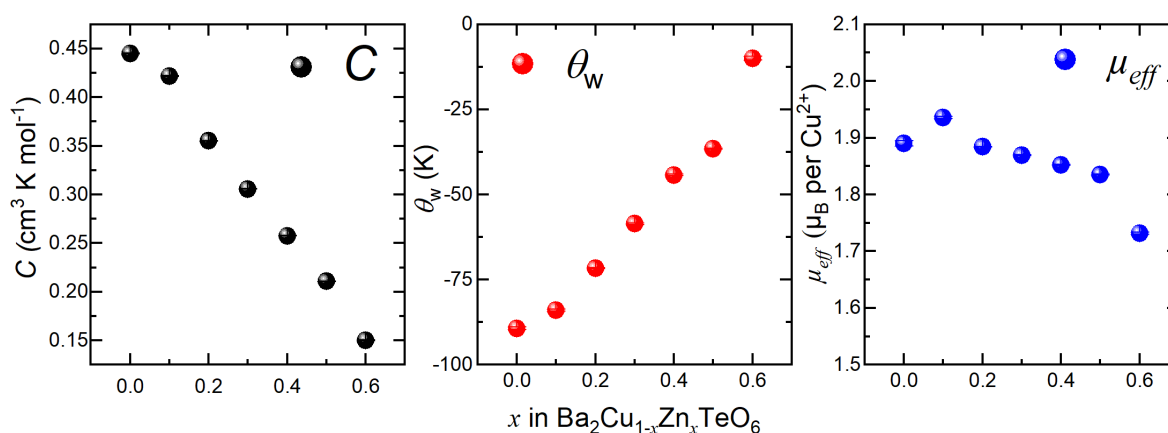


Fig. 6.9 Graphical plots of the Curie-Weiss fitting parameters in Table 6.2. The three panels show: (a) the Curie constant (C); (b) the Weiss constant (θ_W); and (c) the effective magnetic moment (μ_{eff}) as a function of x in $\text{Ba}_2\text{Cu}_x\text{Zn}_{1-x}\text{TeO}_6$.

The DC magnetisation (M) as a function of applied field (H) was measured at 2 K. The M vs H plots between -5 T to 5 T for the $0 \leq x \leq 0.6$ samples are shown in Fig. 6.10. None of the x compositions display any evidence of hysteresis in their magnetisation curve. The M vs H plot of $x = 0$ is shown in black. The magnetization is linear and shows no signs of saturation. Upon introduction of Zn^{2+} , the shape of the magnetization curve changes from linear to curved. The curvature increases with x resulting in a corresponding increase in the magnetisation. The curvature also introduces saturation. The change in the shape of the M vs H curve further supports a change in the magnetic behaviour upon introduction of Zn^{2+} .

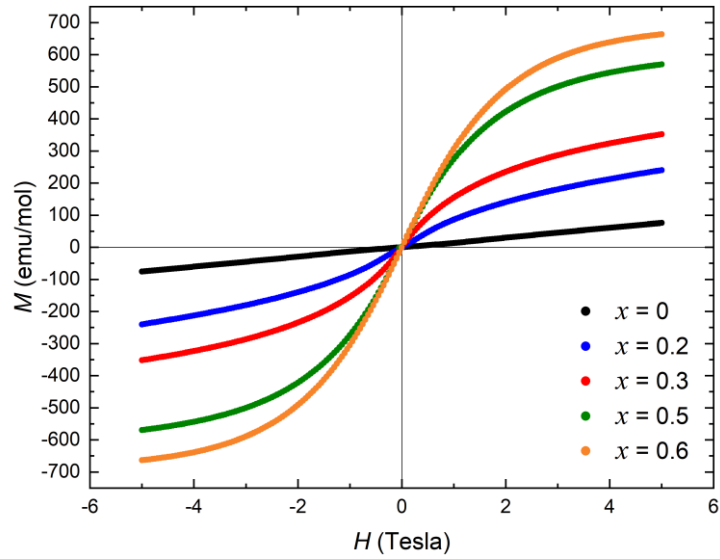


Fig. 6.10 DC M vs H data of the $Ba_2Cu_xZn_{1-x}TeO_6$ compositions between $0 \leq x \leq 0.6$.

c. AC susceptibility

AC susceptibility measurements were performed on the $x = 0.1, 0.2$ and 0.3 samples. The χ'_{AC} vs T curves of (a) $x = 0.1$, (c) $x = 0.2$ and (e) $x = 0.3$ are shown in Fig. 6.11. No frequency dependent shift was observed in the AC susceptibility of any sample. Nor were there any distinctive peaks detected in the imaginary χ''_{AC} susceptibilities plotted in panels (b) $x = 0.1$, (d) $x = 0.2$ and (f) $x = 0.3$ in Fig. 6.11. Hence, there is no evidence to suggest Zn^{2+} induces spin glass behaviour.

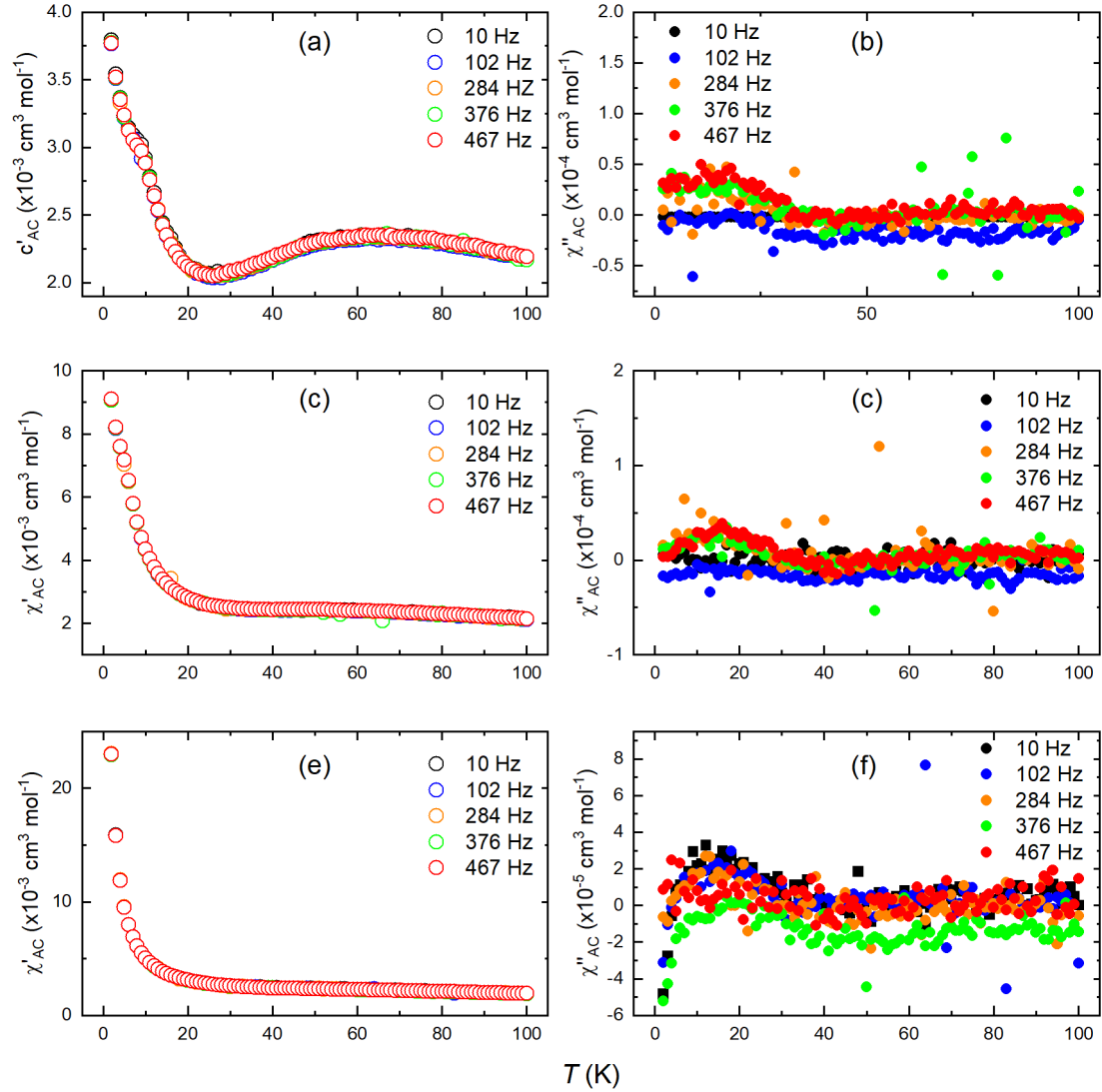


Fig. 6.11 The χ'_{AC} vs T data of (a) $Ba_2Cu_{0.9}Zn_{0.1}TeO_6$ ($x = 0.1$), (c) $Ba_2Cu_{0.8}Zn_{0.2}TeO_6$ ($x = 0.2$) and (e) $Ba_2Cu_{0.7}Zn_{0.3}TeO_6$ ($x = 0.3$) between 2-100 K. The imaginary component χ''_{AC} vs T is shown in panels (b) $x = 0.1$, (d) $x = 0.2$ and (f) $x = 0.3$. No frequency shifts were detected in the χ'_{AC} vs T data and there were no distinctive peaks in the χ''_{AC} vs T data to support spin glass behaviour.

d. Muon spin relaxation (μ SR)

Muon spin relaxation (μ SR) measurements were performed on the $x = 0, 0.1, 0.2$ and 0.3 samples to learn more about how the local magnetic environment changes upon Zn^{2+} substitution. The results from μ SR experiments on GPS are presented below.

$x = 0$

ZF- μ SR measurements on $x = 0$ were presented in chapter 5, and by ref. ¹² previously. Both measurements were independently performed using the pulsed muon source at the ISIS Neutron and Muon facility. Continuous muon sources offer improved time resolution and can detect higher frequency oscillations compared to pulsed muon sources. This is because at a continuous source the arrival time of each muon event is known. Whereas, at a pulsed source muons arrive in bunches creating a distribution of arrival times. Hence, by performing measurements on GPS using the

continuous muon source at PSI, more detailed information about the muon environment in the $x = 0$ sample can be obtained.

The GPS ZF- μ SR data for $x = 0$ at 1.5 K is shown in Fig. 6.12b. As seen previously, there are clear oscillations signifying long-range magnetic order. However, there are differences in the oscillatory features when comparing the HIFI and PSI data in Fig. 6.12a and Fig. 6.12b, respectively. The HIFI data contains a single oscillation, while two oscillatory features can be observed in the PSI ZF- μ SR data. The ZF- μ SR PSI data for $x = 0$ could be fitted using the sum of a Gaussian cosine and exponentially relaxing cosine to describe the two oscillations as shown in equation 6.2. The exponential term describes the background.

$$P(t) = A_0 e^{-\sigma^2 t^2} \cos(2\pi f_1 t + \phi_1) + A_1 e^{-\lambda_1 t} \cos(2\pi f_2 t + \phi_2) + A_2 e^{-\lambda_2 t} \quad (6.2)$$

Here, $A_{0,1,2}$ are the asymmetry at time zero, σ is the decay rate of the Gaussian oscillation, λ_1 is the decay rate of the exponentially relaxing cosine, λ_2 is the decay rate of the exponential background term, f_1 and f_2 are the frequencies of the oscillations, and ϕ_1 and ϕ_2 the phases of the oscillations. The red fit line in Fig. 6.12b shows equation 6.2 provides a good description of the ZF data. The frequencies of the oscillations were determined as: $f_1 = 3.81(1)$ MHz and $f_2 = 6.67(9)$ MHz. Therefore, the PSI data allowed the higher frequency oscillation to be resolved. The presence of two oscillations shows there are two muon stopping sites in the material. The decay rates of the Gaussian cosine and exponentially relaxing cosine were: $\sigma = 1.4(1) \mu\text{s}^{-1}$ and $\lambda_1 = 12.3(8) \mu\text{s}^{-1}$, respectively (the decay rate of the background term was $\lambda_2 = 0.007(1) \mu\text{s}^{-1}$). The values for σ and λ_1 show the muon polarization decays faster in the muon stopping site described by an exponentially relaxing cosine.

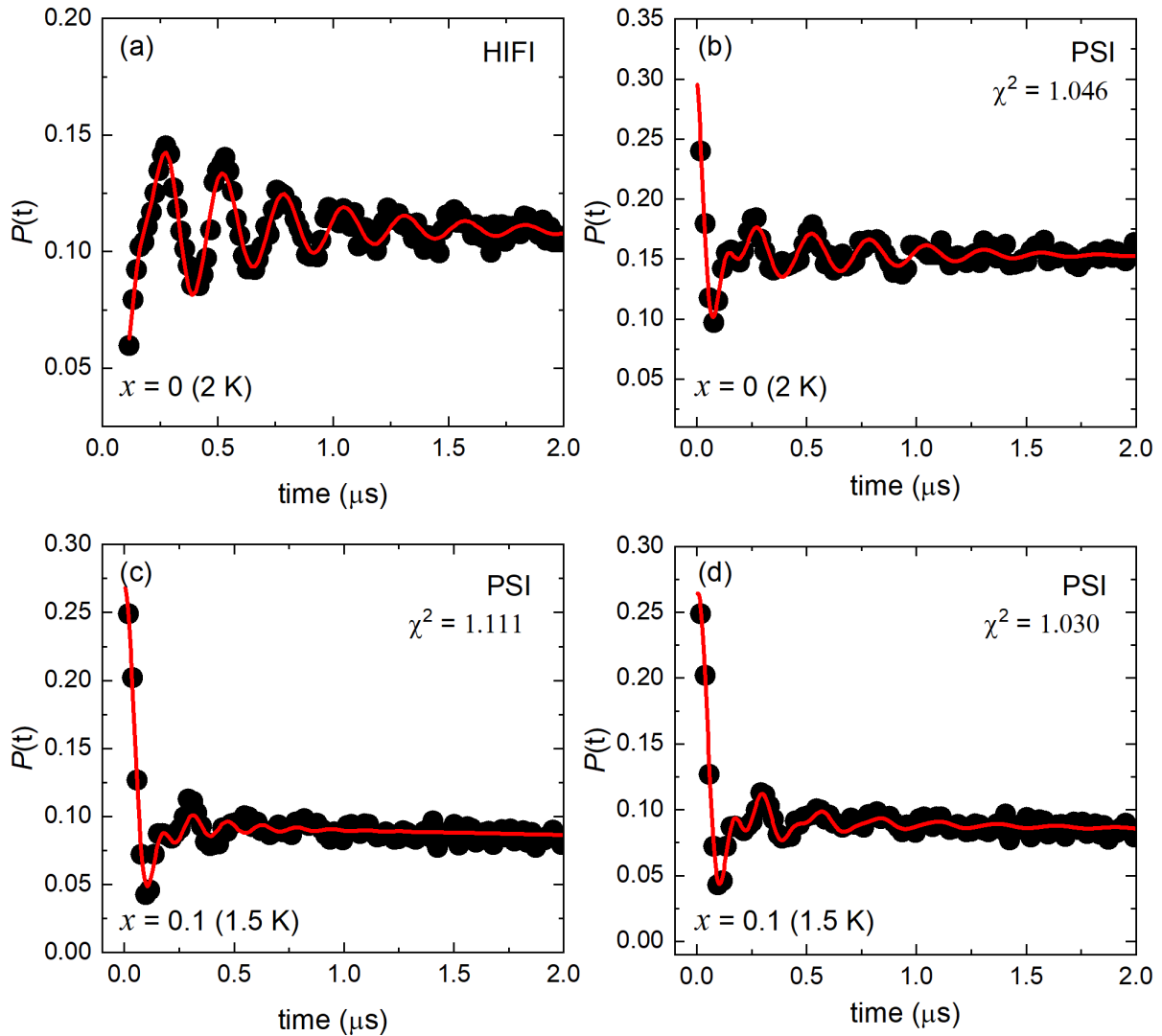


Fig. 6.12 (a) The ZF- μ SR data of $\text{Ba}_2\text{CuTeO}_6$ ($x = 0$) measured at 1.5 K using the HIFI beamline (pulsed-ISIS). (b) The ZF- μ SR data of $x = 0$ measured at 2 K using the GPS beamline (continuous-PSI). There are two oscillations in the PSI data, which could not be resolved in the lower time resolution HIFI data. The $x = 0$ data in panel (b) was fitted using the muon polarization function in equation 6.2. (c) The ZF- μ SR data of $\text{Ba}_2\text{Cu}_{0.9}\text{Zn}_{0.1}\text{TeO}_6$ ($x = 0.1$) measured at 1.5 K using GPS. Oscillations are still present, indicating magnetic ordering, but the fit using the same polarization function (equation 6.2) for $x = 0$ in panel (c) is poor. Instead, the muon polarization is better described using a function involving Bessel functions implying an incommensurate magnetic structure. (d) The fit to the 2 K ZF- μ SR data of $x = 0.1$ using Bessel functions in equation 6.6. The improvement in the fit can be observed visually by comparison to panel (c), and also from the improved goodness of fit (χ^2). The fits to the data are shown by the solid red lines.

$x = 0.1$

Fig. 6.12c shows the ZF- μ SR data for $x = 0.1$ at 1.5 K. The data show oscillations are still present upon 10% Zn^{2+} substitution showing $x = 0.1$ is long-range ordered. Initially, fitting was performed using the $x = 0$ polarization function in equation 6.2. The fit in Fig. 6.12c shows equation 6.2 failed to

adequately describe the oscillations. Instead, the ZF- μ SR data was more accurately described using zeroth order Bessel functions. Bessel functions are the solutions to the differential equation:

$$x^2 \frac{d^2 y}{dx^2} + x \frac{dy}{dx} + (x^2 - n^2)y = 0 \quad (6.3)$$

Where, n is a non-negative real number. The first order differential solutions of equation 6.3 are called Bessel functions of the first kind ($J_n(x)$) and the second order differential solutions are Bessel functions of the second kind ($Y_n(x)$). Bessel functions of the first kind ($J_0(x)$) are used to describe the muon polarization $P(t)$ below:

$$P(t) = A_0 J_0(2\pi\nu t + \phi) \quad (6.4)$$

$$J_0(x) = \sum_{l=0}^{\infty} \frac{(-1)^l}{2^{2l}(l!)^2} x^{2l} \quad \text{Where, } x = 2\pi\nu t + \phi \quad (6.5)$$

The $x = 0.1$ muon polarization was fitted using a combination of two exponential Bessel functions for each of the two muon sites and an exponential relaxation function to describe the background. The $P(t)$ function is shown below:

$$P(t) = A_0 e^{-\lambda_1 t} J_0(2\pi\nu_1 t + \phi_1) + A_1 e^{-\lambda_2 t} J_0(2\pi\nu_2 t + \phi_2) + A_2 e^{-\lambda_3 t} \quad (6.6)$$

The fit using equation 6.6 is shown in Fig. 6.12d. Compared to the fit using equation 6.2 in Fig. 6.12c, the fit involving Bessel functions clearly provides a superior description of the muon polarization. The use of Bessel functions implies the magnetic structure is incommensurate.

Commensurate structures have a magnetic periodicity that is related to the crystallographic periodicity by an integer or half-integer value of n ; where, magnetic unit cell = $n \times$ nuclear unit cell. In an incommensurate magnetic structure, n is not an integer or half-integer number, but an irrational number. When muons are implanted into a sample they can reside in a number of magnetically inequivalent sites at different positions within the crystal lattice. In a commensurate structure, the total number of magnetically inequivalent sites is finite due to the integer/half-integer relationship between the magnetic and nuclear unit cells. As a result, the muons located at the different muon sites experience a sharp distribution of local fields that can be described as Gaussian.¹⁸ Alternatively, in an incommensurate structure there are an infinite number of inequivalent muons sites. Each muon senses a different local field, resulting in a continuous distribution of local fields up to a maximum cut off field (B_{\max}).¹⁹ This type of field distribution is described using a first order Bessel function (equation 6.5).²⁰ With cosine functions the phase is constant; however Bessel functions introduce a constantly changing phase which can produce a phase shift.^{18,21,22} The data in Fig. 6.12d was only described well using equation 6.6 when the phases of the Bessel functions were non-zero. The phases derived from the fit were approximately the same magnitude but have opposite signs, with $\phi_1 = 33.9(4.2)^\circ$ and $\phi_2 = -35.9(4.4)^\circ$.

ZF measurements on warming in Fig. 6.13a show the oscillations decay and are no longer visible above 8 K. This indicates Zn^{2+} substitution lowered the transition temperature compared to $\text{Ba}_2\text{CuTeO}_6$ ($T_N = 14$ K). The ZF data above 1.5 K was fitted using equation 6.6 and the fitting parameters plotted in Fig. 6.13c-d. The values show the muon oscillations decay, with the values of the decay rates (λ_1 and λ_2) increasing as the spin fluctuations increase as the temperature rises to 10 K. Above 10 K the values of λ_1 and λ_2 are zero showing complete decay of the oscillations.

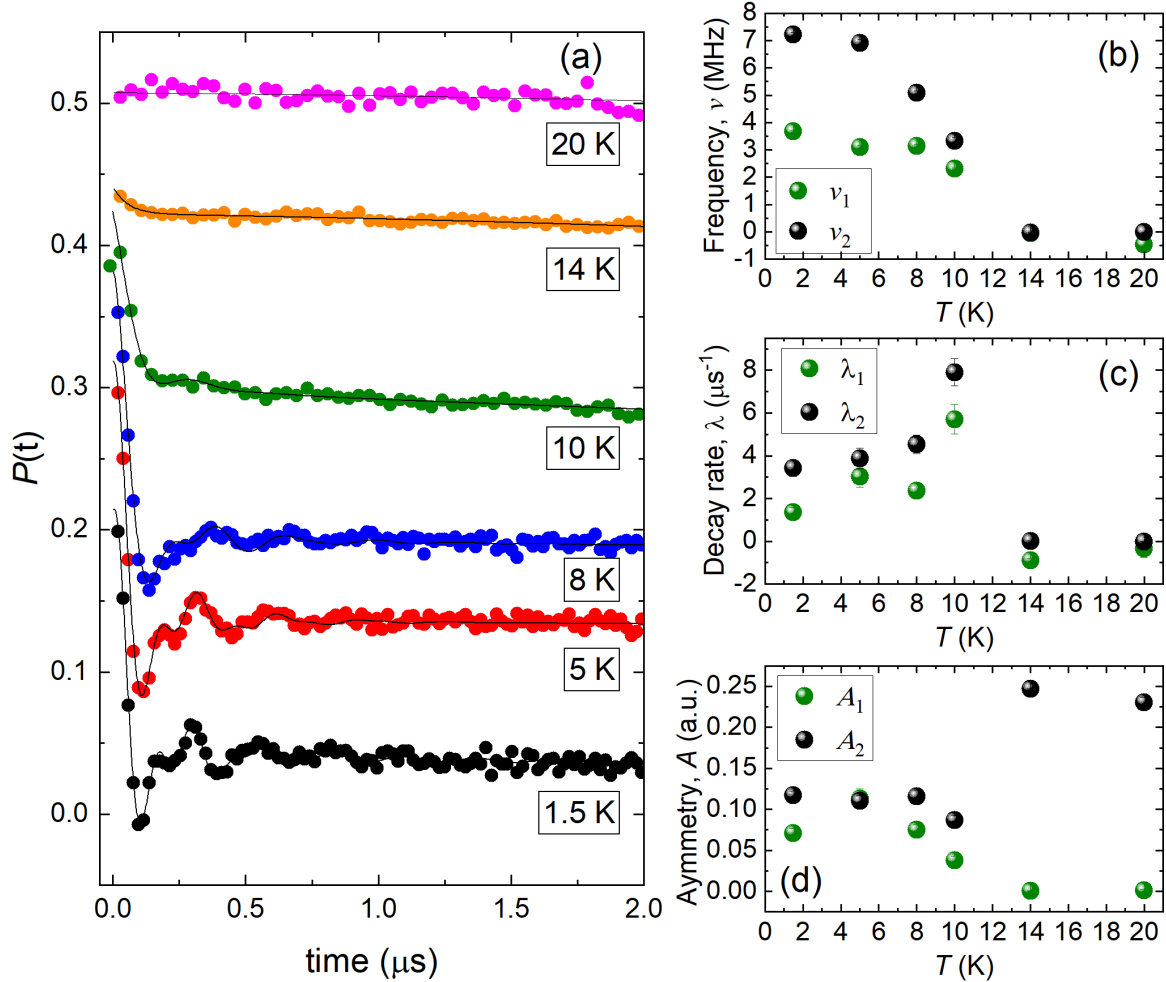


Fig. 6.13 (a) The ZF- μ SR data for $\text{Ba}_2\text{Cu}_{0.9}\text{Zn}_{0.1}\text{TeO}_6$ ($x = 0.1$) on warming between 1.5-20 K. The 1.5 K oscillations are damped as the temperature increases, with no clear oscillations observed above 8 K. Panels (b) to (d) show the values of the parameters obtained from the fit using equation 6.6. Panel (b) shows the values of the frequencies (ν_1 and ν_2); (c) the values of the decay rates (λ_1 and λ_2); and (d) the values of the asymmetries (A_1 and A_2); as a function of temperature.

$x = 0.2$

The ZF- μ SR data of $x = 0.2$ at 1.5 K is shown in Fig. 6.14a. Now there are no clear oscillations at 1.5 K showing the $x = 0.2$ sample is not long-range magnetically ordered. Instead, the ZF muon polarization sharply drops at low times, but then recovers 1/3 of the initial asymmetry at long times. Recovery of 1/3 of the initial asymmetry implies there is a static component to the magnetism. In a random statically ordered material, 1/3 of the initial asymmetry is retained as this represents the 1/3 fraction of spins in the direction of the muon spin along z . The remaining 2/3 of the spins perpendicular to z along the x and y directions are depolarized. This behaviour is described using the static Kubo-Toyabe function. The lack of a minimum and fast relaxation at low times indicates there is also a dynamic component to the magnetism. The combination of static and dynamic behaviour could be phenomenologically described using the dynamic Kubo-Toyabe function and an exponential term using equation 6.7.

$$P(t) = \left(g_z(t) + v \int_0^t g_z(t_1) P_z(t - t_1) dt_1 \right) + A_1 e^{-\lambda t} \quad (6.7)$$

$$g_z(t) = A_0 \left(\frac{1}{3} + \frac{2}{3} e^{-\frac{1}{2}\delta^2 t^2} (1 - \delta^2 t^2) \right) \quad (6.8)$$

$g_z(t)$ is the static Kubo-Toyabe function (defined in equation 6.8). ν is the muon hopping rate, λ the exponential decay rate and δ is the width of the local field distribution. Equation 6.7 was used to fit the 1.5 K ZF- μ SR data in Fig. 6.14a and the ZF data on warming in Fig. 6.15. Fig. 6.15c shows at low temperatures the muon hopping rate is close to zero, therefore the static Kubo-Toyabe function ($g_z(t)$) mainly contributes to the relaxation. This accounts for the 1/3 recovery of the initial asymmetry. Hence, at 1.5 K the spins are mostly frozen in the $x = 0.2$ sample. Fig. 6.15c shows the hopping rate increases on warming as spin fluctuations increase. λ is inversely proportional to ν , meaning as the hopping rate increases at higher temperatures, the muon feels more of an average field leading to a decrease in the muon decay rate in Fig. 6.15d. Fig. 6.15a shows the 1/3 tail is lost around 4 K implying spin freezing develops below this temperature.

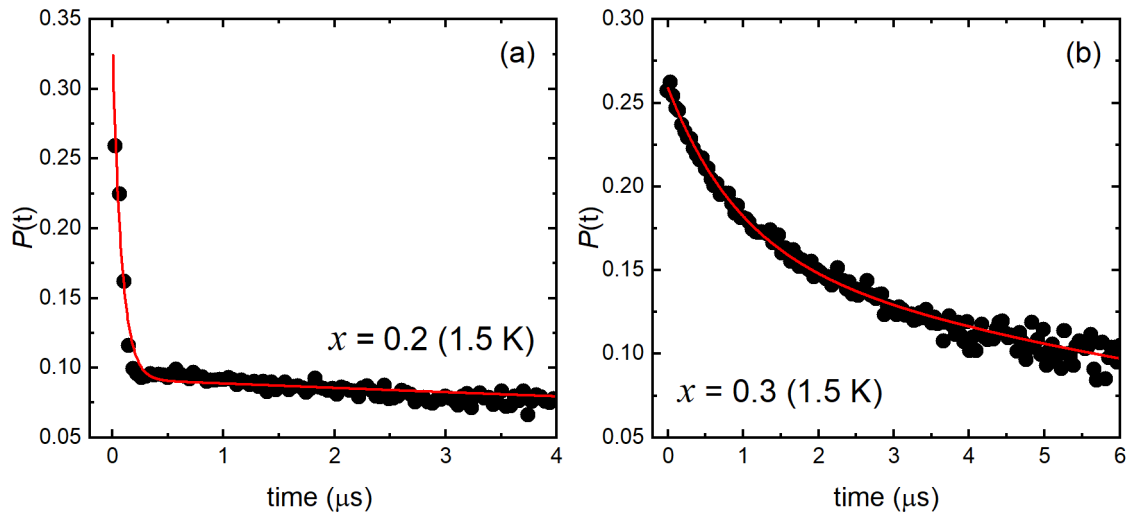


Fig. 6.14 (a) The $Ba_2Cu_{0.8}Zn_{0.2}TeO_6$ ($x = 0.2$) ZF- μ SR data at 1.5 K. Fitting (shown by the solid red line) was performed using the muon polarization function in equation 6.7. Recovery of 1/3 of the initial asymmetry implies a static disordered contribution to the relaxation. The fast relaxation at low times indicates there is also a dynamic component to the relaxation. (b) The $Ba_2Cu_{0.7}Zn_{0.3}TeO_6$ ($x = 0.3$) ZF- μ SR data at 1.5 K. No clear oscillations or recovery of 1/3 of the initial asymmetry is observed implying a mainly dynamic magnetic environment. The data was fitted using equation 6.11 which uses two exponential functions to account for the two muon sites.

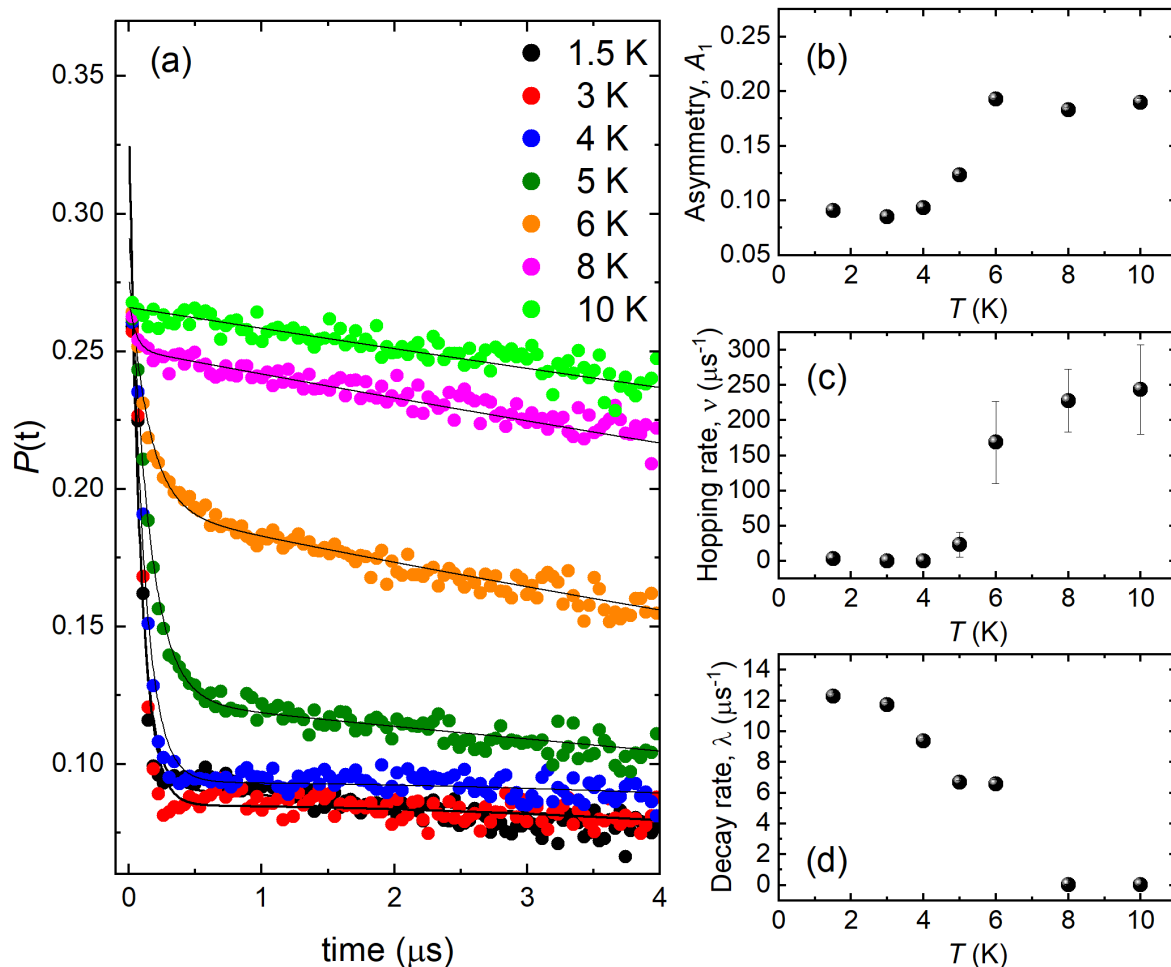


Fig. 6.15 (a) The ZF- μ SR data of $\text{Ba}_2\text{Cu}_{0.8}\text{Zn}_{0.2}\text{TeO}_6$ ($x = 0.2$) between 1.5-10 K. The data were fitted using the muon polarization function in equation 6.7. The parameters obtained from the fit are plotted as a function of temperature (T) in panels (b) - (d). Panel (b) shows the initial asymmetry (A_1), (c) the muon hopping rate (ν) and (d) the exponential decay rate (λ).

The $x = 0.2$ ZF- μ SR data also resembles that of a spin glass. The AC susceptibility data provided no indication of spin glass behaviour. To confirm, the $x = 0.2$ ZF- μ SR data was also fitted using stretched exponentials (equation 6.9).

$$P(t) = Ae^{(-\lambda t)^\beta} \quad (6.9)$$

Here, A is the initial asymmetry, λ is the decay rate and β is the stretching exponent. A value of $\beta = 1$ indicates a typical exponential relaxation, $\beta = 2$ indicates a Gaussian relaxation and $\beta < 0.5$ indicates a spin glass.²²⁻²⁴ The ZF- μ SR data was fitted using a combination of two stretched exponentials and an exponential term to describe the background. While seemingly providing a good fit, the values obtained for β were meaningless ($\beta_1 = 2.95$ and $\beta_2 = -2.9$) and do not indicate spin glass behaviour.

$x = 0.3$

The ZF- μ SR data for $x = 0.3$ at 1.5 K in Fig. 6.14b shows no indication of magnetic ordering. There are no oscillations or 1/3 recovery of the initial asymmetry. Instead, the muon polarization relaxes exponentially reflecting a dynamic muon environment. The muon polarization was described using a

combination of two exponential relaxation functions to account for the two muon sites. The equation for $P(t)$ is given below:

$$P(t) = A_1 e^{-\lambda_1 t} + A_2 e^{-\lambda_2 t} \quad (6.10)$$

The fit in Fig. 6.14b describes the muon polarization well. Fig. 6.16a shows the ZF- μ SR data on warming. Above 1.5 K, the high temperature muon polarization is quickly recovered. The initial asymmetries (A_1 and A_2) determined from the fits are plotted as a function of temperature in Fig. 6.16b. As the temperature approaches 5 K, the value of A_2 decreases towards zero while A_1 increases to a plateau showing the high temperature muon polarization is recovered above 5 K. This is in agreement with the values of the decay rates λ_1 and λ_2 in Fig. 6.16c and Fig. 6.16d, respectively. The value of λ_2 is much higher at low temperatures compared to λ_1 showing the majority of the low temperature relaxation is accounted for by the second exponential term. The value of λ_2 increases as the field fluctuation increases above 1.5 K. λ_2 increases up to 5 K, after which the value falls indicating the field fluctuation rate is on a timescale faster than the muon relaxation rate.

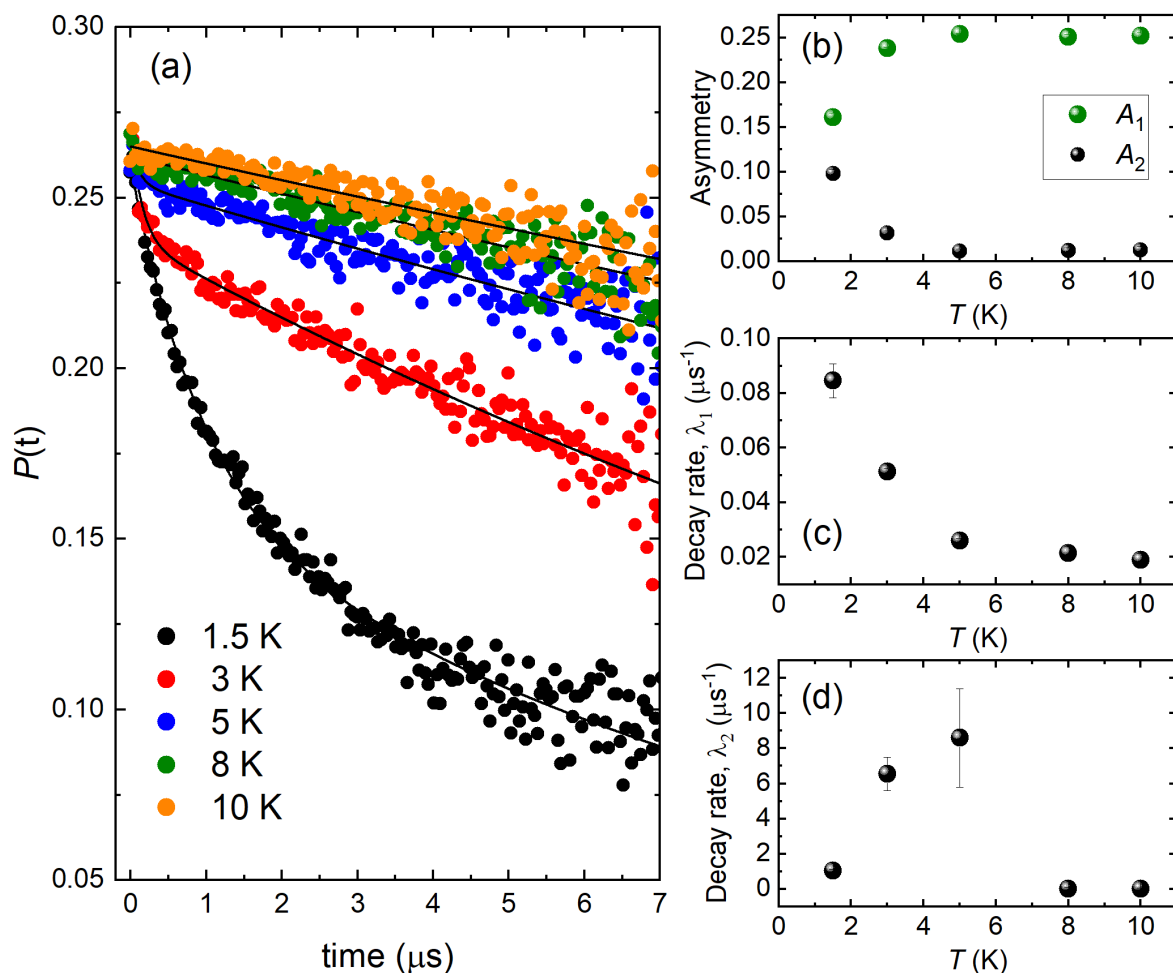


Fig. 6.16 (a) The ZF- μ SR data of $\text{Ba}_2\text{Cu}_{0.7}\text{Zn}_{0.3}\text{TeO}_6$ ($x = 0.3$) between 1.5-10 K. The data were fitted using the muon polarization function in equation 6.10. The parameters obtained from the fit are plotted as a function of temperature (T) in panels (b)-(d); where (b) shows the initial asymmetries (A_1 and A_2) and (c) and (d) are the decay rates, λ_1 and λ_2 , of the respective exponential terms.

Transverse-Field (TF)- μ SR measurements

Transverse-field (TF)- μ SR measurements were performed on the $x = 0.1, 0.2$ and 0.3 samples at temperatures between 1.5 - 20 K. A 30 G transverse-field was applied and the muon response measured. At 20 K, the muon spins oscillated in the direction of the applied TF field. On cooling, dampening of the TF oscillation was clearly observed for $x = 0.1$ and $x = 0.2$. This indicates static magnetic ordering as the muon spins begin to decouple from the TF field and couple to the developing internal magnetic field. The TF- μ SR data for $x = 0.1$ and $x = 0.2$ are shown in Fig. 6.17a and Fig. 6.17b, respectively. The TF asymmetry ($A_T(T)$) was determined by fitting the TF- μ SR data using equation 6.11.

$$P(t) = A_L e^{-\lambda_L t} + A_T e^{-\lambda_T t} \cos(2\pi f t + \phi) + A_{Bkgd} e^{-\lambda_L t} \quad (6.11)$$

By plotting the normalized TF asymmetry ($A_T(T)/A_T(40\text{ K})$) as a function of temperature (T) the transition temperatures were determined. Fig. 6.17d shows the value of $A_T(T)/A_T(40\text{ K})$ decreases gradually on cooling for both $x = 0.1$ and $x = 0.2$. The transitions are gradual, occurring over a wide temperature range. The value of $A_T(T)/A_T(40\text{ K})$ approaches zero at 8 K for $x = 0.1$ showing long-range magnetic order is complete. For $x = 0.2$, the value of $A_T(T)/A_T(40\text{ K})$ plateaus to a constant value below 4 K indicating spin freezing is complete below 4 K. It was noted that the value of $A_T(T)/A_T(40\text{ K})$ does not completely go to zero and there are still weak oscillations visible in the TF- μ SR data of $x = 0.2$ at 1.5 K in Fig. 6.17b, whereas the TF oscillations were completely damped for $x = 0.1$ in Fig. 6.17a. This suggests a small $\sim 6\%$ dynamic fraction exists at 1.5 K for $x = 0.2$.

While the ZF- μ SR data for $x = 0.3$ suggests a purely dynamic system, dampening of the TF oscillations was observed on cooling as the temperatures approached 1.5 K. Slight dampening of the TF oscillations can be seen in the TF- μ SR data for $x = 0.3$ in Fig. 6.17c. This suggests a small fraction of frozen spins. The $A_T(T)/A_T(40\text{ K})$ data for $x = 0.3$ in Fig. 6.17d shows dampening occurs below 10 K. From the ratio of the $A_T(T)/A_T(40\text{ K})$ value at 1.5 K and 20 K, the frozen fraction was calculated to be $\sim 14\%$.

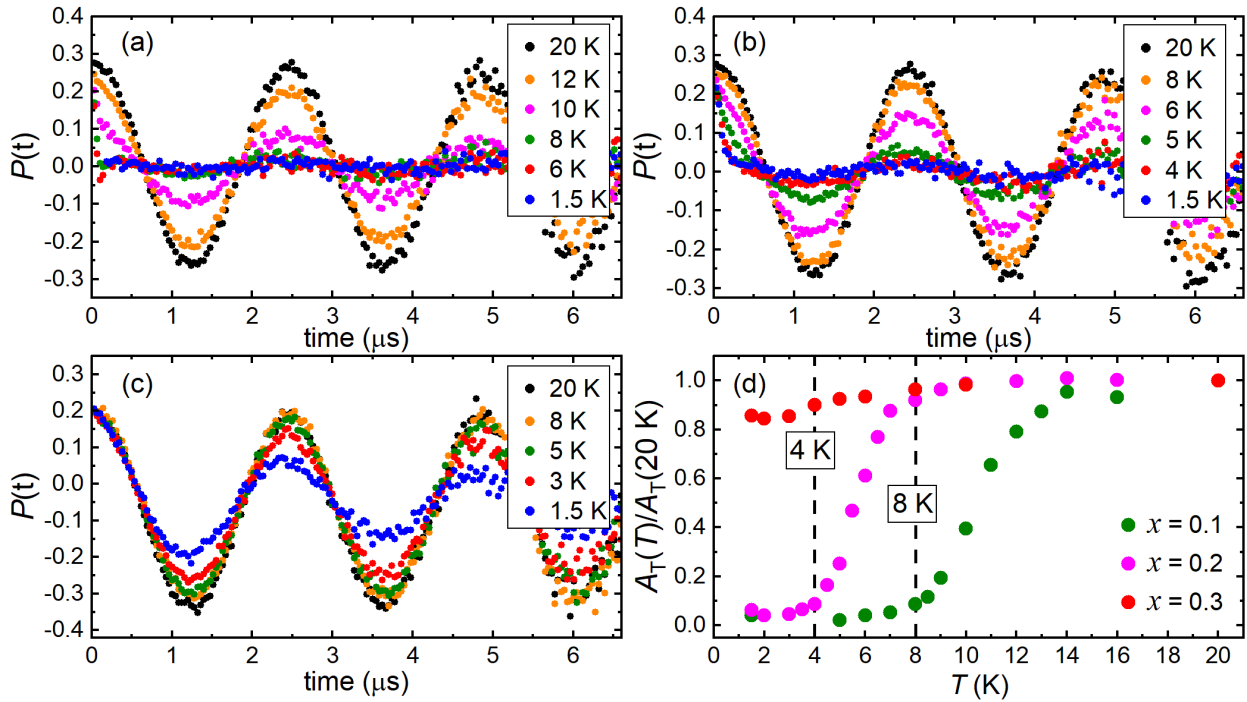


Fig. 6.17 The TF- μ SR data for (a) $\text{Ba}_2\text{Cu}_{0.9}\text{Zn}_{0.1}\text{TeO}_6$ ($x = 0.1$), (b) $\text{Ba}_2\text{Cu}_{0.8}\text{Zn}_{0.2}\text{TeO}_6$ ($x = 0.2$) and (c) $\text{Ba}_2\text{Cu}_{0.7}\text{Zn}_{0.3}\text{TeO}_6$ ($x = 0.3$) collected between 1.5-20 K using a TF field of 30 G. Complete dampening is observed for $x = 0.1$, and the TF oscillations for $x = 0.2$ are almost completely damped. Only slight dampening is observed for $x = 0.3$ showing only partial freezing of the magnetic moments. The TF asymmetry ($A_T(T)$) was determined by fitting the data using equation 6.9. The normalized $A_T(T)/A_T(40\text{ K})$ is plotted as a function of temperature (T) for the $x = 0.1$, $x = 0.2$ and $x = 0.3$ samples in panel (d).

Longitudinal-field (LF)- μ SR measurements

Longitudinal-field (LF)- μ SR measurements were performed at 1.5 K on the $x = 0.1$, 0.2 and 0.3 samples using LF fields between 50-1000 G. The LF- μ SR measurements in Fig. 6.18 help to indicate the strength of the LF field required to decouple the muon spin from the magnetic moments in the sample, hence providing information on the nature of the sample magnetic moments. The data for $x = 0.1$ in Fig. 6.18a shows only above 100 G did the muons begin to decouple from the internal magnetic field and repolarize in the direction of the LF field. Complete repolarization occurs between the relatively weak LF fields of 500-1000 G owing to the weak Cu^{2+} moment and quantum fluctuations. Small decoupling was observed at 50 G, and represents decoupling from weaker static nuclear magnetic moments. The data above 100 G represents decoupling from stronger electronic magnetic moments.

Repolarization requires weaker LF fields for $x = 0.2$. Decoupling from the internal fields is clearly visible at 100 G in the $x = 0.2$ LF- μ SR data in Fig. 6.18b. Stronger repolarization below 100 G is likely to represent decoupling from a combination of dynamic and static electronic spins, as well as static nuclear spins. The muon spin is almost fully repolarized at fields of 500 G.

The behaviour of $x = 0.3$ is different to the other samples. The data in Fig. 6.18c shows the muon polarization is gradually recovered as the LF field increases. As with the other samples, decoupling from static nuclear spins, as well as electronic spins, contributes to the repolarization below 100 G.

The gradual recovery above 50 G is typical of the LF field repolarization of a system with dynamic electronic spins.

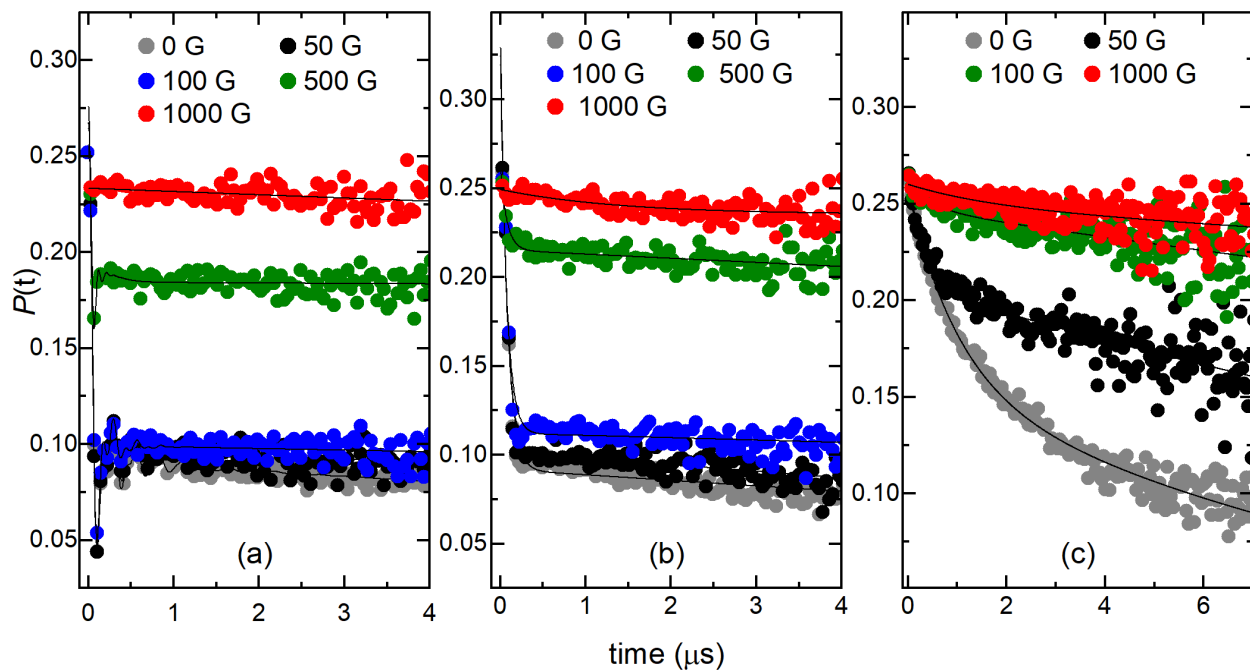


Fig. 6.18 The LF- μ SR data of (a) $\text{Ba}_2\text{Cu}_{0.9}\text{Zn}_{0.1}\text{TeO}_6$ ($x = 0.1$), (b) $\text{Ba}_2\text{Cu}_{0.8}\text{Zn}_{0.2}\text{TeO}_6$ ($x = 0.2$) and (c) $\text{Ba}_2\text{Cu}_{0.7}\text{Zn}_{0.3}\text{TeO}_6$ ($x = 0.3$) measured at 1.5 K using LF fields between 50-1000 G. The 0 G ZF- μ SR data is shown for comparison.

5. Discussion

The X-ray and neutron data confirmed successful Cu^{2+} substitution for Zn^{2+} in $\text{Ba}_2\text{Cu}_{1-x}\text{Zn}_x\text{TeO}_6$, with the results from structural characterization agreeing with previous reports. Magnetic characterization showed the spin ladder behaviour changed upon introduction of Zn^{2+} , and might represent segmentation of the spin ladders. The DC susceptibility data shows weakening of the magnetic interactions from the increase in the Weiss constant (θ_W) and decrease in the effective magnetic moment between $x = 0$ to $x = 0.6$. θ_W increases towards zero showing the interactions become increasingly paramagnetic-like. A large paramagnetic tail developed upon introduction of Zn^{2+} . The paramagnetic tail grew with increasing x , implying an increasing concentration of ‘free spins’ as Zn^{2+} breaks the spin ladder interactions. The DC susceptibility data did not reveal whether the introduction of ‘free’ spins prevented antiferromagnetic ordering due to the weak magnetism in these samples. Therefore, muon spin relaxation (μ SR) experiments were performed.

The μ SR experiments on GPS provided more detailed information about the muon environment in $\text{Ba}_2\text{CuTeO}_6$ compared to the HIFI data. There were two oscillations in the 1.5 K $x = 0$ ZF- μ SR data, indicating the presence of two muon stopping sites. To reflect this, two components were employed when fitting the $\text{Ba}_2\text{CuTeO}_6$ and $\text{Ba}_2\text{Cu}_{1-x}\text{Zn}_x\text{TeO}_6$ data to describe the two muon sites. There were clear oscillations in the $x = 0.1$ data showing 10% Zn^{2+} does not prevent ordering. The transition temperature was reduced from $T_N(x = 0) = 14$ K to $T_N(x = 0.1) = 8$. The low temperature oscillations at 1.5 K were described well using Bessel functions with non-zero phases instead of cosines. The use of Bessel functions implies the magnetic structure of $\text{Ba}_2\text{Cu}_{0.9}\text{Zn}_{0.1}\text{TeO}_6$ is incommensurate. The phases were of the same magnitude, but with opposite signs. This could imply a helical

incommensurate structure composed of two helices that are out-of-phase with each other. Low temperature neutron diffraction experiments are required to confirm this. This would show how closely the low temperature magnetic structure resembles a two-leg spin ladder.

No clear oscillations were observed for $x = 0.2$, although recovery of 1/3 of the initial asymmetry implies static magnetic ordering. The relaxation could be described using the combination of a dynamic Kubo-Toyabe function and an exponential relaxation term. Dampening of the transverse-field (TF)- μ SR oscillations confirmed the establishment of a static magnetic state below 4 K. The transition occurred gradually and does not represent long-range magnetic order or a spin glass. Instead, 1/3 recovery implies the presence of a long-range disordered static magnetic state, generated by segmentation of the ladders by Zn^{2+} . This might create fragments of ladder interactions that are statically ordered within the fragment, but between fragments are long-range disordered. The fast muon relaxation at low times and weak TF oscillations at 1.5 K imply there is also a dynamic contribution, most likely from free Cu^{2+} spins introduced by Zn^{2+} .

The zero-field muon environment in $x = 0.3$ appears to be completely dynamic at 1.5 K, with no oscillations or 1/3 recovery of the initial asymmetry. However, the TF- μ SR data on cooling shows slight dampening of the TF asymmetry below 10 K. At 1.5 K, $\sim 14\%$ of the spins are 'frozen' while the majority are dynamic. Dilution fridge experiments are required to determine whether the frozen fraction increases below 1.5 K. Based on these findings it is expected the frozen fraction will be further diminished or non-existent in the $x \geq 0.4$ samples. Therefore, even if further spin freezing occurs below 1.5 K in $x = 0.3$, the magnetic interactions are unlikely to resemble a two-leg spin ladder beyond $x = 0.3$ due to extensive segmentation of the ladder interactions.

6. Conclusions

The Cu^{2+} spin ladder cations were successfully substituted for non-magnetic Zn^{2+} in $\text{Ba}_2\text{Cu}_{1-x}\text{Zn}_x\text{TeO}_6$. This demonstrates the hexagonal $\text{Ba}_2\text{CuTeO}_6$ structure can accommodate chemical substitution at the magnetic B' site and non-magnetic B'' site. Comparing the magnetic properties of $\text{Ba}_2\text{Cu}_{1-x}\text{Zn}_x\text{TeO}_6$ to that of $\text{Ba}_2\text{CuTeO}_6$ showed a clear change in the magnetic behaviour. The DC susceptibility data indicated the introduction of 'free' spins and weakening of the antiferromagnetic interactions. The muon spin relaxation data shows Zn^{2+} prevented long-range magnetic ordering beyond $x = 0.2$, however it remains unclear how closely the magnetic interactions in $\text{Ba}_2\text{Cu}_{1-x}\text{Zn}_x\text{TeO}_6$ resemble that of a Néel ordered spin ladder. The muon data for $x = 0.1$ implies the magnetic structure might be incommensurate. Neutron diffraction studies are required to establish this and determine whether the extended two-leg spin ladder structure is retained upon Zn^{2+} substitution.

7. References

1. Johnston, D. C. *et al.* Magnetic Susceptibilities of Spin-1/2 Antiferromagnetic Heisenberg Ladders and Applications to Ladder Oxide Compounds. *arXiv:cond-mat/0001147 [cond-mat]* (2000).
2. Nagaosa, N., Furusaki, A., Sigrist, M. & Fukuyama, H. Nonmagnetic Impurities in Spin Gap Systems. *J. Phys. Soc. Japan* **65**, 3724–3727 (1996).
3. Iino, Y. & Imada, M. Effects of Nonmagnetic Impurity Doping on Spin Ladder System. *Journal*

of the Physical Society of Japan **65**, 3728–3731 (1996).

4. Kanbur, U., Polat, H. & Vatansever, E. Thermal properties of rung-disordered two-leg quantum spin ladders: Quantum Monte Carlo study. *Phys. Rev. E* **102**, 042104 (2020).
5. Schmidiger, D. *et al.* Emergent Interacting Spin Islands in a Depleted Strong-Leg Heisenberg Ladder. *Phys. Rev. Lett.* **116**, 257203 (2016).
6. Krasnikova, Y. V. *et al.* Electron spin resonance study of spin relaxation in the strong-leg spin ladder with nonmagnetic dilution. *Phys. Rev. B* **100**, 144446 (2019).
7. Fukaya, A., Higemoto, W., Hagiwara, M. & Nagamine, K. μ SR study of a spin ladder system $(\text{Cu}_{1-x}\text{Zn}_x)_2(1,4\text{-diazacycloheptane})_2\text{Cl}_4$. *Phys. B* **289–290**, 189–193 (2000).
8. Bobroff, J. *et al.* Impurity-induced magnetic order in low-dimensional spin-gapped materials. *Phys. Rev. Lett.* **103**, 047201 (2009).
9. Mikeska, H., Neugebauer, U. & Schollwöck, U. Spin ladders with nonmagnetic impurities. *Phys. Rev. B* **55**, 2955–2963 (1997).
10. Kohl, P. & Reinen, D. Structural and Spectroscopic Investigations on $\text{Ba}_2\text{CuTeO}_6$. *Zeitschrift für Anorg. Und Allg. Chemie* **409**, 257–272 (1974).
11. Gibbs, A. S. *et al.* $S = 1/2$ quantum critical spin ladders produced by orbital ordering in $\text{Ba}_2\text{CuTeO}_6$. *Phys. Rev. B* **95**, 104428 (2017).
12. Glamazda, A. *et al.* Quantum criticality in the coupled two-leg spin ladder $\text{Ba}_2\text{CuTeO}_6$. *Phys. Rev. B* **95**, 184430 (2017).
13. Toby, B. H. & Von Dreele, R. B. GSAS-II: the genesis of a modern open-source all purpose crystallography software package. *J. Appl. Cryst.* **46**, 544–549 (2013).
14. Mccusker, L. B., Dreele, R. B. Von, Cox, D. E., Loue, D. & Scardi, P. Rietveld refinement guidelines. *J. Appl. Cryst.* **32**, 36–50 (1999).
15. Flores, A. V. *et al.* Comparison of the crystal chemistry of tellurium (VI), molybdenum (VI), and tungsten (VI) in double perovskite oxides and related materials. *Prog. Solid State Chem.* **56**, 100251 (2019).
16. Cussen, E. J., Gibbs, A. S., Mustonen, O. H. J. & Pughe, C. E. Structural Distortion and Magnetic Transitions in Spin Ladder Compounds $\text{Ba}_2\text{CuTe}_{1-x}\text{W}_x\text{O}_6$.
17. Pughe, C. *et al.* Site-Selective d^{10}/d^0 Substitution in an $S = 1/2$ Spin Ladder $\text{Ba}_2\text{CuTe}_{1-x}\text{W}_x\text{O}_6$ ($0 \leq x \leq 0.3$). *Inorg. Chem.* **61**, 4033–4045 (2022).
18. Blundell, S. J. Spin-polarized muons in condensed matter physics. *Contemp. Phys.* **40**, 175–192 (1999).
19. de Réotier, P. D. *et al.* On the robustness of the MnSi magnetic structure determined by muon spin rotation. *Quantum Beam Sci.* **2**, 19 (2018).
20. Amato, A. *et al.* Muon-spin-relaxation studies on the heavy-fermion system with non-Fermi-liquid behavior $\text{CeCu}_{5.9}\text{Au}_{0.1}$. *Phys. Rev. B* **52**, 54–56 (1995).
21. Amato, A. Heavy-fermion systems studied by μ SR technique. *Rev. Mod. Phys.* **69**, 1119–1179 (1997).

22. Dalmas de Réotier, P. & Yaouanc, A. Muon spin rotation and relaxation in magnetic materials. *J. Phys. Condens. Matter* **9**, 9113–9166 (1997).
23. Campbell, I. A. *et al.* Dynamics in canonical spin glasses observed by muon spin depolarization. *Phys. Rev. Lett.* **72**, 1291–1294 (1994).
24. Binder, K. & Young, A. P. Spin glasses: Experimental facts, theoretical concepts, and open questions. *Rev. Mod. Phys.* **58**, 801–976 (1986).

Conclusions and further work

Non-magnetic d^{10} and d^0 cations have been studied in double and hexagonal $A_2B'B''O_6$ perovskites. Using a simple cubic $Ba_2Mn(Te/W)O_6$ double perovskite, the underlying causes of the d^{10}/d^0 effect were understood. Differences in the dominant superexchange pathway arise due to the limited contribution of the d^0 cation towards next-nearest neighbour (J_2) superexchange. This leads to the d^{10}/d^0 effect, where d^{10} cations promote a strong nearest neighbour (J_1) and near-zero J_2 interaction, whereas d^0 cations promote as strong J_2 and suppressed J_1 interaction. The d^{10}/d^0 effect is observed in a number of antiferromagnetically ordered Te^{6+} and W^{6+} double perovskites, as well as Mo^{6+} perovskites.

Having established the d^{10}/d^0 effect, more complex perovskite structures were investigated. The hexagonal Ba_2CuTeO_6 perovskite allowed d^{10}/d^0 interactions to be studied in a corner- and face-sharing structure, instead of a purely corner-sharing double perovskite. Ba_2CuTeO_6 also has a similar Cu^{2+} magnetic geometry to the $Sr_2CuTe_{1-x}W_xO_6$ perovskite structure, where mixtures of d^{10} and d^0 cations suppress magnetic ordering. W^{6+} substitution in Ba_2CuTeO_6 was shown to occur site-selectively at the corner-sharing site. This modified the Cu^{2+} spin ladder interactions, tuning the system from a spin ladder towards a spin-chain. Muon spin relaxation experiments indicated suppressed magnetic ordering when $x \geq 0.05$ in $Ba_2CuTe_{1-x}W_xO_6$. The exact nature of the ground state is unclear without further inelastic neutron scattering experiments. d^{10}/d^0 mixtures could be a useful tool for tuning ordered perovskites into the realms of magnetic disorder. The technique could be shown to be universal if d^{10}/d^0 mixtures were studied in other systems. It would be interesting to observe whether the d^{10} - strong J_1 vs d^0 - strong J_2 competition suppresses magnetic ordering in $Ba_2MnTe_{1-x}W_xO_6$. Different behaviours might also be garnered for Mo^{6+} substitution in Ba_2CuTeO_6 . The strong selectivity for the corner-sharing site is still expected as face-sharing is unfavourable for Mo^{6+} d^0 cations.

The effect of non-magnetic cations at the magnetic B' site was also investigated in $Ba_2Cu_{1-x}Zn_xTeO_6$. The magnetic $S = \frac{1}{2}$ Cu^{2+} spin ladder cations were substituted for non-magnetic Zn^{2+} ($3d^{10}$). There was a change in the magnetic behaviour with large paramagnetic tails in the susceptibility indicating generation of 'free spins' due to segmentation of the ladder interactions by Zn^{2+} . Muon analysis indicates long-range ordering for $x = 0.1$ and spin freezing for $x = 0.2$. The behaviour of $x = 0.3$ was mostly dynamic, with a small frozen fraction ($\sim 14\%$) occurring at 1.5 K. Further muon experiments are required to learn whether the frozen fraction increases below 1.5 K. Neutron diffraction experiments would provide more information on the magnetic structure of $x = 0.1$ and determine whether it is incommensurate. This, along with inelastic neutron scattering experiments, would help determine whether the extended spin ladder structure remains intact upon Zn^{2+} substitution. At present, this work shows non-magnetic cations can garner a range of behaviours through chemical substitution at either the B' or B'' site in Ba_2CuTeO_6 .